Ducted Fan Aerodynamics and Modeling, with Applications of Steady and Synthetic Jet Flow Control

Osgar John Ohanian III

Dissertation submitted to the faculty of the Virginia Polytechnic Institute and State University in partial fulfillment of the requirements for the degree of

Doctor of Philosophy
In
Mechanical Engineering

Daniel J. Inman, Committee Chair
Kevin B. Kochersberger
Andrew J. Kurdila
William H. Mason
Sam B. Wilson

May 4th, 2011
Blacksburg, VA

Keywords: ducted fan, shrouded propeller, synthetic jets, flow control, aerodynamic modeling, non-dimensional, unmanned aerial vehicle, micro air vehicle

Ducted Fan Aerodynamics and Modeling, with Applications of Steady and Synthetic Jet Flow Control

Osgar John Ohanian III

ABSTRACT

Ducted fan vehicles possess a superior ability to maximize payload capacity while minimizing vehicle size. Their ability to both hover and fly at high speed is a key advantage for information-gathering missions, particularly when close proximity to a target is essential. However, the ducted fan's aerodynamic characteristics pose difficulties for stable vehicle flight and therefore require complex control algorithms. In particular, they exhibit a large nose-up pitching moment during wind gusts and when transitioning from hover to forward flight.

Understanding ducted fan aerodynamic behavior and how it can be altered through flow control techniques are the two prime objectives of this work. This dissertation provides a new paradigm for modeling the ducted fan's nonlinear behavior and new methods for changing the duct aerodynamics using active flow control. Steady and piezoelectric synthetic jet blowing are employed in the flow control concepts and are compared.

The new aerodynamic model captures the nonlinear characteristics of the force, moment, and power data for a ducted fan, while representing these terms in a set of simple equations. The model attains excellent agreement with current and legacy experimental data using twelve non-dimensional constants.

Synthetic jet actuators (SJA) have potential for use in flow control applications in UAVs with limited size, weight, and power budgets. Piezoelectric SJAs for a ducted fan vehicle were developed through two rounds of experimental designs. The final SJA design attained peak jet velocities in the range of 225 ft/sec (69 m/s) for a 0.03" x 0.80" rectangular slot.

To reduce the magnitude of the nose-up pitching moment in cross-winds, two flow control concepts were explored: flow separation control at the duct lip, and flow turning at the duct trailing edge using a Coandă surface. Both concepts were experimentally proven to be successful. Synthetic jets and steady jets were capable of modifying the ducted fan flow to reduce pitching moment, but some cases required high values of steady blowing to create significant responses. Triggering leading edge separation on the duct lip was one application where synthetic jets showed comparable performance to steady jets operating at a blowing coefficient an order of magnitude higher.

Acknowledgements

"Trust in the Lord with all your heart, and lean not on your own understanding, in all you ways acknowledge Him, and He shall direct your paths." Proverbs 3:5-6

"Delight yourself in the Lord, and He will give you the desires of your heart." Psalm 37:4

"I am the vine, you are the branches. He who abides in Me, and I in him, bears much fruit; for without Me you can do nothing." -Jesus speaking in John 15:5

First and foremost, I would like to thank my loving Creator for making me a curious being who loves to explore His creation and for giving me the opportunity to write this dissertation. Without Him, I can do nothing.

Next, I would like to thank my supportive and loving wife, Robin, who has made this arduous journey much more pleasant. Her love and helpful spirit have motivated me to achievements beyond my own expectations.

To my children, Ansley, Caleb, Jacob, and Charlotte, thank you for brightening my days when I was uncertain whether I would ever finish, and for your patience when Daddy was busy. I hope to pass on to you my life-long love of learning and exploration of God's creation.

I would like to thank my dad, John, for being a role model in godliness, work ethic, integrity, and care for others. I can't imagine what I would be without your loving guidance over the course of my life.

I would like to thank my mom, Mary, for her spontaneous nature, love of people, and appreciation for education. Mom, I love you, and I couldn't have done this without you.

For my stepmom, Kim, I wish I could have finished this while you were here, but I know you are cheering me on from heaven. I am rejoicing for your freedom from suffering, and look forward to joining you at the celebration banquet table some day.

I would like to thank my advisor, Dr. Dan Inman, for accepting this unconventional Ph.D. student, never losing faith that I would finish, and

encouraging me all along the way. I have learned more from you than you probably realize.

I would like to thank my committee, which includes Dr. Kevin Kochersberger, Dr. Bill Mason, Dr. Andrew Kurdila, and the Right Reverend of the STOVL Faithful, Sam Wilson. Your time and service is sincerely appreciated, and your insights and input to my work have been valuable.

To all of my colleagues at AVID LLC, I owe great thanks for their encouragement, helpful collaboration, and creative ideas. Specifically I would like to thank Paul Gelhausen for allowing me the opportunity to pursue a PhD while working full time and supporting me along the way. Now I can get back to work.

I would also like to thank all the team members on my SBIR project that contributed to the larger research effort in one way or another. From AVID: Etan Karni, for helping in almost every aspect of the project; Kelly Londenberg, for his CFD work; Adam Entsminger, for his design insights; Chris Hickling, for all the CAD work; Brandon Stiltner, for help with simulations; Chris Olien, for help with experiments; Ignacio Guerrero, for help in vehicle sizing and design; Andy Turnbull, for help with fan designs; Dr. Andy Ko for his general insights; Scott Helsing, for his program management input; and Seth Taylor, for his aerodynamic modeling in Phase I. From Virginia Tech: Onur Bilgen, who pioneered MFC morphing control surfaces on our project; and Bill Otjens and Dr. William Devenport for their support at the Virginia Tech Stability Wind Tunnel. From Techsburg, Inc: Jon Fleming, Sarah Tweedie, and Matt Langford for their help fabricating the test model and executing the wind tunnel tests. From Honeywell Labs: Dale Enns and Eric Euteneuer, for their help in simulation and flight control insights. And from the Air Force Research Lab: James Davis, and Chris Perry, the Air Force program managers on my project.

I would like to acknowledge and thank the Air Force Research Lab/Munitions Directorate at Eglin AFB and the Air Force Office of Sponsored Research for funding this research.

Table of Contents

List of Figures

List of Tables

Chapter 1 Introduction and Motivation

Ducted fan vehicles are unique in many respects: they can hover, but are unlike helicopters; they can dash at high speeds, but are unlike airplanes. Much of the design intuition within the aerospace community is no longer applicable when venturing into the realm of vertical takeoff and landing (VTOL) ducted fan vehicle design. In this dissertation, I aim to clarify and deepen the understanding of ducted fan aerodynamics.

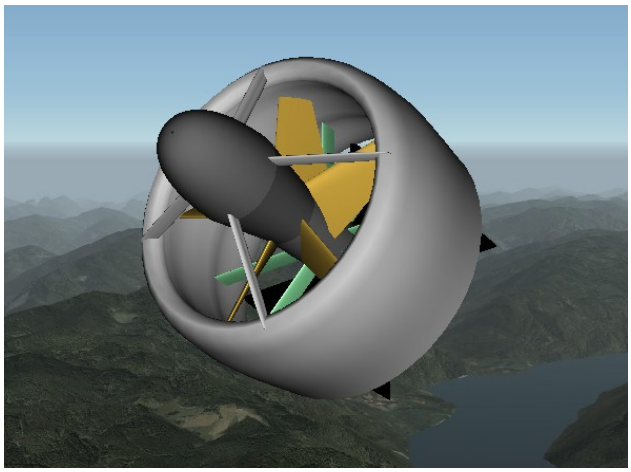

Figure 1-1. Notional ducted fan aircraft.

To orient the reader, a conceptual rendering of a ducted fan unmanned aerial vehicle (UAV) is shown in Figure 1-1. The "fan" is the propeller at the center of the vehicle, which is supported by the fuselage. The fuselage is connected to the duct by struts, and the duct encases the remaining internal components. The stators are located downstream of the fan, inside the duct, straightening the swirling flow induced by the fan. Finally, the control vanes are downstream of the stators, creating control forces and moments from the high-speed exit flow to stabilize and steer the vehicle.

Interest in ducted fan vehicles has grown in recent years as the UAV and micro air vehicle (MAV) market has expanded and the unique advantages of this vehicle configuration have been recognized as perfectly suited for certain

missions. Ducted fan UAVs takeoff vertically, hover, and tilt into the wind for high-speed flight in any direction. The vehicle can be used as a movable sensor, forward scout, or laser-targeting device [1], and in situations where up-close inspection of an area or object is critical. Some prominent examples of ducted fan UAVs are shown in Figure 1-2: the Honeywell RQ-16 T-Hawk, which has been deployed to military operations in Iraq [2]; the Allied Aerospace 29" iSTAR; the Aurora Flight Sciences GoldenEye; and the MASS HeliSpy.

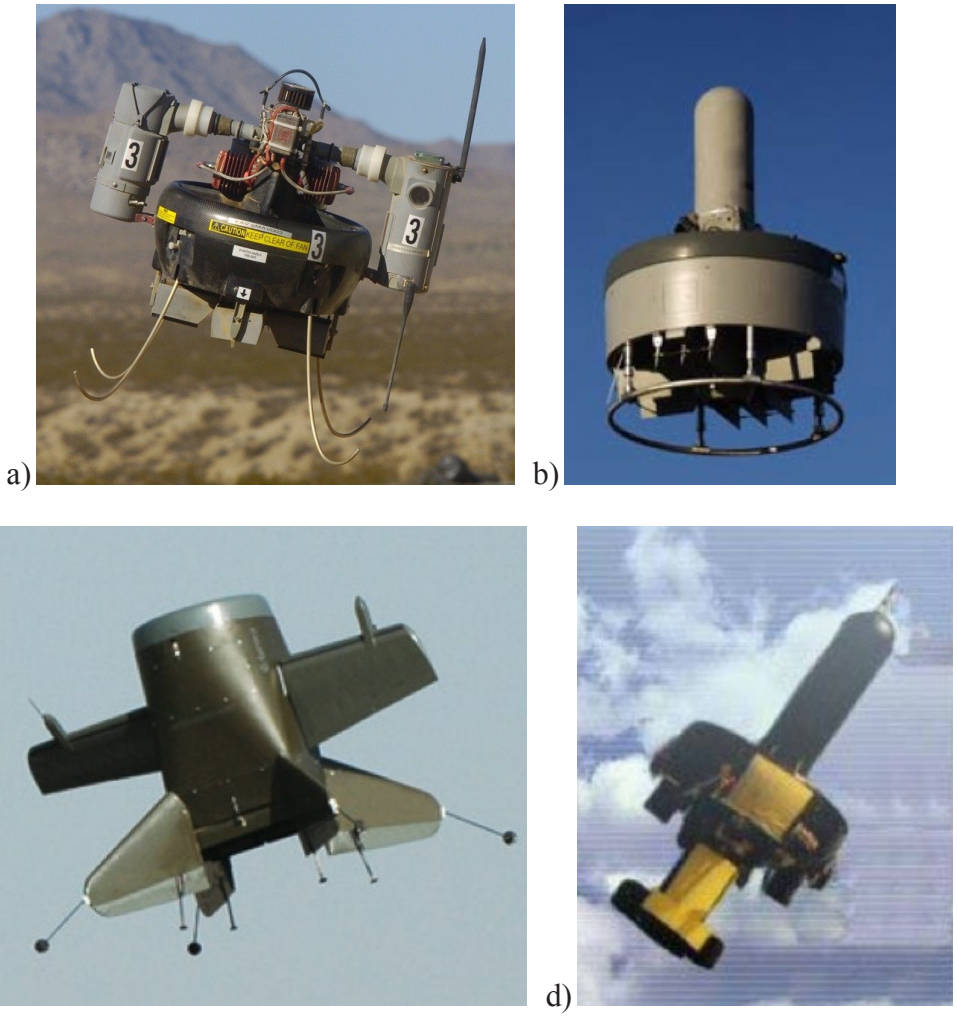

Figure 1-2. Example ducted fan unmanned air vehicles:
a) Honeywell RQ-16 T-Hawk (public domain[3]),
b) Allied Aerospace 29" iSTAR (public domain[4]),
c) Aurora Flight Sciences GoldenEye (public domain[5]),
d) MASS HeliSpy (public domain [4]).

Also known as a shrouded propeller, a ducted fan produces more thrust than a free propeller of the same diameter and of equivalent power [6]. In common terms, this means that ducted fans hover more efficiently than an open rotor or propeller. This greater efficiency is a consequence of the duct producing thrust and eliminating tip losses. In general, the pressures on the duct surface created by the flow induced by the fan contribute significantly to the overall forces and moments on the ducted fan unit. In particular, the high-speed flow into the duct causes a low-pressure region on the lip. This phenomenon results in a net force in the thrust direction during hover and can produce lift and pitching moment in forward flight [7]. Under certain conditions the flow over the duct lip can separate, affecting the thrust, lift, and pitching moment. This complex problem depends on lip geometry, angle of attack, free stream velocity, and fan RPM [8][9]. During transition from hover to cruise, which occurs at low speed and high angle of attack, ducted fans experience large nose-up pitching moments. This same phenomenon is also present while hovering in a crosswind. These conditions typically require the most control surface allocation within the flight envelope. While the duct enhances efficiency, it also generates the destabilizing pitching moment that is one of the key challenges in designing and controlling ducted fan vehicles.

1.1 Coordinate System

Ducted fans have been described using conventions from both airplane and helicopter perspectives. To avoid confusion, it is important to establish up front the reference frame used throughout this document to describe the forces, moments, and angle of attack. The “angle of attack”, also denoted as α, is defined as the angle between the thrust axis of the vehicle and the oncoming wind vector. A body-fixed coordinate system (one that rotates with the vehicle) will be used in all descriptions of the aerodynamics, and is depicted in Figure 1-3.

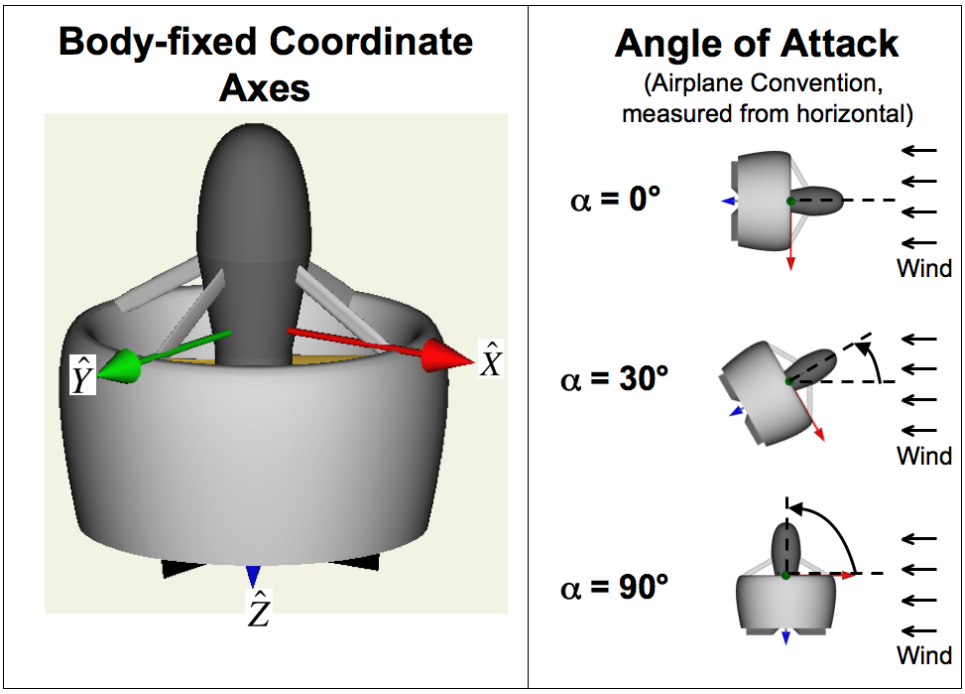

Figure 1-3. Vehicle body-fixed coordinate system and angle of attack convention.

The coordinate system for the vehicle has its origin at the intersection of the fan rotation axis with the plane of the highest point on the duct lip. All moments are referenced to this origin. The x-axis points radially out of the duct in the preferred flight direction; the y-axis points out the right side of the duct; and the z-axis points down the fan axis in the same direction as the fan flow. This results in thrust producing a negative force in the z-direction ($C_T = -C_Z$), and a positive normal force producing a negative force in the x-direction ($C_N = -C_X$). To illustrate the nose-up moment characteristics, a wind approaching the vehicle the negative x-axis direction would cause a positive moment about the y-axis (according to the "right hand rule"). This wind is equivalent to the vehicle traveling in the positive x-axis direction through still air.

The "airplane" convention for angle of attack is used throughout (also illustrated in Figure 1-3). In this convention $\alpha = 0^\circ$ orients the nose directly into the wind (also the condition for a pure vertical climb), and $\alpha = 90^\circ$ orients the vehicle vertically in a pure horizontal wind. Descent would equate to a 180° angle of attack, illustrating the large 180° angle of attack range of such a vehicle.

1.2 Comparison to Other UAV Configurations

Unmanned aerial vehicle designs show greater variety than manned aircraft designs because a cockpit and suitable conditions for a human pilot are not required. UAVs and MAVs presently serve in many roles and missions that are dangerous or impractical for human pilots. Military Intelligence, Surveillance, and Reconnaissance (ISR) missions are the primary use of UAVs at this stage in history. In the future, UAV roles will most likely expand into the commercial, industrial, agricultural, and law enforcement markets.

The majority of UAVs fall into the category of traditional, fixed-wing airplane designs. A classic example is the RQ-11 Raven, pictured in Figure 1-4, that has been deployed for U.S. military operations. Fixed-wing UAVs have a speed range centered on their most efficient cruise speed, with limited minimum and maximum flight speeds. For example, the RQ-11 depicted in Figure 1-4 has a minimum speed of 20 mph and a maximum speed of 50 mph [10]. While this type of configuration is suitable for long endurance flight, the minimum speed restricts its ability to inspect a fixed target on the ground. A fixed-wing UAV must circle a target site, banking and turning, attempting to keep its camera/sensor pointed at the region of interest, while not exceeding its minimum or maximum speed constraints. The plane's minimum turn radius limits how close it can get to the target. In contrast, a ducted-fan UAV can stop, hover, and investigate an area, rotating to pan the sensor right and left, zooming in and out. Observing much like a human would naturally investigate an area, this capability enables a more thorough and intuitive search of any target site. Therefore, the ducted fan's efficient hover capability is a distinct advantage for tactical and up-close ISR missions, while the configuration's maximum speed capability is comparable or even superior to fixed-wing designs of the same size. The configuration's ability to enter a building through

open doors or windows and fly in tight quarters would be very difficult to mimic with a fixed-wing vehicle.

Figure 1-4. Fixed-wing UAV example, AeroVironment RQ-11 Raven (public domain [11]).

Many fixed-wing UAVs are hand-launched or catapult-launched. They are typically recovered through deep stall landings, netting harnesses, or runway landings. These characteristics place constraints on operating procedures and have associated costs. Ducted fans, on the other hand, are inherently a vertical takeoff and landing (VTOL) vehicle, dramatically reducing the logistics footprint for launch and recovery. Fixed-wing UAVs' exposed propellers are damage-prone and a safety hazard for the operator. However, the enclosed propeller of the ducted fan provides added safety for UAV operators, as does the elimination of hand-launching procedures. The enclosed propeller also adds the potential to reduce acoustic propeller noise.

In regards to hovering UAVs, ducted fans are just one of several types of vehicles that are operating today. Other prominent approaches for hovering flight include helicopters, quadcopters, tailsitters/3-D aerobatic airplanes, and flapping wing vehicles. Each of these configurations has its own strengths, but the advantages of the ducted fan are distinct from each.

Figure 1-5. Hovering UAV example: Yamaha R-Max helicopter (public domain [12]).

Compared to the helicopter (an example shown in Figure 1-5), the fundamental advantage of the ducted fan is hover efficiency. Helicopter rotors are optimized for aerodynamic performance, but there are losses associated with the vortices created at the rotor tips. Adding a duct to a rotor eliminates the majority of these losses, making the size of the gap between the fan tip and duct the driving parameter. For an open rotor and a ducted fan designed with the same level of expertise for the same diameter and thrust loading, the ducted fan will consume significantly less power. Trading these parameters shows other benefits of the duct: if the diameter and power available were held constant, then the thrust output for the ducted fan would be greater; and if the thrust and power requirement were fixed, then the ducted fan would have a smaller diameter. These facts are shown through the propeller momentum theory [13] representation of power required for an open propeller and ducted propeller, respectively, in Equation 1 and the ration of the two in Equation 2:

$$P_{open} = \frac{T^{3/2}}{\sqrt{2\rho A_{disk}}}, \quad P_{ducted} = \frac{T^{3/2}}{\sqrt{4\rho A_{disk}\sigma_d}} \tag{1}$$

$$\frac{P_{open}}{P_{ducted}} = \sqrt{2\sigma_d} \tag{2}$$

Here P is the power required, T is the thrust, ρ is the air density, A_{disk} is the disk area of the propeller, and σ_d is the duct expansion ratio (ratio of exit area

to disk area). Notice the only difference in the ducted fan equation is under the square root in the denominator where there is an extra factor of two and the addition of the expansion ratio. This is made evident in Eq. 2 where the ratio of the open propeller power to ducted propeller power shows that the ducted fan will always required less hover power. The exception is for expansion ratios less than 0.5, which contract the wake more than what is characteristic of an open propeller. For a straight duct without expansion ($\sigma_d = 1$), these equations show that the ducted propeller will require only 71% of the power required by the open propeller. As the expansion ratio increases, the hover efficiency improves further. For the same gross weight and power plant, a ducted fan will require only half of the disk area (71% of the rotor diameter). These benefits must be weighed against the additional structure needed to implement a ducted propeller. While the ducted fan possesses clear advantages in hover, there is a flight velocity at which the drag from the duct negates the thrust benefits of the duct. Above this velocity the ducted fan's overall efficiency will be less than an open propeller. This threshold velocity is design dependent, and ducts that are designed for cruise will have a higher threshold velocity than designs optimized for hover.

Ducted fans tilt into the wind for high-speed flight, orienting their propeller thrust in the direction of flight. For this reason, the ducted fan possesses the potential for higher top speeds than helicopters, in general. Helicopters have exposed rotating blades in the main rotor and tail rotor. These are a hazard to the operator, and are a single point of failure if a rotor blade contacts a hard surface such as a wall or the ground. The enclosed blades of the ducted fan significantly increase safety and make the vehicle more robust for flying in close quarters, where bumping into a wall is an expected occurrence.

Figure 1-6. Hovering UAV example: Parrot AR.Drone quadcopter (public domain [14]).

Quadcopters, also known as quad-rotors, are a growing research interest (Figure 1-6). They offer many of the same capabilities as ducted fans, and are easier to stabilize. For the open rotor quadcopters, the same hover efficiency benefit exists for the ducted fan. However, quadcopter rotors, if enclosed, can easily gain the benefits of the duct effect. The advantages of the ducted fan are subtler for this case. While a quadcopter tends to be flatter, to attain the same disk area as a ducted fan it will have a larger dimension in the plane of the fan. For a one-foot diameter single ducted fan, a ducted quadcopter with no clearance between rotors would measure 20% wider corner-to-corner. For a more realistic minimal clearance of one inch between rotors, the ducted quadcopter would be more than 30% wider. Consequently, if the vehicle's mission requires access to tight spaces, a ducted fan can be smaller or carry more payload than a quadcopter.

Quadcopters also tend to cancel angular momentum by employing two clockwise spinning rotors and two counter-clockwise rotors. Yaw control is typically actuated through differential fan RPM (reaction torque). This approach works, but can yield lower yaw authority than desired in some situations. In contrast, ducted fans typically employ control vanes in the high dynamic pressure flow exiting the duct and can attain very high yaw control authority.

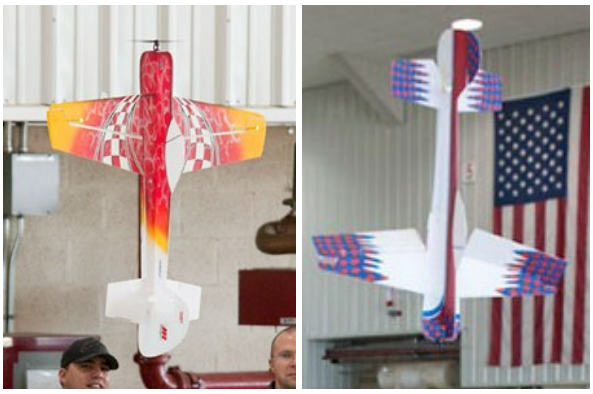

Figure 1-7. Hovering UAV example: hovering aerobatic ultra-light airplane (public domain [15]).

Airplanes that can hover using their propeller thrust are also competitors with ducted fan aircraft. Remote control (R/C) pilots have demonstrated amazing aerobatics with airplanes that have a thrust-to-weight ratio above 1.0 (Figure 1-7). These configurations can cruise like regular fixed-wing aircraft, but their motor will be oversized for that condition. In hover they cannot attain the same level of efficiency as the ducted fan due to the tip losses mentioned previously. In comparison, the ducted fan will have superior performance in payload capacity.

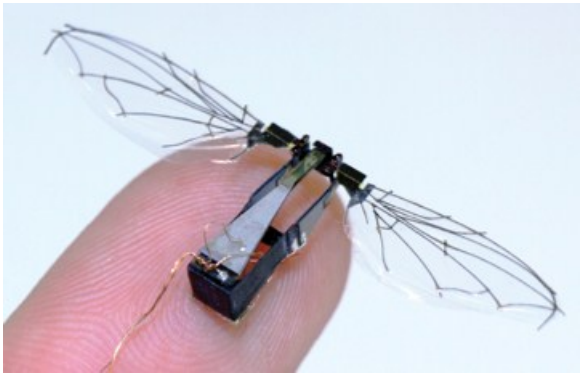

Figure 1-8. Hovering UAV example: Harvard Microrobotic Fly (public domain [16]).

Flapping wing vehicles are presently an area of active research (Figure 1-8). This approach of mimicking biological systems holds the potential for attaining exceptional agility at micro scales. This technology is currently not mature enough to fully compare it to the ducted fan in lifting capability or hover efficiency. However, it is probable that the payload carrying capacity of such

devices will be dramatically less than that of a ducted fan of the same length scale. This can be supported by the fact that the flapping wings will experience tip vortex losses similar to open propellers, but this is yet to be proven or fully quantified. Flapping wing aerodynamics also likely have an inherent upper bound on scalability, as there are very few birds larger than eagles and condors.

In comparison to all these vehicle types, ducted fan vehicles excel in applications where simultaneously minimizing vehicle dimensions and maximizing payload capacity is a top priority. Its efficient hovering performance surpasses that of many other UAV configurations. The ability to hover in close proximity to targets, the safety of enclosed rotor blades, and the simplicity of VTOL launch and recovery are all clear advantages. These benefits are motivation for overcoming the challenging aerodynamic behavior of the ducted fan configuration.

1.3 Research Objectives

The first objective of this research is to better understand the fundamental nature and structure of tilting ducted fan aerodynamics, in order to concisely model the complex characteristics. The second objective is to explore how active flow control techniques may beneficially alter these characteristics. More specifically, this second objective seeks to determine whether synthetic jet actuators are a practical approach for ducted fan flow control. These developments will aid in creating improved vehicle designs as well as insightful approaches for vehicle control.

The specific objective of each flow control concept investigated is to reduce the pitching moment of the vehicle in a controllable manner. This reduction in pitching moment would reduce the amount of control vane deflection required to trim (achieve equilibrium) during transition to forward flight. For a fixed amount of control vane deflection available, reducing the trim deflection leaves

additional vane travel for maneuvering or combating wind gusts. The newly developed flow control techniques are explained further in the next section.

1.4 Flow Control Concepts

The flow control concepts I have explored are uniquely tailored to the ducted fan flow phenomenon. If the flow over the duct surface can be controlled—i.e. flow turned, accelerated, separation eliminated or produced on demand—then a ducted-fan vehicle could be optimized for combating gusting winds. Asymmetric lift resulting from one side of the duct having attached flow, while the opposite side is separated, could be used as a control moment or to alleviate undesirable moments due to wind gusts. Achieving attached flow on the entire duct during a typical stall condition could enhance vehicle performance and efficiency. The concepts use separation on the leading edge to affect thrust and pitching moment, and a Coandă surface at the trailing edge to create a normal force, thereby reducing pitching moment. Discovered and documented by the Hungarian scientist Henri Coandă, the “Coandă effect” is the tendency of a fluid jet or stream to attach itself to a nearby curved surface.

In the first flow control concept, a steady or synthetic jet is applied against the existing flow over the duct lip, resulting in separation. When the jets are turned off the flow naturally reattaches. Figure 1-9 illustrates this concept. Inducing flow separation can decrease the pitching moment experienced during wind gusts and could reduce the amount of flight control actuator usage to maintain stable flight.

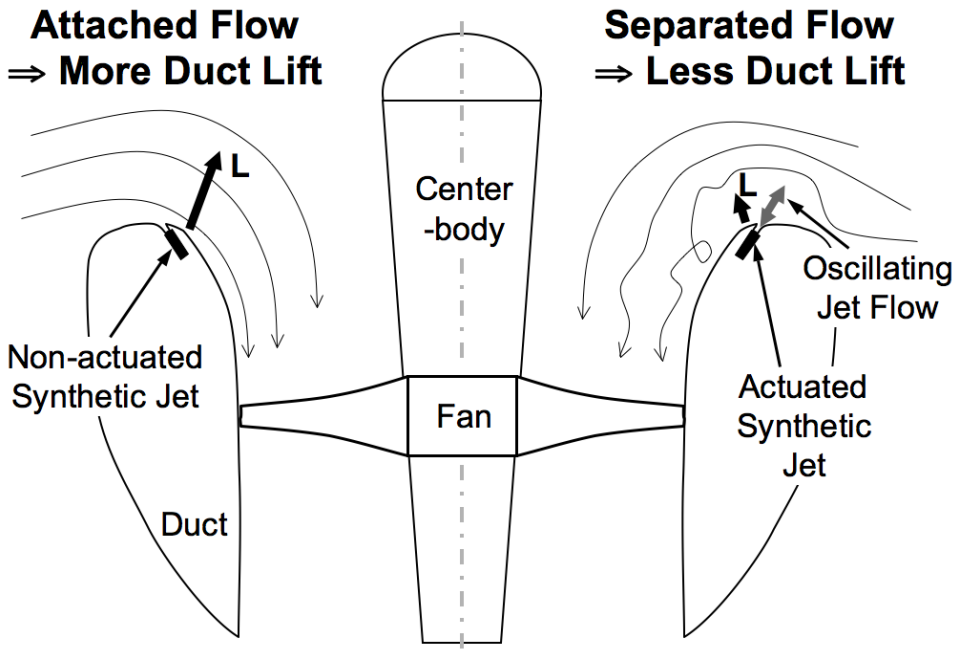

Figure 1-9. Duct lip synthetic jet flow control concept.

In the second concept, the traditional duct trailing edge is replaced by a Coandă surface geometry and a rearward-facing step. When the synthetic jet emanating from the step is turned on, it causes the flow to stay attached to the Coandă surface, thereby causing the primary flow out of the duct to turn. This results in a normal force opposite to the turned flow and a corresponding moment about the vehicle center of gravity (typically above the duct trailing edge). When the jet is turned off, the flow separates off the bluff corner and the flow travels straight out of the duct. This concept is shown in Figure 1-10.

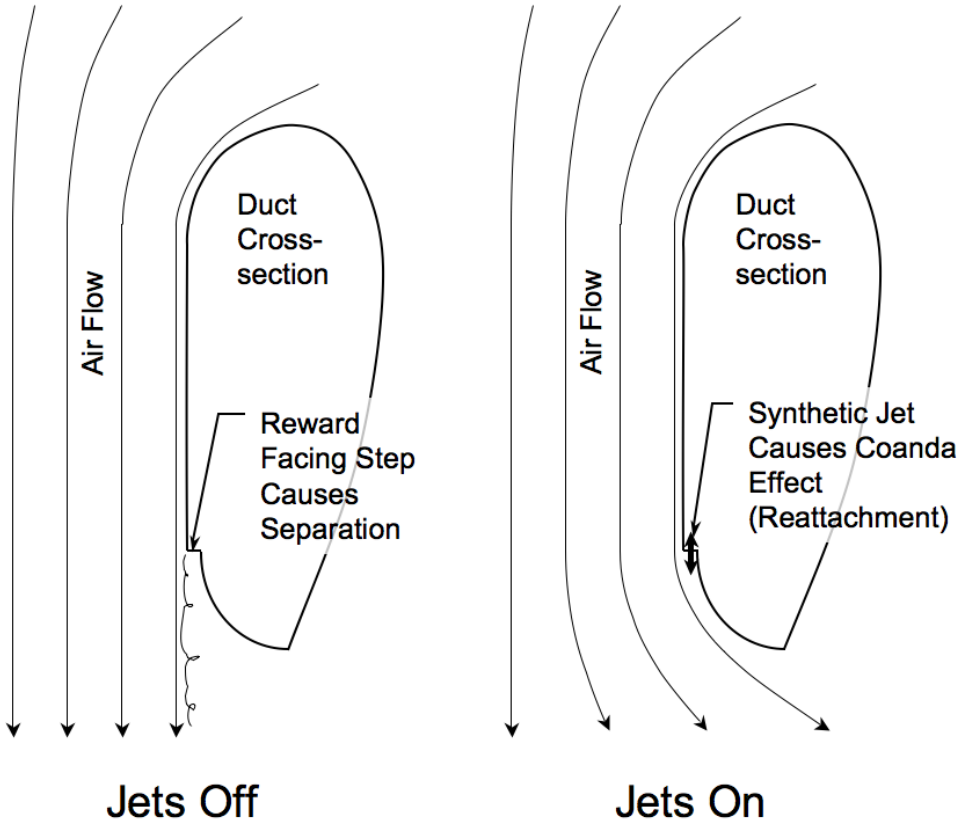

Figure 1-10. Duct trailing edge synthetic jet flow control concept.

A novel use of these two flow control concepts involves applying the control asymmetrically to the duct in order to produce an imbalance in forces, resulting in a moment. The net force and moment caused by the asymmetric flow control could be used to control or augment the motion of a ducted fan vehicle. Trimmed horizontal flight at 35 ft/s free-stream velocity with 70˚ angle of attack (20˚ tilt into the wind) is the target condition for affecting pitching moment on the vehicle design used for this study. This flight speed represents the critical condition of transition between hover and high-speed flight. Transition from hover to forward flight typically requires the most control surface allocation of any condition in the flight envelope, thereby justifying it as a sizing condition for control power.

Researchers have investigated steady blowing to create ducted fan control forces and moments in hover [17] and to enhance shrouded propeller static thrust [18][19]. This present effort investigates the effects of synthetic and

steady jets for hover as well as forward flight conditions over a large range of angles of attack. Other researchers have investigated synthetic jets on the stator blades of a ducted-fan to control vehicle rotation about the propeller axis [20], but controlling the flow over the duct surface here presents a larger opportunity for affecting the overall vehicle aerodynamics. Comparisons between steady and unsteady (synthetic) jets in isolation have been documented [21], but it is the intent of this research to compare steady and unsteady blowing in a specific application of flow control.

Chapter 2 Literature Review and Background

The topic of this research is a synthesis of several different areas. Particularly, it combines the realms of ducted fan aerodynamics, piezoelectric synthetic jet actuators, and active flow control. The following sections will describe existing work within these research areas to illustrate what has been accomplished, what has not, and how this present research can help to fill these gaps.

2.1 Ducted Fan Aerodynamics

The earliest known work regarding ducted fans or shrouded propellers dates to the early 1930's. Stipa in Italy [22] and Kort in Germany [23] were pioneers in the field. Stipa experimented with propellers upstream of Venturi tubes, while Kort developed and patented a propeller surrounded by a nozzle (duct) for ship propulsion. Sacks and Burnell [24] provide a good survey of all the early work. In the 1950's and 1960's, NASA invested significant effort in researching ducted fan configurations, but the challenging aerodynamic phenomena precluded ducted fans from wider use at that time. With the advent of more advanced control systems in recent years, many of the challenges of ducted fan vehicles can now be overcome. This, in conjunction with the growth of the unmanned air vehicle market, has caused a resurgence of interest in ducted fan vehicles. The literature on the subject can be divided into several categories: fundamental aerodynamics, modeling, vehicle design, flight controls, and aerodynamic flow control.

2.1.1 Fundamental Aerodynamics

Kruger [25] was one of the first researchers to rigorously investigate ducted fan configurations. He evaluated fifteen different duct cross-sections and two propellers. He observed the benefits of the ducted fan compared to a free propeller, and also noted the necessity of a stator for highly loaded propellers, to avoid rotational losses. He was one of the first to observe experimentally that the wake diameter exiting the ducted fan is purely a function of the duct geometry and not the fan, and concluded that it does not contract via smoke flow visualization.

Yaggy and Mort [26] and Yaggy and Goodson [27] investigated tilting wing-tip mounted ducted fan aerodynamics of the Doak VZ-4 VTOL aircraft, and were some of the first to note the nose-up pitching moment challenges of the configuration. They investigated inlet guide vane effects on thrust and control moment, and also concluded that vanes in the duct exit flow were the solution to countering the nose-up pitching moment of the ducted fan.

Grunwald and Goodson [28],[29] explored how the loads on the fan and duct contributed to the overall aerodynamics of the configuration. They confirmed that the duct is the main source of normal force and pitching moment at angle of attack. The propeller thrust versus angle of attack was relatively constant, while the duct thrust grew with increasing angle of attack, supporting the idea that the pitching moment comes from the windward duct lip. They also verified the fact that in hover roughly half of the thrust is provided by the duct, and in forward flight, at angle of attack, the duct carries even more of the load.

Mort and Yaggy started looking at ducted fan aerodynamics from a tip-speed based non-dimensional approach in [30], and identified duct stall by observing a change in $dC_m/d\alpha$, the pitching moment slope with respect to angle of attack. Mort [31] demonstrated that ducts that were designed for static conditions (larger bell-mouth shaped lips) degraded in performance at high advance ratios, while a duct designed for axial cruise could regain good high-speed performance at the expense of static figure of merit.

Mort and Gamse presented one of the most comprehensive accountings of ducted fan aerodynamics in [32]. In it they characterize the aerodynamics of the Bell X-22A ducted fan unit, an experimental vehicle with four tilting ducted fans for vertical and forward flight. They described static performance using Figure of Merit (FM) and documented climb and angle of attack trends. They also characterized duct lip stall by looking at the inverse of the thrust, non-dimensionalized by free-stream dynamic pressure and disk area (thrust coefficient in actuator disk momentum theory). An example of their non-dimensional results (normalized by free-stream dynamic pressure) is shown in Figure 2-1, showing clean trends but no cohesive structure relating all the aerodynamic terms.

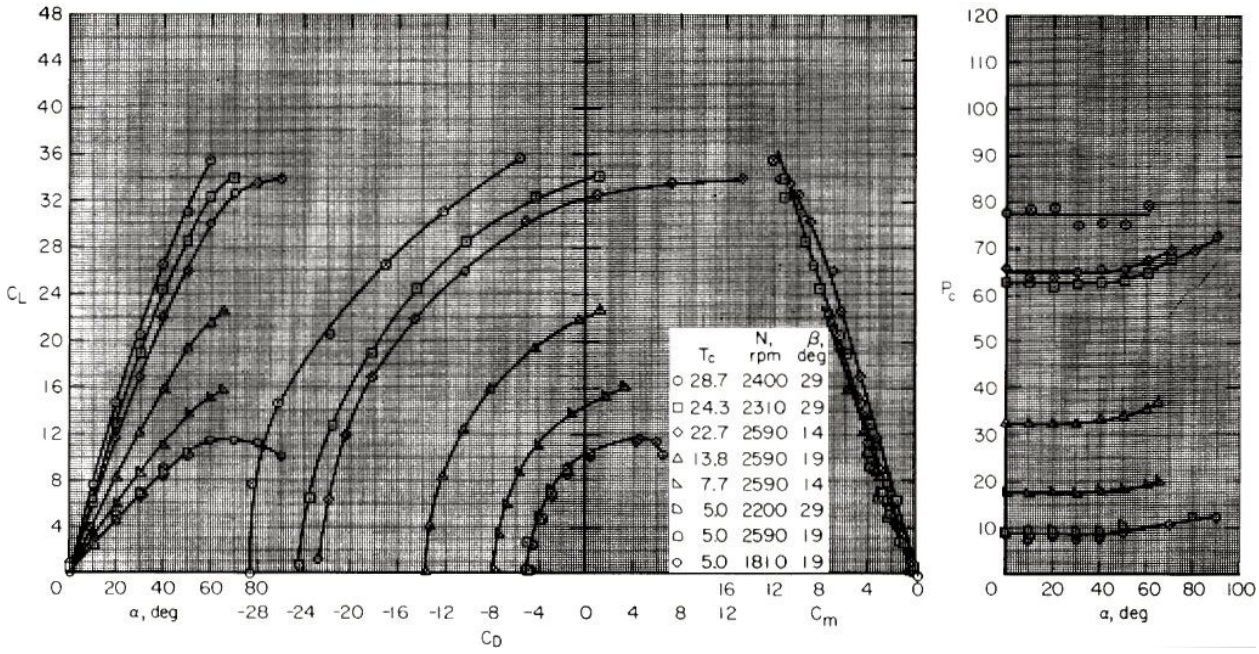

Figure 2-1. Example of Mort and Gamse non-dimensional ducted fan data [32] (public domain).

Black and Wainauski [33] gave an extensive look at the effect of the duct in axial flight and pointed out many advantages such as increased thrust and decreased power requirements compared to a free-tip propeller. They noted that while momentum theory suggests that the stream-tube should not contract aft of the duct trailing edge, experiments showed that the pressure was slightly higher than ambient at the duct exit. They showed the detrimental effects of

increasing the gap size between the fan tip and the duct, however the external design of the duct had much less effect. Through pressure measurements they determined that the vast majority of duct forces come from the inside region of the duct lip, particularly from the fan up to the leading edge.

More recent additions include Abrego and Bulaga [34] who tested a 38" diameter ducted fan. They investigated the effects of duct chord on overall performance as well as exit vane flaps to produce side force for flight control. Martin and Tung [35] investigated the ducted fan flow field, with emphasis on tip gap and duct shape effects. Graf et al. [8],[36] focused on how the duct lip geometry affects the pitching moment characteristics in forward flight and how the center of pressure moves over the flight regime. Thipyopas et al. [37] tested a coaxial rotor ducted fan configuration, investigating blade pitch effects on thrust and torque cancellation. Akturk et al. [38] used PIV to investigate the flow field through the duct.

Pereira gives a comprehensive literature survey of ducted fan research in [13] and presents results for hover and wind tunnel tests comparing open rotors to shrouded rotors. His measurements include wake velocity contours, duct surface pressures, and total forces and moments for a range of duct designs. An appendix in that work provides an excellent description of momentum theory for shrouded propellers with insightful comparisons to the traditional open propeller results.

2.1.2 Ducted Fan Aerodynamic Modeling

While the payoffs in capabilities make ducted fan vehicles desirable, special care must be taken to successfully develop a flight vehicle with adequate performance and control power. Kriebel [39] was one of the first to model ducted fan aerodynamics for forward flight and angle of attack using a potential flow method. He derived expressions for the forces and pitching moments, and investigated stability derivatives for longitudinal flight.

Mendenhall and Spangler [40] were some of the first to develop a computer code to predict ducted fan flow fields and pressure distributions. They compared their model to the Mort and Gamse data presented in [32], with fair agreement.

Chang and Rajagopalan [41] developed an incompressible Navier-Stokes Computational Fluid Dynamics (CFD) solver for axisymmetric ducted fans. The modeled the fan through a 'momentum source' concept. There code was compared to wind tunnel data for the Trek Aerospace ducted fan [34] and Micro-Craft's LADFUAV, showing good agreement. However, the code was limited to pure axial flight only (vertical climb).

Quackenbush et al. [42] developed a free-wake potential flow method for propellers and coupled it with a fast surface method for fuselages and ducts to enable analysis of ducted fan aerodynamics. They showed good agreement for isolated annular wing without propellers presented by Fletcher [43] as well as the X-22A ducted rotor powered data from Mort and Gamse [32]. Their results matched for a range of angles of attack that were below the duct stall condition.

Drela and Youngren [44] developed a design code for duct, fan, and stator geometry called DFDC (Ducted Fan Design Code). They included both actuator disk and blade element treatments of the fan and stator, and used a panel method for duct, fuselage, and blockage objects within the duct. The code is available under the GNU general public license, but is in an unfinished state.

Lind et al. [45] described a potential flow method coupled with a blade-element treatment of the propeller for aerodynamic modeling of ducted fans. The method is capable of modeling the ducted fan at an angle of attack. The results showed good agreement with test data forces, but pitching moment agreement was not as good. di Vitiis [46] used a potential flow approach as well, and explicitly modeled ground effect.

2.1.3 Ducted Fan Vehicle Design

Weir [47] showed good understanding of ducted fan vehicle design, and this reference was one of the first documented methodologies on the subject. He compared a toroidal duct shape to a traditional duct cross-section, and concluded that the toroidal duct produced more pitching moment. He describes methods for modeling the fan, flow straighteners (stators), control vanes, as well as the free-stream effect on system control authority.

Avanzini et al. [48] developed models of ducted fan aerodynamics with the intent to evaluate vehicle dynamics. They present 'trim' analysis versus flight speed to show the vehicle's forward flight performance. Linear stability analysis of the trimmed equilibrium conditions leads to a discussion of eigenvalues and eigenvectors, root locus plots, and mode shapes for various flight conditions.

Guerrero et al. [49] presented a parametric aerodynamic buildup approach to modeling ducted fan systems explicitly modeling the effects of the duct, propeller, control vanes, stators, and pods. They implemented a multidisciplinary design optimization framework to enable conceptual design of ducted fan UAVs. Their results showed good agreement with wind tunnel test data of the Allied Aerospace 29" iSTAR vehicle.

Ko et al. [50] described the multidisciplinary methodology employed in their design tool, with considerations for airframe geometry, aerodynamics, propulsion, stability, mass properties, vehicle trim, and mission performance. The design tool's purpose is to enable multidisciplinary design optimization (MDO) and trade studies in the conceptual and preliminary phases of design. Under the aerodynamic modeling section, they describe one way of modeling the ram drag and pitching moment characteristics of the vehicle, as seen in Figure 2-2. They model the center of pressure as remaining on the vehicle axis of symmetry, with vertical movement to account for pitching moment changes due to angle of attack and thrust variation.

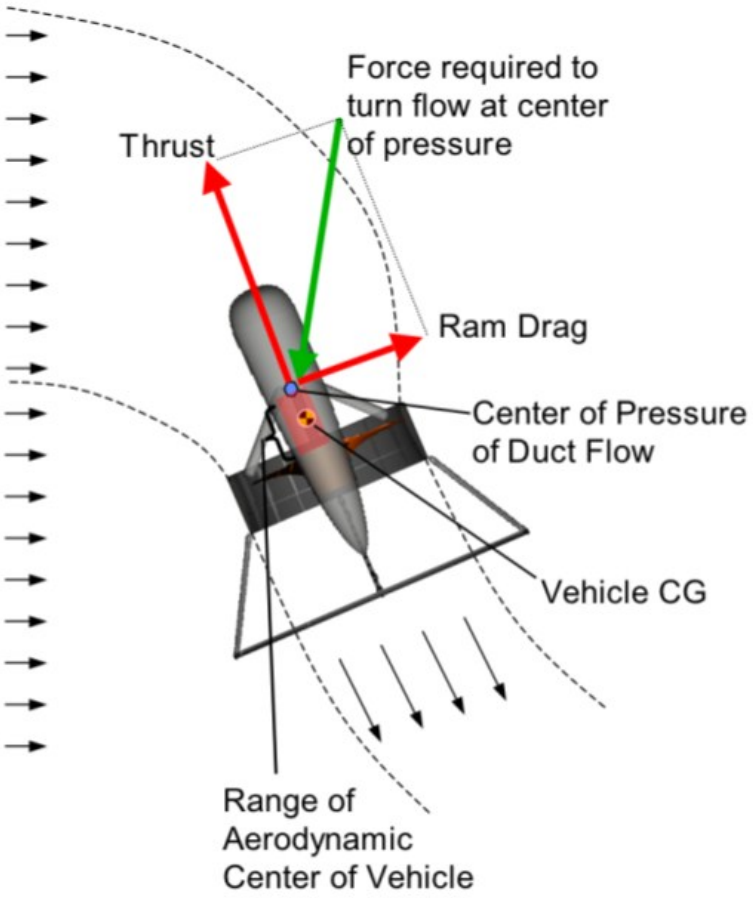

Figure 2-2. Ram drag and center of pressure modeling approach from [50] (used with permission).

They note that as the vehicle passes through the extents of the flight envelope that the center of pressure of the vehicle moves. The relative position of the center of gravity to the center of pressure will determine whether the resulting pitching moment is nose-up (positive) or nose-down (negative). They showed good agreement with flight test data of the Honeywell RQ-16 T-Hawk (aka Honeywell MAV).

Tobias et al. [51] gave a thorough approach to modeling a tandem ducted fan vehicle. The vehicle design is assumed to have collective and cyclic pitch rotor control as well as control vanes in the duct exit flow. One unique feature of their paper is the center of pressure modeling, and the description of the two prevailing schools of thought.

2.1.4 Ducted Fan Flight Control

The nonlinearities in ducted fan aerodynamics directly affect the complexity of the vehicle's flight control algorithms. This has hindered more prevalent use of this aerodynamic configuration in the aerospace community. Many linear and nonlinear control schemes have been applied to ducted fans. The approaches span linear PID control, switching between robust linear controllers, receding horizon control, sliding mode control, linear dynamic inversion, nonlinear dynamic inversion, dynamic inversion with adaptation, and back-stepping combined with adaptive control.

Pflimlin et al. [52] developed an aerodynamic model of a ducted fan from wind tunnel tests, derived the equations of motion, and linearized about the hover condition. They identified the unstable poles in the vehicle modes (via root locus plots), and implemented proportional-integral-derivative (PID) control to stabilize the vehicle using sensor feedback. They showed good agreement between simulation and flight test results.

Avanzini, Ciniglio, and de Matteis [53] used the "structured singular value μ synthesis [54]" to design two robust linear controllers, one for low-speed flight and one for high-speed flight. The two controllers are switched as the vehicle passes a threshold velocity. One concern with this approach is the dynamics as the vehicle transitions from one controller to the other. They claim a smooth transition of actuator commands during switching via the "so-called high gain approach [55]". However, they note "relaxed requirements on transient motion during switching, in comparison with manned vehicles, can be acceptable for a remotely piloted vehicle."

Franz et al. [56] applied a constrained receding horizon control (RHC) strategy to a ducted fan. Periodically, a finite-horizon optimal control problem is solved using the vehicle state at that instant. The resulting control law is used for a certain amount of time (a fraction of the horizon length), and then the control recalculated. One of the benefits of this approach is the inherent ability to include constraints in the state and control, such as obstacles to avoid

or actuator saturation. They compare their final control law with a highly-tuned gain-scheduled linear quadratic regulator (LQR) controller and show that the RHC controller has faster step response rise time and better gust rejection.

Hess and Bakhtiari-Nejad [57] apply pseudo-sliding mode control (SMC) to a model of the iSTAR 29" vehicle ("pseudo" implies that a boundary layer is used around the sliding manifold to avoid actuator chatter). They compare the results of SMC to a nonlinear dynamic inversion controller operating on the same vehicle model created from wind tunnel data. The gain and phase margins are comparable for the two flight conditions tested, but the authors acknowledge their expectation that the dynamic inversion controller will be superior. They state the gain and phase margins should be maintained for all flight conditions while that is not guaranteed with SMC. The SMC controller was robust to large steady wind gusts, something that posed problems for the dynamic inversion if a wind estimator was not used. The authors conclude this implies the SMC controller has significant robustness to errors in the vehicle model.

Li [58] presented an approach combining linear control for hover and steady level flight conditions and nonlinear dynamic inversion for the difficult aerodynamics encountered during transition between the two flight regimes. The vehicle being analyzed was comprised of two ducts each having pitch and yaw control vanes, resulting in six control inputs to control four outputs. An optimization technique was used to perform the required control allocation.

Spaulding et al. [59] gave a comprehensive explanation of nonlinear (and linear) dynamic inversion (NDI) with specific application to ducted fan aerodynamics. The authors claimed the following benefits for this approach: NDI does not require gain scheduling, the inversion cancels the nonlinear dynamics and replaces it with simple integral response, and the approach is well-suited for mission and failure reconfiguration as well as mass property changes. The typical drawback of dynamic inversion systems, namely lack of robustness to model plant uncertainty, is address by the authors. They

evaluated robustness to uncertainties such as time delay, measurement noise and bias, and inertia error. Finally they discussed the need for a wind estimator. If velocity sensing is acquired from GPS signals, the relative air speed could be significantly different than the measured ground velocity, causing the inverted model to be inaccurate. A state estimator to approximate winds greatly improved the response to large steady winds.

Johnson and Turbe [60] used a simplified model of a ducted fan vehicle, the GTSpy, for dynamic inversion, and then augmented it with a neural network for adapting to errors in the simplified vehicle model. They opted for this combination of adaptation and dynamic inversion because no accurate model of the vehicle was available. The neural network was trained online to adapt to the modeling errors. They presented simulation results for vehicle trajectory tracking in the presence of turbulent winds, and then showed the comparison to actual flight tests. While the results were fairly successful, the authors noted the limitation of the control due to the model being primarily of near-hover conditions. The adaptive neural network was unable to cope with model mismatch at higher velocities. The vehicle was airdropped from an unmanned helicopter and stabilized itself successfully.

Pflimlin et al. [61] designed a controller via back-stepping based on simulation, and included adaptive online estimations of the unknown aerodynamics of the vehicle. They decoupled the yaw dynamics from and handle them in a separate control law. They claimed global adaptive stability for the system. They considered two types of uncertainty: the aerodynamic forces on the vehicle, and the locations at which those forces act (essentially aerodynamic moments).

2.2 Synthetic Jets

Many researchers have investigated synthetic jet design and flow control applications, looking for opportunities to leverage the small form factor of SJAs

while enabling new flow control benefits. There is a vast amount of published work on synthetic jet actuator research; only a brief review of the topic will be included here.

2.2.1 Synthetic Jet Fluid Mechanics

As research interest began to build in the 1990's, Smith and Glezer addressed many of the fundamental characteristics of jet formation and evolution in [62]. Through phase-locked Schlieren imagery they showed the evolution of the twin vortices emanating from a rectangular slot. They showed how the velocity of the flow changes as the axial distance away from the slot increases, transitioning from an oscillating flow to a mean flow indistinguishable from the mean flow.

In [63], Glezer and Amitay reviewed much of the early research that documented jet behavior and applications. They described the applicability of SJA to flow control and explain the effects of the injected momentum (without mass flux) can change the streamlines of the mean flow with length scales one to two orders of magnitude larger than the length scale of the synthetic jets. They also pointed out that the difference in time scales of the high frequency jets and the mean flow allows for effective decoupling of the resulting aerodynamic forces from the operating frequency of the SJA.

Smith and Swift presented an important comparison between synthetic and steady jets in [21] and [64] at matched Reynolds numbers. They showed that synthetic jets are typically wider and slower than a self-similar continuous jet. They discussed the importance of dimensionless stroke length as a criterion for jet formation, and a predictor for near-field behavior of the jet. While their comparison with continuous jets was groundbreaking, they did not quantify how these attributes affect performance in actual flow control applications.

Holman et al. [65] presented a non-dimensional approach for jet formation criteria. They defined jet formation as "the appearance of a time-averaged outward velocity along the jet axis and corresponds to the generation and

subsequent convection of escape of a vortex ring." They claimed the fundamental parameter for jet formation is the jet Strouhal number, which is a function of the jet Reynolds number and Stokes number. They determined that for 2D jets (infinite rectangular slot) and axisymmetric jets the inverse Strouhal number must be greater than 1 and 0.16, respectively.

Zhong et al. [66] presented an extensive investigation into the fluid mechanics of synthetic jet formation, categorizing the many possible jet structures observed in cross-flow according to dimensionless stroke length, velocity ratio, and Strouhal number. In contrast to many previous papers, they detailed the interaction of the jet with a cross flow. The velocity ratio, representing the relative strength between the jet and the flow, is a driving parameter for how the SJA affects the flow has implications on flow control potential. It should be noted that the jet velocity used in this ratio is the "time-averaged blowing velocity over the entire cycle". In other words, it is the integration of the outstroke velocity (during one half of the jet cycle) divided by the full period of the jet cycle. The result is that the time-averaged jet velocity is substantially smaller than the peak jet velocity, therefore very high peak velocities may be required to successfully alter a mean flow.

Ramasamy, Wilson, and Martin [67] presented a detailed investigation into SJA interaction with a cross-flow boundary layer using micro particle image velocimetry (μPIV). They investigated synthetic jet evolution in quiescent (still) air and in a cross-flow boundary layer. Their findings showed that the jet evolution in these two regimes was quite different. Consequently, they concluded that using quiescent test results to predict effects in boundary layer flow control is inappropriate.

2.2.2 Synthetic Jet Modeling

Many modeling techniques have been developed for SJAs, including both analytical and numerical approaches. The approaches span reduced order

modeling (ROM) all the way up to direct numerical simulation (DNS) in high-fidelity CFD.

One prominent analytical model is that developed by Gallas et al. [68] (described in depth in Gallas [69]), in which an analogous 'equivalent circuit' model represents the electromechanical SJA system. The differential equations in the model correspond to electrical components such as capacitors, resistors, inductors, and transformers. Good agreement was attained with experimental results, but the method requires some parameter tuning. While this is a viable way to model SJA operation, it is an abstract approach to modeling the actual mechanical system, making it less intuitive than other techniques.

Lockerby and Carpenter [70] modeled the SJA using a mechanical approach. They modeled the piezoelectric diaphragm using classical thin-plate theory and the flow in the orifice using 1-dimensional Navier-Stokes equations, but did not explicitly model the flow in the cavity to reduce computational complexity. Instead, the ideal gas law was used to model only the pressure in the cavity, and not the velocity. Only limited validation data was presented, but the method showed good agreement with predicting the actuation frequency for maximum jet velocity.

Sharma [71] also directly modeled the physical nature of the SJA setup with a model that is less complex, but also showed excellent agreement with experimental data. The driving wall of the cavity was abstractly modeled as a moving wall that forces a volume displacement, but its dynamics can be modeled as a 1-degree-of-freedom mechanical system. This allows for one model to be used for piston-driven, piezoelectric-driven, and electromagnetic-driven designs, however it assumes that the structural dynamics of the driving element are well known beforehand. The dynamics of the fluid in the cavity were modeled using the unsteady form of the continuity and Bernoulli equations. The result was a set of differential equations that are easier to solve than many other models, but the model showed excellent agreement with experimental data. Compared to the experimental data from Gallas et al. [72],

Sharma's model more accurately matched two different data sets than the equivalent circuit model presented by Gallas. One important finding from Sharma's model was that the flow inside the cavity is compressible only for cases above the Helmholtz frequency. If the natural frequency of the mechanical diaphragm is lower than the Helmholtz frequency, then the flow can be sufficiently modeled using incompressible flow analysis.

Tang et al. [73] compared three analytical models to assess which approach was the best for SJA design. The three models were the "dynamic incompressible" model, the "static compressible" model, and the "lumped parameter" model that was similar to the equivalent circuit modeling by Gallas [68]. The dynamic incompressible model makes the simplifying assumption that the diaphragm deflects according to thin-plate theory and is not affected by the pressure in the cavity. The change in volume of the cavity is directly translated to velocity through the orifice opening. This approach is obviously only applicable when the flow is not compressible, and grossly over-predicted jet velocity in that case. The static compressible model is similar to that of Lockerby and Carpenter [70], and models the compressible flow in the orifice using the Navier-Stokes equations, and the air in the cavity using the ideal gas law. This model tended to over-predict the velocity near the optimum orifice diameter that corresponded to maximum jet velocity. Tang et al. noted that while it does not match experiment fully, it is still a useful tool for determining optimal design parameters. Lastly, the lumped element equivalent circuit model matched experiment data better than the other methods, but was more complex and not as conducive to design optimization.

Numerical approaches using 2D and 3D unsteady computational fluid dynamics (CFD) have been used extensively to study flow inside the cavity and orifice as well as interacting with cross-flows. Carpenter et al. gave a survey of unsteady CFD practices in [74], with a section devoted to the modeling of synthetic jets. The discussion centers on what level of cavity/orifice modeling is sufficient for predicting the effects in active flow control applications. The

options range from applying an oscillatory velocity boundary condition at some interface in the model, to 1-D Navier-Stokes modeling of the flow in the orifice, to explicit modeling of the flowing in the cavity. The most advanced approaches use time-varying geometry in the grid to model the diaphragm movement.

Viken et al. [75] analyzed 2-dimensional synthetic jet flow interaction with a cross-flow over a 'hump' model developed at NASA Langley. They compared two structured mesh codes, TLNS3D and CFL3D, with an unstructured method, FUN2D, along with experimental results. Using a prescribed velocity boundary condition the methods attained fair agreement with experimental data, and the difference between the structured and unstructured methods was most notable in the region of separated flow.

Roth et al. [76] explored the effects of synthetic jets on the boundary layer of flat plates, cylinders, and airfoils using 2-dimensional CFD. They noted significant separation reduction on the cylinder and airfoil when the jets were employed, as well as increases in performance in lift and reduction of drag.

Dandois et al. [77] used Large Eddy Simulation (LES) to analyze synthetic jets in cross-flow in 3-dimensions. They attained good agreement with experiment, but noted that unsteady Reynolds Averaged Navier-Stokes (URANS) solvers provided similar accuracy for the main dynamic of the flow in the particular case analyzed. However, they concluded that LES (or direct numerical simulation, DNS) is necessary to fully capture the turbulent structures such as the counter rotating vortex pair.

Park et al. [78] compared turbulence models in 2-D CFD analysis of a synthetic jet in quiescent air. They concluded that the k-ω SST (sheer stress transport) model provided better agreement with experimental data than either the Spalart-Allmaras and k-ε SST models.

Rumsey et al. [79] compared URANS predictions for circular synthetic jets interacting with a cross-flow to experimental data, showing fair agreement. Rumsey [80] compared the same three turbulence models as Park et al. for the NASA Langley hump model, but concluded that none of them significantly

change the results or agreement with experiment. More importantly, the lack of matching in turbulent shear stress in the separated region points out flaws in all of the turbulence models currently used in RANS and URANS solvers. Rumsey concluded that URANS analysis for characterizing the mean flow characteristics is sufficient, but inappropriate for analysis of separated flows.

Sharma and Siong [81] used CFD to investigate flows over cylinders. They compared the flow structures generated for the cases of uniform free-stream flow, a steady jet, and a synthetic jet flowing over the cylinder.

2.2.3 Synthetic Jet Actuator Design

While studies of the flow phenomenon of synthetic jets are essential, the design of the actuators to create the jets is also an important topic. Many different approaches have been taken to drive the oscillating jet flow. Most designs incorporate piezoelectric vibrating diaphragms, but other popular approaches include mechanical pistons and acoustic speakers. Below is a sampling of the literature on the subject.

Utturkar et al. [82] approached the actuator design problem using CFD flow simulation to investigate sensitivities of jet output to cavity geometry. They used an incompressible flow Cartesian grid solver that allows for moving grid boundaries to directly model the motion of a piezoelectric diaphragm. They evaluated the following cases: a single diaphragm oriented perpendicularly to the jet direction; a single diaphragm parallel to jet direction; dual diaphragms parallel to the jet direction; and three diaphragms completing a box shape. They concluded that cavity dimensions have little effect on jet output, which contradicts some experimental studies performed by others. The discrepancy is most likely due to compressibility concerns.

Gallas et al. [72] used an equivalent circuit lumped element model that was validated against experimental data to optimize SJA output. They simulated changes in geometry to the cavity and orifice, and showed that reduced cavity volume, orifice radius and orifice depth all improved jet output compared to

the baseline design. Their experiments and modeling of an alternate diaphragm layout also showed higher jet output. The alternate design had the active piezoelectric element applied as a ring to the outside of the diaphragm instead of the typical arrangement with the piezoelectric patch in the middle of the diaphragm.

Gilarranz et al. [83] used a mechanical piston design to achieve very high jet velocities, and chose this approach because it was more power dense than using piezoelectric diaphragms. They pointed out the deficiency in strength of many laboratory SJA developments and aimed to develop a design appropriate for real flow control applications. They achieved jet velocities as high as 124 m/s for six jets, requiring 1200 W (1.6 HP). While they achieved impressive jet velocities, the piston and crankshaft structure to drive the synthetic jets was bulky and likely weight-prohibitive for most aircraft applications.

Mossi et al. [84] explored SJA driven by several piezoelectric diaphragm technologies. They compared bimorph, Thunder actuator, and Radial Field Diaphragm (RFD) circular bender actuators. The RFD was a new technology based on inter-digitated electrodes (similar to Macro Fiber Composites) that takes advantage of the stronger d_{33} electromechanical coupling than typical actuators based on a d_{31} coupling. One deficiency or restriction in their approach was they only tested at low frequencies and did not evaluate the mechanical resonance frequency or the Helmholtz (acoustic resonance) frequency. The bimorph SJA design out-performed both the Thunder and RFD-based SJA designs in their experiments.

Gomes et al. [85] demonstrated exceptional jet output velocities in SJA designs using small piezoelectric unimorph disks, reaching peak velocities of 130 m/s. They mapped out the performance for a large range of driving frequency and chamber heights, two of the most influential design parameters. In their experiments the mechanical resonance produced much larger jet velocities than the Helmholtz frequency. Some design principles derived from

their findings were that increased orifice depth adds damping and decreases jet output, and in general shallower chambers result in higher jet velocity.

Kim and Garry [86] investigated the effects of a rectangular slot orifice's aspect ratio on SJA output. They varied the length-to-width ratio of the slots but did not maintain a uniform orifice area, making it difficult to assess the true impact of aspect ratio for equivalent designs. They did note that decreased cavity depth increased the jet output, a finding that agrees with many other researchers. Regarding the rectangular slot performance, they noted that aspect ratios less than 10 tend to have more uniform velocity distribution.

Lee et al. [87] modeled the use of Ionic Polymer-Metal Composite (IMPC) actuators to drive SJA output. This material type is capable of larger displacement movements than piezoelectric diaphragms, but also typically provide lower force and response time. It was unclear from their analysis what limitation in frequency actuation should be expected. They predicted average jet velocities of roughly 10 m/s at a driving frequency of 30 Hz.

Liang et al. [88] take a unique approach to actuator design, using a shape memory alloy (SMA) diaphragm with attached iron pads driven electromagnetically to achieve extremely high jet velocities (190 m/s). They utilize the super-elastic nature of the SMA rather than the shape-resetting phase change that is used in many smart material morphing applications. Their design uses large magnets and coils to drive their hybrid SMA-iron diaphragms. While the jet output attained is impressive, it required 200 W (0.27 HP) of electrical power, and the SJA apparatus weighed 1.36 kg (3 lb). These characteristics, in addition to the large dimensions, would make this approach less attractive for integration in most air vehicles. Only very large aircraft could sustain the weight and power impact and possibly improve vehicle performance through the use of these flow control actuators.

Ohanian et al. [89] explored the use of Macro Fiber Composite (MFC) piezoelectric actuators in synthetic jet design. They used star-shaped MFC

elements bonded to brass substrates in a unimorph configuration to drive the volumetric displacement of the SJA cavity. They compared performance to a piezoelectric bimorph disk. The MFC actuators in this application did not show any aerodynamic performance advantages over the bimorph, but were more robust and easy to handle in comparison to the fragile bimorphs.

Yang [90] presented a comparison of theoretical predictions from CFD simulation to experimental SJA flow measurements for piezoelectric-based actuators. His results show good agreement. He notes that decreasing slot width and cavity depth increase jet output, and that the velocity magnitude was easily controlled through voltage magnitude adjustment.

2.2.4 Synthetic Jet Applications

Applications of synthetic jet flow control span a diverse range of engineering problems. Amitay et al. [91] studied the use of synthetic jets in engine inlet ducts that exhibit flow separation. This is one of the first applications to internal flow rather than external flow applications, such as wings and bluff bodies. They introduce disturbances to the 2-dimensional serpentine duct flow to cause separation, and then place the SJAs in the separated region to control the amount of separation. The jets were oriented in a normal direction instead of tangential to the mean duct flow. In lower speed duct flows the separation bubble is completely eliminated. They note that performance at higher duct flow velocities is limited by the SJA output strength, and could be improved with stronger jets.

McMichael et al. [92] developed a novel application of synthetic jets to spinning projectiles, where the frequency of jet actuation was matched to the projectile spin rate. The compact form factor of the projectile was a perfect match for the small volume required by a SJA. A bluff corner and Coandă surface were used on the aft section of the projectile to create separation and allow for SJAs to reattach the flow. Operational tests of prototypes demonstrated the capability of SJAs to steer the projectiles that were spinning

at rates of roughly 60 Hz. This was one of the most impressive applications of SJAs in my opinion, having demonstrated the intended system level-capability in operational tests. This particular reference served as inspiration for several of the ducted fan flow control concepts explored in the present research.

Another application of synthetic jets is airfoil separation control, with Gilarranz et al. [93] as an example. They increased stall angle of attack and gained a corresponding increase in maximum lift coefficient. They employ a piston-driven SJA array on a NACA 0015 airfoil, with the jet blowing tangentially along the surface of the wing near the leading edge. The jets used were capable of relatively high output (peak velocity 81 m/s) compared to the free-stream airflow velocity of 35 m/s. The jet blowing was able to delay airfoil stall (flow separation on top suction surface) from 10 deg up to 18 deg with the highest blowing. The maximum lift coefficient increased from roughly 1.0 to 1.4 for these extremes. They thoroughly investigated the aerodynamic characteristics through flow visualization, pressure taps, and wake surveys downstream of the airfoil (to assess drag reduction).

Whitehead and Gursal [94] explore SJA as a form of propulsion for micro air vehicles using thin airfoil wings, and demonstrated the elimination of airfoil drag and the addition of small amounts of thrust. They drive the SJAs using a loudspeaker. The wake deficit (drag) of the airfoil observed in a velocity survey downstream of the airfoil was completely eliminated when the jets were activated and became positive (thrust) for higher blowing coefficient levels.

Pavlova and Amitay [95] investigated use of synthetic jet actuators to cool electronic microchips. They found that for a similar jet Reynolds number the heat dissipation was roughly three times greater for synthetic jets compared to steady jets. They also reported that for larger ratios of jet distance from the impingement surface to jet diameter, lower frequency jets performed better than high frequency jets. In contrast, they found that when the jet was in close proximity to the impingement surface, that higher frequency jets dissipate into a quasi-steady flow more rapidly and were more effective. The lower frequency

jets generated vortex rings that kept their shape and traveled further until impinging the electronic heat source.

Ciuryla et al. explore flight control of a scaled Cessna 182 civil manned aircraft in [96]. They tested both conventional ailerons and synthetic jets and compared the roll control of the aircraft for these two configurations. One innovation employed was a closed loop/adaptive actuation of the jets based on feedback from hot-film shear stress sensors placed downstream of the actuators. This approach eliminated wing tip stall for moderate conditions. They also noted that at high angles of attack the SJA were sufficient for controlling the aircraft in roll. This is likely due to the fact that the main effect of the SJA is only applicable to unstable flow conditions like wing stall.

Farnsworth et al. present synthetic jet flow control on a UAV from low to high angles of attack in [97]. Their wind tunnel tests show that the SJA could mimic the effects of traditional control surfaces to some extent. They explored controlling the magnitude of the SJA effect for closed loop vehicle control through either altering the blowing momentum coefficient or through a pulse modulation (applying SJA drive signal at some reduced duty cycle).

Vukasinovic et al. is an example of synthetic jet flow control employed in flows over bluff bodies [98]. They reduced the extent of flow separation through actuation around the circumference of a hemispherical turret. Because the actuation frequency is much higher than characteristic frequencies of the separated flow, they also used lower frequency amplitude modulation while still driving the piezoelectric SJA at their high frequency optimum.

2.3 Ducted Fan Flow Control

The combination of the two preceding topics (ducted fan aerodynamics and synthetic jet flow control) leads to the topic of flow control applications to ducted fan configurations. Due to the unique aerodynamics of the ducted fan configuration, several researchers have investigated ways to improve or control

the flow through the duct. The approaches include steady blowing, physical obstructions or guides for the flow, duct shape morphing, and synthetic jet flow control.

Burley and Hwang [99] showed that tangential blowing of V/STOL engine inlets and diffusers for turbofan engines could delay flow separation to higher angles-of-attack. Their analysis used high velocity ratio steady blowing, applied tangentially to the flow over the inlet lip. In their investigation, blowing of the inlet lip was more successful than blowing further downstream in the nacelle.

Kondor and Heiges [17] investigated steady tangential blowing at the trailing edge of a ducted fan. They employed a semicircular Coandă surface at the trailing edge to cause the flow to stay attached to the duct surface when the blowing was activated. Asymmetric blowing applied to only one side of the duct trailing edge produced a normal force away from that side of the duct, a reaction force resulting from the flow being turned at the Coandă surface. A pitching moment would result from this normal force at the duct trailing edge, if the vehicle center of gravity were above this location (which is the case for most ducted fan vehicles). This pitching moment would tilt the vehicle thrust vector in the opposite direction to the normal force. Kondor and Heiges noted that this pitching moment was an unintended effect that would adversely affect vehicle control. This is due to their assumption that a ducted fan vehicle would translate laterally without change in attitude, using the normal force alone for control. They applied normal blowing on the opposite duct wall to eliminate the pitching moment. In contrast, most ducted fan vehicles tilt into the wind for forward flight to use their thrust to not only stay aloft, but also to accelerate laterally and counter the drag encountered during high-speed flight. Such vehicles need a mechanism to counter the nose-up pitching moment encountered during transition from hover to high-speed flight. Typically, control surfaces are used to accomplish this, and the normal force these yield is opposite to the flight direction, the same result as in these flow control experiments. Both approaches cause a lateral change in momentum of the exit

flow. The resulting moment is critical for control while the normal force is a secondary byproduct.

Kondor et al. [18][19] continued investigations using a larger ducted fan test setup (inspired by the NASA Personal Air Vehicle (PAV) project to investigate uniform blowing around the duct trailing edge. They found that tangential blowing could expand the flow exiting the duct to large diffusion angles, thereby affecting duct mass flow and static thrust. Some flow visualization results from this effort are shown in Figure 2-3, demonstrating the flow-expanding capability of trailing edge steady blowing on a ducted fan.

Figure 10 (a).

Fan Exhaust Flow Visualization with $C_{\mu s\ aft} = 0$

Figure 10 (b).

Fan Exhaust Flow Visualization with $C_{\mu s\ aft} = 0.007$

Figure 10 (a).

Fan Exhaust Flow Visualization with $C_{\mu s\ aft} > 0.007$

Nacelle Inlet Circulation Control

Figure 2-3. Ducted fan steady blowing flow control using Coandă surface trailing edge [100] (public domain).

Fung and Amitay [20] used synthetic jets on the stator blades of a cyclic-pitch ducted fan to control the yaw angle of the vehicle. The motivation was to enable a ducted fan vehicle controlled solely through cyclic rotor actuation and SJA flow control. This would eliminate the need for moving parts such as

hinged control surfaces. They used a prevalent approach with SJA to allow flow to separate and then use the jets to reattach the flow. The forces on the stator blades differ under these two conditions, with the attached flow generating more lift, and consequently a control moment about the vehicle propeller axis. The jet was oriented perpendicular to the flow, rather than in a tangential orientation. Through phase-locked particle image velocimetry (PIV) they observed the flow structures of the SJA, and noted that the turbulent vortex structures had fully dissipated before reaching the stator blade trailing edge, resulting in quasi-steady flow effects. They showed that this approach could successfully reattach the flow and produce control moments, but gave no assessment of whether this was sufficient authority for full vehicle flight control.

Fleming et al. [101][102] explored numerous ways to affect the flow through the duct and over the leading and trailing edges to improve the aerodynamic performance in wind gust rejection and transition from hover to forward flight. The concepts they investigated included internal duct vanes, flow deflectors, thrust reversers, fences on the duct leading edge, leading edge flow control, and trailing edge flaps. They also documented the equation for calculating the magnitude of momentum drag. Their findings showed that mechanisms inside the duct, rather than outside the duct or on the leading/trailing edges, were most effective at reducing pitching moment. The most successful concepts were: a deflector (flow obstruction plate) below the fan with a bleed door beneath it allowing flow to travel from inside the duct to the outside, and vice versa; outward tangential blowing at the duct lip; and an internal vane below the fan that could be deflected. The flow control was deemed impractical due to the size, weight, and power requirements to provide a steady high-pressure air supply. All of the approaches reduced pitching moment through increased drag or reduction in thrust. In each case, the new control effectors could not replace traditional control surfaces, but would augment their performance in wind gust situations.

An alternate approach for generating control forces and moments from a ducted propulsor (underwater) is duct morphing. Quackenbush et al. [103] used shape memory alloy wires to change the shape of the aft section of a ducted propulsor. Morphing the geometry in this way laterally displaced the flow exiting the duct, causing a side force due to the lateral momentum imparted to the flow. Their tests showed successful generation of side forces that would enable control of submersible vehicles.

Ohanian et al. [104] explored ducted fan leading edge and trailing edge flow control using synthetic jets, since the minimal packaging volume requirements were feasible for implementation in a small unmanned air vehicle. The unsteady blowing of the SJAs was compared to steady blowing to assess pitching moment reduction performance. The flow control was analyzed statically as well as for forward flight conditions over a range of angles of attack. That reference summarizes the flow control research presented in this dissertation.

2.4 Literature Review Summary

Substantial research effort has been invested into understanding the aerodynamics of the ducted fan configuration. Many of the benefits and advantages have been quantified and the challenging aerodynamic characteristics that have been explored. There are examples of successful flight vehicles that prove the merit of this VTOL vehicle type for certain missions. Aerodynamic modeling methods and vehicle design methods have been developed to better apply this technology to aircraft systems. Flight control algorithms have been developed to stabilize, control, and navigate these unique vehicles.

With all that has been accomplished, there is still at least one thing lacking: a parametric model that describes the form of ducted fan aerodynamics in simple equations that capture all of the essential characteristics. This model

should be analogous to the linear models of airfoil performance versus angle of attack: $C_L = C_{L_{\alpha=0}} + \left(\partial C_L / \partial \alpha\right) \cdot \alpha$. While this simplified model does not describe how to design an airfoil, it does characterize the behavior for a vast majority of airfoil designs. It stands as a framework that design methods would work within to optimize and report airfoil performance. At the present, there is no such representation for ducted fan aerodynamics. One of the prime objectives of this research is to provide this valuable framework and simplified model for ducted fans.

Researchers in the field of synthetic jet actuators have documented the fundamental flow structures produced by SJAs. Criteria for jet formation have been established using a non-dimensional approach. Many modeling techniques have been developed in both the analytical and numerical schools of thought. Analytical models range in complexity from simple volumetric displacement calculations, to equivalent circuit representations, to evaluating simplified versions of the Navier-Stokes equations. Numerical modeling has focused on applications of CFD to SJA flow prediction. Methods range in complexity from RANS solvers with prescribed oscillatory boundary conditions to models with deforming grids, and use of LES flow simulation. Design methods, experimental optimization, and creative exploration of various actuator implementations have also been documented. Applications of SJA flow control range from cooling microelectronics to steering spinning projectiles.

Ducted fan flow control has been used to affect the duct stall characteristics, augment thrust, alter the pitching moment characteristics, and provide yaw control. The only application of synthetic jets to ducted fan vehicles has been related to flow control on the stators. Controlling the flow over the leading and trailing edge of the duct provides much more potential for large-scale effects than controlling the flow over the stators. The second objective of this research is to explore and quantify the performance of synthetic jet flow control to a ducted fan in these key areas.

Chapter 3 Approach and Experimental Setup

This chapter describes the experimental setup necessary to pursue the objectives of exploring ducted fan aerodynamics, synthetic jet actuators, and new flow control concepts. The purpose is to document the approach, procedure, and setup. The sections outline the overall approach, ducted fan wind tunnel setup, synthetic jet bench tests, and the flow control hardware.

3.1 Overall Approach

The objectives of this research required a multidisciplinary approach to the problem that would result in a successful system. The necessary disciplines spanned aerodynamic, mechanical, and electrical engineering, and entailed design, modeling, simulation, and experimental testing. The overall approach incorporated several phases: researching existing work to gain knowledge and insight; modeling the phenomena to be investigated using established models; design of the vehicle, synthetic jet actuators, and flow control geometry; collecting experimental data from the designs; and analyzing the results to develop new understanding and models.

This research effort in ducted fan aerodynamics and synthetic jet flow control was funded by a Phase II SBIR contract from the U. S. Air Force Research Laboratory (contract #FA8651-07-C-0091), specifically the Air Vehicles Integration Branch of the Munitions Directorate at Eglin AFB. As the Primary Investigator (PI) on this research project at AVID LLC, my employer for the past seven years, I originated all of the concepts being investigated. However, a

team of AVID engineers (ranging from three to ten at various times) and two subcontractors, all under my direction, were necessary to achieve this project's overall goals. Only a subset of the results is presented here as relevant to the topic of this dissertation and as my original work. Work that entailed collaboration between others and myself or was performed primarily by others within the team will be denoted in the text. Two particular areas that fall under that category are the wind tunnel model fabrication and the synthetic jet flow control CFD. These are fundamental to the overall thrust of the research and will be included for completeness, with credit given to the appropriate parties.

The design of ducted fan vehicles is a core competency of AVID LLC, and the proprietary methods used to design the aerodynamic components of the vehicle will not be a focus of the work presented, nor will the details of the geometric designs be included. The ducted fan vehicle design tested is a sufficient platform for evaluating the merit of the flow control concepts proposed. The wind tunnel model and the tests performed at the Virginia Tech Stability Tunnel will be documented below. The synthetic jet actuator design was a purely new development and will be documented in its entirety. The flow control integration of the SJAs involved an intensive design study to determine configurations and geometries that produce the intended effects. The vehicle integration of the actuators is also detailed below.

3.2 Ducted Fan Experimental Setup

A generic vehicle design was employed to evaluate the fundamental aerodynamics of a ducted fan configuration. The base configuration consisted of a duct, 1 ft. diameter fan, stator assembly, and fuselage. Techsburg Inc. constructed the wind tunnel model in a modular fashion such that various control vanes, duct lips and trailing edges could be tested using the same apparatus. For the data presented in this dissertation, control vanes were not installed, and the axisymmetric lip and trailing edge geometries were held

constant. Techsburg's 6-component force and moment balance was used to record the complete set of forces and moments the model experienced in static and wind tunnel tests. Fan torque required was recorded from the motor controller, which was calibrated through dynamometer tests to relate the shaft output power to the electrical input power. Pictures of the balance and model during static tests are shown in Figure 3-1. A schematic of the force and moment balance that attaches to the model, and the shroud to eliminate aerodynamic loading on the balance, are shown in Figure 3-2.

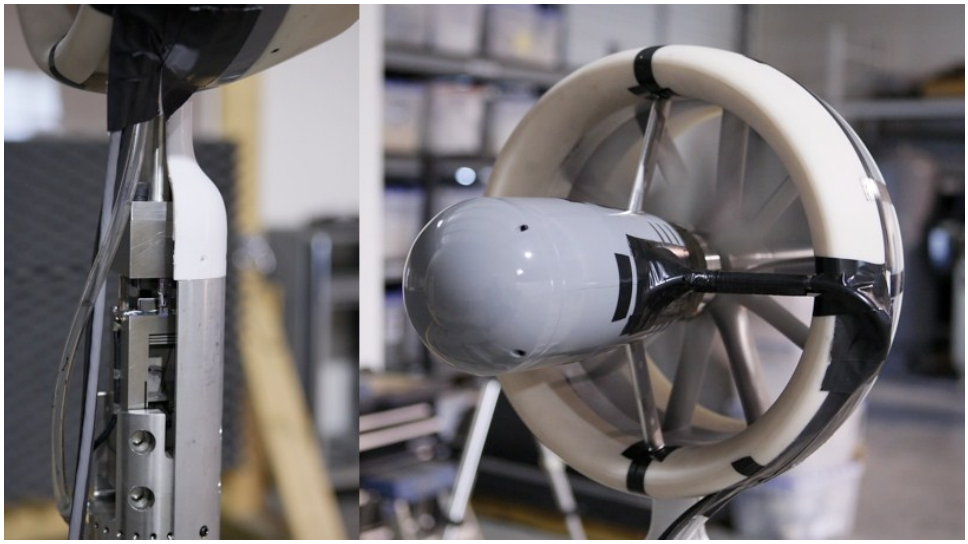

Figure 3-1. Experimental setup: (left) Force and moment balance; (right) Vehicle model with fan spinning.

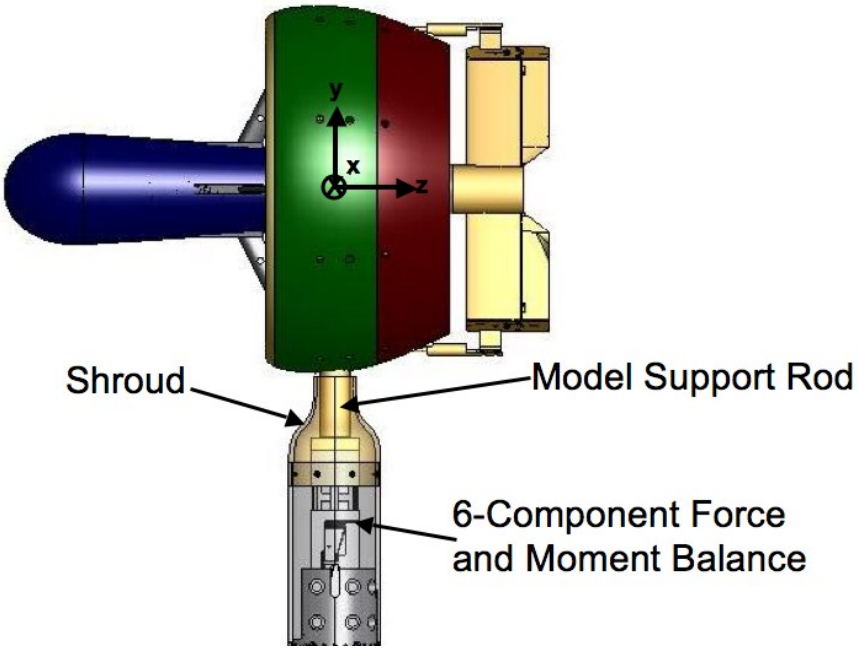

Figure 3-2. Balance mounting of wind tunnel model.

The model was installed in the Virginia Tech 6'x6' Stability Wind Tunnel for wind-on testing, and is pictured in Figure 3-3. That image represents a case with control vanes installed in the model, but these were excluded in the basic configuration that was used to derive the new ducted fan aerodynamic modeling scheme. Static tests were performed outside of the wind tunnel in a high bay area to avoid pumping effects in the tunnel. The balance and test-stand rotated on a turntable. Therefore, the vehicle was mounted on its side with the body y-axis pointing up, to be able to evaluate a pitch angle (angle of attack) sweep via turntable rotation.

Figure 3-3. Vehicle model installed in Virginia Tech 6 ft x 6 ft Stability Wind Tunnel.

The force and moment balance range, and the uncertainty in measured forces and moments at the model reference center, are reported in Table 1. The uncertainty in non-dimensional variables derived from the test data is also shown, as calculated using the procedure found in AIAA standard S-071A-1999 [106] for the coefficient formulas described in Chapters 4 and 6. The primary terms of interest for this analysis are F_X, F_Z, and M_Y in the body-fixed coordinate frame (normal force, thrust, and pitching moment, respectively). Therefore, the most accurate moment axis of the balance was aligned with the vehicle pitch axis, as can be seen in the table. The relatively large uncertainty in Figure of Merit (FM) compared to the other quantities is due to the fact that it is a function of both thrust and power, and must account for uncertainty in both sources. The uncertainty in turntable angular values (vehicle angle of attack) is estimated at 0.2 degrees, as this represents the maximum value observed in daily re-alignment procedures after many turntable sweeps.

Table 1. Balance Range and Uncertainty

Term	Balance Range	Uncertainty (dimensional)	Uncertainty (non-dimensional)	Non-dimensional Term
F_X	±120 lb	0.25 lb	0.011	C_X and C_N
F_Y	±120 lb	0.2 lb	0.008	C_Y
F_Z	±120 lb	0.25 lb	0.011	C_Z and C_T
M_X	±100 ft-lb	0.4 ft-lb	0.017	C_l
M_Y	±30 ft-lb	0.1 ft-lb	0.004	C_m
M_Z	±100 ft-lb	0.4 ft-lb	0.017	C_n
Shaft Power	-	0.08 HP	0.019	C_P
FM	-	-	0.047	FM

3.3 Synthetic Jet Actuator Experimental Setup

The synthetic jet actuator design was accomplished through two rounds of design and experimentation. The first round was exploratory, and aimed to compare different piezoelectric elements to drive the synthetic jet vibrating diaphragm. Bimorph disks and custom made Macro Fiber Composite (MFC) actuators were compared during this phase. The second round of SJA experiments was focused on optimizing performance for the specific flow control application that was wind tunnel tested. Mass-produced and inexpensive piezoelectric unimorph disks were used for this round of development. The machined parts required for the first round of testing were fabricated in the Virginia Tech Engineering Science and Mechanics machine shop. Techsburg Inc. fabricated the machined parts for the second round of tests. Colleagues at AVID LLC created the computer aided design (CAD) detailed drawings, but the designs were solely my creation. The CAD drawings are included for reference in Appendix B. The following sections describe the experimental setup for each of these rounds of tests.

3.3.1 Round 1 Synthetic Jet Actuator Development: Bimorphs and MFCs

The motivation for this round of investigation was to determine if a new design of MFC was a good choice to base a SJA design around. The element in question was the star-shaped M20-4D50-80star8P1 from Smart Materials Corp., which can expand and contract in a radial direction (Figure 3-4). If bonded to a passive substrate (a unimorph configuration), a doming deflection can be produced as the MFC strains.

Figure 3-4. Star-shaped MFC actuator.

Macro Fiber Composites were invented at NASA Langley Research Center in 2000 [105]. MFC actuators consist of rectangular unidirectional piezoceramic fibers (PZT-5A) embedded in a thermosetting polymer matrix. This layer is then sandwiched between copper-clad Kapton (polyimide) film layers that have an inter-digitated electrode pattern. This assembly enables in-plane poling, actuation, and sensing in a sealed, durable, ready-to-use package. When embedded in a surface or attached to flexible structures, the MFC provides distributed solid-state deflection actuation and/or strain measurements. MFCs are also flexible, durable, damage tolerant, conformal to surfaces, readily embeddable in structures, and have environmentally sealed packaging. The in-plane poling and subsequent voltage actuation allows the MFC to utilize the d_{33}

piezoelectric effect, which is much stronger than the d_{31} effect used by traditional PZT actuators with through-the-thickness poling.

The allowable input voltage for MFCs range from -500 Volts to +1500 Volts, resulting in a larger expansion strain than contraction. This causes the MFC unimorph to have a predominant deflection direction toward the side of the substrate with the bonded MFC. By supplying an oscillating input, the actuator will function as a vibrating diaphragm that will drive a SJA.

The experimental setup was fabricated in a modular way to accommodate different diaphragm elements, chamber depths, and orifice geometries. This was accomplished by stacking a base plate, piezoelectric diaphragm, cavity plates, and an orifice plate. Each stacked configuration was bolted with six equally spaced bolts to fix the plates together uniformly. For most cases, only one orifice was used, with 0.05" depth and 0.125" diameter. The tested piezoelectric diaphragms were two MFC unimorphs, one with a 0.005" brass substrate, and the other with a 0.010" brass substrate. The MFC elements were bonded to the brass with 3M 460DP epoxy using a vacuum bag to ensure uniform bonding. An image of the 0.010" brass substrate actuator is shown in Figure 3-5. The rectangle in the center is reflective tape for taking laser measurements, the cutouts on the edges are to match the bolt pattern of the clamping setup, and the radial wedge cutouts were added by the manufacturer to avoid de-lamination of the Kapton under extreme deflection.

Figure 3-5. Star-shaped MFC unimorph, 0.010" brass substrate.

The bimorph diaphragm evaluated was a Piezoelectric Systems Inc. model number T216-A4NO-573X, 2.5” diameter diaphragm without a center shim. The input voltage limits for the MFC were -500 V to +1500 V, while the bimorph had limits -180 V to +180 V. The back of the mounting base plate was left open so that optical measurements of diaphragm position and velocity could be obtained via a Polytec PI laser-doppler vibrometer. Jet velocities were measured with a Dantec 55M01 anemometer with TSI hotwire probe 1210-T1.5. Hotwire anemometry can measure velocities at frequencies up to 50 kHz, and is therefore a favored instrument for measuring SJA flows. The anemometer was calibrated over the range of expected jet velocities (0 to 200 ft/sec), and a fourth order polynomial was used to translate output voltage to air velocity. The hotwire probe (approximately 0.08” long filament, microns in diameter) was positioned at the center of the 0.125” orifice, one diameter away in the axial direction. Other researchers have recognized this practice as a sufficient method to characterize and compare SJA performance [85]. A dSPACE™ data acquisition system with SIMULINK™ integration was used to run the experiments, automate tests, and collect data. A Trek 50/750 power supply/amplifier was used to generate the high voltages (1500V) necessary for the piezoelectric elements. Figure 3-6 shows the overall setup, and Figure 3-7 shows a close up view of the hotwire probe and SJA.

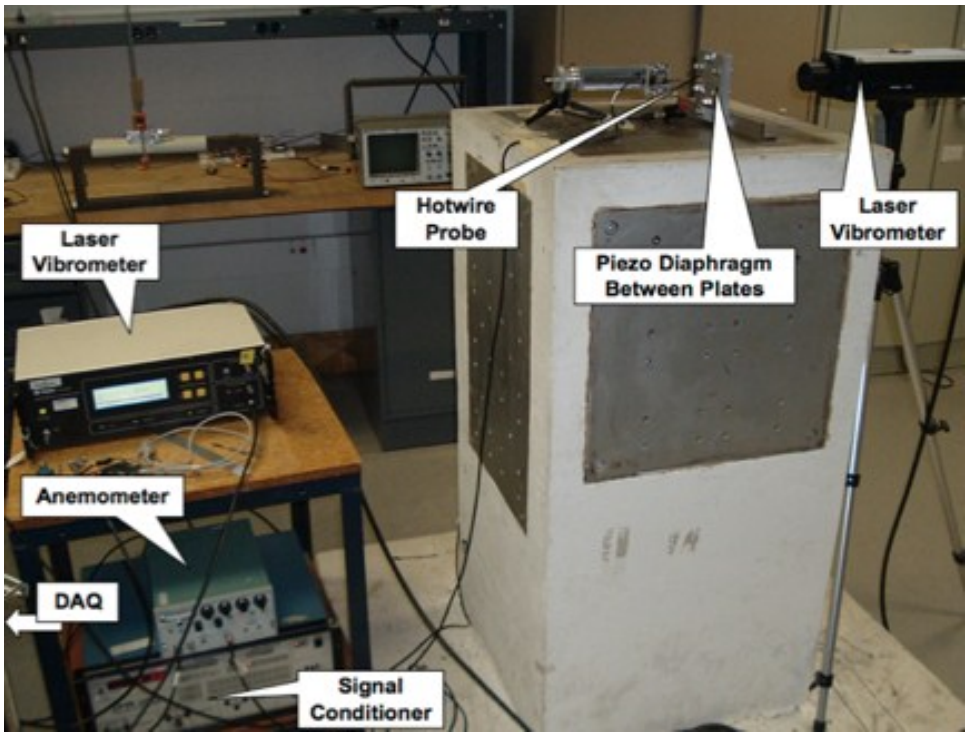

Figure 3-6. Complete synthetic jet experimental setup.

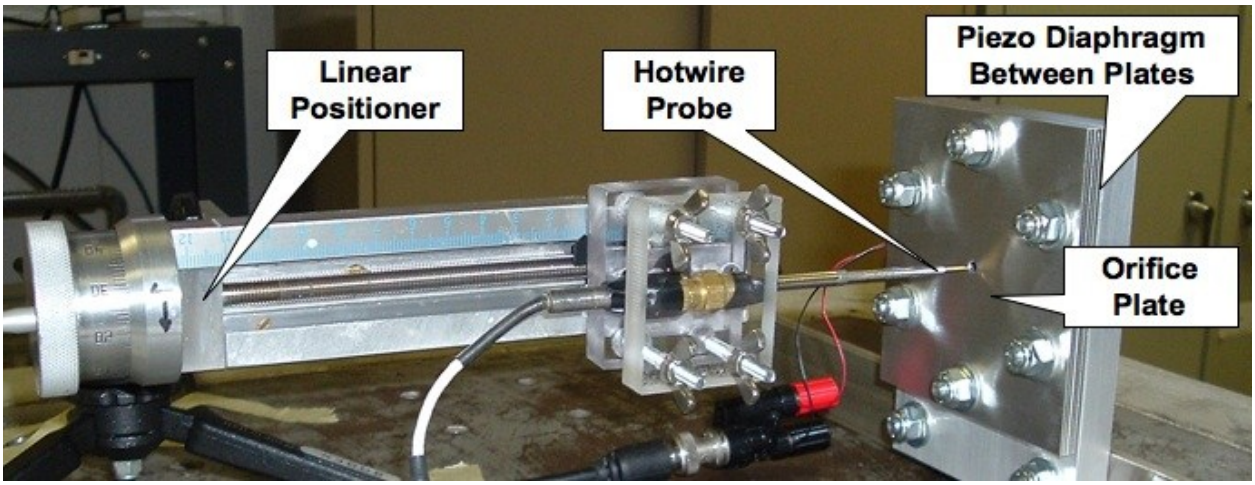

Figure 3-7. Synthetic jet actuator and hotwire anemometer probe and positioning stage.

3.3.2 Round 2 Synthetic Jet Actuator Development: Unimorphs

A second round of component development was undertaken to design and bench test synthetic jet actuators based on flight-size piezoelectric elements (27mm diameter APC FT-27T-3.9A1). The intent was to identify anticipated jet

velocities for vehicle wind tunnel testing. The piezoelectric element selected was a mass-produced unit with the intended use as a piezoelectric buzzer, and consequently was relatively inexpensive (roughly $1 each). This element was used by Gomes et al. [85] to produce a peak jet velocity of 420 ft/sec (130 m/s) for a 0.05" circular orifice in a normal orientation configuration (jet perpendicular to diaphragm). One of the objectives of this test was to quantify the expected jet velocities for a laterally oriented (jet parallel to diaphragm) rectangular slot with orifice area more than ten times greater than the results in Gomes et al. A long slot orifice is more applicable to the tangential flow control concepts investigated for the ducted fan application. The bench test setup is shown in Figure 3-8, with a schematic of the cavity layout with the slot length dimension going into the page.

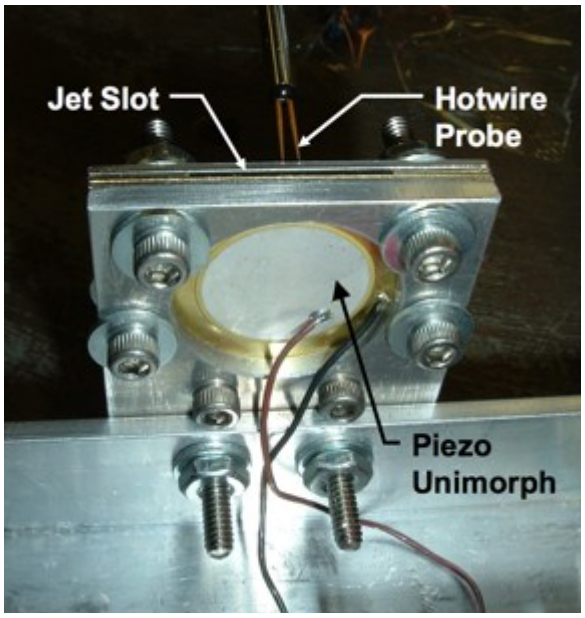

(a)

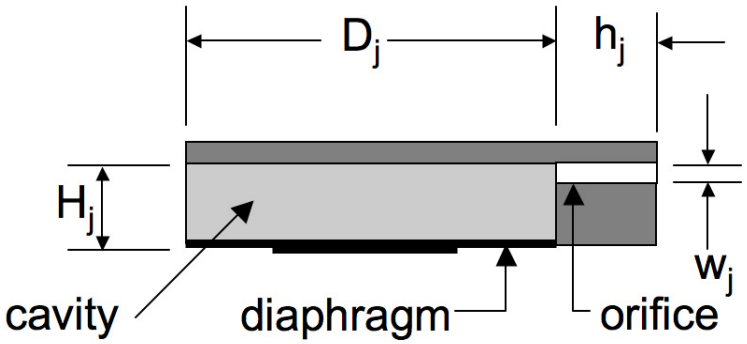

(b)

Figure 3-8. Unimorph synthetic jet setup: (a) Close-up of experimental setup for synthetic jet testing, (b) Schematic of lateral jet cavity layout.

The input voltage limits used for the piezoelectric diaphragm were +/-150 V. Jet velocities were measured with a Dantec 55M01 anemometer with TSI hotwire probe 1210-T1.5. The hotwire probe was positioned at the center of the slot orifice width and length, one slot width away in the axial direction as mentioned previously for the first round of experiments. The hotwire data was sampled at 40 kHz, the maximum speed attainable by the data acquisition system to capture as many data points within a jet cycle. The smaller unimorphs operated at much higher frequencies (1900 to 2500 Hz) than the bimorph and MFC diaphragms tested. This sampling speed provided roughly

twenty data points per jet cycle (with variation from this value based on driving frequency). A dSPACE™ data acquisition system with SIMULINK™ integration was used to run the experiments, automate tests, and collect data. A Trek 50/750 power supply/amplifier was used to generate the high voltages (+/-150V) necessary for the piezoelectric elements, but was limited in current to 50 mA.

3.3.3 Hotwire Anemometer Calibration

Hotwire anemometry requires a very specialized set of equipment and a detailed procedure to attain valid results. The fundamental principle behind its operation is based on the convective heat transfer from the wire filament. For a constant temperature probe/anemometer, the measurement of velocity is based on the electrical current required to keep the filament at the predetermined operating temperature. Internal to the anemometer, a feedback loop controls this current. The output voltage signal from the anemometer is derived from the amount of current passing through the hotwire filament. The temperature of the heated wire is proportional to the resistance of the filament, and each probe must be uniquely characterized. A calibration curve must be derived to relate voltage output from the anemometer to the velocity magnitude of air passing over the probe.

The anemometer was calibrated over the range of expected jet velocities using the Virginia Tech Aerospace and Ocean Engineering department's hotwire calibrator. The ambient temperature, pressure, and jet velocity were recorded along with the raw anemometer output voltage. The range of air velocities in the calibration dataset spanned from 0 to 300 ft/s. A signal conditioner was required to scale and bias the raw voltage output signal (variation originally in mV) to yield maximum resolution over the +/-5V range of the data acquisition hardware. A fourth order polynomial was used to translate the conditioned output voltage to air velocity. The calibration curve can be seen in Figure 3-9, which includes the polynomial equation and coefficient of multiple

determination (R^2 value). This approach was selected because it yielded better agreement with the data than the traditional King's Law equation [107], seen in Figure 3-10, which had a lower R^2 value for the curve fit.

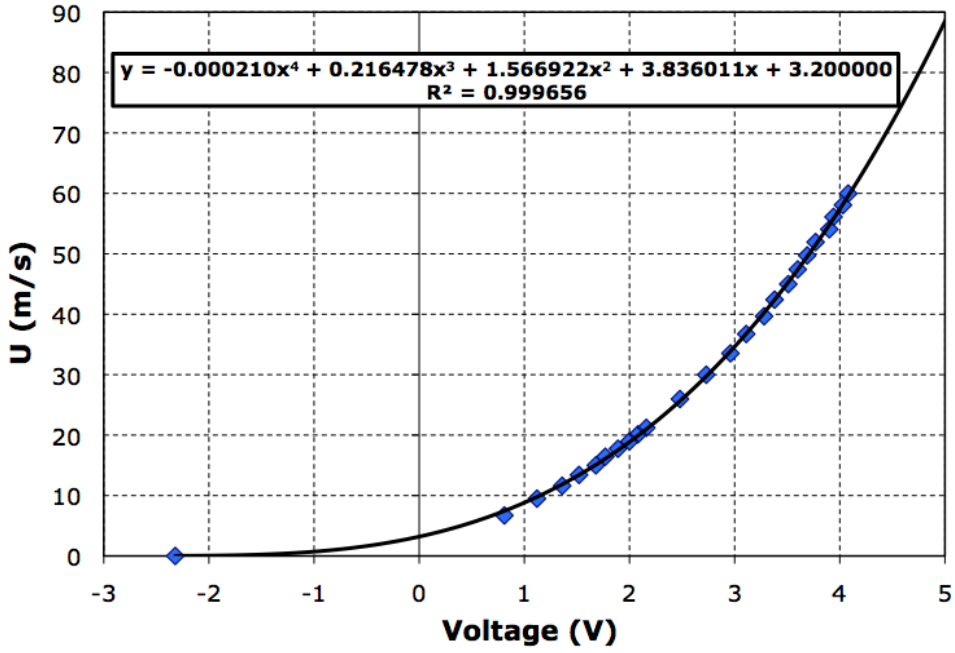

Figure 3-9. Fourth order calibration curve used for collecting jet velocity measurements.

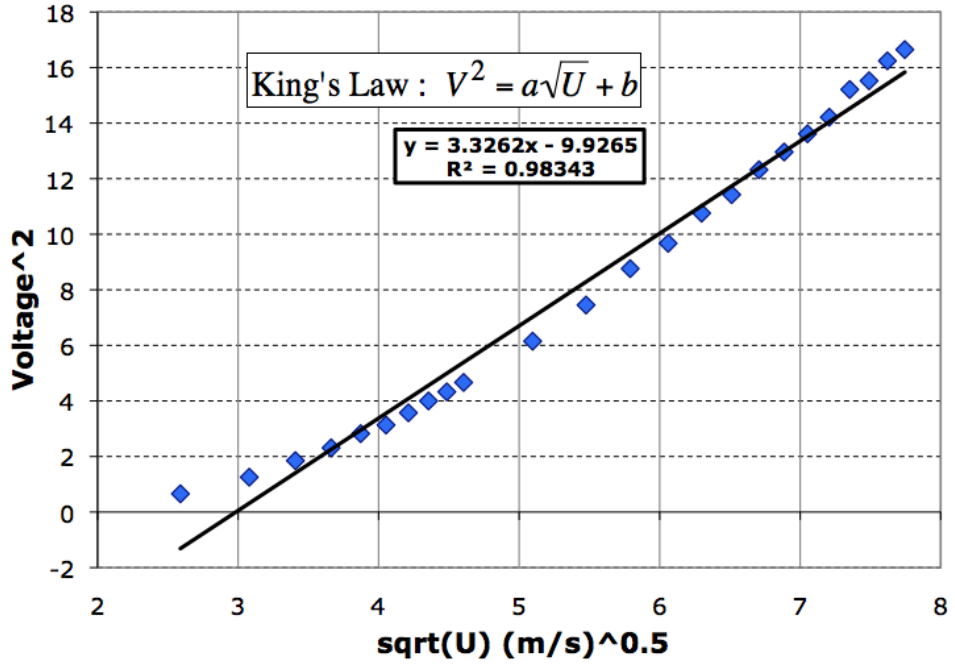

Figure 3-10. Traditional "King's Law" calibration curve used for hotwire anemometry.

3.4 Flow Control Experimental Setup

Multiple configurations of the vehicle model, with flow control on the duct leading and trailing edge, were used to explore the effects of the synthetic jets as well as steady blowing using a compressed air supply. Synthetic jet velocities in the vehicle slots were measured statically (no fan or tunnel flow) with the hotwire anemometry as described in the previous section. The duct trailing edge flow control peak velocities were comparable to bench test results (~200 ft/s), but the duct leading edge peak velocities were roughly 60% of the bench test values. This was attributed to the orifice depth being longer (due to manufacturing constraints) and the resulting additional losses caused a lower jet output and damped natural frequency. The optimum drive frequency for trailing edge actuation was 2300 Hz and for leading edge actuation was 1900 Hz. The test configurations used for leading edge and trailing edge flow control are shown in Figure 3-11.

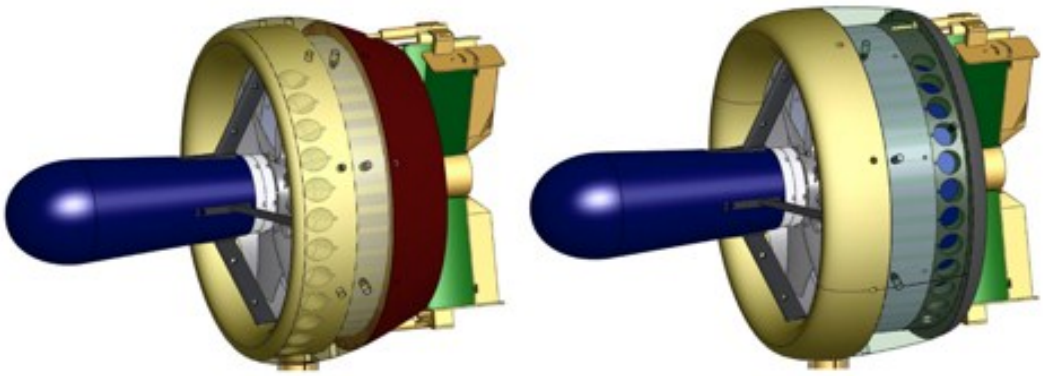

(a) **(b)**

Figure 3-11. Flow control vehicle configurations: (a) Leading edge blowing, (b) Trailing edge Coandă blowing.

Removing the piezoelectric diaphragms and related mounting hardware created a plenum channel in the model. Supplying pressurized air to this plenum channel that connected the jet cavities enabled steady blowing with minimal change to the model. Steady blowing velocities were set using a Dwyer in-line Visi-float® mass flow meter, with pressure-corrected volumetric flow

rates ranging from 15 to 50 cubic feet per minute (cfm). This translated to steady blowing velocities ranging from 160 to 510 ft/s. Hotwire anemometry was used to verify the flow speed and uniformity between jets. The flexible tubing for supply air was affixed to the rigid shroud outside the balance (as seen in Figure 3-2) with slack between the shroud and vehicle model to isolate the force and moment measurements from unintended interference effects. Steady and synthetic jet blowing tare runs with the propeller stopped and wind off did not show significant force and moment response. Only eight of the slots were employed in tests, accounting for one quarter of the duct circumference on the windward side.

Figure 3-12 shows the Coandă trailing edge component installed in the vehicle, with a close-up view of the curved 0.030" slot geometry. The leading edge and trailing edge flow control components were both machined from aluminum, and EDM (electrical discharge machining) was employed to obtain precise slot geometry. The components were anodized to electrically isolate the piezoelectric components from the rest of the model.

Figure 3-12. Coandă trailing edge flow control slot geometry, viewing the duct from below.

Figure 3-13 shows the leading edge flow control duct lip installed in the vehicle. The airflow over the duct naturally comes from the outside of the duct toward the fan. The slots are oriented to point outward such that when blowing is actuated the flow over the lip could be caused to separate on demand.

Figure 3-13. Leading edge flow control configuration in the wind tunnel.

3.4.1 Synthetic Jet Drive Circuitry

Two methods of driving the piezoelectric diaphragms were used during testing. Both were based on COTS technology. The first was a Trek PZD350 M/S power amplifier. This device was specifically suited to driving capacitive loads such as the piezoelectric SJA array. It was internally current-limited to 400mA. This limit was encountered when driving the eight-element sub-array with a sine wave at near maximum voltage. When driving with a square wave, this current limit was encountered at moderate voltages. This was as expected because the waveform of the electric current due to square wave driving consists of very short-duration, high-amplitude spikes at each rising and falling edge.

The second drive method was based on an Apex Microtechnology (subsidiary of Cirrus Logic) PA93 high voltage op-amp integrated circuit (chip) and associated EK16 evaluation kit. The PA93 was capable of outputting +/-200V at 8A, with slew rates as high as 50V/μs. A classical inverting op-amp circuit configuration was used. A minimalist bipolar DC power supply was constructed to power this circuit using a variac (variable transformer) for isolation/voltage adjustment, two diodes acting as half wave rectifiers, and two 1500μF bulk storage capacitors. The purpose of the half wave rectification was

to provide symmetric positive and negative rail voltages to the op-amp. These aspects of the circuit are shown below in Figure 3-14. Although the PA93 included current limiting via a current sensing resistor, it did not respond fast enough to protect the device against square wave current spikes. Thus, this circuit was restricted to sine wave operation at the higher power operating condition. The development of this electric circuit design was performed by colleagues at AVID LLC, and is included here for completeness.

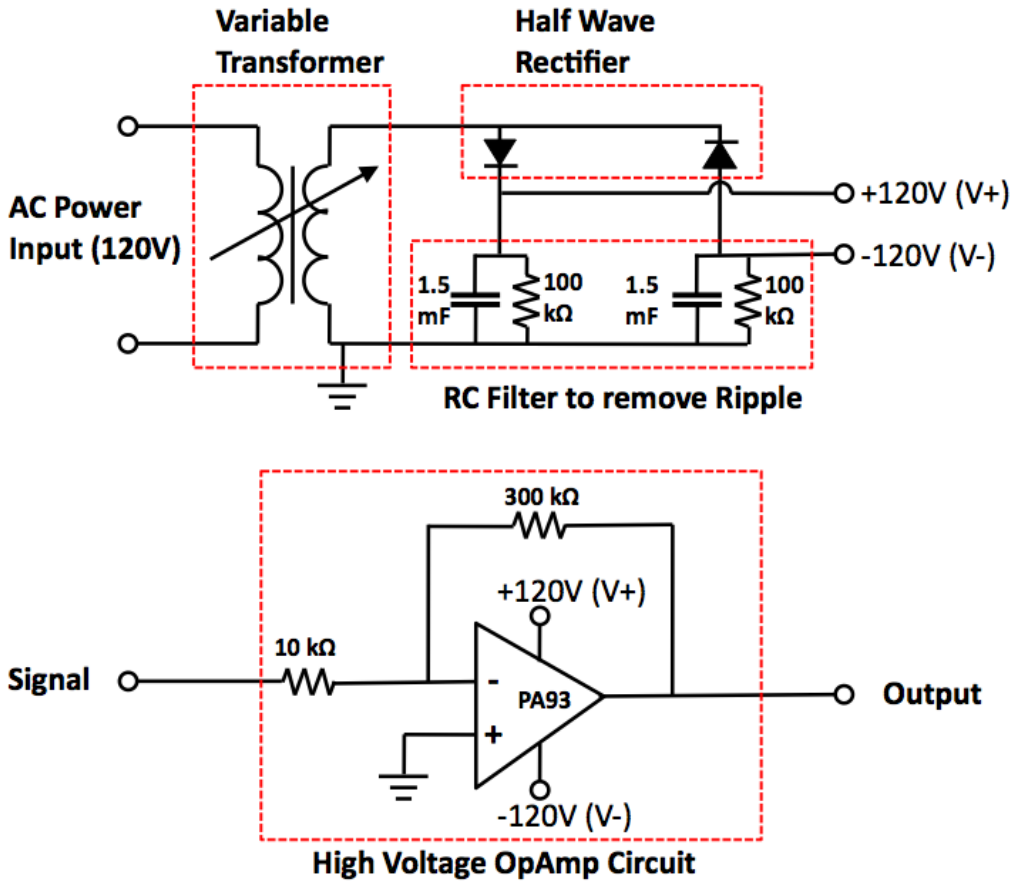

Figure 3-14. Simplified schematic of PA93/EK16 based drive circuit.

The synthetic jet actuator piezoelectric elements installed in the vehicle are shown in Figure 3-15. The piezoelectric diaphragms were wired in parallel using a bus of wires that was connected to the drive circuits detailed above. A cover was then attached to the model to conceal the SJAs and provide smooth aerodynamic surfaces for wind tunnel testing.

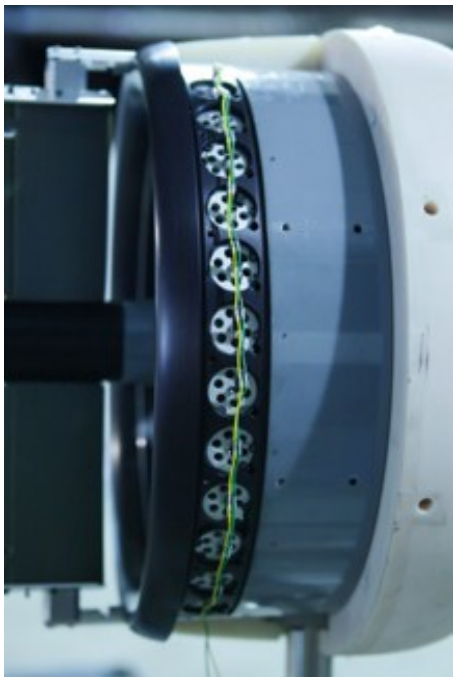

Figure 3-15. Wiring of SJAs in wind tunnel model.

Chapter 4 Ducted Fan Aerodynamics and Modeling

This chapter details the developments of a new approach to modeling ducted fan aerodynamics. The findings were made through observations of patterns within the aerodynamic experimental data collected. A non-dimensional scheme is developed to concisely describe the nature of the ducted fan characteristics, and is also applied to a legacy data set from NASA ducted fan wind tunnel tests to show its general applicability.

The vehicle aerodynamics using the baseline configuration of the vehicle without control vanes were evaluated for a range of free-stream velocities up to 85 ft/s. These tests used three fan RPM settings and a range of angles of attack that cover the entire flight envelope. This range of angles of attack is much larger than that of conventional helicopters or airplanes. A listing of flight conditions tested is shown in Table 2.

Table 2. Test Run Matrix

Velocity	Angle of Attack Range	RPM Range
0 ft/s	N/A	5000 to 7000, increments of 1000
17 ft/s	0° to 100°, increments of 10°	5000 to 7000, increments of 1000
35 ft/s	0° to 90°, increments of 10°	5000 to 7000, increments of 1000
60 ft/s	0° to 70°, increments of 10°	5000 to 7000, increments of 1000
85 ft/s	0° to 50°, increments of 10°	5000 to 7000, increments of 1000

4.1 Wind Tunnel Correction Derivation

Before we can discuss the results in the experimental data, corrections to the wind tunnel data must be applied. The flow induced through the ducted fan is a dominant contributor to the configuration's own aerodynamics. Therefore, its effect on the wind tunnel flow must also be considered carefully when interpreting test results. While the flow speed within the tunnel can be controlled, the forces developed by the ducted fan may differ significantly from the comparable free air case of the same speed. This is particularly the case when a closed-jet tunnel is used, as in the results presented here.

The tunnel walls, which constrain the flow, alter the speed and pressure of the air in the vicinity of the duct and down stream from the model. After surveying the possible corrections to wind tunnel data listed in Barlow, Rae, and Pope [108], I identified that the most significant consideration was this effect of the powered model on the effective velocity in the tunnel. Another concern is the possibility of V/STOL flow breakdown when the slipstream (high-speed flow coming out of the duct) interacts with the tunnel walls. These two effects are more dominant than the typical corrections employed for 2-dimensional airfoil or 3-dimensional unpowered wing tests such as: buoyancy, solid blockage, wake blockage, and angle of attack corrections.

For reference, the solid and wake blockage assessed using the principles in [108] for unusual shapes is 0.59 ft^2 compared to a tunnel cross section area of 36 ft^2. This would normally result in higher velocities than the nominal tunnel velocity passing around the model. However, with a powered model, the fan entrains a significant portion of the wind tunnel flow resulting in the opposite effect. The net result is a flow around the model that is slower than the nominal tunnel velocity, as explained in Glauert [109] where he derives corrections for testing propellers in closed wind tunnels. Other approaches include the Hackett-Wilsden [110] and Mikkelsen and Sørensen [111] techniques, but experimental results by Fitzgerald [112] suggest the Glauert correction matched empirical observation best. For lifting rotors perpendicular

to the tunnel flow, Heyson's method using images and modeling of the deflected rotor wake [113] is a well-accepted approach. In a similar vein, Loeffler and Steinhoff [114] present a method of images to correct for closed wind tunnel tests of pure axial flow for propellers located at the inlet of diffuser cones with aggressive expansion angles. For simplicity, the development here will follow Glauert's argument from first principles and adjust the derivation to account for the effect of the duct on the propeller flow.

Glauert's general approach is to apply the principles of mass conservation, momentum conservation, and Bernoulli's equation to the aerodynamic case of a free propeller. The intent is to ascertain the free-air velocity that is equivalent to the test conditions. A schematic of the problem is shown in Figure 4-1, where C is the tunnel cross section area, A is the propeller disk area, S is the final slipstream area, p is the static pressure upstream of the model, V is the tunnel velocity upstream of the model (nominal tunnel velocity), u is the speed of the flow at the fan plane, u_0 is the speed of flow outside the slipstream exiting the control volume, u_1 is the final slipstream velocity, and p_1 is the static pressure downstream of the model.

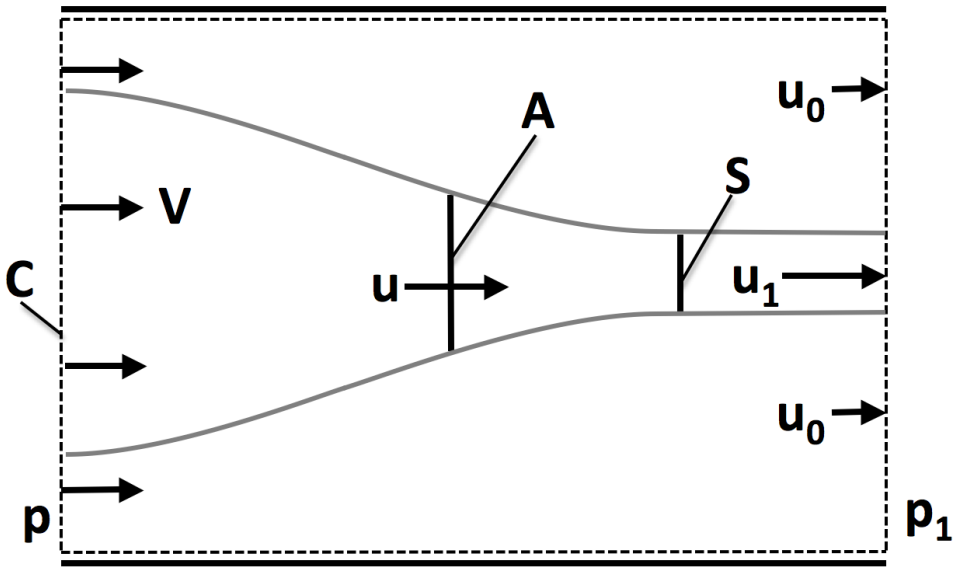

Figure 4-1. Control volume schematic of isolated propeller in closed wind tunnel.

Because the flow through the fan (u) is higher than the tunnel datum velocity (V), mass conservation implies the flow around the fan and downstream outside the slipstream must be slower than the tunnel datum velocity. In Glauert's approach, the far-field slipstream velocity and diameter are determined using continuity (Eq. 3), the momentum equation (Eq. 4), and Bernoulli's equation with a pressure discontinuity across the fan to account for the thrust (Eq. 5):

$$\rho VC = \rho u_1 S + \rho u_0 (C - S) \tag{3}$$

$$T = \rho S u_1 (u_1 - V) + \rho (C - S) u_0 (u_0 - V) + C(p_1 - p) \tag{4}$$

$$\frac{T}{A} = \left(p_1 + \frac{1}{2}\rho {u_1}^2\right) - \left(p + \frac{1}{2}\rho V^2\right) = \frac{1}{2}\rho\left({u_1}^2 - {u_0}^2\right) \tag{5}$$

where ρ is air density, and T is thrust. The momentum equation includes a pressure term not usually present in free-air momentum theory, but is present in this case due to the tunnel walls constraining the flow. The Bernoulli thrust equation is further simplified to be merely a function of the downstream velocities inside and outside the slipstream, accomplished by applying Bernoulli's equation outside the propeller streamlines to eliminate the tunnel velocity and pressure from the equation. The momentum and Bernoulli's equations both address the relationship between thrust and velocities. These two equations are necessary because the slipstream velocity *and* diameter are unknown. The slipstream diameter differs from the free-air solution because of the presence of the tunnel walls. From the wake velocity, tunnel velocity, and measured thrust, Glauert deduces the equivalent free-air climb velocity from momentum theory using Eq. 6. Here, V' is the equivalent free-air climb speed corresponding to the tested conditions. The final result is a ratio of equivalent airspeed to nominal tunnel airspeed in Eq. 7, which is a function of velocity, non-dimensional area, and non-dimensional thrust as defined by Glauert (Eq. 8).

$$T = \dot{m}\left(u_1 - V'\right) = \rho S u_1 \left(u_1 - V'\right) \tag{6}$$

$$\frac{V'}{V} = 1 - \frac{\alpha_p \tau_p}{2\sqrt{1 + 2\tau_p}} \tag{7}$$

$$\alpha_p = \frac{A}{C}, \quad \tau_p = \frac{T}{\rho A V^2} \tag{8}$$

The presence of a duct or shroud around a propeller significantly changes the mechanism of thrust production and the resulting slipstream diameter. The typical assumption made in 'simple' momentum theory, as noted in [24], is that the flow exiting the duct will be at the same pressure as the air outside the duct (ambient pressure for the free-air solution), and thus will not contract. This causes the slipstream diameter to be equal to the exit diameter of the duct. Black and Wainauski [33] noted that the total pressure in the slipstream was slightly higher than ambient pressure in their tests, and concluded that there may be a small contraction of the slipstream aft of the duct during wind tunnel tests. However, the experiments of Pereira [13] showed the surface pressures along the inside of the duct returning to ambient at the duct trailing edge, implying no significant contraction aft of the duct. While the possibility of marginal wake contraction exists, it is still a reasonable simplifying assumption to assume the wake area is equal to the duct exit area, as it has been assumed throughout much of the literature. Applying these assumptions, the new schematic of the problem is shown in Figure 4-2. It should also be noted that the simple momentum theory assumptions imply steady, incompressible, and inviscid flow.

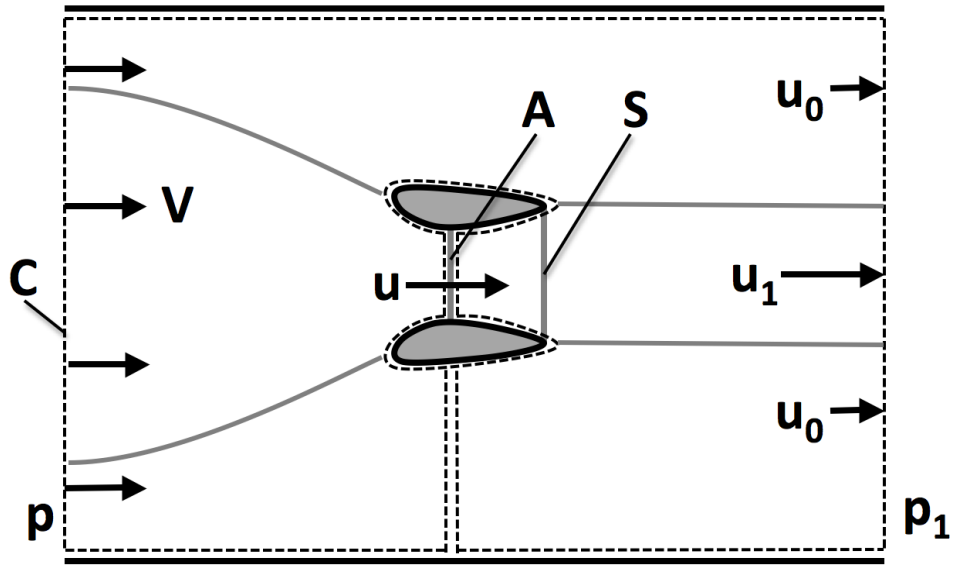

Figure 4-2. Control volume schematic of ducted propeller in closed wind tunnel.

With the area of the slipstream determined by the duct exit diameter, either the momentum equation or Bernoulli's equation can be eliminated from the set of equations necessary to characterize the flow. It is advantageous to eliminate Bernoulli's equation since it is based on the pressure discontinuity across the fan, and the exact thrust split between the fan and duct is unknown (dependent on expansion ratio and flow speed). The remaining mass conservation equation can be solved for u_0, and converting to use an area ratio of duct exit area (slipstream area) to tunnel cross-section area the result is shown in Eq. 9. The non-dimensional area and thrust for the ducted fan corrections are now based on duct exit area instead of fan disk area (Eq. 10).

$$u_0 = \frac{V - \alpha_d u_1}{1 - \alpha_d} \tag{9}$$

$$\alpha_d = \frac{S}{C}, \quad \tau_d = \frac{T}{\rho S V^2} \tag{10}$$

and substituting Eq. 9 into Eq. 4 and solving for u_1/V yields:

$$U = \frac{u_1}{V} = \frac{1 - 2\alpha_d + (1 - \alpha_d)\sqrt{(4 - 6\alpha_d)\tau_d + 1}}{2 - 3\alpha_d} \tag{11}$$

Equation 11 can be substituted into Eq. 6 and rearranged to form an equation comparable to Eq. 7, but for ducted propellers:

$$\frac{V'}{V} = U - \frac{\tau_d}{U} \tag{12}$$

The final result is a new correction equation for ducted propellers (Eq. 12) that can predict the equivalent air velocity for any combination of specified tunnel velocity, measured thrust, fan area and tunnel cross-section area. A visual comparison between Glauert's correction (Eq. 7) and the new correction for ducted fans (Eq. 12) is shown in Figure 4-3.

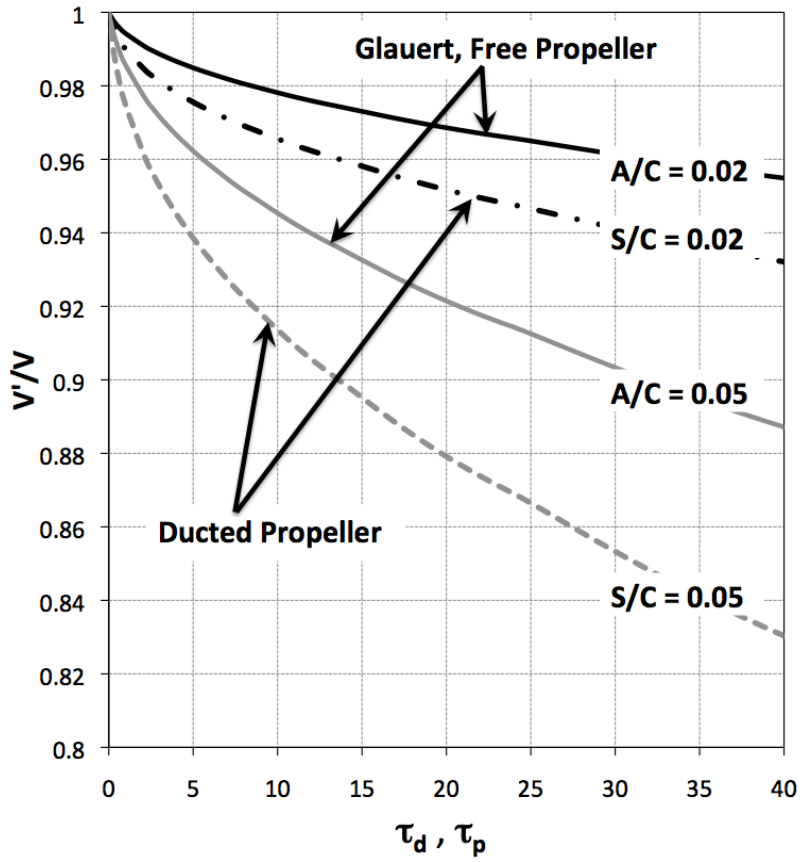

Figure 4-3. Comparison of ducted fan velocity correction to Glauert's free propeller correction.

For the same thrust, velocity, and comparable area, the equivalent air velocity for the ducted fan shows a larger reduction from the nominal tunnel velocity than the free propeller. The slipstream does not contract significantly for a ducted fan; therefore, the same thrust level results in an exit flow speed that is slower but with a higher mass flow. This higher mass flow through the duct captures a larger portion of the tunnel flow, forcing the flow outside the duct to be slower than the flow around a similar free propeller. This new velocity correction technique has been applied to the wind tunnel data presented in the following sections.

4.2 Wind Tunnel and Static Experimental Results

The key parameters to modeling a ducted fan vehicle's performance are the aerodynamic forces, moments, and the power required to produce those quantities. Measurement of these parameters was performed for the axisymmetric ducted fan, as described in the section concerning experimental setup. Because the vehicle is axisymmetric, the force and moment data for a single pitch sweep can be used to model the vehicle flying in any direction. To fly forward, the vehicle pitches into the wind. For flight speeds of 85 ft/s the vehicle can tilt 45° to 60° into the wind to attain equilibrium ("trim"), depending on the design. The wind tunnel test plan was devised to cover all equilibrium flight conditions by the range of flight parameters tested. The raw force and power data versus angle of attack ("alpha") for a fixed fan RPM of 6,000 are shown in Figure 4-4 through Figure 4-7 for forward pitch sweeps at each nominal tunnel velocity listed in the plot. All forces and moments are reported in the body-fixed coordinate system. The complete set of raw data from the tests is included in Appendix A.

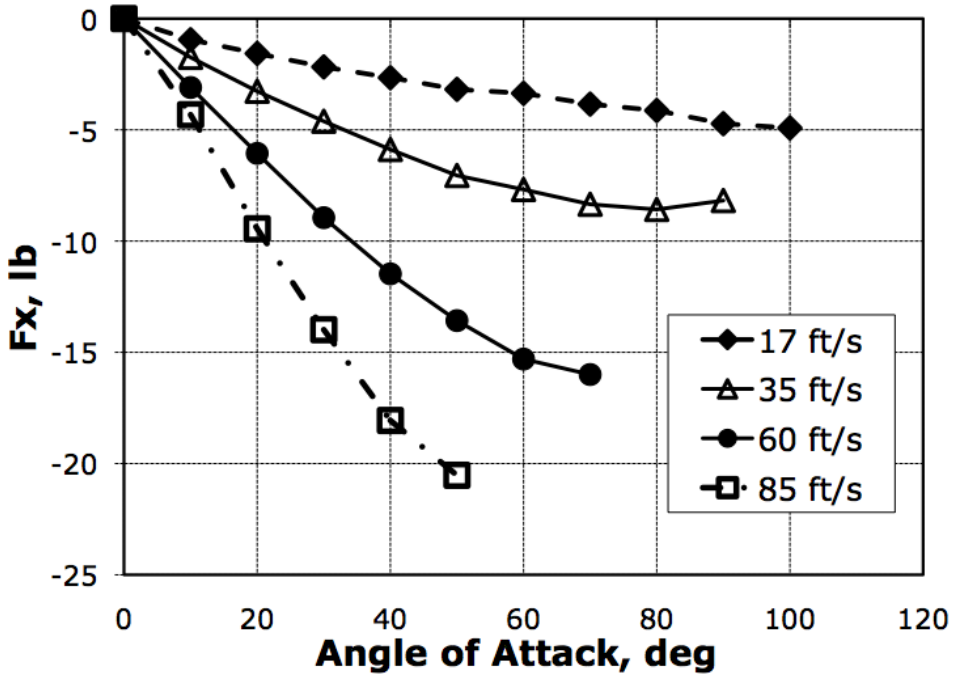

Figure 4-4. Normal force vs. angle of attack and free-stream velocity at a fan RPM of 6,000.

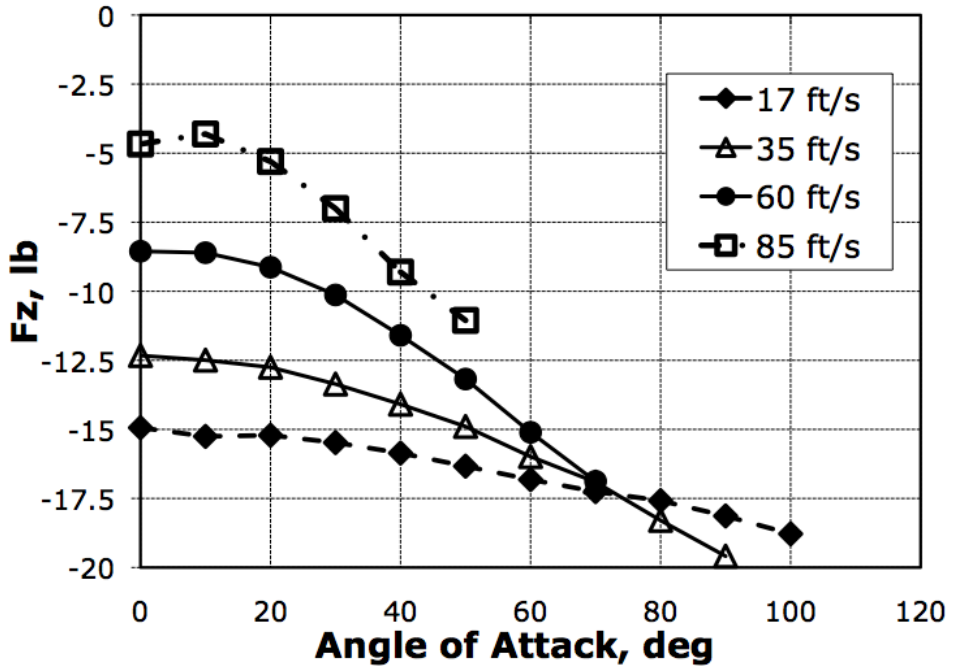

Figure 4-5. Thrust force vs. angle of attack and free-stream velocity at a fan RPM of 6,000.

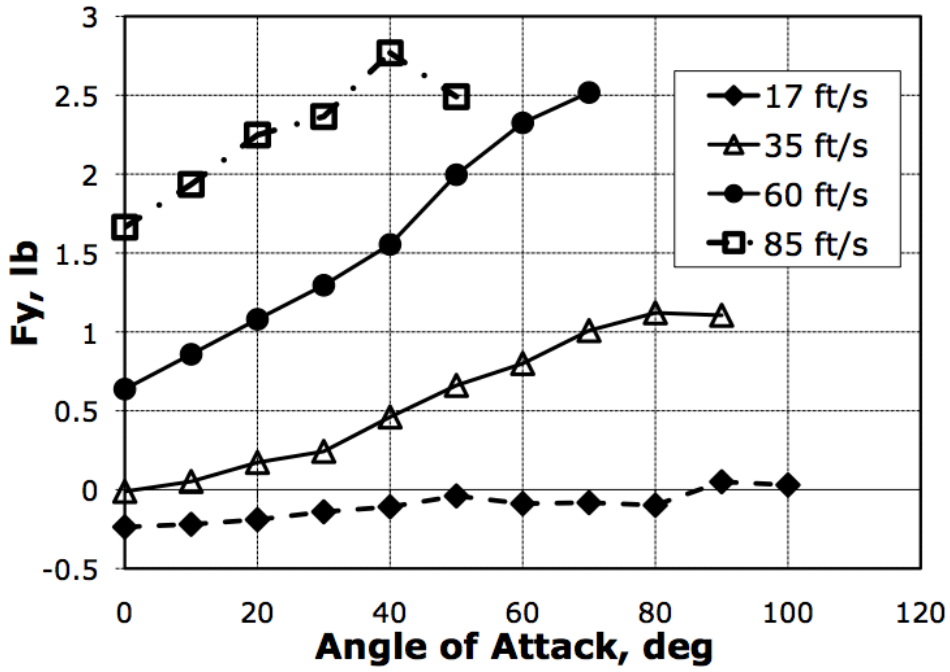

Figure 4-6. Side force vs. angle of attack and free-stream velocity at a fan RPM of 6,000.

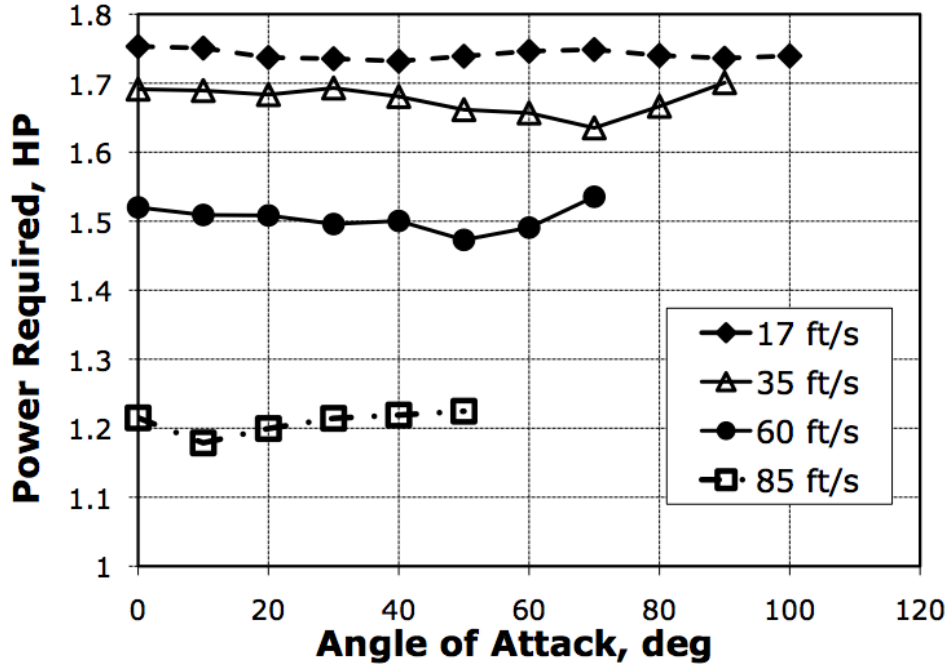

Figure 4-7. Power required vs. angle of attack and free-stream velocity at a fan RPM of 6,000.

The primary forces are the normal and axial/thrust forces, F_X and F_Z respectively. The normal force grows with both increasing free-stream velocity and angle of attack. The side force, F_Y, is relatively small for a symmetric vehicle

(it is assumed that the presence of the balance sting on one side of the vehicle is the source of variation in the results) and is neglected in the subsequent analysis. The thrust decreases during axial flight (angle of attack 0°) as the free-stream velocity increases, similar to a free propeller. This loss in thrust is due to the fact that for a fixed pitch fan at a fixed RPM the potential to accelerate the flow decreases for higher flight speeds. The growing drag of the duct also contributes to the decreased thrust at high flight speeds. As angle of attack increases at a fixed free-stream velocity the thrust also increases. At very high angles of attack, it is possible that thrust can increase with free-stream velocity for the ducted fan. This is demonstrated in Figure 4-5 at an angle of attack of 90°, where the 35 ft/s data point exhibits more thrust than the 17 ft/s data. The power required is derived from the shaft torque required to turn the fan at a specified RPM. There are small changes in power required with angle of attack change, but more noticeable is a large decrease in power required with increasing free-stream velocity and a fixed fan RPM.

Similar plots of the roll, pitch, and yaw moments, for the same conditions, are shown in Figure 4-8 through Figure 4-10.

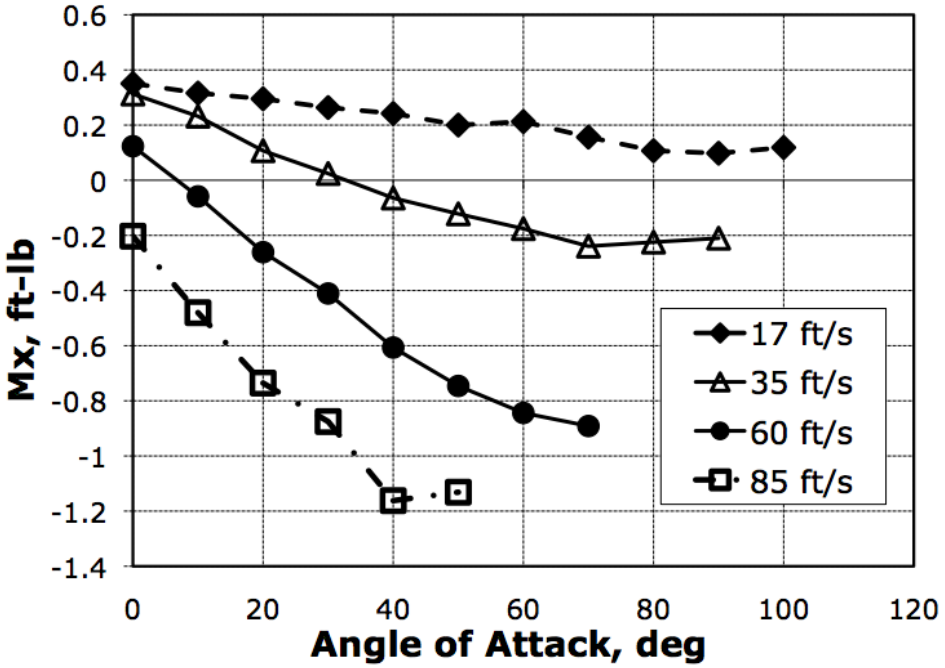

Figure 4-8. Roll moments vs. angle of attack and free-stream velocity at a fan RPM of 6,000.

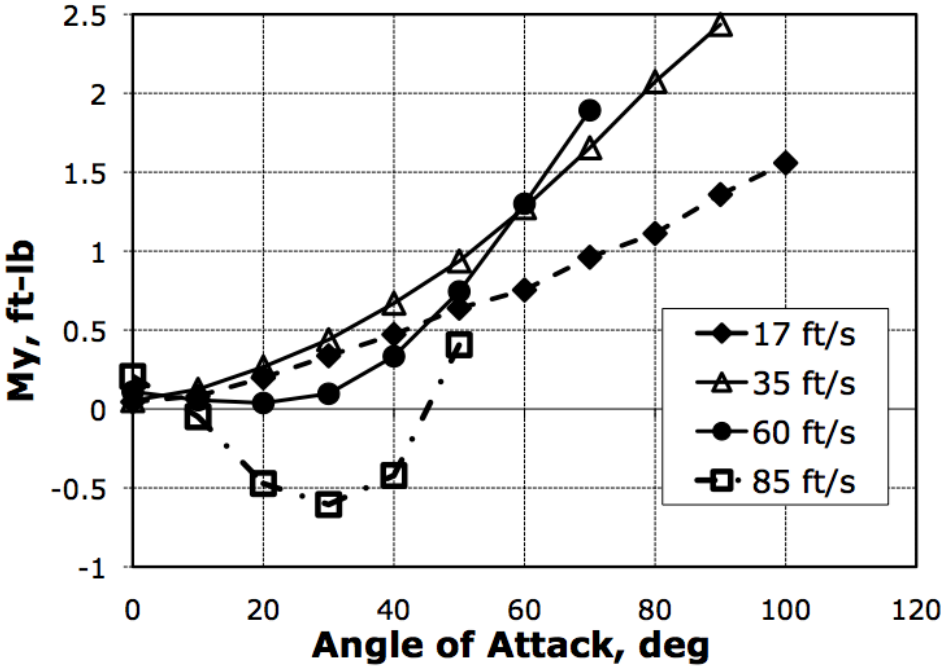

Figure 4-9. Pitching moments vs. angle of attack and free-stream velocity at a fan RPM of 6,000.

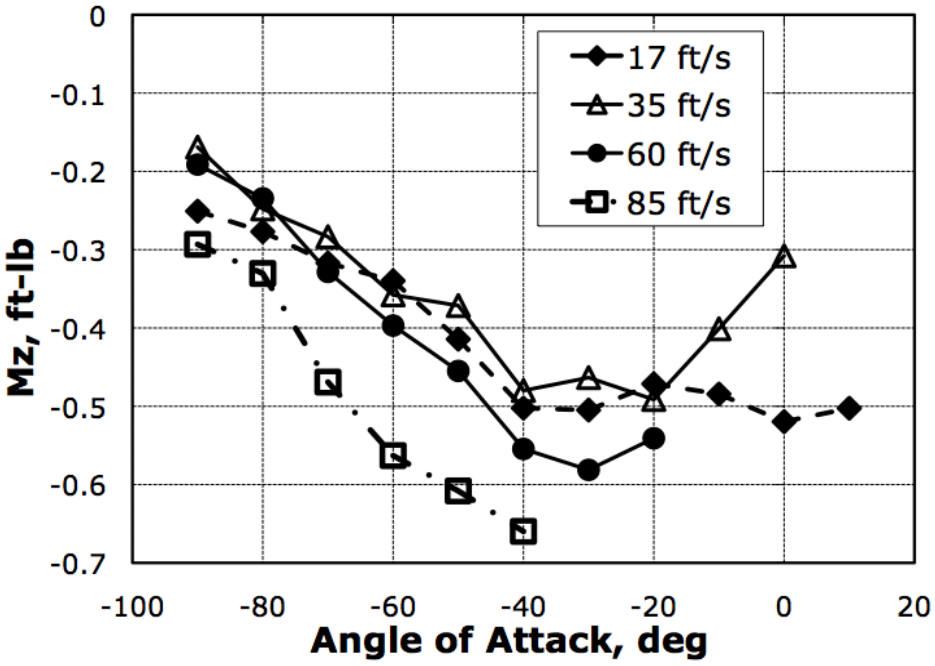

Figure 4-10. Yaw moments vs. angle of attack and free-stream velocity at a fan RPM of 6,000.

The roll moment, M_X, increases magnitude as angle of attack increases, and this is mainly attributed to the advancing-retreating blade phenomenon seen in a fixed pitch rotor (the blade traveling forward sees higher speed flow and produces more lift, while the retreating blade produces less lift). This effect grows with free-stream velocity, and the sign of the moment and slope is dictated by the fan rotation direction.

The pitching moment, M_Y, is the nose-up moment created due to changing the momentum of the portion of the free-stream flow that passes through the fan. The pitching moment is typically the largest magnitude moment and is one of the driving requirements for control surface sizing. The pitching moment is largest at high angles of attack at low velocities, when the duct influence is greatest. As velocity increases and angle of attack decreases (as it does for equilibrium or "trimmed" flight), the pitching moment can become negative. This change can be explained as the shift in influence of the momentum drag at low speeds to the lift and drag of the duct planform area (like a wing) at high speeds.

The yaw moment, M_z, is primarily the residual of the reaction torque from the motor turning the fan minus the counter torque of the stators that straighten the flow. The magnitude of the yaw moment for an axisymmetric vehicle is therefore primarily a function of the stator design. This quantity is assumed to be relatively small as shown here, and will not be specifically addressed in the subsequent analysis.

The nonlinear nature of the forces and moments observed in these plots, combined with the large range of angle of attack for trimmed forward flight demonstrates why flying a ducted fan vehicle requires an advanced flight control law. A concise and complete model of these characteristics will aid in creating robust ducted fan flight control systems.

4.3 Non-dimensional Modeling Scheme

Due to the complicated and nonlinear nature of the ducted fan data, it was desired to determine if a non-dimensionalization technique could be used to concisely express the characteristics of the ducted-fan aerodynamics. The traditional technique using lift and drag coefficients based on the free-stream velocity (dynamic pressure) fails to make the data collapse to a single trend, as seen in Figure 2-1. This is because the aerodynamics are tightly coupled to the thrust generated by inducing flow through the duct, while the traditional lift and drag coefficients work best with un-powered configurations.

A typical way of non-dimensionalizing propeller data is to plot thrust coefficient, C_T, and power coefficient, C_P, versus advance ratio, J. Many times this approach results in a linear equation for thrust coefficient (slope and intercept) in terms of advance ratio. For static/hover performance, “Figure of Merit”, FM, is used. The definitions used for these terms are included in Eq. 13:

$$J = \frac{V_\infty}{nD}, \quad C_T = \frac{T}{\rho D^4 n^2}, \quad C_P = \frac{P}{\rho D^5 n^3}, \quad FM = \frac{C_T^{1.5}}{\sqrt{\pi} C_P} \tag{13}$$

where V_∞ is the free-stream velocity in ft/sec, n is the rotational velocity of the fan in revolutions per second, D is the diameter of the fan in feet, ρ is the air density in slugs/ft^3, T is the thrust in lb_f, and P is the power in ft-lb_f/sec. These non-dimensional terms can be recreated using the Buckingham Pi theorem [115], but it does require some mathematical manipulation of the method's default output to attain these physically meaningful terms. This analysis is included in Appendix C for reference.

The advance ratio represents the influence of the free-stream velocity relative to the fan tip velocity. There are many definitions of FM, the form used here is equivalent to that of Mort and Gamse [32], but simplified slightly to ignore the effect of duct expansion, as the configuration tested used a straight duct with exit area equal to fan disk area. The coefficients allow for evaluating thrust or power for any RPM, diameter, and air density. This approach is normally used only for axial flight, where the free-stream air is aligned with the axis of the propeller (the case where angle of attack = 0°, in airplane convention).

Taking this approach for non-dimensionalization and extending it to all angles of attack has led to a remarkable discovery: the linear nature of the coefficient with respect to advance ratio is still present at other angles of attack, but with a different slope. This can be seen in Figure 4-11, where individual linear regression fits are shown for several angle of attack data sets. Note that data points that represent stalled duct conditions were removed.

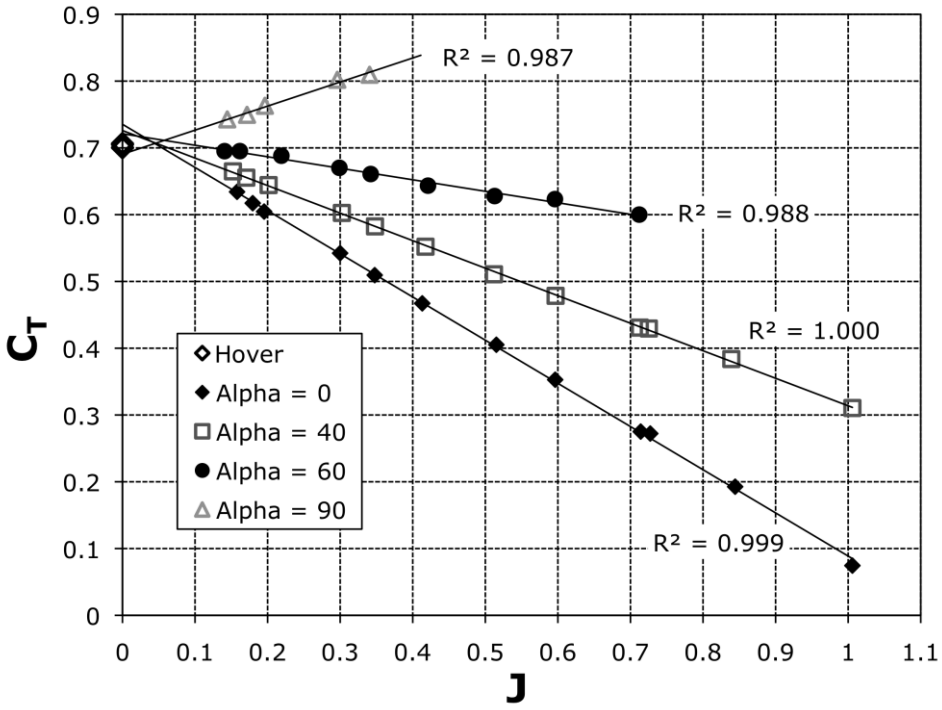

Figure 4-11. Non-dimensionalized thrust vs. advance ratio.

Upon further inspection, one will notice that many of the linear trends for each angle of attack do not converge to the static value where advance ratio is assumed to be zero. These linear trends do pass through a single point, making it possible to represent the effects of angle of attack as an additional factor in defining the slope, but this fulcrum through which the linear trends pass is not at an advance ratio of zero (i.e. zero free stream velocity). However, the coefficient magnitude at this fulcrum does match the experimental static thrust coefficient. Taking advantage of these observations, the data are re-plotted in Figure 4-12 with a single equation fit to represent all of the data simultaneously.

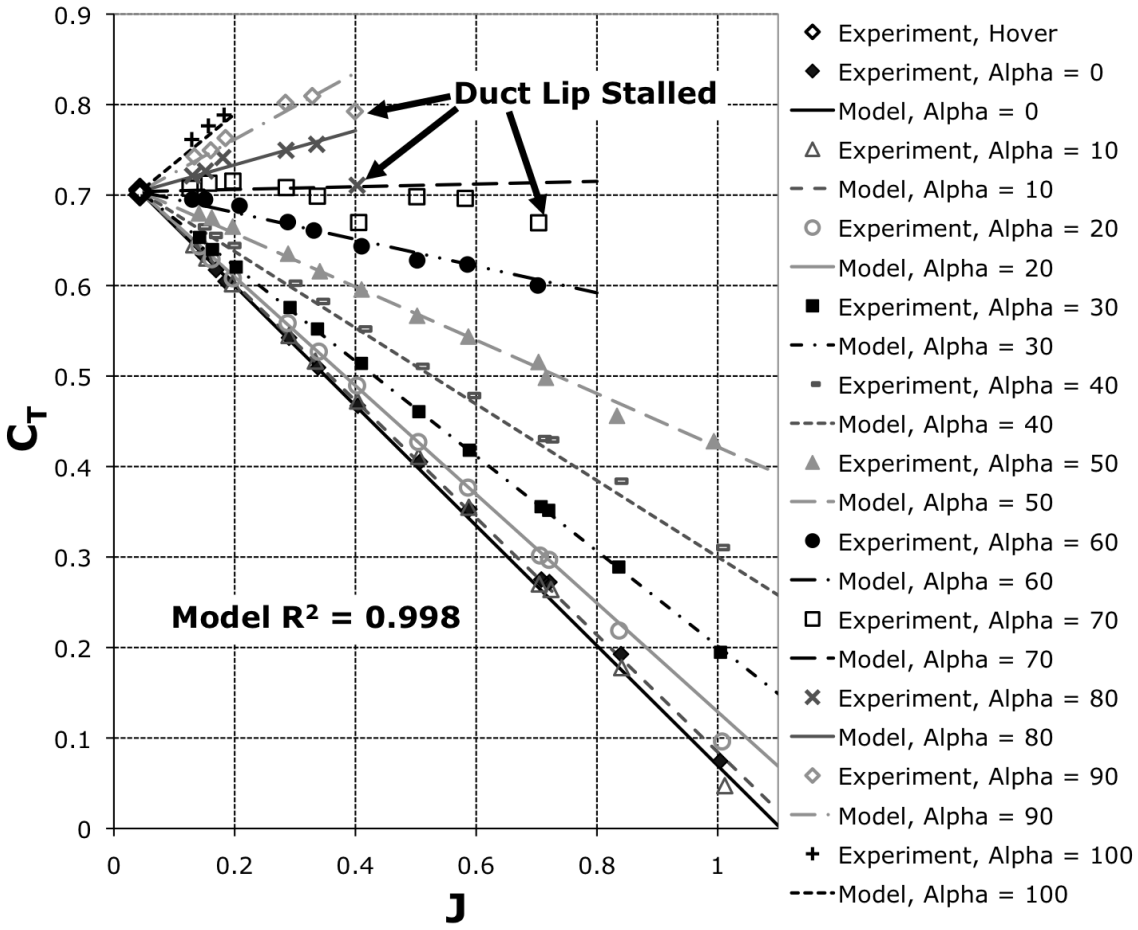

Figure 4-12. Non-dimensional thrust vs. J and alpha, model compared to experiment with static data moved to self-induced advance ratio location.

The plot shows the static thrust coefficient data points moved horizontally to the non-zero value of J where the lines converge. The implications of this suggest that hover is not appropriately modeled by an advance ratio of zero, if it is to be consistent with forward flight behavior. Rather, the ducted fan causes a self-induced free-stream velocity when it is stationary (hovering) via its thrust generation.

This coherent structure of the data has led to representing the data with a compact equation, which has attained a very high coefficient of multiple determination (R^2) value of 0.998, as defined in the statistical text [116]. The meaning of this coefficient of multiple determination is that the model explains 99.8% of the variation observed in the raw data. It should be noted that the data points identified as having a stalled duct lip were excluded from the curve

fit solution and reported R^2 value, as they represent nonlinear departures from the linear trends observed in normal operation.

There are four coefficient terms in the model equation, each with a physical explanation. Using the airplane convention for angle of attack (α) resulted in the simplest equation, where α = 0° when the propeller axis is parallel to the wind instead of the helicopter convention where α = -90° for this same condition. The form of the equation used is shown in Eq. 14:

$$C_T = C_{T_0} + \left(J - J_0\right) \cdot \left(C_{T_{J,\alpha=90}} + C_{T_{J\cos\alpha}} \cos\alpha\right) \tag{14}$$

where C_{T_0} is the static (hover) thrust coefficient value, J_0 is the self-induced advance ratio offset, $C_{T_{J,\,\alpha=90}}$ is the coefficient for advance ratio slope when the fan axis is perpendicular to the wind, and $C_{T_{J\cos\alpha}}$ is the coefficient for advance ratio slope that accounts for the magnitude of cos(α) effects. The cosine function appropriately describes the slow increase in thrust at low angles of attack and then a more steep addition of thrust with added angle of attack near a pure crosswind condition. Adding the values of $C_{T_{J,\,\alpha=90}}$ and $C_{T_{J\cos\alpha}}$ together gives the slope with respect to J for axial flight or α = 0 (traditional use of C_T).

This approach also yielded an excellent correlation for normal force. The normal force will equal zero at an angle of attack of zero for a symmetrically shaped ducted fan. This further simplifies the parametric representation by eliminating the coefficients associated with static and climb conditions. The same value for self-induced advance ratio offset from the axial force representation was used for normal force as well, with good agreement. When solved independently, the value J_0 was within 12% of the value determined for the thrust model, and had negligible effect on overall R^2 correlation metrics. The equation for C_N is shown in Eq. 15:

$$C_N = \left(J - J_0\right) \cdot C_{N_{J\sin\alpha}} \sin\alpha \tag{15}$$

The simplifying assumptions result in only one coefficient that needs to be identified for normal force modeling, $C_{N_{J\sin\alpha}}$, which is the coefficient for advance ratio slope change due to a sin(α) effect. The angle of attack effects were modeled with a sine term instead of a cosine term as in the thrust model because an axisymmetric vehicle at zero angle of attack should not produce normal force. Small biases in the experimental data normal force at 0° angle of attack (reference F_X raw data at 0° angle of attack in Figure 4-7 over velocity range) were removed from each angle of attack sweep to enforce this principle and improve the coherence of the data. This technique has been applied to all X and Y terms, as they should be zero for an axisymmetric vehicle pointed directly into the wind (α = 0°). The resulting data and model are shown in Figure 4-13.

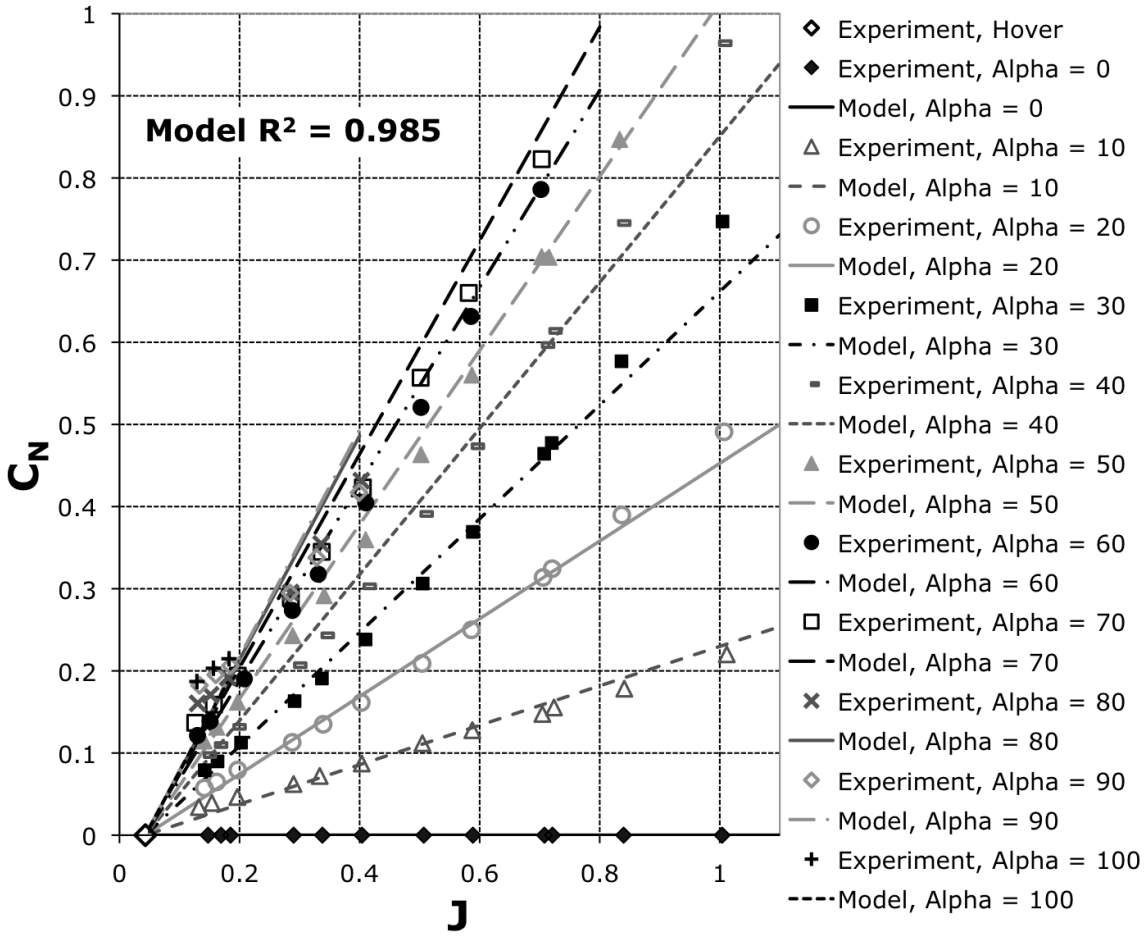

Figure 4-13. Non-dimensionalized normal force vs. advance ratio.

The coefficient of multiple determination for the normal force coefficient equation is 0.985, still a remarkably high value, suggesting this is a valid way to represent the vast majority of the data. Agreement at high angles of attack and low advance ratio is not as good as the higher speed data points. This may imply there are additional nonlinearities near duct stall that are not captured with this model.

The fact that the thrust and normal force models include simple cosine and sine terms (instead of arbitrary polynomial basis functions) does suggest the notion of some physically grounded behavior with angle of attack change. However, the change in thrust magnitude from angle of attack of 0˚ to 90˚ is smaller than the change in normal force from angle of attack of 0˚ to 90˚, negating the possibility of simple vector addition of two forces (thrust and

drag). These results show similar trends as those in Grunwald [28] where measurements of fan and duct forces were measured separately. They found that the fan thrust was roughly constant over angle of attack sweeps with constant RPM, while the duct thrust and duct normal force grew greatly with angle of attack. It is hypothesized in this dissertation that the fundamental cause of this angle of attack effect is that the velocity of the flow entering the duct over the windward lip must accelerate more with increasing angle of attack to stay attached. This angle of attack phenomenon is reproducible and predictable using sine and cosine terms such that the advance ratio effects are linear for the entire data set. The accelerated flow over the windward duct lip results in greater suction and consequently more thrust from the duct. This suction effect has components in the axial and normal directions. The flow does not need to accelerate over the leeward lip nearly as much, so summing the normal components of the duct lip suction results in a net positive normal force. Considering the same phenomenon from a "control volume" perspective, the turning of the free-stream flow a large angle results in substantial momentum drag (or "ram drag") in the normal direction. This source is the main component of the growing normal force with angle of attack, as the equation for normal component of momentum drag has a $\sin(\alpha)$ factor as referenced in [50].

The pitching moment of the ducted fan is one of the most nonlinear aerodynamic terms. It is a function of thrust and/or momentum drag for a given geometry and mass-flow, and is one of the main sources of difficulty in controlling ducted fan vehicles [102]. Non-dimensionalizing the moments in the same fashion used above resulted in lower coefficients of multiple determination than desired (roughly 0.85), so an alternative approach was explored. The concept of Center of Pressure (CP) is that there is a point in space about which there are no aerodynamic moments, only forces applied. The moments measured for the test vehicle were collected at a specific point on

the vehicle, which is not necessarily the CP. From the collected force and moment data, a CP location can be determined.

Some simplifying assumptions must be made to calculate the location of the CP. Based on the definition above, an equation relating forces, moments, and location of CP from the measurement reference center is shown in Eq. 16:

$$\mathbf{M} = \mathbf{r}_{CP} \times \mathbf{F} \tag{16}$$

Trying to solve this vector cross-product equation for the position of the CP is equivalent to the matrix problem posed in Eq. 17:

$$\begin{bmatrix} 0 & F_Z & -F_Y \\ -F_Z & 0 & F_X \\ F_Y & -F_X & 0 \end{bmatrix} \begin{Bmatrix} X_{CP} \\ Y_{CP} \\ Z_{CP} \end{Bmatrix} = \begin{Bmatrix} M_X \\ M_Y \\ M_Z \end{Bmatrix} \tag{17}$$

The matrix in Eq. 17 is skew symmetric and singular (only rank 2 for 3x3 matrix), and cannot be explicitly solved. Physically speaking, this means that there is no solution to an exact 3-dimensional location for the center of pressure. Usually, a simplifying assumption is made that results in an approximation of a CP location. For a traditional wing, the quarter chord approximates the center of pressure, but the actual value depends on the airfoil design. In reality, all points along the resultant force vector from the wing pressure distribution could be deemed a CP, but for simplicity we constrain the CP to the airfoil chord line to attain a single location for the CP.

For a ducted fan, two schools of thought have emerged for determining a CP location. The first (for example [36]) assumes the CP lies along the vertical axis of the vehicle (Z-axis for present coordinate system). In Eq. 17 this equates to setting X_{CP} and Y_{CP} equal to zero, and the normal force and pitching moment are used to determine the vertical location. Typically the side force is zero, so that there is usually no conflict with the corresponding roll moment equation. With this approach, the CP is usually located above the duct lip geometry, floating in space. One deficiency with this approach is that in hover the CP is undefined, as the normal force is generally zero without free-stream velocity.

The second approach (for example [51]) assumes that the CP moves forward and/or laterally in a plane parallel to the fan (fixed value of Z_{CP}). For the calculations here, assume Z_{CP} is equal to zero, as it can be adjusted through defining the coordinate system to align with the moment reference center. This approach makes more sense from a physical standpoint, with the CP usually staying within the extents of the duct geometry. It also supports the idea of the pitching moment being generated by increased lift on the windward lip, as well as the roll moment being mainly attributed to an advancing-retreating fan blade effect. This concept is depicted in Figure 4-14.

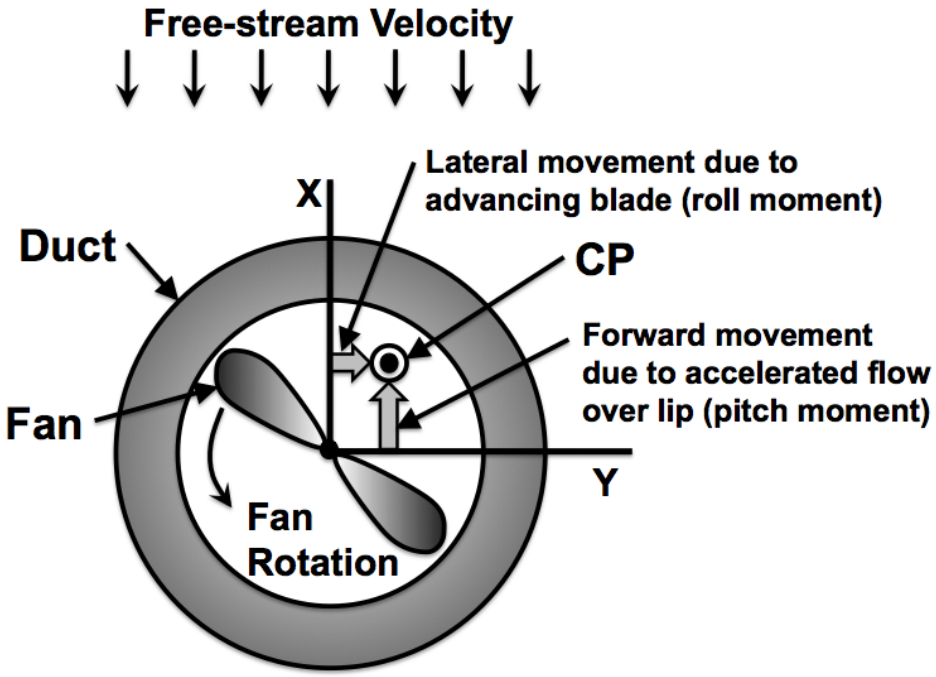

Figure 4-14. Center of pressure movement due to free-stream flow.

This approach allows for solving the M_X and M_Y rows of the matrix equation independently, however an inequality can arise in the M_Z equation. This is where a restriction in the concept of center of pressure becomes apparent. The assumption is that every moment is due to a force vector that can be independently modeled. There is the possibility of many force vectors that cancel but produce a moment (a "couple"), resulting in a bias in one or more of the moment terms. The most relevant example in a ducted fan is the residual moment between the stators and fan. Each blade of the stator is canceling swirl

from the fan and creating a local lift vector; combined, the stator blade forces in the X and Y directions cancel, but they produce a net moment about the z-axis. For this reason, it is proposed to exclude the M_z row from Eq. 17, leaving the CP location directly related to vehicle thrust. This second approach has two main advantages over the first approach: it can potentially model both roll and pitching moment behavior; and it has a well-defined CP location for the entire flight envelope including hover, since thrust is always present for normal flight operation.

Using this second approach to understand the pitching moment resulted in a more coherent structure to the data. The moment reference center of the data was moved to the duct quarter chord (new fixed Z plane for CP movement) to optimize correlation. To non-dimensionalize the location of the CP, it is simply divided by the fan diameter, the most obvious reference length for thrust-based quantities. This representation is equivalent to dividing the moment coefficient by the thrust coefficient (Eq. 18), providing a simple way to recover the moment coefficient using the modeled thrust. The resulting model can be seen in Figure 4-15.

$$\frac{X_{CP}}{D} = \frac{C_m}{C_T} \tag{18}$$

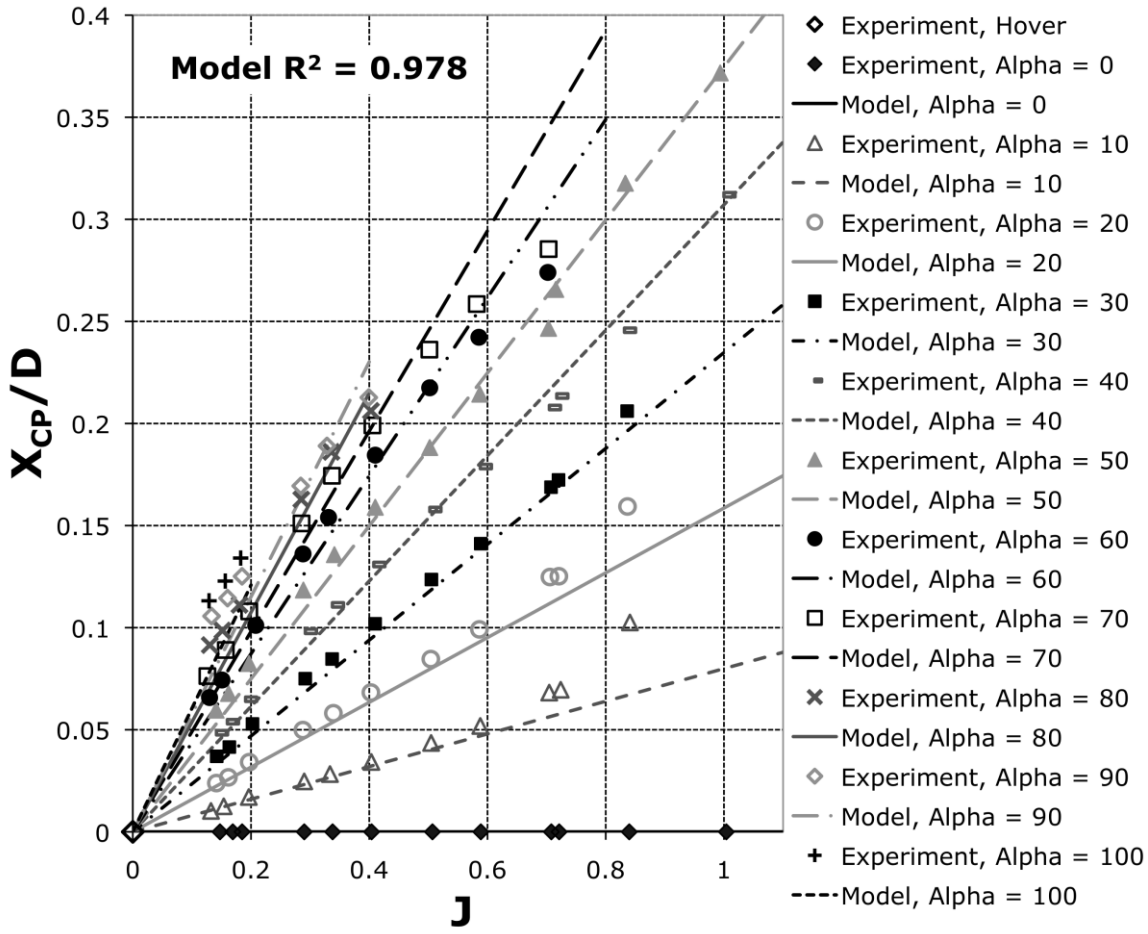

Figure 4-15. Non-dimensionalized center of pressure X-location (due to pitching moment) vs. advance ratio.

The coefficient of multiple determination for the pitching moment-based X_{CP} equation is 0.978, a significant value for the most difficult ducted fan aerodynamic term to characterize. The model takes the form of Eq. 19:

$$\frac{X_{CP}}{D} = X_{CP_{J\sin\alpha}} J \cdot \sin\left(X_{CP_\alpha}\alpha\right) \tag{19}$$

There are two differences in the center of pressure equation from the previous force equations' structure. The data did not support the self-induced advance ratio seen in the primary forces, and a pure sine term did not model the data adequately. Therefore the equation reduces to a factor, $X_{CP_{J\sin\alpha}}$, applied to the product of advance ratio and a sine function with an added multiplier for

angle of attack to capture the spacing seen in the data, X_{CP_α}. The unique nature of ducted fan pitching moment is tied to the flow characteristics over the windward lip. This more intricate behavior would not necessarily line up directly with the overall changes in thrust and normal force, and therefore the models may be different in structure.

The same equation form was used to model the Y_{CP} location movement that results from the advancing-retreating blade phenomenon on the fixed-pitch fan. The resulting model is plotted in Figure 4-16, and the equation form can be seen in Eq. 20:

$$\frac{Y_{CP}}{D} = Y_{CP_{J\sin\alpha}} J \cdot \sin\left(Y_{CP_\alpha}\alpha\right) \tag{20}$$

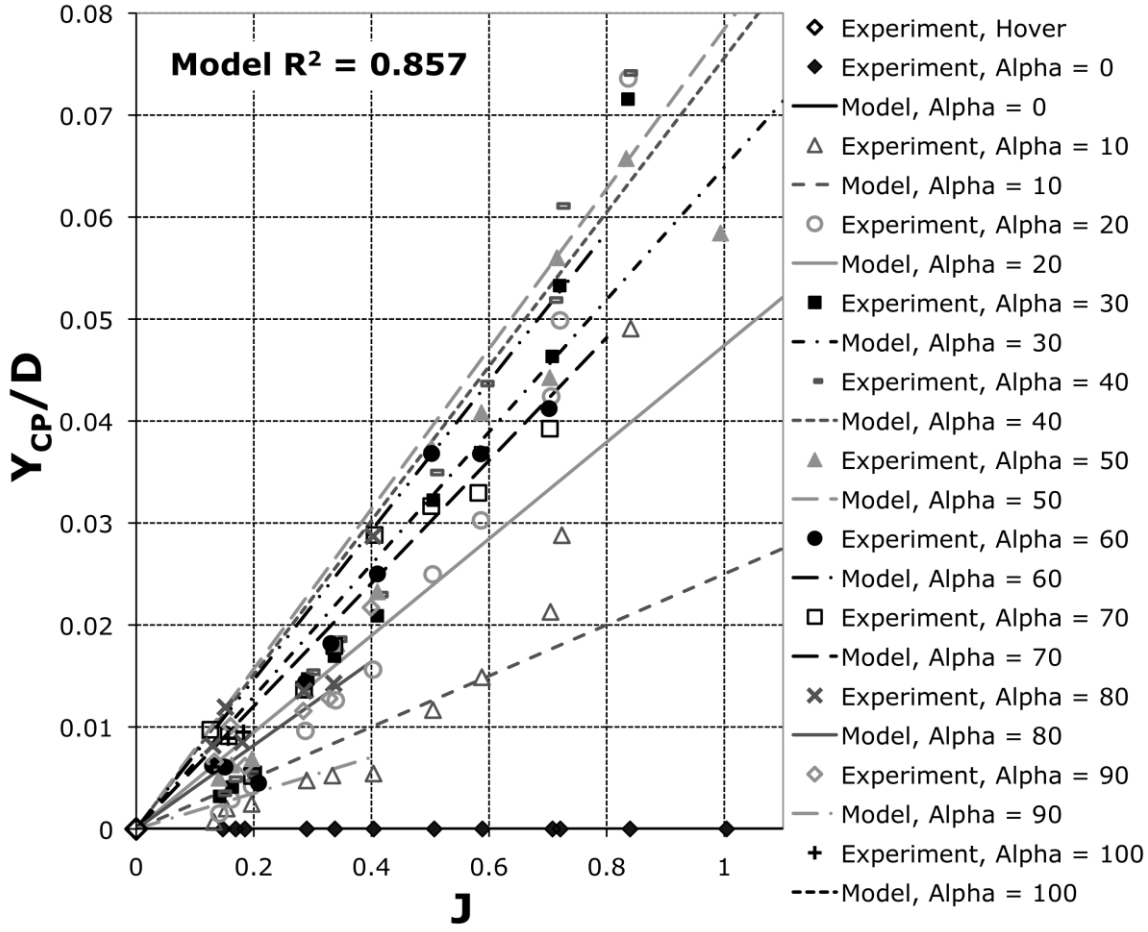

Figure 4-16. Non-dimensionalized center of pressure Y-location (due to roll moment) vs. advance ratio.

The first thing to note is that the magnitude of lateral CP movement representing roll moment is much smaller than the longitudinal movement that corresponds to pitching moment. The agreement of the model with the data is less satisfactory for this term (R^2 of 0.857), and there can be several reasons for this. First, the roll channel uncertainty in the balance measurements was four times greater than the pitch channel uncertainty. This was compounded by the fact that the roll moment values measured were smaller in magnitude than the pitching moment data. It is also possible that there are other phenomena occurring that are not fully modeled. The longitudinal aspects of the ducted fan are the primary focus of this effort as they are the most influential in vehicle flight performance and control. Further investigation will be needed to better understand the source and nature of roll moments generated by ducted fan systems.

The power required to generate the required thrust for steady level flight is another important aspect to include in the model. The variation of power coefficient usually has a quadratic shape with respect to advance ratio for axial flight. It is less apparent what relationship power coefficient has with angle of attack. An example plot of all the angle of attack power data is shown in Figure 4-17. At first glance it looks as if the data is clumped together in a cloud of points that roughly approximate the axial flight results, but the data does not fully collapse. The second plot within Figure 4-17 is a potentially more instructive view where power coefficient is plotted versus thrust coefficient. As would be expected, there is a close relationship between the thrust generated and the power required; the important observation is that this relationship changes with angle of attack in a structured way.

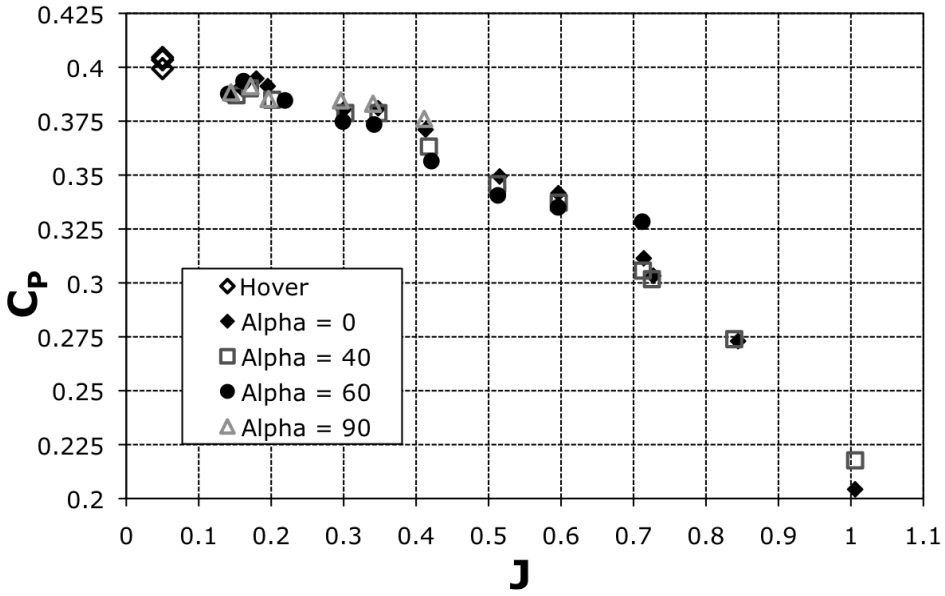

a)

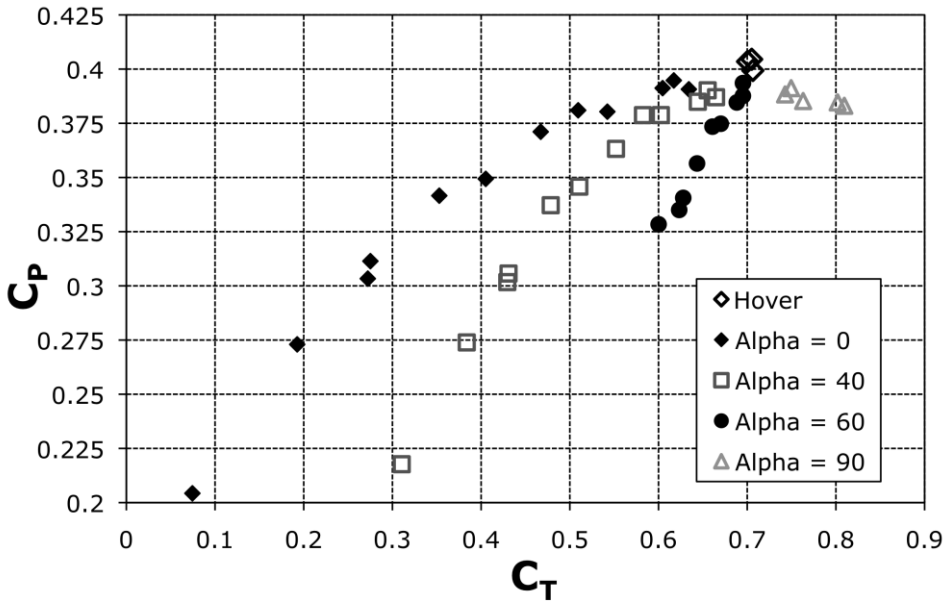

b)

Figure 4-17. Trends in power required: (a) Non-dimensionalized power vs. advance ratio; (b) Non-dimensionalized power vs. non-dimensionalized thrust.

With further exploration, an even clearer relationship was discovered. Figure of Merit (FM) is typically used to only characterize performance in static conditions (hover). It relates the thrust generation to the power required, with the C_T being raised to the 1.5 power. Many versions of FM exist, and the history is complicated, but the version used here (Eq. 13) is equivalent to the final form used by NASA in their extensive ducted fan wind tunnel tests of the 1960's. The

innovation in modeling I introduced was to use this static performance metric across the entire flight regime to concisely predict the power of the vehicle. The results can be seen in Figure 4-18.

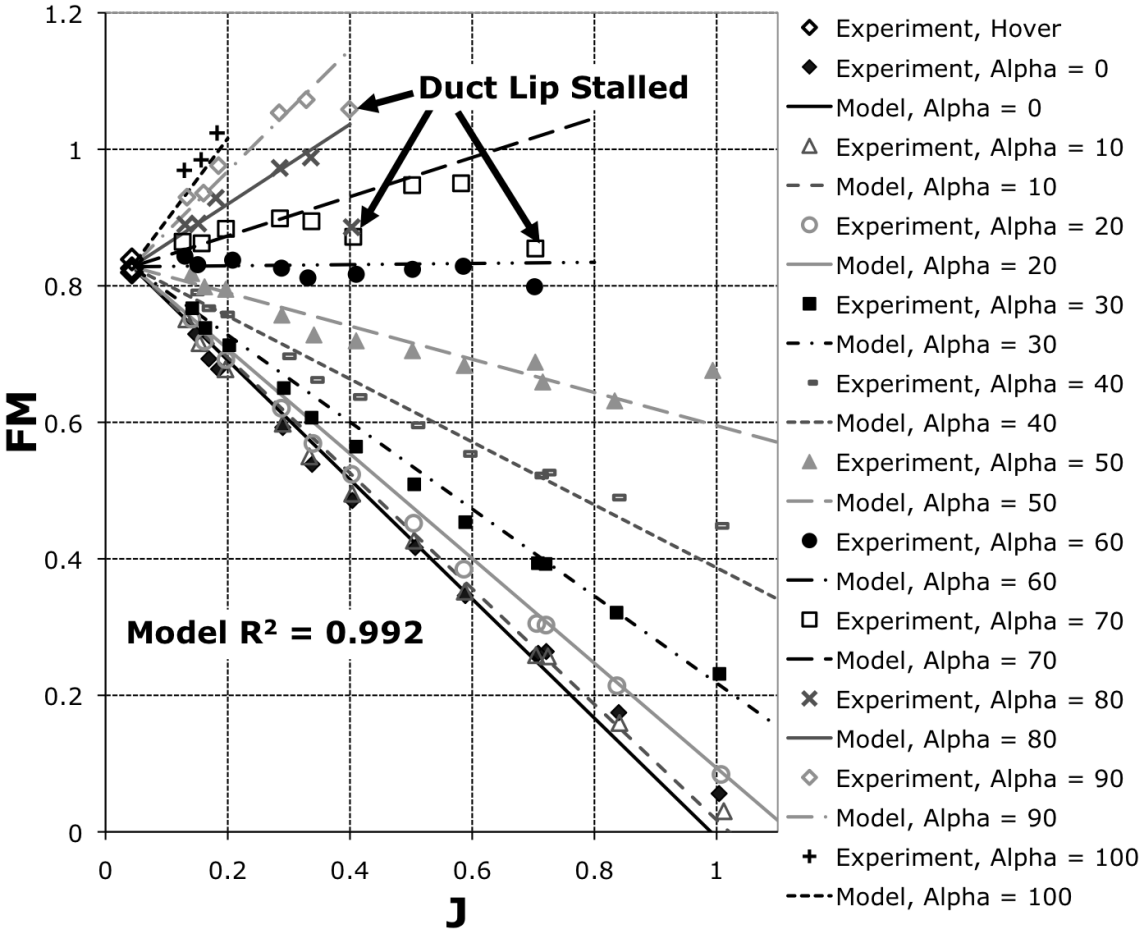

Figure 4-18. Figure of merit vs. advance ratio.

The R^2 correlation value for this fit is 0.992, suggesting an excellent representation of how the power required changes over the entire flight regime. Plotting the data in this fashion accomplishes a second goal: identifying flight conditions that represent a stalled duct. For each angle of attack there is usually an advance ratio value beyond which the duct will stall. This is due to the increasing influence of the free-stream flow relative to the induced flow, as J increases. These stalled points can be seen in the C_T plot as well, but are more pronounced when including power. This is because typically thrust decreases and shaft power increases when the duct lip stalls. It should be noted that the

models presented capture the behavior well only when the flow over the duct lip stays attached. Additional nonlinearities would need to be modeled to fully describe the stalled behavior observed.

The resulting form of the modeling equation is similar in structure to the C_T equation and is shown in Eq. 21:

$$FM = \frac{C_T^{1.5}}{\sqrt{\pi} C_P} = FM_0 + \left(J - J_0\right) \cdot \left(FM_{J,\alpha=90} + FM_{J\cos\alpha} \cos\alpha\right) \tag{21}$$

FM_0 is the static value of FM traditionally calculated. It is a benefit of the model that it can incorporate this standard value with additional terms to account for wind effects. $FM_{J,\,\alpha=90}$ is the slope of FM with advance ratio at an angle of attack of 90°, and $FM_{J\cos\alpha}$ specifies the influence of the cos(α) effect. To calculate the C_P value for one of these conditions, first the C_T and FM model equations (Eq. 14 and Eq. 21, respectively) must be evaluated. Then the C_P can be solved for from the FM definition equation. One restriction is that this operation is only valid when the thrust coefficient is positive, which is a valid assumption for normal flight.

The form of the equation gives some physical insight to the efficiency of ducted fan flight, relating thrust and power over the entire flight regime. The static figure of merit is an intrinsic quality of a ducted fan or propeller design that is used to judge its performance. This is separate from its flight performance, as it has been noted that ducts and fans optimized for hover conditions may perform worse in cruise than a more general design that sacrifices some static performance [31]. The cruise performance is solely defined by the slope coefficients in the equation. Summed together they describe how fast the relationship between thrust and power in axial flight degrades with increasing velocity. These characteristics will be a function of fan blade design, duct thrust, and duct frontal area. The cos(α) term quantifies how well the duct generates thrust and increases efficiency when flying at an angle of attack.

The collection of equations used here to model the primary aerodynamics of the ducted fan show several general principles. First, the thrust force and power used to generate that thrust are the only terms in hover. As free-stream velocity increases, many new phenomena arise. Thrust decreases with increasing advance ratio at an angle of attack of 0°, but increases at an angle of attack of 90° showing the great influence of the duct on the overall thrust. A normal force that is linear with respect to advance ratio at each angle of attack is apparent, and is attributed to momentum drag and duct lip pressure asymmetries. A large nose-up pitching moment due to this same duct lip pressure asymmetry is modeled as the center of pressure moving forward towards the windward lip. A roll moment due to the advancing-retreating blade effect of a fixed pitch rotor is modeled as a lateral movement of center of pressure. Finally, the power required is best represented using "Figure of Merit" over the entire flight regime, and is directly related to the amount of thrust generated. The values of the non-dimensional coefficients are mainly a function of duct and fan blade design.

This new modeling technique is analogous to linear models of airfoils and wings, something that has been missing for ducted fans. The classic parametric equation for total lift, $C_L = C_{L_{\alpha=0}} + \left(\partial C_L / \partial \alpha\right) \cdot \alpha$, is mimicked here with a slightly more complex formulation: a constant coefficient, and coefficients to define linear dependence on advance ratio, and sine/cosine dependence on α. Just as the linear airfoil model is valid until stall occurs, this simplified ducted fan model is valid for un-stalled duct conditions. The airfoil model has its limitations, but is well accepted and helpful in modeling aerodynamic behavior. This new model for ducted fan aerodynamics will be similarly useful.

4.4 Model Applied to Legacy Data

One question that arises when a new model is proposed is, "Does it work with other published data?" A model that is only representative for one

specific test has very limited value. However, a model that applies generally to some spectrum of similar cases is of greater value and will enjoy longevity in its use. The use of non-dimensional terms, such as thrust coefficient and Figure of Merit, provides a straightforward way to address scaling between different sizes of aircraft. The new model operates within this framework, thereby making it appropriate for ducted fans of any size. The more fundamental question is whether the equations of the new model sufficiently capture the trends in ducted fan data for a range of vehicle designs.

There have been many ducted fan research programs, but most times the focus of the effort or the results presented are not comprehensive. Some of the more comprehensive accountings of ducted fan aerodynamics are the NASA reports listed in the literature review section. For the purposes of this research, the data presented by Mort and Yaggy [30] was selected as the most applicable and will be compared to the data already presented (referred to as "baseline" data hereafter).

Mort and Yaggy tested a 4-foot diameter ducted fan in the 40 x 80 foot closed jet tunnel at NASA Ames. The tests evaluated a range of angles of attack, velocity, and fan RPM to show the effects on lift, drag, thrust, normal force, pitching moment, and power required. The thrust and normal force coefficient data used to evaluate the new model is shown in Figure 4-19, and the pitching moment and power coefficient data is shown in Figure 4-20. The data was extracted from the plots using the open source program Plot Digitizer [117]. The uncertainty added due to the digitization process is summarized in Table 3, based on the resolution of the plot scale per pixel and a comparison of the results observed for a common quantity, C_N, extracted from both plots.

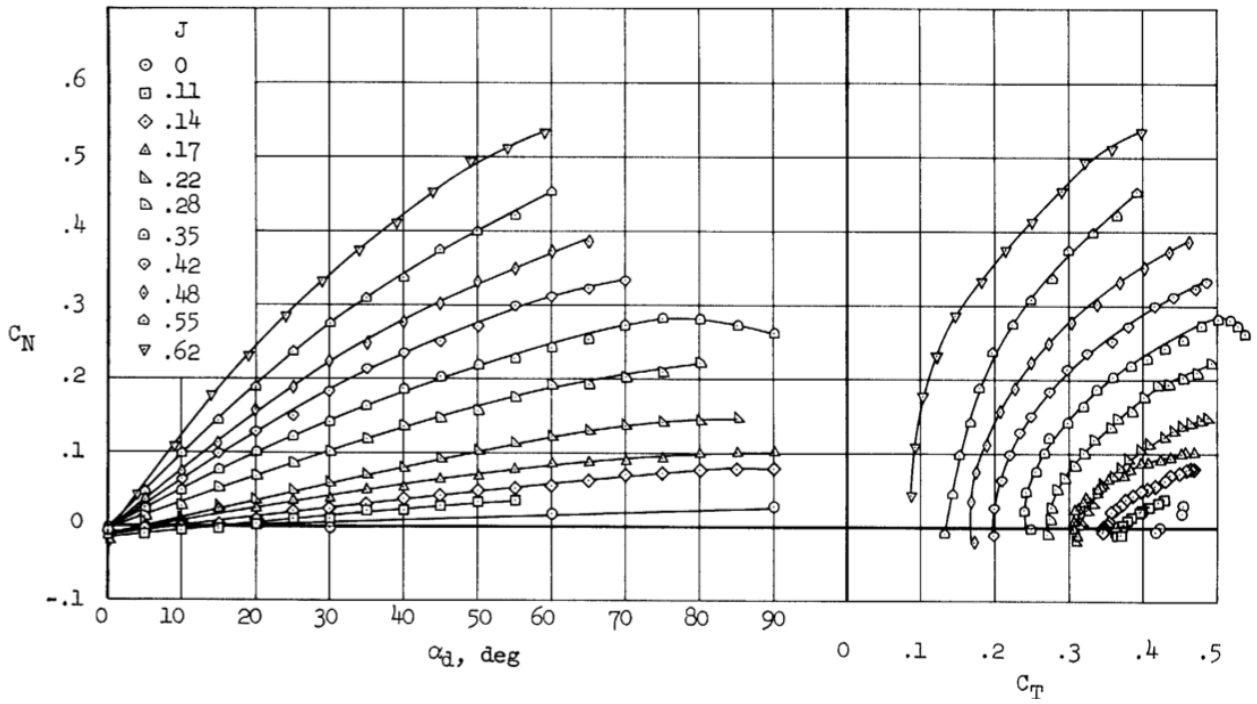

Figure 4-19. Mort and Yaggy thrust and normal force data [30] (public domain).

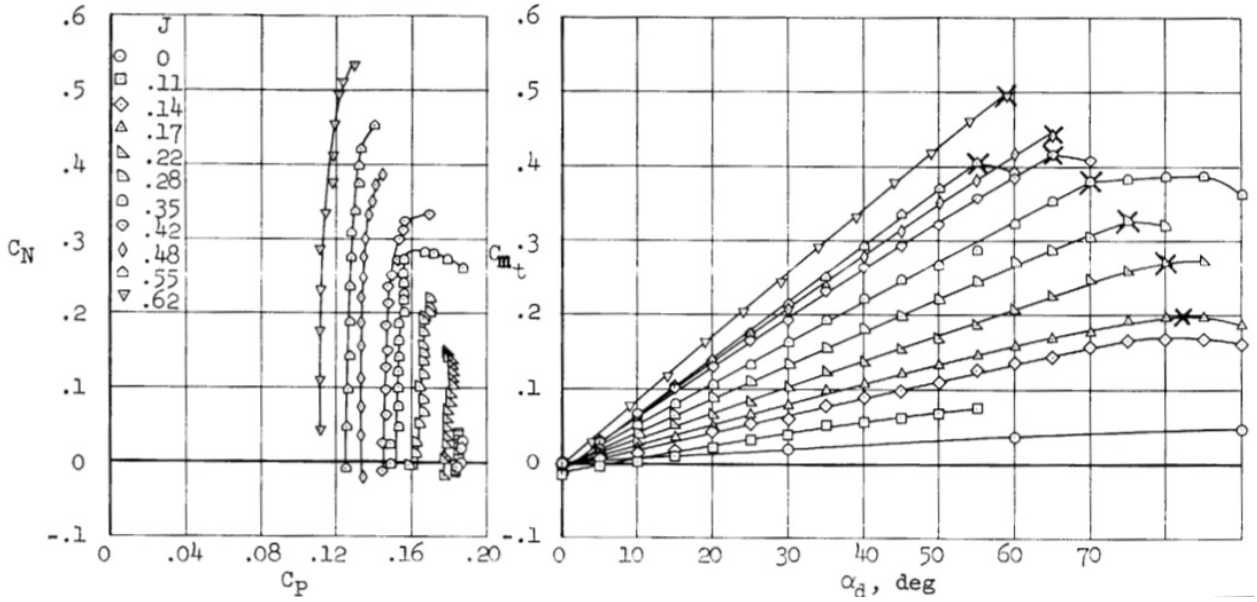

Figure 4-20. Mort and Yaggy power and pitching moment data [30] (public domain).

Table 3. Uncertainty in Digitization Process

Term	Uncertainty
C_T	0.003
C_N	0.003
C_m	0.003
C_P	0.001
α	0.2°

Because the results in [30] are presented in non-dimensional form, without reporting the raw velocity, thrust, and RPM values, applying the equivalent velocity correction method used with the baseline data was not possible. The wind tunnel cross-sectional area in the NASA tests was very large relative to the duct exit area, resulting in a value of S/C = 0.004 as compared to 0.022 for the baseline data. Therefore, the velocity corrections are not as critical for interpreting the NASA data.

The new model applied to the Mort and Yaggy thrust coefficient data is plotted in Figure 4-21, showing the same structure as observed previously. The correlation of the model to the data is excellent (coefficient of multiple determination of 0.99), and is comparable to the value attained in the baseline experiments and analysis. It is also informative that the non-zero "self-induced" advance ratio, J_0, has a similar value to those observed in the baseline data presented in the previous section. This observation in conjunction with the fact that the NASA data was collected in a much larger tunnel (very low fan to tunnel area ratio) suggests this is not an isolated effect specific to the present test setup.

It should be noted that the static data used in the model generation process was from the case where J = 0 and α = 0°. This data point was selected because the cases where the angle of attack was higher (model perpendicular to tunnel at α = 90°) showed strange trends in normal force and pitching moment that should not be present for a axisymmetric configuration, and was deemed unrepresentative of a true hover condition. With regard to the current equation

fitting metrics, it should also be noted that the points identified with a stalled duct lip condition (by Mort and Yaggy) were excluded from the model solution.

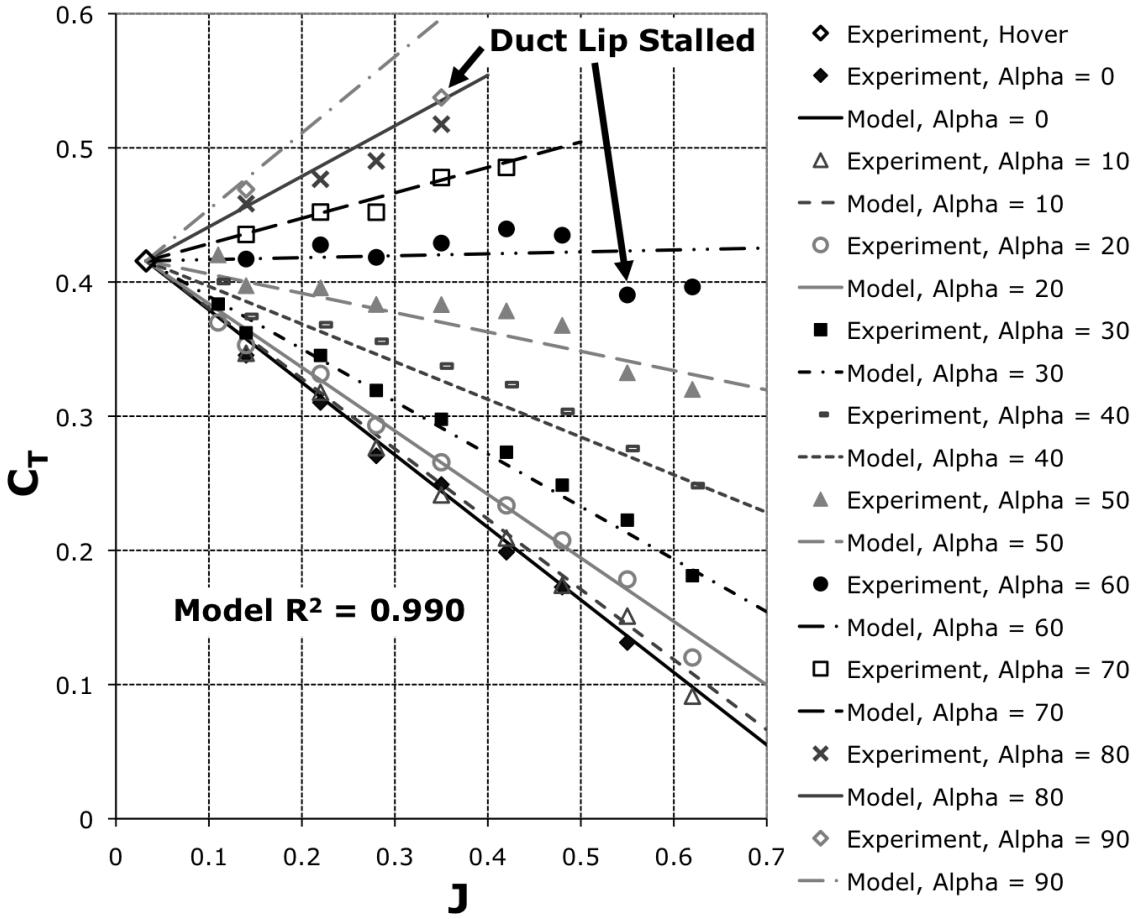

Figure 4-21. Thrust coefficient model applied to Mort and Yaggy data (1962).

Similarly, the model for normal force was applied to the Mort and Yaggy data, as seen in Figure 4-22. The equation correlation is not as good as in the baseline data and model, but is still very high (R^2 = 0.975). This good agreement suggests that the modeling technique is sufficient for representing the two most fundamental forces that ducted fan generate (thrust and normal force).

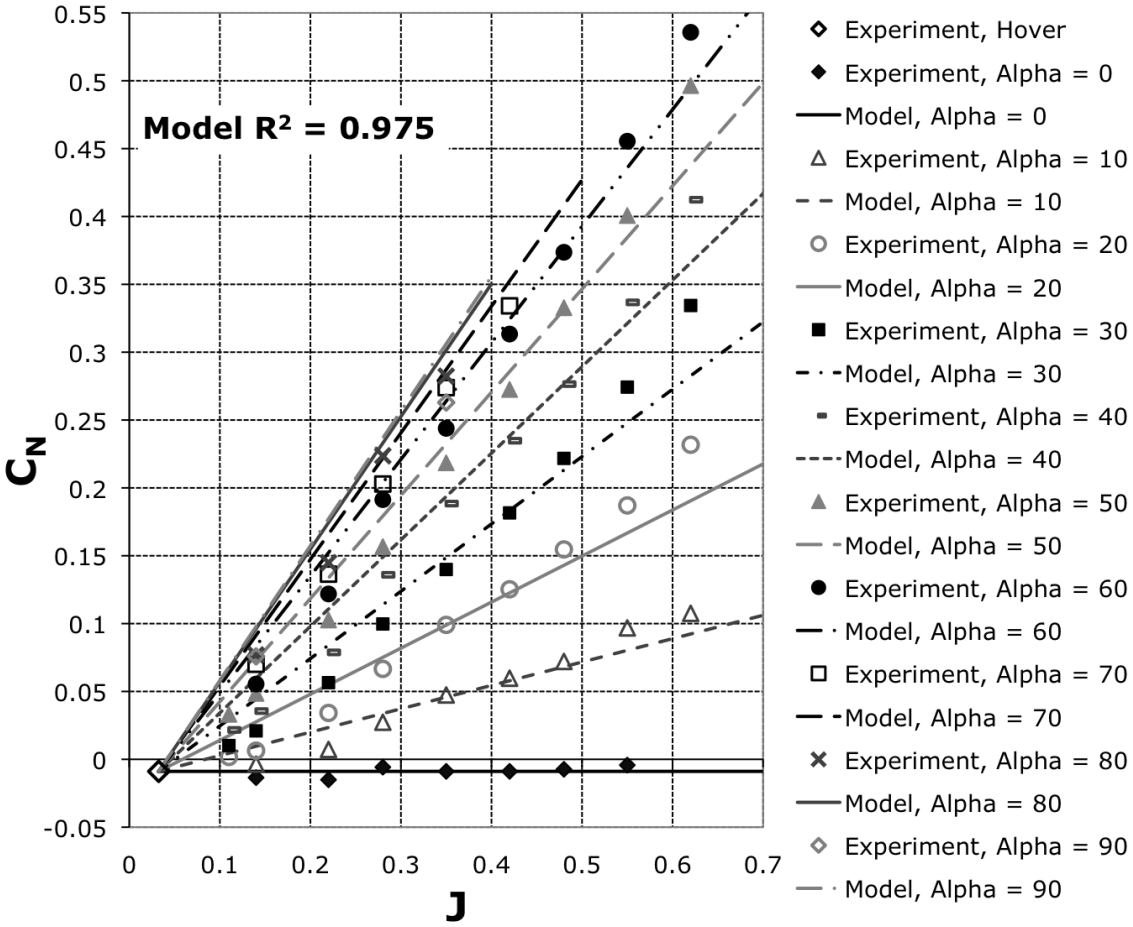

Figure 4-22. Normal force coefficient model applied to Mort and Yaggy data (1962).

The center of pressure modeling of the legacy data was limited to fore/aft movement since only pitching moment data was reported by Mort and Yaggy. The pitching moment is the most significant aerodynamic moment for this type of configuration, and typically shows the most nonlinearity. The new modeling technique applied to the pitching moment data in [30] is depicted in Figure 4-23. The moments in the test were originally referenced from the half-chord station of the duct, and in this analysis the moments were transformed to the quarter-chord of duct.

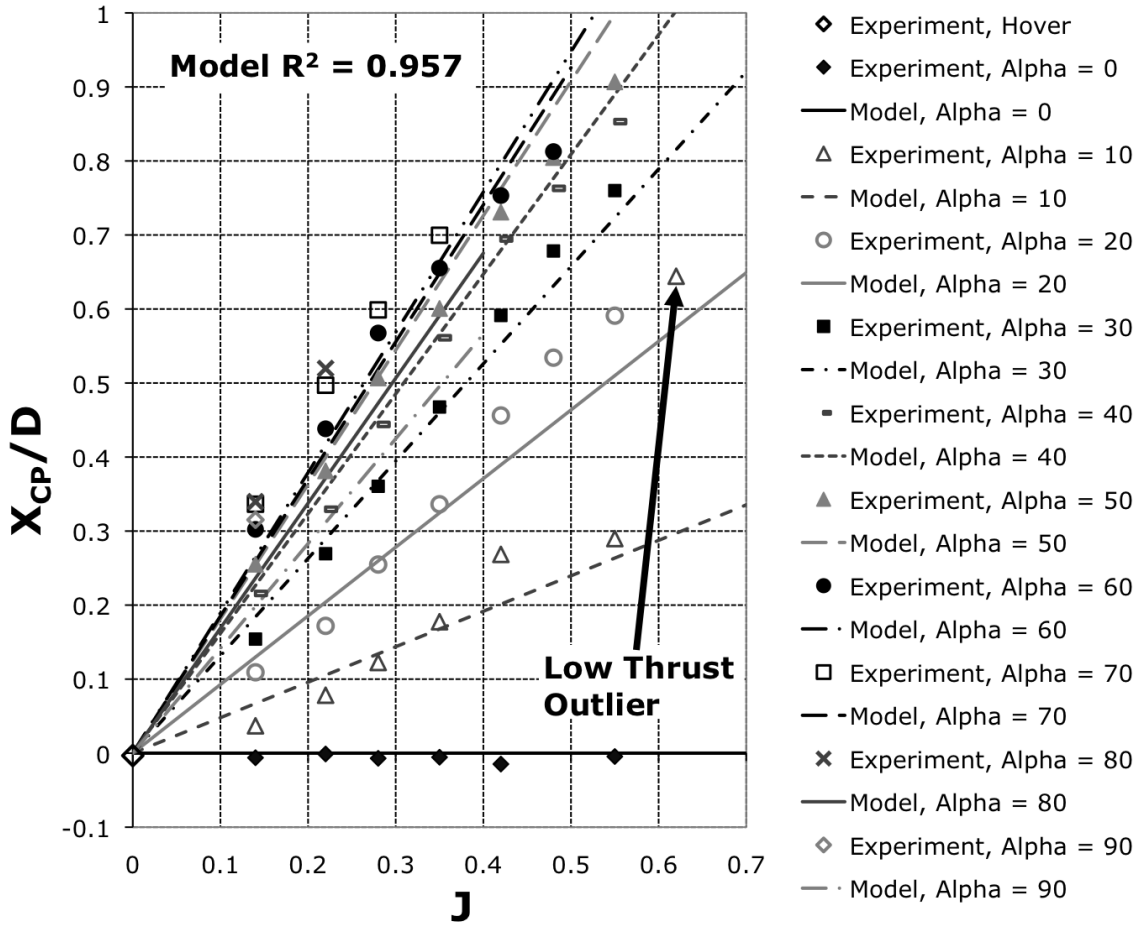

Figure 4-23. Non-dimensionalized center of pressure X-location model applied to Mort and Yaggy data (1962).

While the correlation level shown in Figure 4-23 is less than that seen in the baseline data ($R^2 = 0.957$ instead of $R^2 = 0.978$), this is still a relatively good fit for a term that is difficult to model. Several high-speed data points corresponding to low thrust conditions (at high J and low α) were problematic for this formulation. For the curve fitting process they were omitted as outliers, but an example can be seen as called out in Figure 4-23. As seen in Eq. 18, the CP location is inversely proportional to thrust coefficient, causing the resulting CP calculation to become noisy as thrust approaches zero. The model should be valid for predicting CP in such conditions, but it would be difficult to generate the model from data exhibiting very low thrust. These points demonstrate that the model is primarily intended for positive thrust

conditions, a reasonable assumption for ducted fans used as propulsion in air vehicles.

One point of concern is the physical meaning of the center of pressure location. In the baseline data, the location of the CP never moved beyond the extents of the duct radius ($X_{CP}/D = 0.5$), but in this case the values as high as 0.9 would imply that the CP has moved outside the vehicle, which is possible but hard to comprehend. Consequently, the sensitivity of the center of pressure model to the axial location of the assumed plane of travel was evaluated (previously set at the quarter-chord of the duct for the baseline data). The purpose was to identify whether another selection of axial plane for CP movement would improve the correlation, while also keeping the CP within the geometric confines of the physical model. The analysis showed that the quarter-chord location resulted in the highest model correlation. To return the measured CP data to within one radius of the duct, it required moving the axial plane at least one quarter-chord above the duct lip and significantly decreased the correlation between the model and the data ($R^2 = 0.852$). These observations concerning the modeling of the center of pressure and vehicle moments show that further investigation is needed to fully understand the origins of this unique behavior. Nonetheless, the modeling approach is sufficient for representing the significant trends in moment data in a concise manner with relatively high confidence.

The power model, using Figure of Merit, was applied to the Mort and Yaggy data, and the results are shown in Figure 4-24. The R^2 correlation value for this fit is 0.981, again showing its appropriateness for modeling the unique aerodynamics of the ducted fan. Overall, the new model captures the essence of the Mort and Yaggy data, with particularly high correlations for thrust and power.

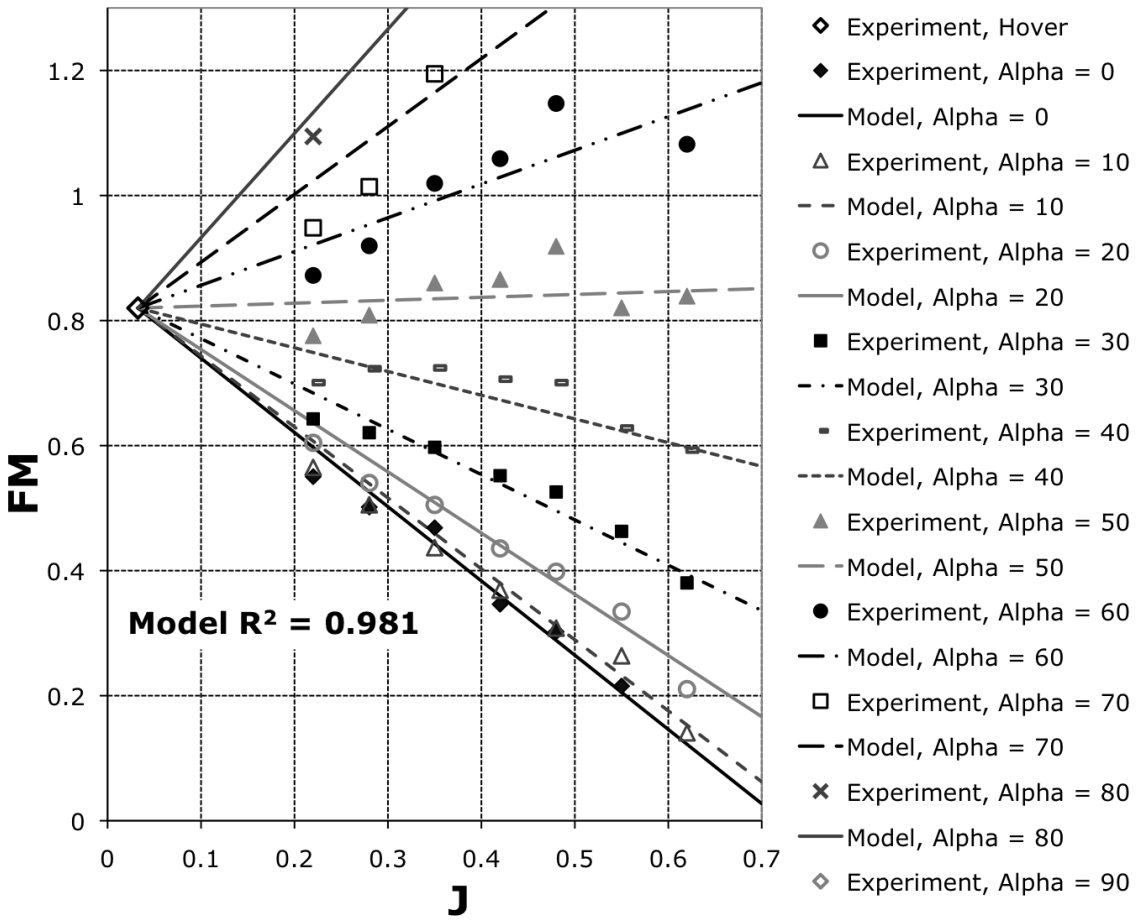

Figure 4-24. Figure of Merit model applied to Mort and Yaggy data (1962).

4.5 Chapter Summary

Wind tunnel tests of a generic, axisymmetric ducted fan design provided ample data for analysis and modeling. When testing powered models in a closed-jet test section, wind tunnel corrections are needed to account for the presence of the walls and their effect on the test measurements. The ducted fan accelerates a portion of the tunnel mean flow, causing the remaining flow around the model to be slower than the nominal tunnel speed. Following Glauert's traditional approach for free propeller velocity corrections, I derived a new velocity correction specifically for the case of ducted fans. The flow exiting a ducted fan does not contract like a free propeller, but rather the wake maintains the same diameter as the duct exit. For the same thrust level, the

ducted fan will have a slower wake velocity than a free propeller, and will entrain more of the tunnel flow. This higher mass flow through the duct results in a relatively larger velocity correction.

Analysis of the corrected wind tunnel data for a generic ducted fan configuration has led to a new concise non-dimensional modeling scheme. This new approach captures the nonlinear characteristics of the force, moment, and power data while representing these terms in a set of simple equations. Force coefficients based on fan tip speed are plotted versus advance ratio for a range of angles of attack, yielding several observations. Each angle of attack yields a linear trend as a function of advance ratio but with differing slopes, with all lines converging through a single point. This fulcrum point shares the same thrust coefficient value as static/hover tests, but at a non-zero advance ratio value. This suggests that while the vehicle is stationary, a ducted fan self-induces a free-stream flow in the hover thrust direction equivalent to a small non-zero advance ratio.

Pitch and roll moments are successfully modeled through center of pressure movement as a function of advance ratio and angle of attack. The power required to turn the fan is modeled using Figure of Merit. This term is typically a hover performance metric; however, I use this representation over the entire flight regime to produce a clear relationship relating power required to thrust generated. The excellent correlation between the model and the data supports the validity of modeling the power in this way.

The new model is applied to a respected legacy dataset from NASA tests in the 1960s to verify the model's general validity and applicability to other datasets. The model shows excellent agreement with the NASA force and power data. This well-accepted dataset also shows the non-zero advance ratio characteristic in hover tests. The pitching moment correlation showed good agreement, but may merit further investigation.

The model is appropriate for typical ducted fan flight conditions, but does not address the nonlinear effects of duct lip stall. The model was developed

using an axisymmetric ducted fan configuration; accounting for asymmetries in future vehicle configurations would require enhancements to the model. The vehicle moment modeling via center of pressure movement and the power modeling via Figure of Merit are restricted to positive thrust conditions. The model was successfully applied to data spanning angles of attack from 0° to 100°, and velocities from hover to 80 knots (40 m/s).

In summary, the most influential aerodynamic terms (F_X, F_Z, M_X, M_Y, Power) for an axisymmetric ducted fan configuration can be modeled with a total of twelve non-dimensional terms. The new modeling technique attains very high correlation values for both recent and legacy ducted fan data, supporting the model's validity. These new developments offer a new paradigm for understanding the fundamentals of ducted fan aerodynamics. The resulting model can concisely describe the aerodynamics of a ducted fan configuration, and can serve in future modeling of vehicles for simulation and flight control development.

Chapter 5 Synthetic Jet Actuators

Synthetic Jet Actuators (SJA) have generated considerable research interest because they are wider and entrain more flow than similar steady jets [21] and also can be used in situations where steady blowing flow control is not feasible [92]. One such application is active flow control in unmanned air vehicles (UAVs). Depending on the scale of such aircraft, there may not be available volume or weight/power budget to implement a traditional flow control scheme. The advent of "zero net mass flux" actuators (another name for SJAs) has theoretically eliminated this hurdle; however, many technical issues must be overcome to successfully implement a system that can meet the performance requirements as well as size, weight, and power constraints of a UAV.

The objective of the SJA designs developed was not to study the fundamental fluid mechanics of such systems, but rather to evaluate the performance of synthetic jets in a challenging flow control application. Given that perspective, it was desired to produce the maximum jet strength in the smallest form-factor that was feasible for integration in the vehicle design. The constraints inherent in this optimization process were mainly due to vehicle geometry (lengths of orifices, size of cavity, etc.) and the flow control application (rectangular slots preferred over circular orifices for tangential blowing).

Several designs were developed and evaluated to better understand what configuration would work best for the ducted fan flow control application, and to gage what level of blowing was to be expected. These developments were generally grouped into two rounds of design and experiment. The first round

of SJA actuator experiments compared designs based on large bimorph disks and Macro Fiber Composite (MFC) actuators. This first round was to determine if the MFC technology was advantageous for inclusion in the final design. The second round was focused on developing a flight-weight design that would be easily integrated in the vehicle flow control geometry. In both cases, maximizing jet output was the prime objective.

5.1 Bimorph and MFC Synthetic Jet Comparison

In this first round of design and evaluation, jets were tested in two different orientations. Most literature addresses the "normal" orientation, where the orifice is located directly above the center of the diaphragm, as seen in Figure 3-7, with the jet proceeding perpendicular or normal to the diaphragm. A "lateral" orientation allows the jet to emerge from the side of the cavity. A schematic of the two orientations is shown in Figure 5-1. A lateral orientation may have advantages for vehicle integration in a UAV, depending on the available space and desired jet effect. The majority of tests performed in this study use a normal orientation.

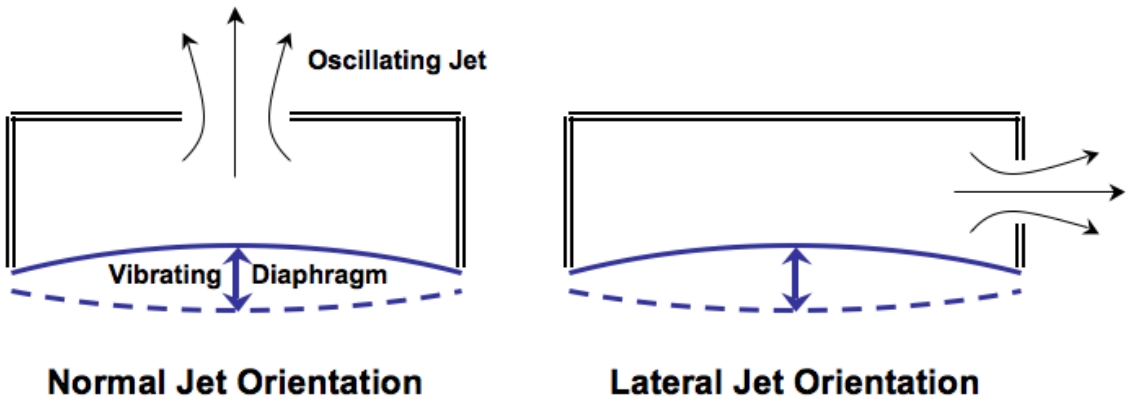

Figure 5-1. Normal and lateral jet orientations.

A summary of the cases tested is shown in Table 4, with the corresponding Helmholtz frequency for the specified geometry. Equation 22 defines the Helmholtz frequency. In all cases the diameter of the cavity, D_j, was constant.

A plot of Helmholtz frequency versus cavity depth, H_j, for each orifice tested is shown in Figure 5-2. Others have found that the natural frequency of the mechanical diaphragm element is more influential than the Helmholtz frequency in producing the highest jet velocities [85]. In many of the tests performed the Helmholtz frequency was above the range appropriate for the mechanical diaphragm.

Table 4. Summary of Test Case Parameters

Orifice Type	D_j, in	H_j, in	Volume, in^3	d_j,, in	a_j, in^2	h_j, in	Helmholtz Freq., Hz
0.125" Diameter, Normal	2.3	0.05	0.208	0.125	0.0123	0.05	2317
0.125" Diameter, Normal	2.3	0.10	0.415	0.125	0.0123	0.05	1638
0.125" Diameter, Normal	2.3	0.15	0.623	0.125	0.0123	0.05	1338
0.125" Diameter, Normal	2.3	0.20	0.831	0.125	0.0123	0.05	1158
0.05" x 1.0" Slot, Normal	2.3	0.05	0.208	N/A	0.05	0.05	4676
0.05" x 1.0" Slot, Normal	2.3	0.10	0.415	N/A	0.05	0.05	3307
0.05" x 1.0" Slot, Normal	2.3	0.15	0.623	N/A	0.05	0.05	2700
0.05" x 1.0" Slot, Normal	2.3	0.20	0.831	N/A	0.05	0.05	2338
0.05" x 1.0" Slot, Lateral	2.3	0.05	0.208	N/A	0.05	0.60	1350
0.05" x 1.0" Slot, Lateral	2.3	0.10	0.415	N/A	0.05	0.60	955
0.05" x 1.0" Slot, Lateral	2.3	0.15	0.623	N/A	0.05	0.60	779
0.05" x 1.0" Slot, Lateral	2.3	0.20	0.831	N/A	0.05	0.60	675
0.02" x 1.0" Slot, Lateral	2.3	0.05	0.208	N/A	0.02	0.60	854
0.02" x 1.0" Slot, Lateral	2.3	0.10	0.415	N/A	0.02	0.60	604
0.02" x 1.0" Slot, Lateral	2.3	0.15	0.623	N/A	0.02	0.60	493
0.02" x 1.0" Slot, Lateral	2.3	0.20	0.831	N/A	0.02	0.60	427

$$f_H = \frac{c_s}{2\pi}\sqrt{\frac{a_j}{h_j V_{cavity}}} \tag{22}$$

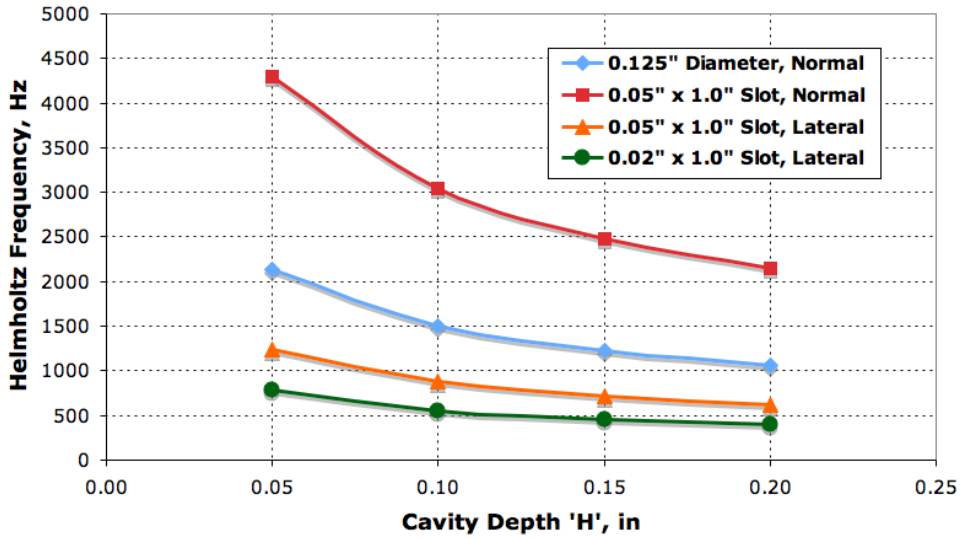

Figure 5-2. Calculated Helmholtz frequency vs. cavity depth for several orifice geometries.

Frequency sweeps were used to identify the range of inputs that produced the highest jet velocities for each configuration. Then detailed parametric sweeps of driving frequency, peak-to-peak voltage, and driving waveform were evaluated for multiple geometries and piezoelectric elements. Twenty periods of the waveform were recorded for each run, and the resulting data sets were processed in MATLAB to find the peak velocity and RMS velocity averages over the twenty periods.

5.1.1 Static Deflection

To first characterize the piezoelectric elements in a traditional fashion, static displacement measurements were taken via laser vibrometer while supplying a step input voltage to the diaphragms. The results are shown in Figure 5-3.

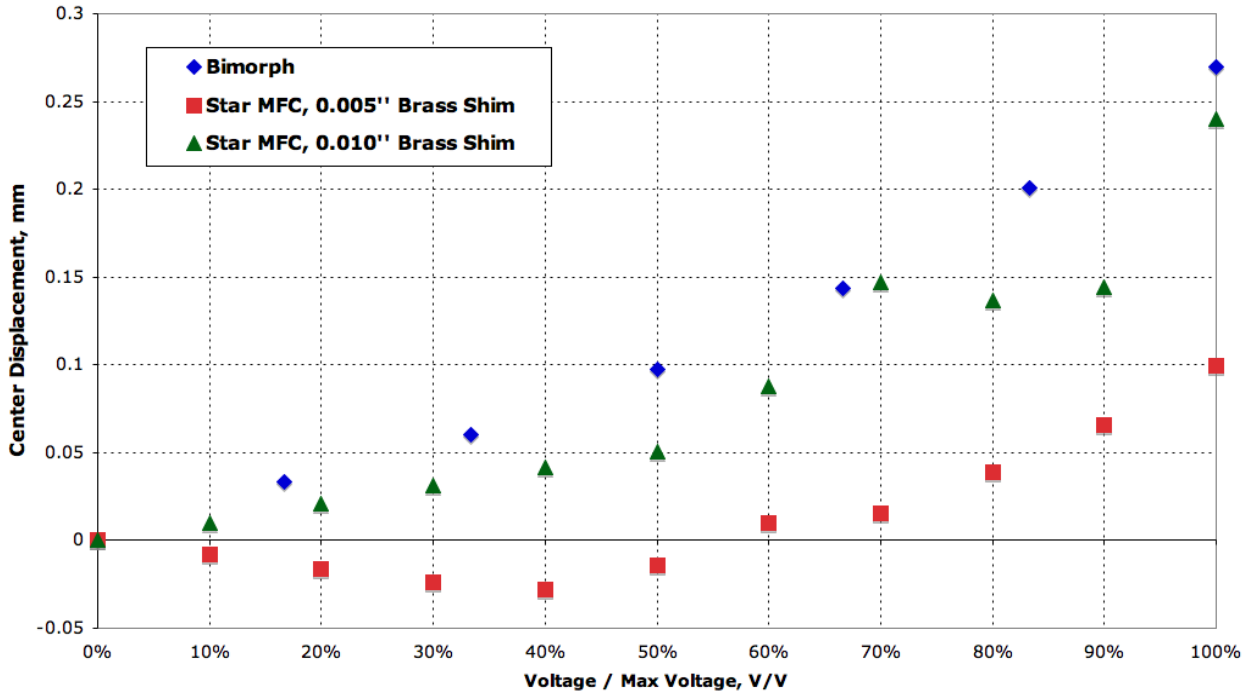

Figure 5-3. Static diaphragm deflection comparison.

While the required voltage for the MFCs is much higher, the overall deflection of the bimorph and the MFC unimorph with 0.010" shim are quite similar. The MFC unimorph with 0.005" shim exhibited a "snap-through" nonlinearity. As voltage was applied, the diaphragm deflected in the direction opposite to the normal characteristic of a unimorph, then as the voltage increased it changed direction and deflects in the intended orientation. This phenomenon was unintended, and is suspected to be a result of the fabrication process. The 0.005" brass shim stock used as a substrate had a small non-zero curvature prior to bonding. This characteristic is the presumed source of the nonlinear behavior. If this nonlinearity was avoided in future tests, the deflection of this configuration could possibly exceed that of the bimorph and 0.010" shim actuators because it is less stiff. Alternately, if the snap-through behavior was designed with care, it could cause larger deflections than a traditional unimorph.

5.1.2 Identifying Frequencies of Interest

Several references have shown that maximum jet velocities occur at or near the diaphragm natural frequency or the cavity Helmholtz frequency [70][72][85]. The mechanical resonance of the diaphragm element itself was determined using a laser vibrometer to measure displacement and velocity, without the synthetic jet orifice plate and orifice attached. This resulted in measuring just the diaphragm dynamics. A plot of the frequency response is shown in Figure 5-5. The units for gain are inconsequential (laser vibrometer voltage divided by piezo input voltage), rather the shape of the frequency response is most important. The plot shows that the natural frequency for the bimorph element was in the vicinity of 500 Hz. The tightness of the bolts that apply the boundary condition to the diaphragm has a significant effect on the shape and magnitude of the response as well as the natural frequency observed. Therefore, it was necessary to tune the bolt torque to an optimal value using a torque wrench, and ensure that each bolt was tightened identically.

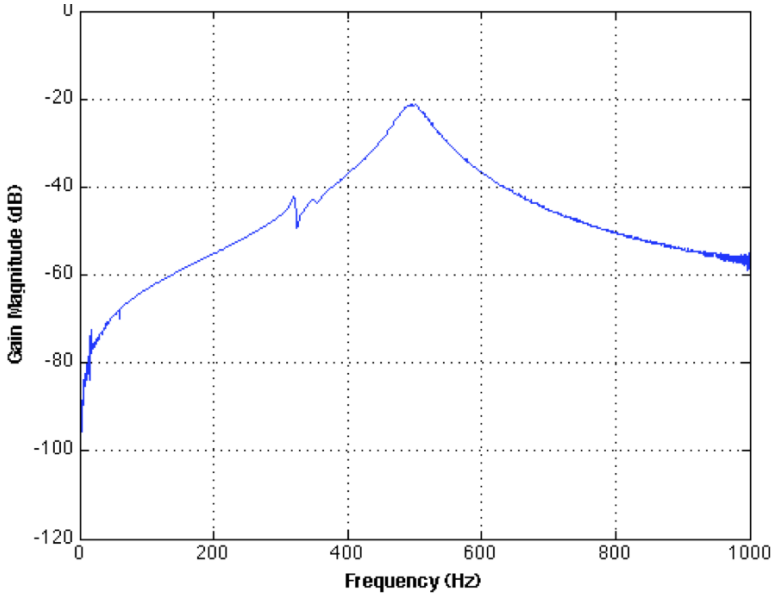

Figure 5-4: Piezoelectric bimorph diaphragm frequency response showing natural resonant frequency.

To identify the frequencies of interest for each diaphragm/cavity geometry configuration with the synthetic orifice jet geometry included, a chirp signal (continuously increasing frequency sinusoidal wave) was used to approximate the frequency response of the system. The response was then quantified as a jet velocity using the hotwire anemometer. An example of resulting data is shown in Figure 5-5.

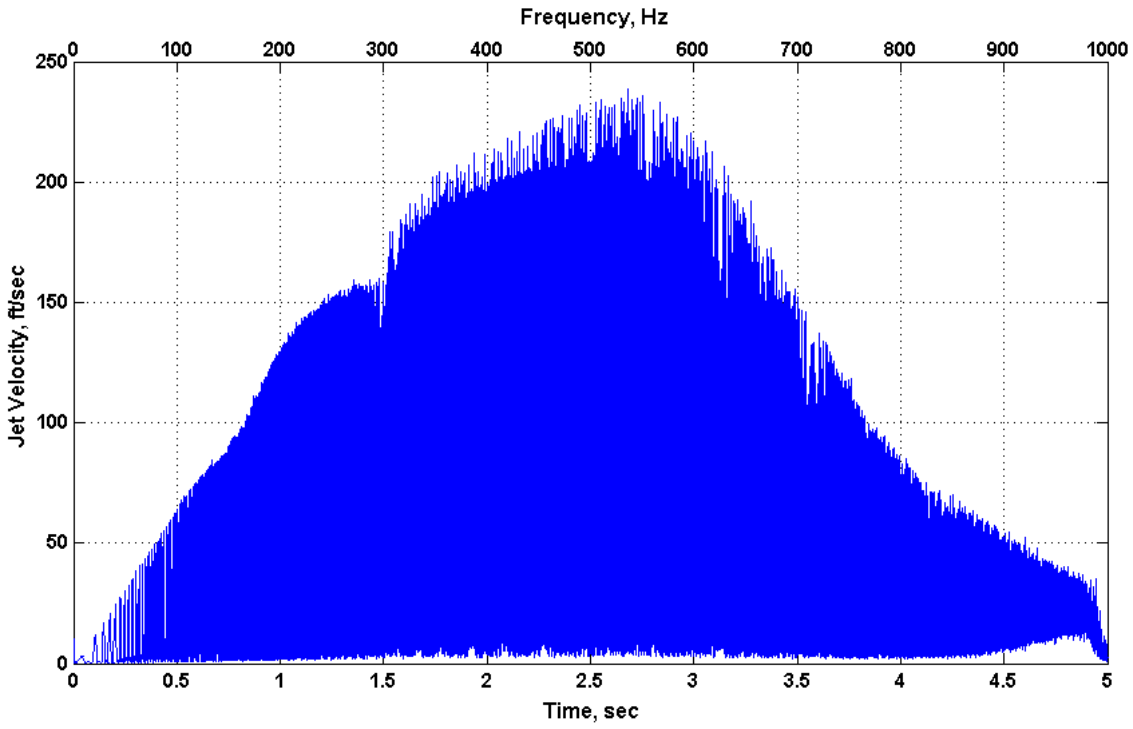

Figure 5-5. Chirp signal response to identify frequencies of interest for piezoelectric bimorph diaphragm.

For the case depicted, the maximum jet velocities are observed in the vicinity of 500 Hz, agreeing well with the natural frequency of the bimorph in isolation. For each design, this method was used to identify the frequencies of interest, and then a detailed sweep of frequency, voltage, and waveform was then executed in that region.

5.1.3 Mapping of Experiment Design Space

The results of the parametric experiment design revealed several interesting features. Plots of the data for the MFC with 0.005" shim are shown in Figure

5-6. All results in this section are for a circular orifice with diameter of 0.125" (D/d = 20).

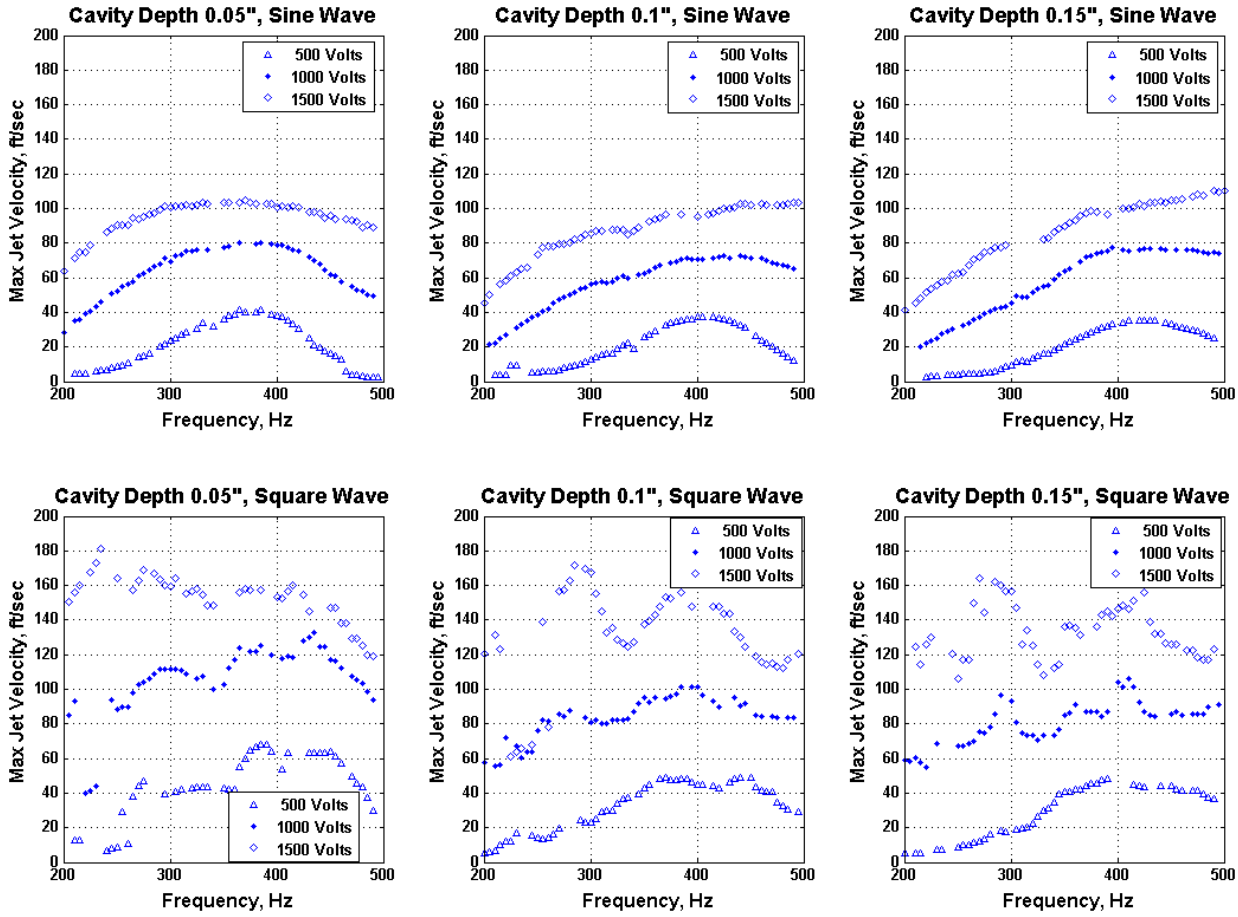

Figure 5-6. MFC with 0.005" shim, max jet velocity vs. frequency and voltage.

For sinusoidal driving functions, the response looks fairly smooth with almost linear response to input voltage. The square wave driving function caused more variability in the response (possibly due to exciting other modes in the diaphragm), but as a first level observation the square wave signals generated much higher jet velocities. As would be expected, the highest jet velocities are obtained with the highest input voltage, and there was also a slight trend towards higher velocities as the cavity depth decreased. The highest jet velocity observed for this diaphragm was 181 ft/sec for the

following configuration specifications: cavity depth of 0.05”, voltage input 0 to +1500 V, frequency of 235 Hz, and a square waveform.

A similar data set for the MFC with 0.010” shim is shown in Figure 5-7.

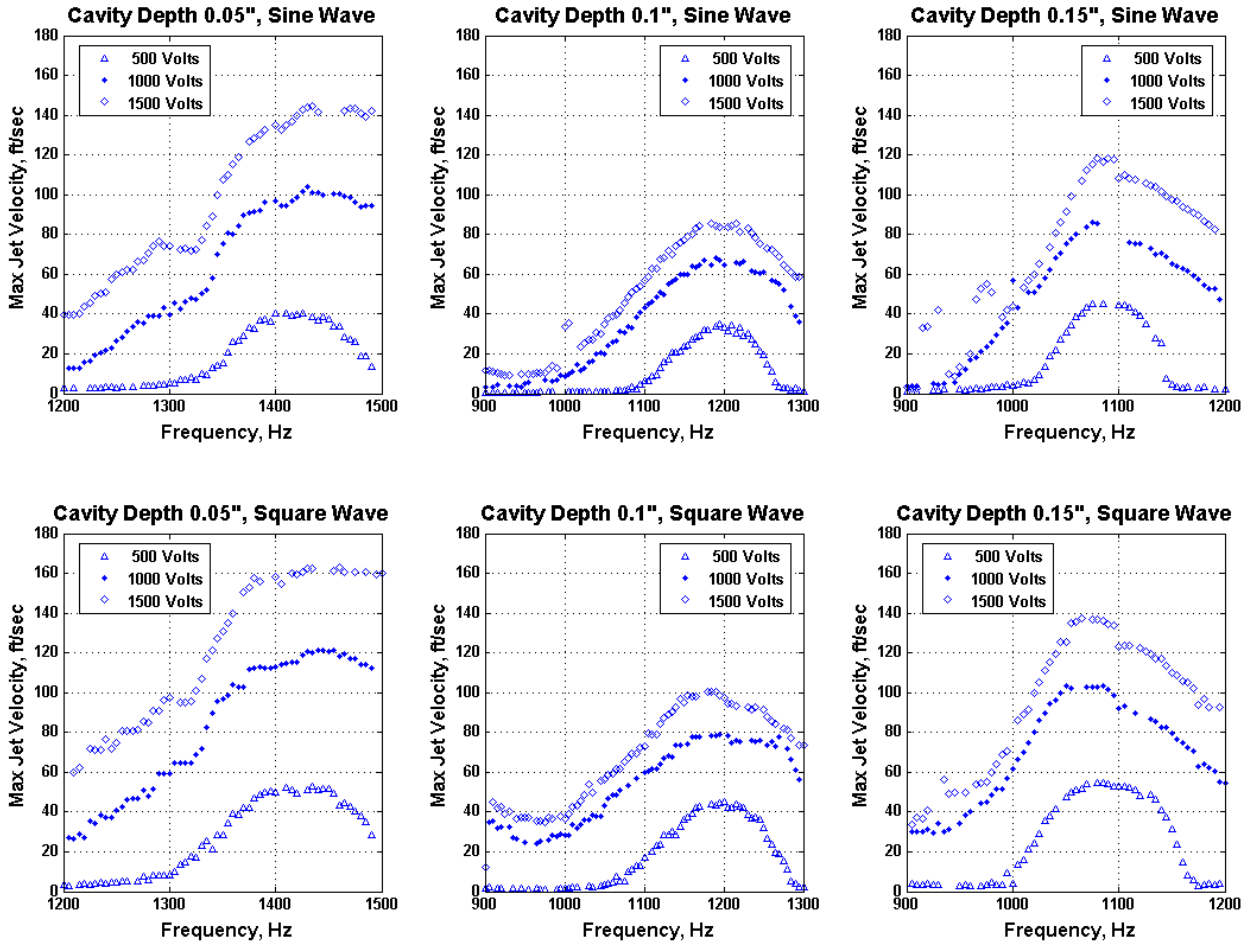

Figure 5-7. MFC with 0.010” shim, max jet velocity vs. frequency and voltage.

Again the highest jet velocities are obtained with the shallowest cavity depth, 0.05”. The highest jet velocity observed for this diaphragm was 166 ft/sec for the following configuration specifications: cavity depth of 0.05”, voltage input 0 to +1500 V, frequency of 1450 Hz, and a square waveform. The fact that the optimal frequency is much higher than that for the 0.005” shim actuator is attributed to a higher natural frequency of the vibrating element due to the increased stiffness of the thicker substrate. One unique observation for this diaphragm was that the peak jet velocities occurred at increasing frequencies as the cavity depth decreased. This would be consistent with a

change in Helmholtz frequency, but these frequencies are lower than the calculated Helmholtz frequency for each geometry. This, in addition to the fact that the difference between the two grows greatly at the smallest cavity (1450 Hz vs. f_H = 2317 Hz), suggests that this is not the Helmholtz frequency observed, but rather the damped natural frequency of the mechanical diaphragm. It is likely that the peak jet frequency is changing because the varying chamber volume alters the damping ratio.

The benchmark dataset for comparing with the MFC data was the bimorph diaphragm SJA data, which is plotted in Figure 5-8. This data set shows much less sensitivity to cavity depth and waveform, with the square wave only slightly performing better. However, the difference in jet velocity between the highest and intermediate voltage is much lower than that of the lowest and the intermediate voltage level. This may imply that the power to drive this diaphragm at resonance has saturated the electric current output of the Trek amplifier used (50 mA). The highest jet velocity observed for the bimorph diaphragm was 235 ft/sec (72 m/s) for the following configuration specifications: cavity depth of 0.15”, voltage input -180 V to +180 V, frequency of 555 Hz, and a square waveform.

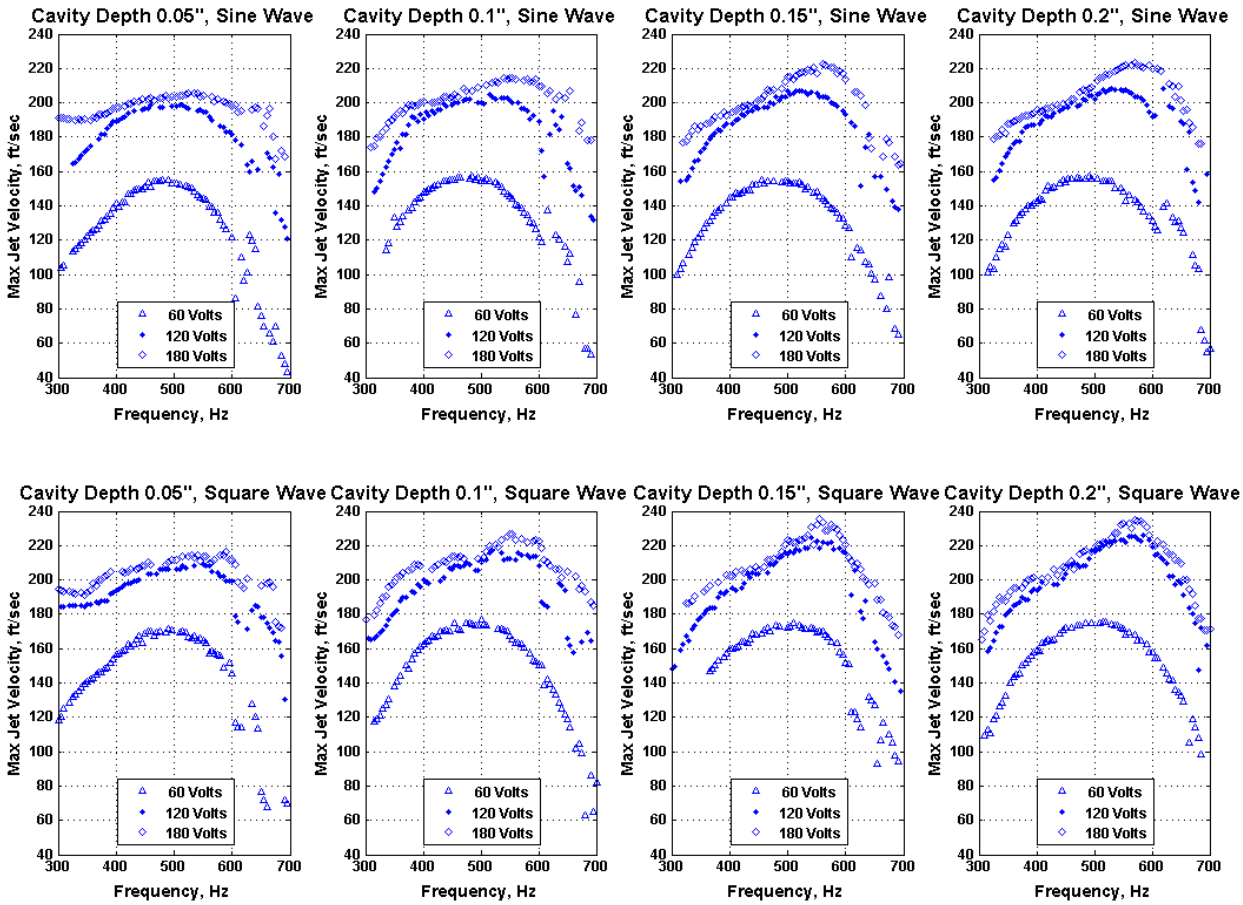

Figure 5-8. Bimorph, max jet velocity vs. frequency and voltage.

5.1.4 Effect of Waveform

Figure 5-9 through Figure 5-11 show the sine wave and square wave results superimposed for the MFC with 0.005" shim, MFC with 0.010" shim, and the bimorph, respectively.

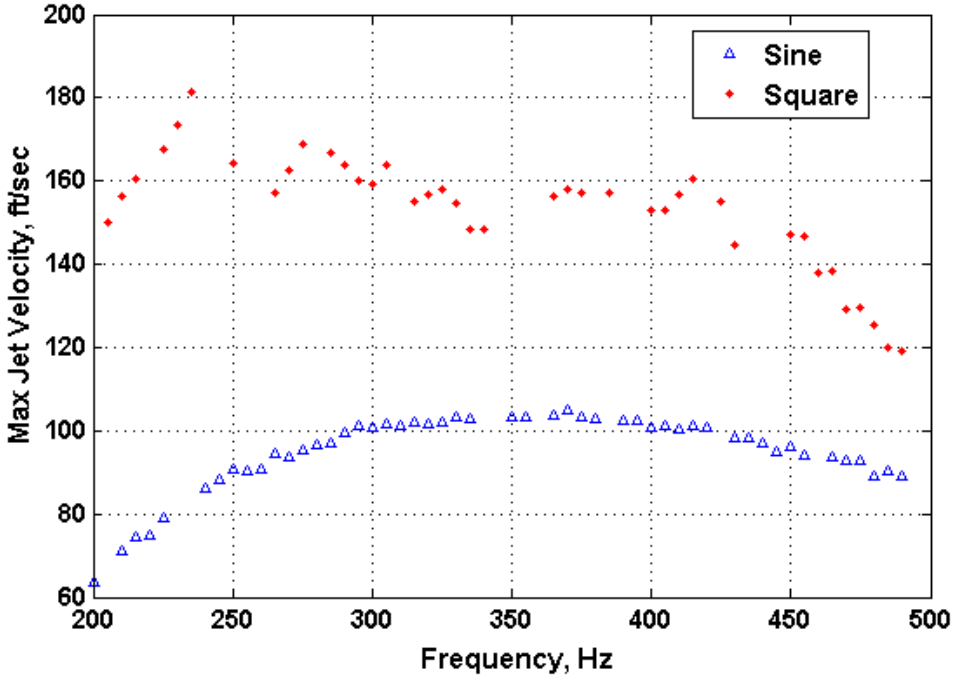

Figure 5-9. MFC with 0.005" shim, effect of waveform on max jet velocity.

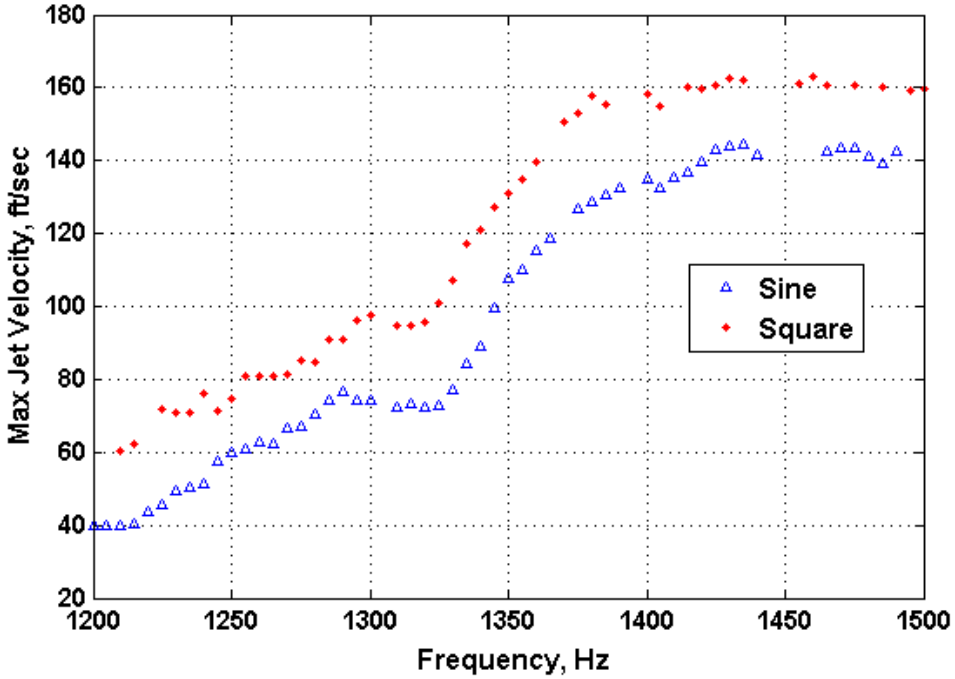

Figure 5-10. MFC with 0.010" shim, effect of waveform on max jet velocity.

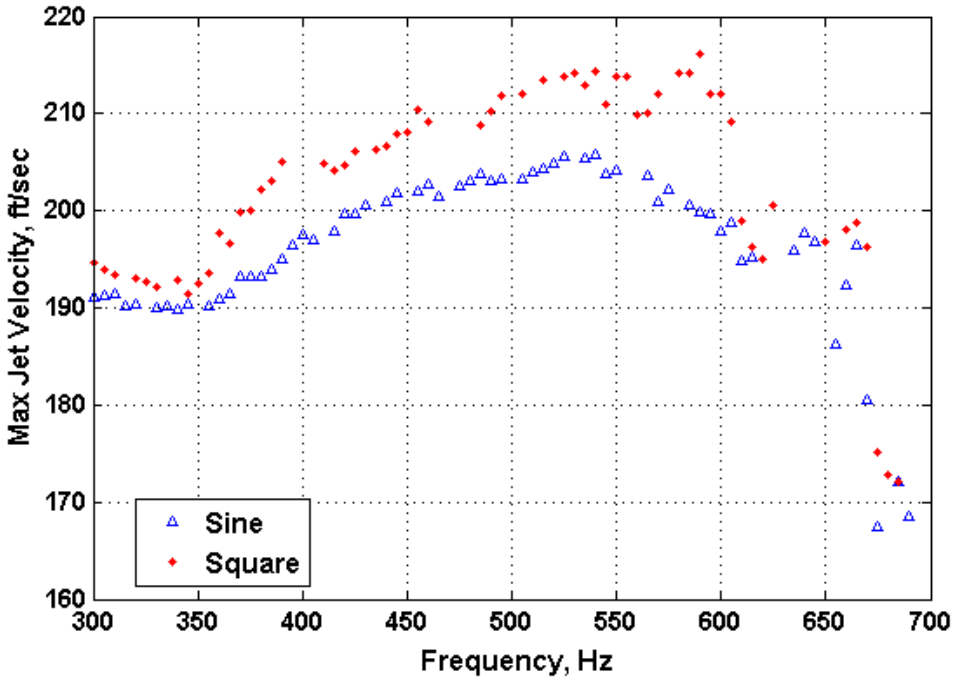

Figure 5-11. Bimorph, effect of waveform on max jet velocity.

While the square wave generally produces the larger jet velocity, the phenomenon is most pronounced in the MFC with 0.005" shim, with differences in peak jet velocity more than 100% higher with the square wave forcing. The phenomenon is less dominant but still evident in the MFC with 0.010" shim and the bimorph as well. Because the square waveform changes voltage so quickly, it would be expected that the corresponding velocity jump at that discontinuity in voltage would be larger than the sine wave forcing. However, it seems that this is not just an isolated peak in velocity, but also an overall increase in performance, since the RMS velocity that averages the complete cycle was also observed to increase the same relative amount with square wave forcing.

5.1.5 Effect of Orifice and Jet Orientation

The baseline orifice, 0.125" diameter hole with normal orientation, was compared to several slot orifice geometries. Hotwire measurements of jet velocity were obtained at the center point of the slot opening, one slot-width above the orifice. Measuring velocity at the center of the length and width dimensions of the slot should minimize the effects of any span-wise variations

in velocity profile [86]. Slot dimensions of 0.05” x 1.0” were tested in both normal and lateral orientations, as well as a 0.02” x 1.0” slot in the lateral orientation. A comparison of averaged peak velocity verses frequency is shown in Figure 5-12 for the bimorph element, at its highest peak-to-peak voltage of +/-180 volts and cavity depth of 0.15”.

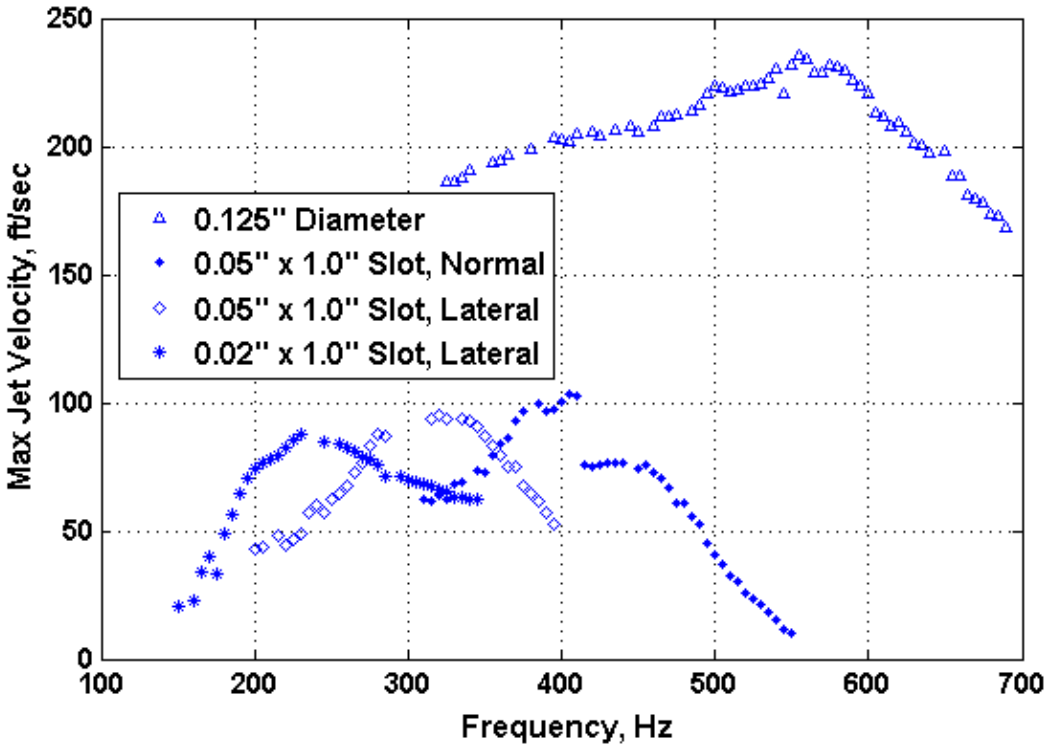

Figure 5-12. Effect of orifice geometry and orientation on jet performance.

The area of the 0.05” wide slot was exactly four times that of the baseline circular orifice, and that is a major reason why the slot jet velocities are lower than the circular orifice case. It should also be noted that the natural frequency of the system decreased when using the slots. There was little difference in peak velocity between the normal and lateral orifices of identical cross section, however the lateral orientation maximum velocity was observed at a lower frequency. This is consistent with increase in orifice depth, either from the perspective of the Helmholtz relationships or the idea that a longer neck will cause more losses and increase damping, thereby decreasing the damped

natural frequency of the system. The 0.02” wide lateral slot showed the lowest natural frequency, but a peak velocity of similar magnitude as the 0.05” wide slots. It is assumed that the expected increase in velocity due a reduction in orifice area is offset by the increased relative losses in the orifice as the width decreases and the length and depth are held constant.

5.1.6 MFC Powered In-stroke versus Powered Out-stroke

One unique aspect of the MFC-based SJA configurations was the dependence on mounting orientation. Because the MFC has a bias in its allowable input voltage, -500 V to +1500 V, the MFC/shim unimorph structure also manifests this behavior in its deflection capability. The unimorph’s intended deflection orientation is toward the side to which the MFC is bonded. As the MFC expands it causes the substrate to dome. In addition, the Trek voltage amplifier can only output 0 to +1500 V, so the excitation during experiments was limited to only the expansion of the MFC. In the initial setup, it was assumed that for maximum jet velocity the doming should be aligned with the direction of the jet, designated here as a powered out-stroke. However, for many cases this result was not true. Figure 5-13 shows a comparison of the in-stroke and out-stroke jet velocity time histories for the same MFC element, cavity dimensions, and boundary conditions.

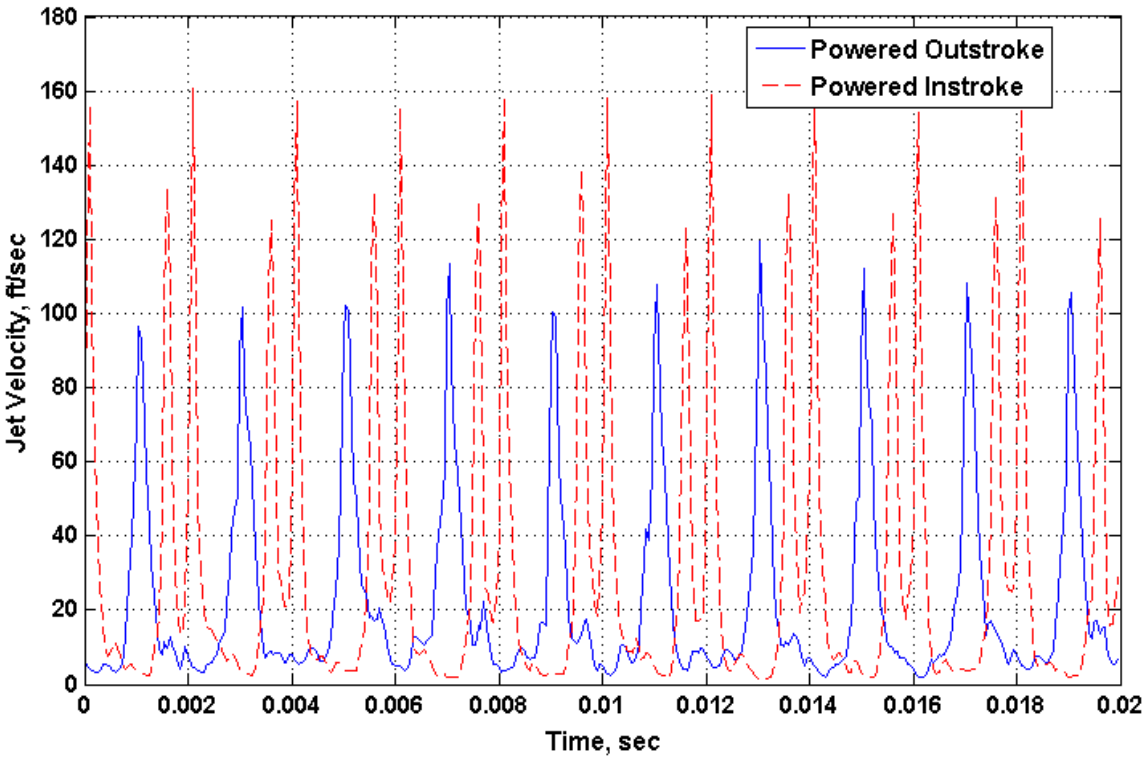

Figure 5-13. Powered in-stroke vs. out-stroke effect on jet velocity waveform, MFC with 0.005" shim, 500 Hz square wave forcing.

The one expected result was that the two waveforms are 180 degrees out of phase, due to the fact that a positive voltage causes opposite diaphragm movements within the cavity for the two cases. The unexpected findings were the double jet velocity peaks and larger magnitudes for the powered in-stroke case. The double peaks are likely a higher order mode being excited in the nonlinear structure that showed a snap-through behavior. Regarding the higher output of the powered in-stroke, it is possible that the restoring force of the brass substrate causes more forceful movement of air than does the active doming from MFC actuation. It is also possible that this is due to the snap-through nonlinearity in the 0.005" shim MFC bimorph. For the case shown, the powered in-stoke produced 47% higher peak jet velocity and 44% higher RMS jet velocity. Further investigation would be needed to understand this phenomenon and whether the double peaks positively or negatively impact the resulting jet flow further down stream from the orifice exit plane. However, it is expected that the increased momentum and mass flow (during out-stroke)

that is imparted by the double peak would make the powered in-stroke more effective at influencing a large scale flow.

5.2 Unimorph Synthetic Jet Actuator

The second round of design was for a smaller scale synthetic jet design based on a 1" unimorph disk, as shown in Figure 3-8. Another fundamental difference from the first round was that the configuration was changed from a normal jet to a lateral jet, as seen in Figure 5-1. The lessons learned from the first round of experiments were brought forward into the second iteration.

It was seen from the first round of tests that synthetic jet output was very dependent on actuation frequency. In general, two main frequencies dominate their behavior: the Helmholtz frequency of the cavity, and the damped natural frequency of the mechanical diaphragm. At the Helmholtz frequency and above, the air in the cavity exhibits compressibility [71]. The relative arrangement of whether the natural frequency of the diaphragm is above or below this frequency dictates what kind of behavior is exhibited. The general finding of this research and other researchers is that the natural frequency of the mechanical diaphragm element produces higher jet velocities than the Helmholtz frequency in producing the highest jet velocities [85].

Aligning the mechanical natural frequency and Helmholtz resonance frequency to coincide gives further increase to jet velocity, and can be attained by designing the cavity and diaphragm to achieve this [71]. This was not practical for the implementation needed for this flow control application, given the space constraints and chosen diaphragm element. In all of the cases tested the damped natural frequency of the diaphragm was below the Helmholtz frequency of the cavity, and produced significantly higher jet output than driving at the Helmholtz frequency. It is possible that for certain designs the Helmholtz frequency could produce higher jet velocities, but this was not observed in the present experiments. A summary of the cases tested is shown

in Table 4, with the corresponding Helmholtz frequency for the specified geometry. In all cases the diameter of the cavity, D_j, was constant.

Table 5. Summary of Synthetic Jet Test Case Parameters

Orifice Type	D_j, in	H_j, in	Volume, in^3	l_j, in	w_j, in	h_j, in	Helmholtz Freq., Hz
0.03" x 0.8" Slot	1	0.05	0.039	0.8	0.03	0.1	5269
0.03" x 0.8" Slot	1	0.06	0.047	0.8	0.03	0.1	4810
0.03" x 0.8" Slot	1	0.07	0.055	0.8	0.03	0.1	4453
0.03" x 0.8" Slot	1	0.08	0.063	0.8	0.03	0.1	4166
0.02" x 0.8" Slot	1	0.06	0.047	0.8	0.02	0.1	3927
0.04" x 0.8" Slot	1	0.06	0.047	0.8	0.04	0.1	5554

After using a sweep of driving frequency to identify the range of the diaphragm damped natural frequency (via a 'chirp' signal), a detailed investigation near the frequency of interest was performed for each configuration. Automated test sweeps were utilized to collect jet velocity data for a range of frequency, voltage, and driving waveform. This procedure was applied to different configurations of SJA geometry including cavity depth and orifice width. Figure 5-14 shows the results of this process for several cavity depths with constant orifice geometry: a 0.030" x 0.8" rectangular slot.

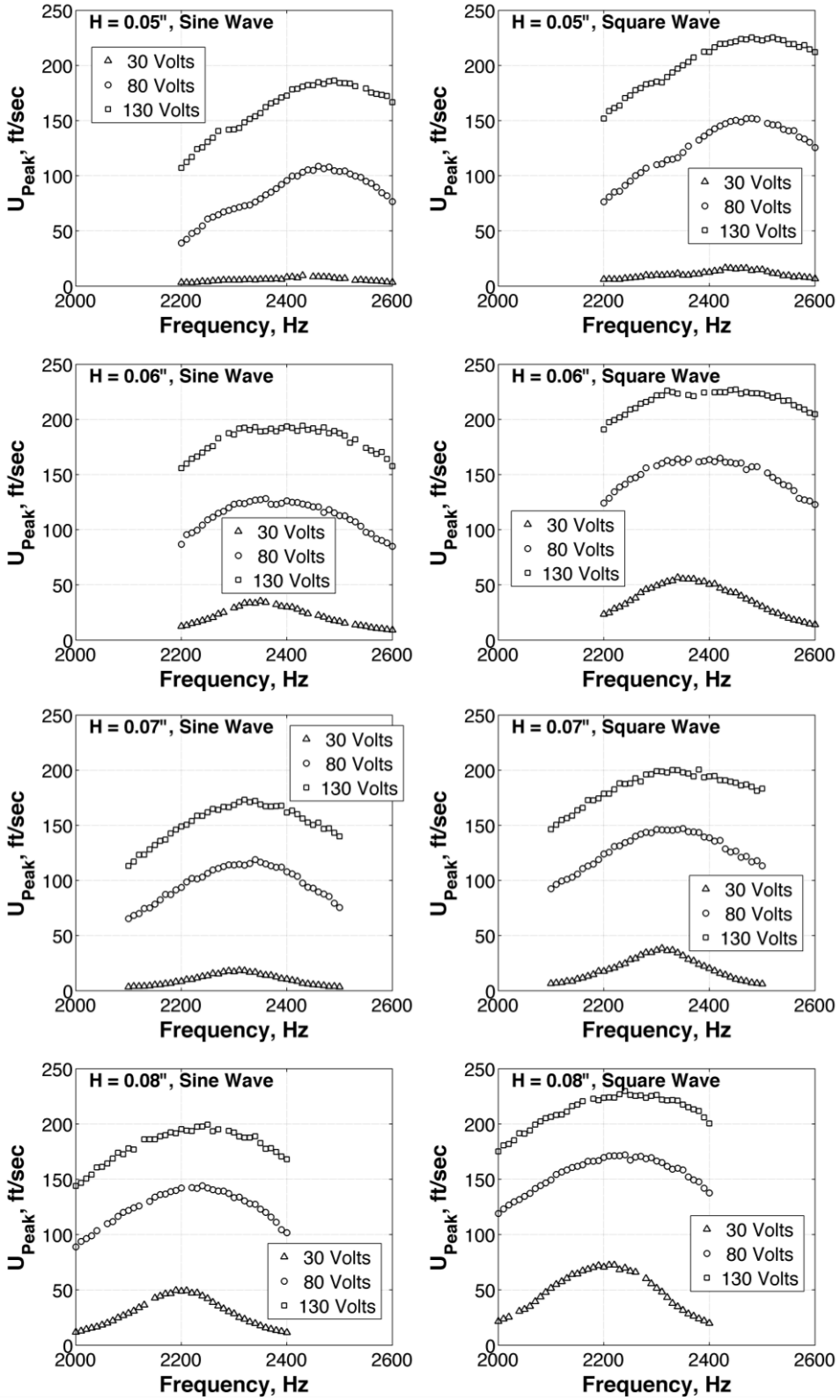

Figure 5-14. Frequency, voltage, and waveform sweep for various cavity depths for fixed slot width of 0.03".

These results show that there is a slight sensitivity in peak jet velocity due to cavity depth. One more noticeable difference due to cavity depth is the frequency at which the peak velocity occurs. This frequency is essentially the damped natural frequency of the piezoelectric diaphragm. As the cavity depth and volume increase, the damped natural frequency decreases. This implies greater damping or losses for larger cavities, and may imply that shallower cavities are superior. From a space and packaging standpoint, this is a positive finding. The peak jet velocity observed from this data is 225 ft/sec (69 m/s) for a 130V amplitude square wave input at 2400 Hz for the minimum cavity depth of 0.06".

The effect of orifice slot width was explored while using a constant cavity depth of 0.06". The general trend is that the widest slot produced the lowest peak velocities. To take a closer look at this trend, only the highest voltage square wave results are superimposed for comparison in Figure 5-15.

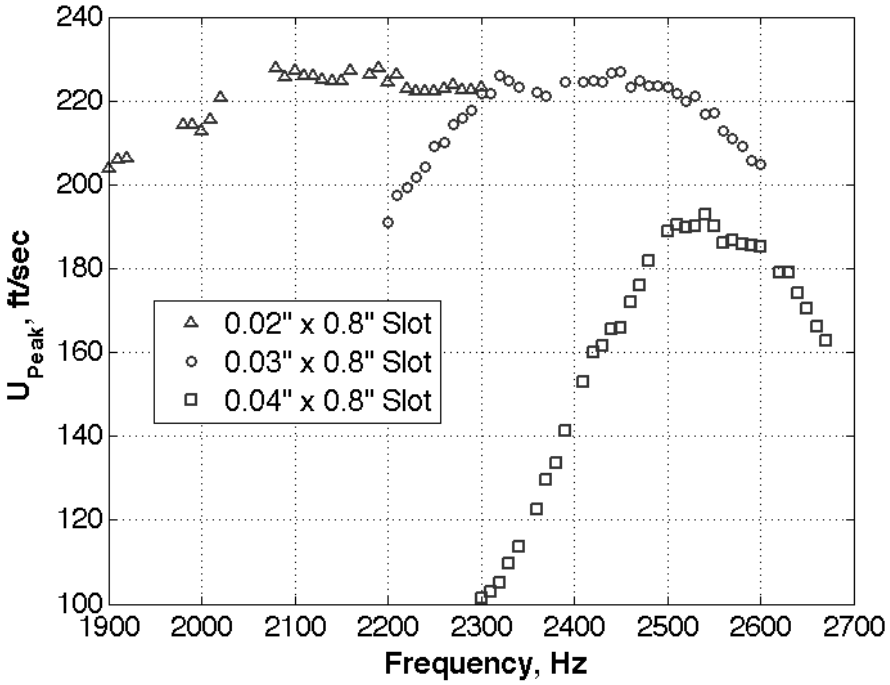

Figure 5-15. Effect of orifice width on peak jet velocity characteristics.

The widest slot tested, 0.040", showed the lowest peak velocity. This makes sense conceptually: for a given volume displacement or mass flow, the velocity

is inversely proportional to exit area. If this trend applied indefinitely, the smallest area slot (0.020”) would show significant increases over the 0.030” slot, but this is not observed. The 0.020” and 0.030” slots produce nearly the same peak velocities, although at different frequencies. This is attributed to losses building up as the orifice width decreases, and is supported by the decrease in damped natural frequency. This implies that there is an optimal jet width for any synthetic jet design that balances orifice losses with orifice area. If the slot width decreased to values smaller than 0.020” in this case, it is anticipated that the overall jet velocity would decrease due to losses. For this setup the optimum width was ascertained to be in the realm of 0.020” to 0.030”. For wind tunnel vehicle testing, the 0.030” width slot was selected for two reasons: first, it is easier to fabricate within tolerances; and second, it attains roughly the same velocity with a larger area and will therefore impart more momentum to the flow.

The difference in jet performance based on driving voltage waveform can be observed in Figure 5-16. The results show that a square wave driving function produce roughly a 20% increase in peak jet velocity over a sinusoidal input.

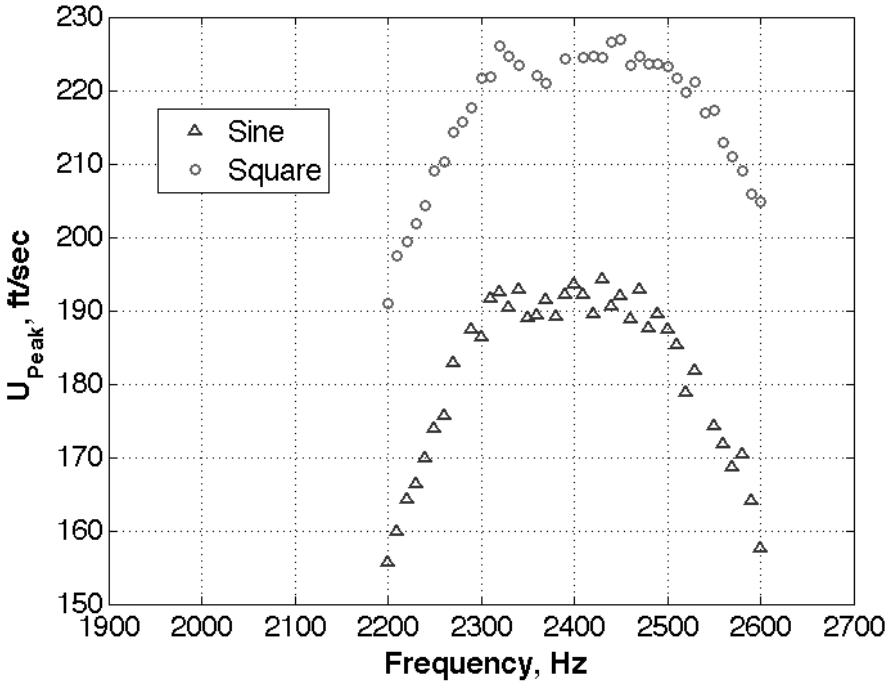

Figure 5-16. Effect of driving waveform on peak jet velocity.

It should be noted that the square wave signal was the input to the high voltage amplifier. Only after further investigation involving measurement of the voltage and current exiting the amplifier and entering the piezoelectric diaphragm was it found that the output of the amplifier was not a pure square waveform. The amplifier (which had current limiting protection) output a signal that was more sinusoidal in nature. The square wave input merely increased the voltage and current amplitude output of the drive circuitry. Driving a capacitive piezoelectric diaphragm with a near square wave input would result in very large instantaneous currents, and large RMS current and power draw while driving it at its natural frequency. Square wave inputs are more wearing on the diaphragm and also tend to excite higher frequency harmonics that are not beneficial. The first bending mode of the diaphragm (depicted in the schematic in Figure 5-1) produces the most jet output, due to that mode creating the largest volume displacement. Therefore, sinusoidal waveforms that maximize voltage and current amplitude within the constraints of the drive electronics are deemed the best option. Using this approach to

avoid longevity concerns for the piezoelectric element will result in the highest sustainable jet outputs that do not damage the piezoelectric diaphragm. The wind tunnel tests using these piezoelectric elements were preformed exclusively with sinusoidal waveforms.

An example of the centerline jet velocity, input voltage, and input current to the synthetic jet is shown in Figure 5-17 for a sinusoidal input of 2300 Hz. The voltage and current are roughly 90 degrees out of phase, which shows that the mechanical system is near resonance, if a second order system (mass-spring-damper) approximation is assumed. A negative current corresponds to an outstroke movement of the diaphragm, as the data show the jet velocity peaks roughly in phase with the current.

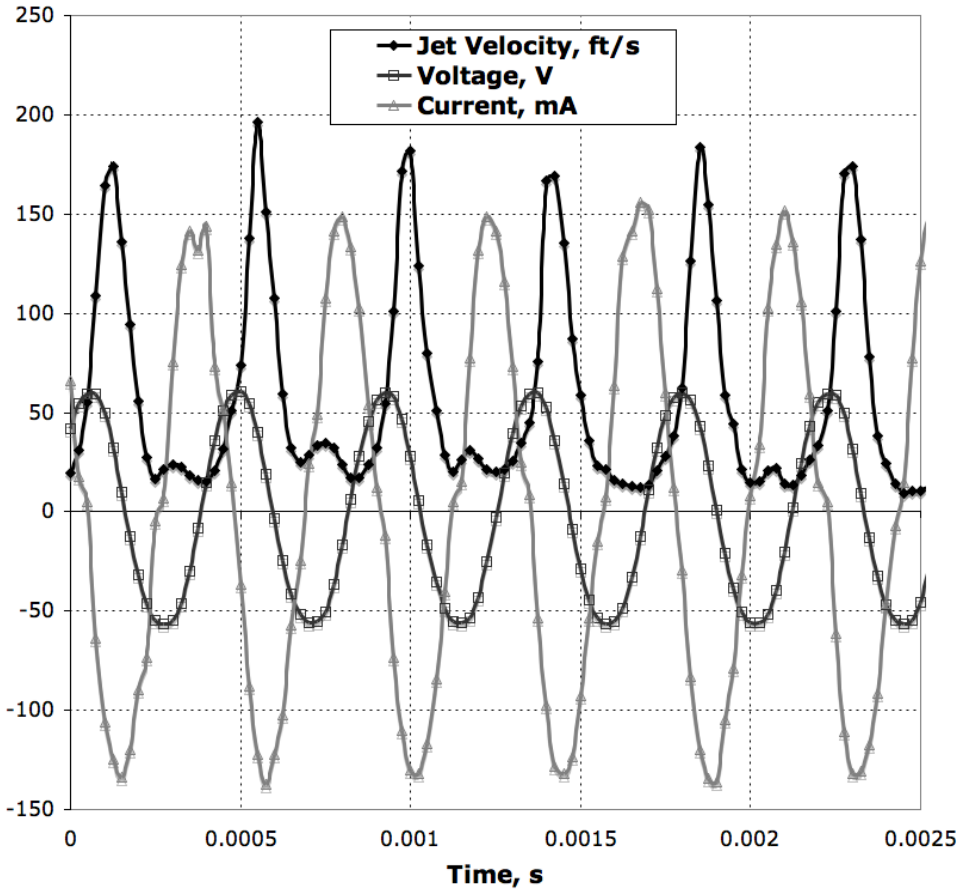

Figure 5-17. Jet velocity, input voltage, and input current signals for 2300 Hz sinusoid drive waveform.

The parameters of the dataset shown in Figure 5-17 are representative of those used in the vehicle wind tunnel tests. The peak jet velocities observed are in the vicinity of 200 ft/s (61 m/s). The small secondary peaks in the troughs of the velocity data are due to the inflow into the slot, measured one slot width downstream. The hotwire anemometer measures the velocity magnitude, thereby resulting in an absolute value of the actual velocity. Due to the small magnitude and absence of a secondary peak in several periods, rectifying the velocity data was omitted. Integrating the centerline velocity shown over the outstroke time period according to Eq. 23 from Holman et al. [65] results in a time averaged velocity, U_0, of 49.8 ft/s and stroke length, L_0, of 0.26". The dimensionless stroke length L_0/w_j for this case is 8.7.

$$U_0 = fL_0 = \frac{1}{T_j}\int_0^{T_j/2} u_j(t)dt \tag{23}$$

Note that the time-averaged velocity, which is used in flow control application calculations, determined from the experimental data is roughly one fourth of the peak jet velocity. This is in fair agreement with the analytical prediction for pure sinusoidal flow velocity in the orifice throat, where average outstroke velocity should be the peak velocity divided by π. The difference observed here may be attributed to measuring the jet velocity one slot width downstream of the orifice instead of directly within the orifice. Since there are practical limits on the maximum peak velocity (transonic and supersonic speeds may be infeasible), this substantial difference from the peak jet velocity makes it more difficult to attain high blowing momentum coefficients using synthetic jets when compared to steady jets.

Using this time-averaged outstroke velocity and adapting the Reynolds number equation from [65] to employ slot width instead of diameter, as seen in Eq. 24, results in a Reynolds number of 818.

$$\mathrm{Re}_{U_0} = \frac{U_0 w_j}{\nu} \tag{24}$$

The inverse of the Strouhal number (a function of Reynolds and Stokes numbers) adapted from [65] to use jet width and Re_{U_0} is depicted in Eq. 25. A value of 2.75 was attained for the data presented and is representative of the jet performance as installed in the vehicle model. This value is well above the jet formation criterion of 0.16 for rectangular jets as predicted by [65].

$$\frac{1}{Sr} = \frac{\left(L_0 / w_j\right)}{\pi} = \frac{2U_0}{\omega w_j} = \frac{\left(2U_0 w_j / \nu\right)}{\left(\omega {w_j}^2 / \nu\right)} = \frac{2\,\mathrm{Re}_{U_0}}{S^2} \tag{25}$$

5.3 Chapter Summary

Synthetic jets have potential for use in flow control applications in UAVs with limited size, weight, and power budgets. The development of SJAs for a ducted fan vehicle was accomplished through two rounds of experimental designs. The first round showed the performance of MFC actuators compared to a pure ceramic bimorph without shim. Star-shaped MFC actuators were bonded to brass substrates to form unimorph diaphragms. Peak jet velocities were measured via hotwire anemometry and were compared to an off-the-shelf bimorph diaphragm. A parametric investigation of the effects of frequency, voltage, chamber depth, and driving waveform was performed.

The peak jet velocities of the MFC-based SJAs were 78% (181 ft/sec) of those generated by an off-the-shelf bimorph diaphragm (235 ft/sec). While they represent an experimental benchmark for performance, bimorph piezoelectric diaphragms are fragile and consequently are not practical for implementation in a UAV. The MFC actuators were robust and easy to handle, but were not selected for use in the final vehicle design due to their large dimensions and lower jet velocities.

The final synthetic jet actuator design resulting from the second round of tests was based on a 1” diameter piezoelectric unimorph disk. The actuator cavity was relatively shallow at 0.06”, and the orifice slot was oriented laterally to the diaphragm to favor the tangential blowing applications in the ducted fan. In general, I found the mechanical resonance of the diaphragm to produce jet velocities larger than the Helmholtz frequency (acoustic resonance). Also, I found shallower cavity depths to be desirable both from a jet performance standpoint, as well as for packaging such actuators in a vehicle with limited volume. Peak jet velocities of 200 to 225 ft/sec were attained for a 0.03” x 0.80” rectangular slot, and this configuration was chosen for testing in the wind tunnel model.

The time-averaged velocity of the outstroke, the most influential parameter in flow control applications, was approximately 50 ft/s. Of particular interest to synthetic jet actuator designers is the difference between this value and the peak jet velocity (near 200 ft/s). In the literature, many researchers report only the peak jet velocity. However, my results affirm the time-averaged outstroke velocity as the proper design metric when designing for flow control applications.

Chapter 6 Ducted Fan Flow Control

The concept of flow control is very attractive to anyone who has designed or worked with aerodynamic configurations. The ability to change the overall nature of a flow through careful application of a relatively small input to the system is intriguing. The resulting effects at the macro scale can translate to significant changes in aerodynamic forces and moments or the power required for operation. It would seem that you could gain much benefit without significant cost. The key is to identify an aerodynamic phenomenon that is capable of being controlled through a small and targeted input. This chapter details the application of unsteady (synthetic jet) and steady flow control to a ducted fan configuration with the following sections: aerodynamic design, vehicle integration of the actuators, and experimental flow visualization and data analysis.

6.1 Aerodynamic Modeling and Design

The flow control concepts being created and evaluated had little precedent for design methodology; therefore, the majority of the design phase was accomplished through Computation Fluid Dynamics (CFD) modeling of the ducted fan and jet flows. CFD analysis solves the Navier-Stokes equations that govern fluid mechanics, over a geometric grid that represents the flight geometry and airflow. Some historical principles for Coandă surface proportions and design were applied from [118] to balance the suction and centripetal loads on the jet flow, but CFD was the primary tool for verifying

designs before fabrication and testing. All CFD solutions incorporated viscous flow and turbulence modeling (Spalart-Allmaras model). Preliminary studies used steady blowing to evaluate the effects of flow control. Then as the designs matured and converged to a final solution, unsteady CFD analysis of the synthetic jet flow in the ducted fan application was performed. This analysis helped to identify flaws in designs early in the design phase. The CFD analysis was a collaboration that I directed, but was primarily performed by other engineers at AVID LLC. A description of the CFD work is presented by Londenberg and Ohanian in [119]. A brief summary is included here to illustrate how the flow control geometry evolved.

Once the synthetic jet actuator design was integrated into the vehicle geometry, 3D time-accurate (unsteady) viscous CFD analysis was used to assess the predicted performance, and improve the integrated design before fabricating the model geometry. The effect of steady and synthetic jet blowing on the ducted fan configuration was analyzed using the NASA Langley FUN3D Reynolds-averaged Navier-Stokes, unstructured mesh method [120]. Incompressible solutions were obtained for the ducted fan configuration at 15-knots (25.3 ft/s) and 14.33˚ tilt from vertical (75.66˚ angle of attack). In each of the CFD solutions, the fan was simulated as an actuator disk, using the rotor method integrated with the FUN3D solver [121]. Using blade geometry and airfoil aerodynamics, this actuator disk method iterates upon the inflow and computes the swirl and pressure increase due to the fan, resulting in a good simulation of first order fan effects. Steady and unsteady blowing conditions were applied as a velocity boundary condition at the beginning of the orifice.

6.1.1 Leading Edge Blowing Analysis

For the leading edge CFD studies, the blowing boundary condition was applied at the exit face of the slot, as seen in Figure 6-1. This reduced order modeling allowed for solution convergence, and three blowing velocities were analyzed: 50-ft/sec, 100-ft/sec, and 200-ft/sec. Comparing the 100-ft/sec and

200-ft/sec blowing with the no blowing case in Figure 6-1 shows that leading-edge blowing causes separated flow over the lip, as intended. When the blowing is not present, the flow proceeds into the duct smoothly, as desired.

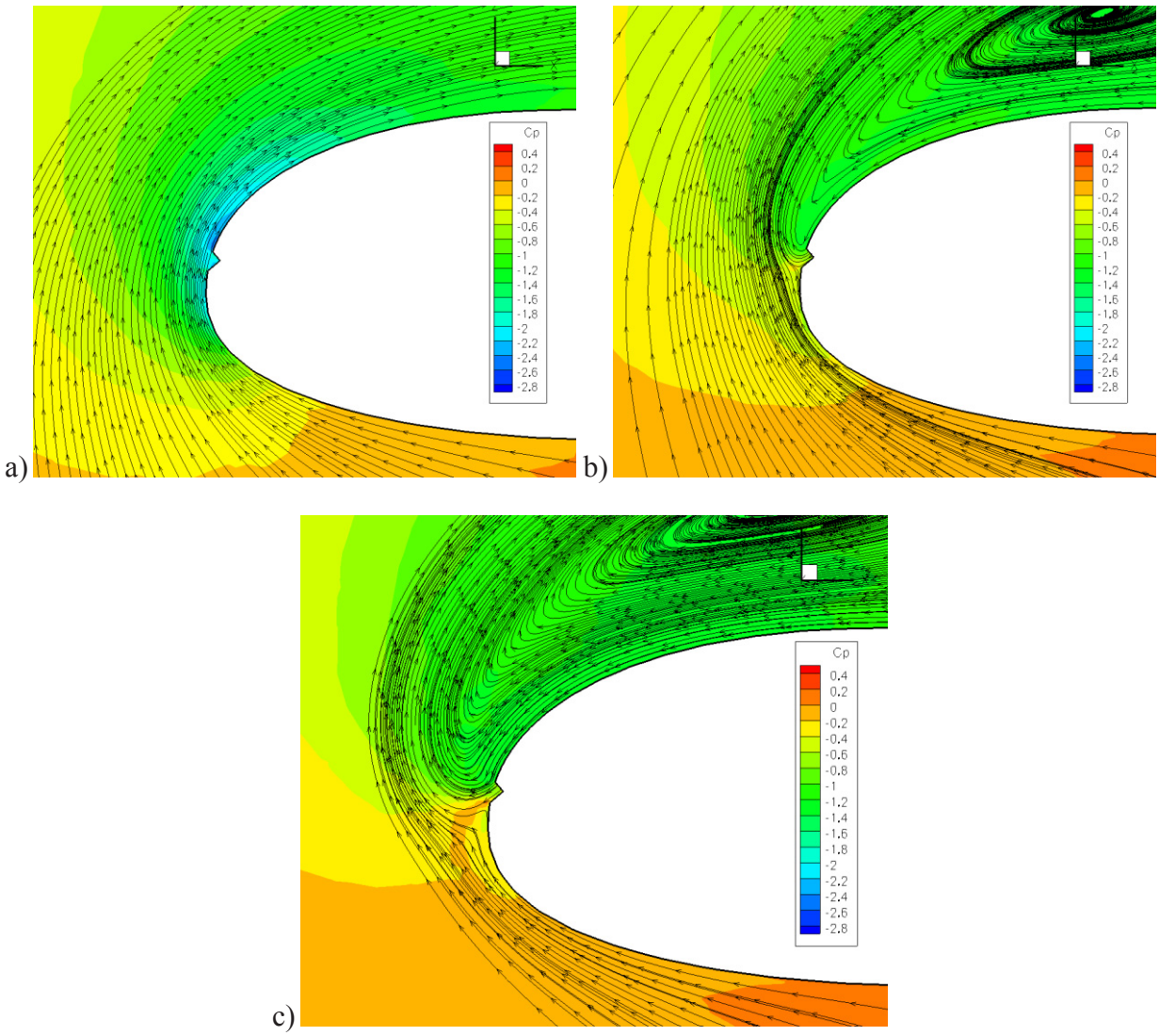

Figure 6-1. The leading-edge blowing: a) no blowing allows clean flow over the lip, b) 100 ft/s blowing causes separation, c) 200 ft/s blowing produces larger scale separation.

As blowing velocity is increased, the core of the separated region is lifted farther off the surface. Also, as blowing velocity is increased, the effect on the vehicle pitching moment is increased, but with diminishing returns. The 50-ft/sec blowing velocity reduced the no blowing configuration pitching moment by more than a third, 100-ft/sec blowing reducing it by half, and 200-ft/sec blowing reducing the no-blowing pitching moment by two-thirds. An

interesting observation is that the difference in pitching moment between full (360 deg) circumferential blowing and windward blowing (front 180 deg of duct circumference) was minimal, implying that the majority of the effect on the flow is occurring at the windward lip. Blowing over the leeward half alone produced negligible effect.

6.1.2 Coandă Trailing Edge Surface Analysis

A trailing edge geometry, as seen in Figure 6-2, was developed for a 0.03" slot width and Coandă surface to match the SJA design developed during bench tests. In initial steady-state analyses, the jet velocity was imposed at the slot exit plane, i.e., the internal slot geometry was not modeled. In the detailed unsteady synthetic jet cases, the internal orifice geometry was modeled with the sinusoidal velocity boundary condition applied at the beginning of the orifice neck instead of the exit. Steady blowing over the windward trailing edge at 200 ft/sec resulted in a normal force and decreased the pitching moment. Although the expansion of the stream-tube resulted in an expected loss of thrust, power required by the fan also decreased.

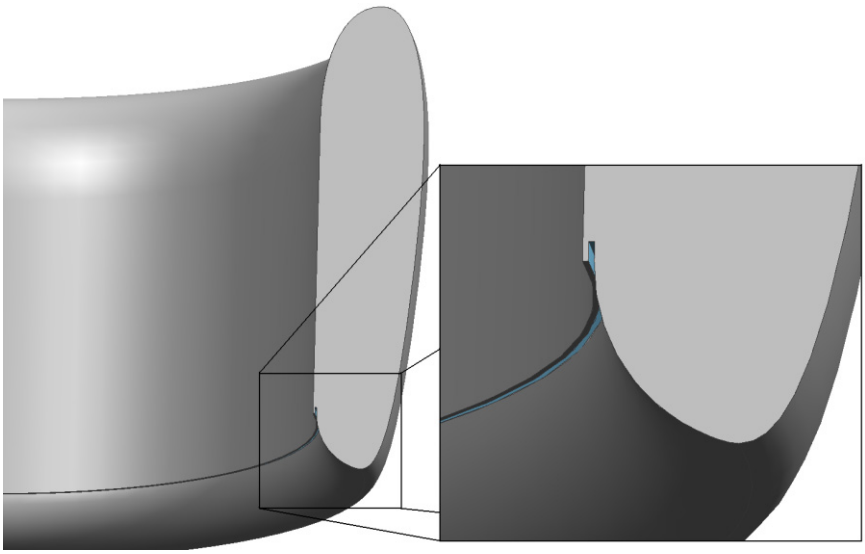

Figure 6-2. Coandă trailing edge geometry with 0.03" jet width and Coandă surface.

Jet velocity was modeled as a time varying sinusoidal function. The 2400-Hz, ±200-ft/sec normal sinusoidal velocity boundary condition (values taken

from bench test performance) was modeled over 100 computational time steps. It was also determined that little difference in pitching moment was obtained between blowing over half of the trailing-edge circumference and a quarter of the trailing-edge circumference, centered about the windward edge. For this reason, many of the analyses had been conducted for the quarter blowing geometry. For efficiency sake, if implemented in a flight vehicle, it would be wise to only actuate the jets toward the direction of the oncoming wind for most effective use of the flow control.

Initial unsteady results exhibited a region of significant flow separation on the Coandă surface. The thin wall between the jet throat and the duct flow had square corners. It was determined that the sharp corner was making it difficult to attain attachment on the Coandă surface, so the thin wall geometry was modified to round the corner closest to the duct flow. The filleting of the corner did not affect the flow when the jets were turned off; it separated off of the corner and proceeded straight out of the duct without turning. This behavior can be seen in Figure 6-3. In Figure 6-4, analysis of the modified geometry shows the flow remaining attached along the Coandă surface curvature when the synthetic jets are actuated.

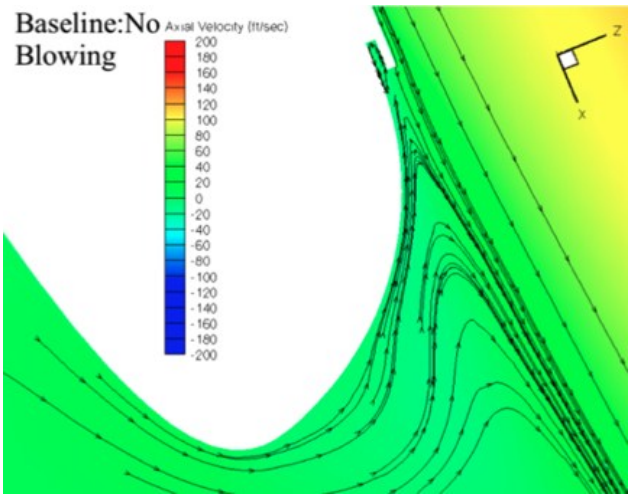

Figure 6-3. Coandă trailing edge flow without blowing passes straight out of duct without turning.

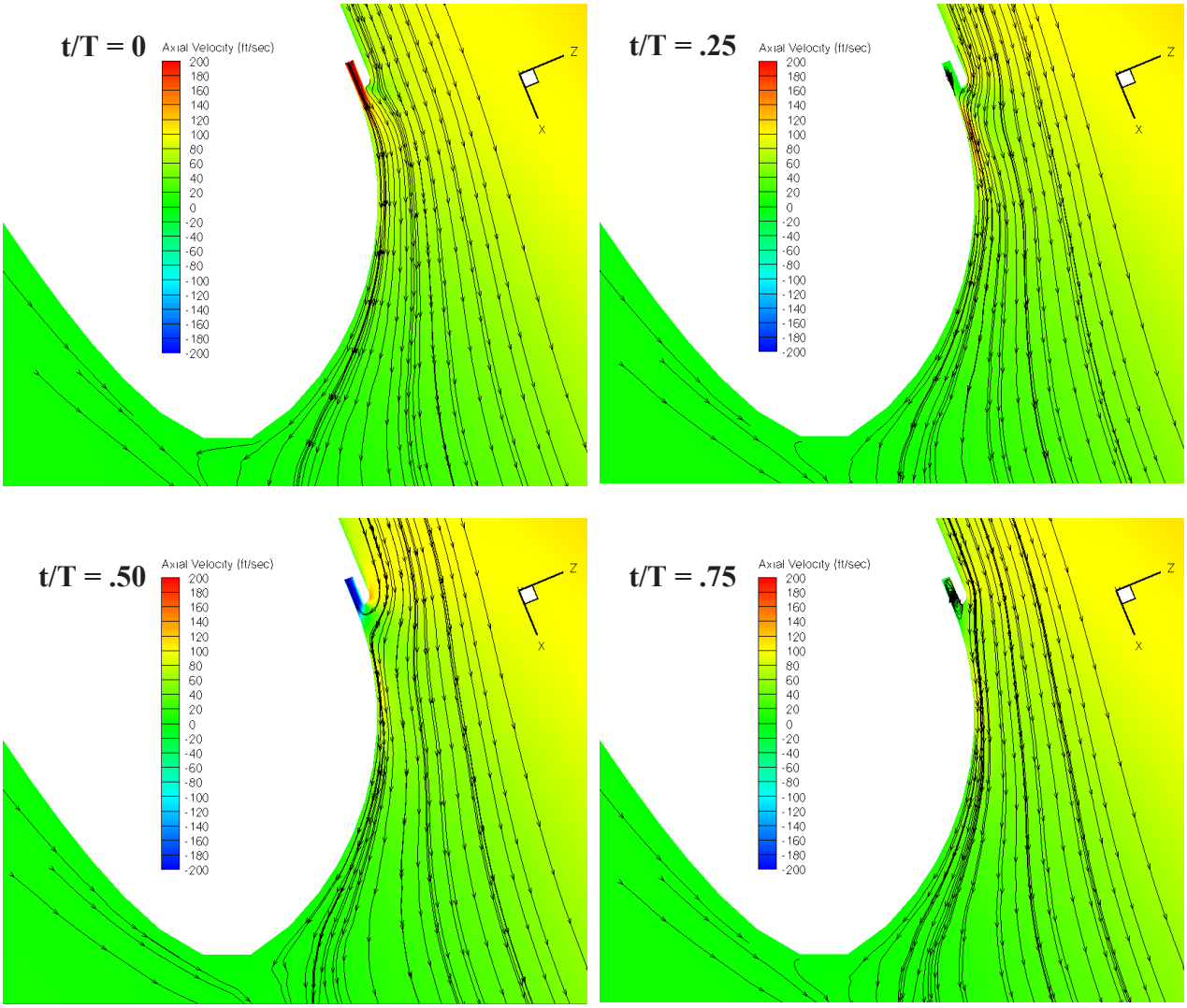

Figure 6-4: Unsteady CFD solution for synthetic jet trailing edge Coandă flow control.

The red color shown in the plots located in the jet orifice corresponds to the outstroke of the synthetic jet (t/T = 0) and the blue denotes the in-stroke or suction phase of the synthetic jet (t/T = 50). The slug of flow that is pushed out during one cycle of the synthetic jet can be observed in subsequent frames (the warm colors moving down the Coandă surface), and is still observable at t/T = 75 close to the time of the next outstroke. With flow remaining attached to the Coandă surface, the streamtube is expanded and turned, with a corresponding normal force and reduction in pitching moment. The rounded corner design was chosen for the wind tunnel experiments. The CFD analysis

was helpful in refining the flow control geometry before finalizing the design for testing.

6.2 Vehicle Integration of Actuators

One of the challenges in developing the wind tunnel vehicle model was the integration of the piezoelectric diaphragm elements. Three main criteria drove the design of the wind tunnel model SJA installation. These were:

1. Minimize the lateral spacing between SJAs, to more closely approximate a uniform jet along the entire circumference of the duct.
2. Provide consistent clamping loads for each SJA, to improve boundary condition uniformity.
3. Securely but non-permanently install the piezoelectric diaphragms in the model. This is necessary to minimize downtime from any diaphragm failures encountered during the wind tunnel test.

The final concept selected was an axial screw clamp, shown below in Figure 6-5. While it requires slightly more parts than other options, it allows for simple replacement of elements and has excellent adjustability through a single torque input. This approach yielded minimum lateral spacing between SJAs, thereby increasing the jet coverage over the duct circumference. In contrast, for a flight implementation the piezoelectric elements would be directly bonded into the cavity to minimize volume and weight.

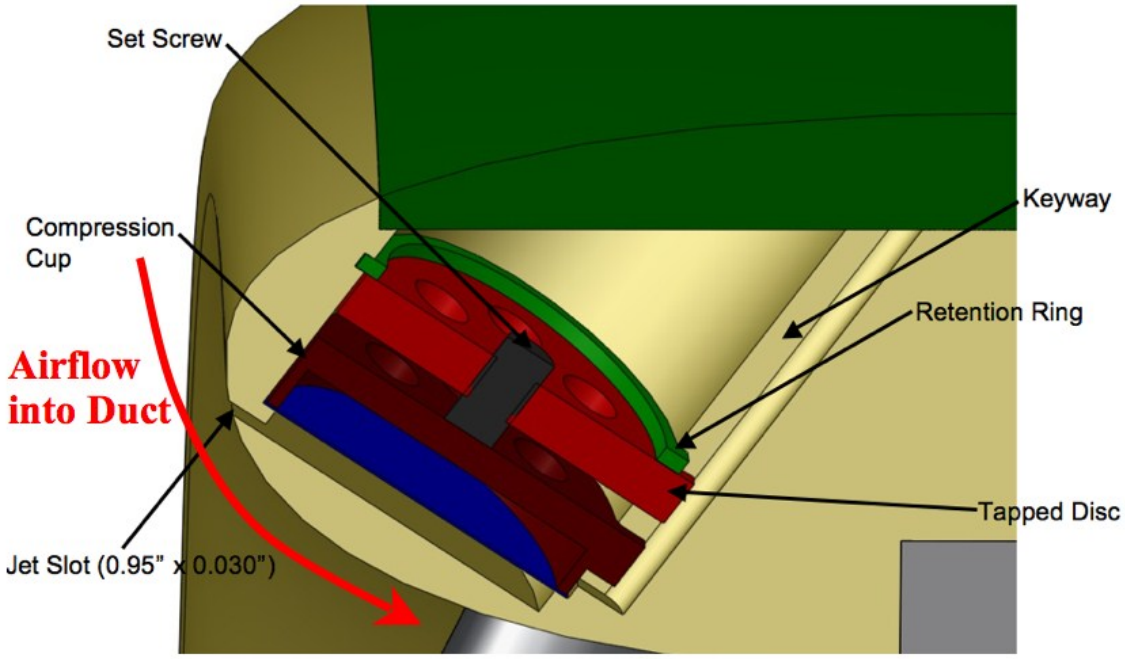

Figure 6-5. Piezoelectric diaphragm mounting for leading edge blowing configuration.

Figure 6-5 shows how the jet and cavity are oriented in the duct lip, with the outside of the duct towards the top of the figure. The flow would proceed into the duct, and the jet orifice is oriented to oppose this flow at roughly 45˚. The internal parts of the wind tunnel model that housed the piezoelectric diaphragms were machined from aluminum, with bored holes to hold the elements. A compression cup pressed down on the edge of the piezoelectric diaphragm to apply a uniform clamping load. A tapped disc with a setscrew through the middle of it was then inserted, with a retention ring finally snapping into place to trap and support the tapped disc. The setscrew was advanced to push on the compression cup and apply the necessary clamping load uniformly to the diaphragm edge. The added benefit of this approach was that a single input (screw torque) was used to tune the boundary condition for the piezoelectric elements. The coverage of the duct lip attained for the leading edge blowing was 75%, as seen in Figure 6-6.

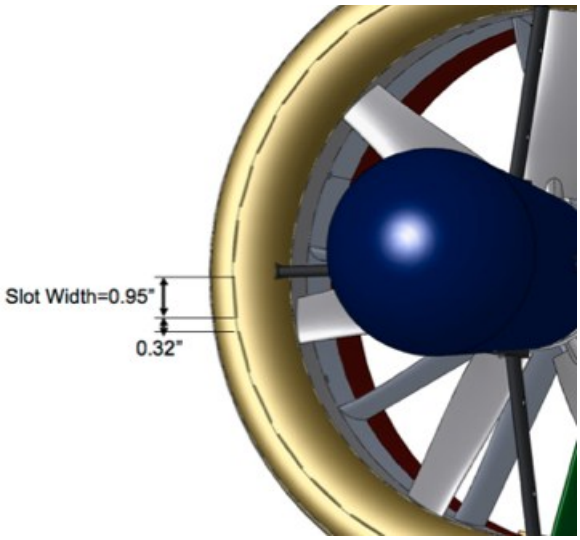

Figure 6-6. Leading edge jet coverage.

The trailing edge actuator integration geometry shown in Figure 6-7 aligns the jet orifice tangentially to the Coandă surface to blow in the same direction as the flow through the duct. To minimize the travel from the cavity to the orifice opening, the jet cavity is oriented such that it is parallel to the duct inside wall (towards the bottom of the figure). The internal features to hold the piezoelectric elements are identical to the leading edge geometry. The jet coverage attained on the Coandă surface is 85%, as seen in Figure 6-8.

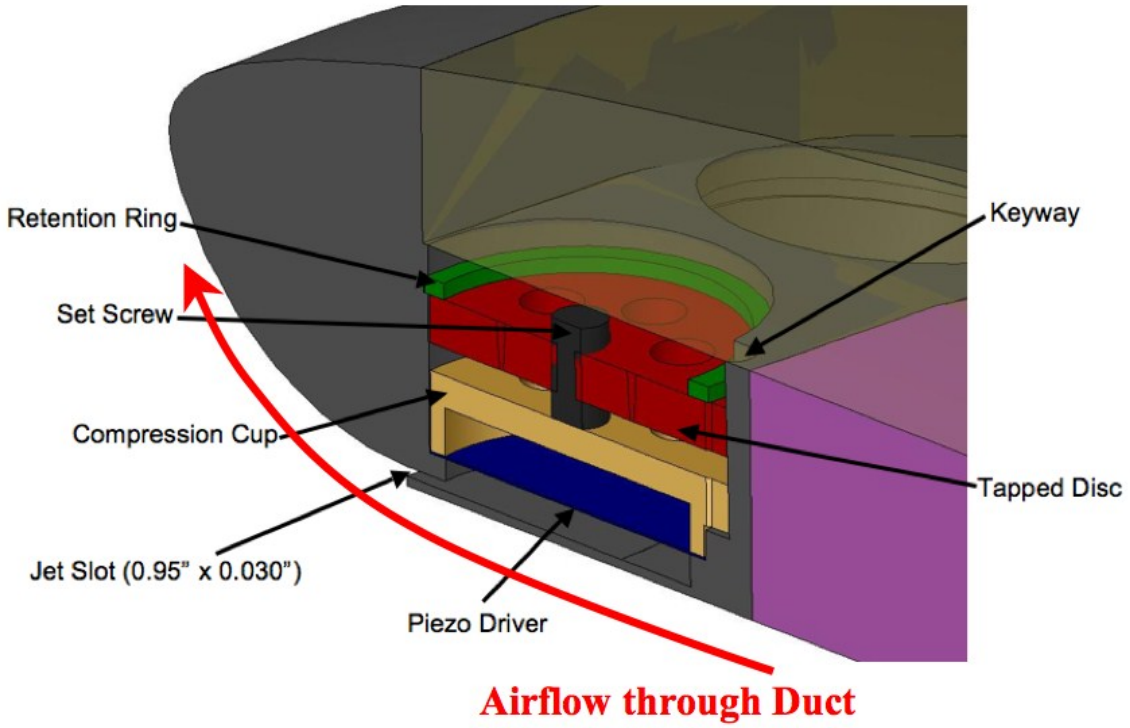

Figure 6-7. Piezoelectric diaphragm mounting for trailing edge blowing configuration.

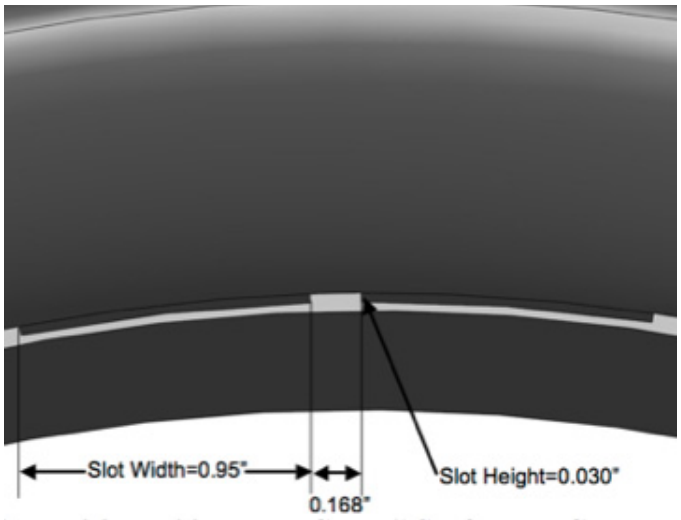

Figure 6-8. Trailing edge Coandă surface jet coverage.

6.3 Flow Visualization of Flow Control Concepts

In addition to collecting data from the force and moment balance, flow visualization was captured via video. This is helpful in communicating the overall phenomenon that is occurring. 'Tufts' (small lightweight strings) were

attached to the model, and self-align themselves with the direction of the local flow. They also visually show whether the localized flow over the tuft is steady or unsteady. When the flow is separated or turbulent the tufts vibrate or flutter rapidly. When the flow stays attached to the surface in question, the tufts will lay down along that surface in the direction of the flow, without much vibration or flutter. A 'tuft wand', a thin pole with one long string attached to the end, was used to interactively probe the flow in the wind tunnel and around the model during testing. Translating the tip of the tuft wand through a region of flow allows for identify how the direction and turbulence change while passing through a specific area.

One of the most successful flow control concepts was the Coandă trailing edge blowing at lower flight speeds and high blowing velocities. Two still frames from the video are shown in Figure 6-9 for a 35 ft/sec free-stream flow, with the vehicle tilted 20 degrees into the wind (the wind tunnel flow is coming from the right in the photograph).

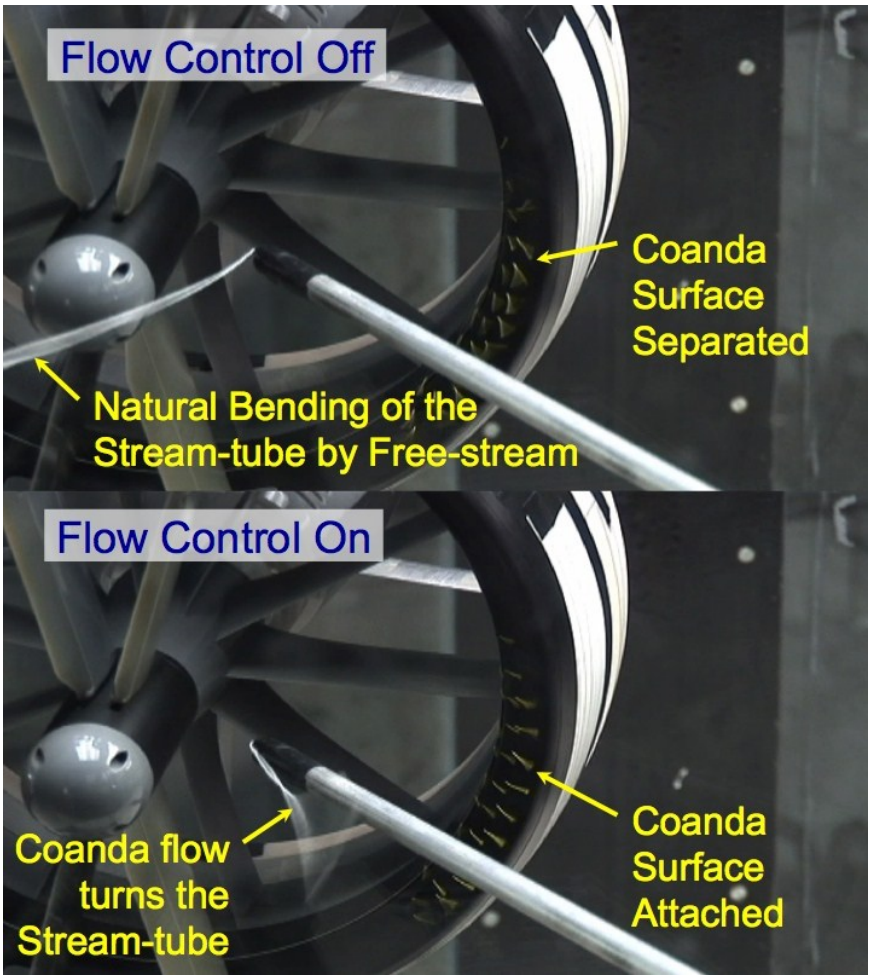

Figure 6-9. Trailing edge flow visualization: (top) No blowing, Coandă trailing edge surface is separated, V_∞= 35 ft/s, α = 70°, c_μ = 0; (bottom) Steady blowing, Coandă surface fully attached, V_∞= 35 ft/s, α = 70°, c_μ = 0.128.

In the top image, the Coandă blowing is turned off and the tufts on the Coandă surface at the duct exit are fluttering, thereby implying separated flow. For that case, the tuft wand in the duct exit flow ("stream tube") is being greatly influenced by the free-stream flow coming from the right, and is bending past the lower centerbody. In the bottom image, the highest steady blowing rate is in effect and the tufts on the Coandă surface are fully attached, implying that the duct flow is staying attached to the flow control surface. This flow causes the whole stream tube exiting the duct to expand and turn upstream, as can be noted from the large angular change in the tuft wand.

Figure 6-10 shows similar visualization for the leading edge concept for a 35 ft/s free-stream flow at an angle of attack of 70 deg (tilted 20 deg into the wind).

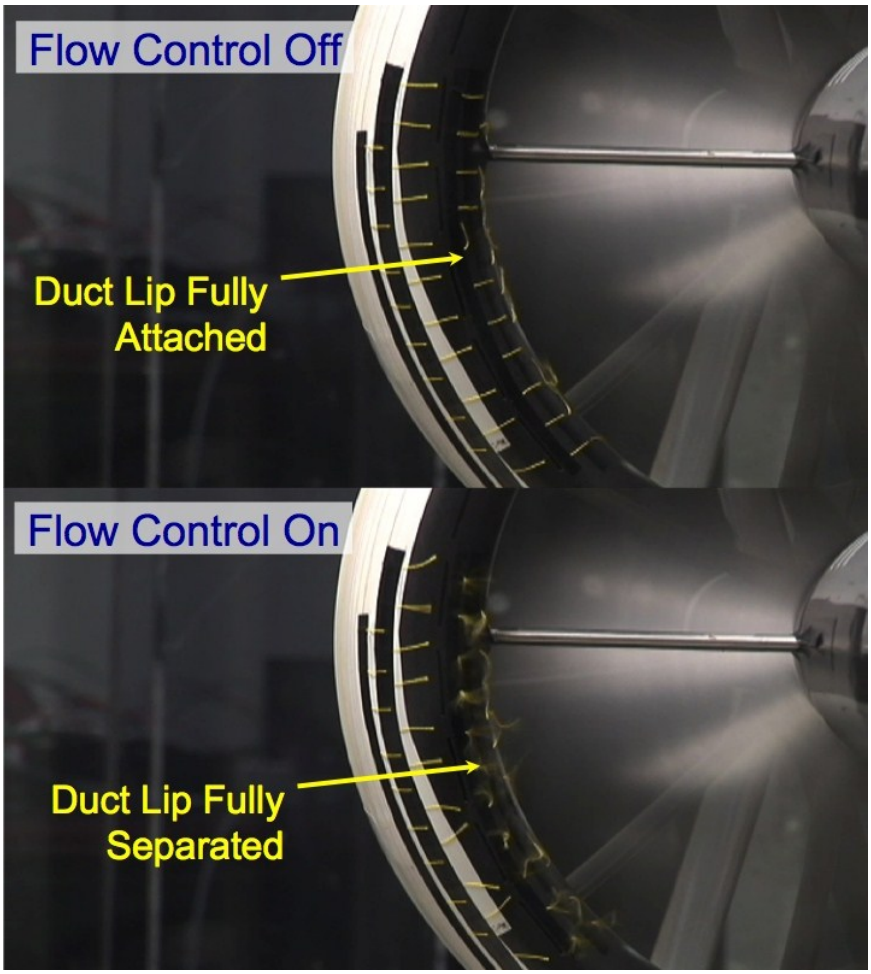

Figure 6-10. Leading edge flow visualization: (top) No blowing, leading edge is attached, V_∞= 35 ft/s, α = 70 deg, c_μ = 0; (bottom) Steady blowing, duct lip fully separated, V_∞= 35 ft/s, α = 70 deg, c_μ = 0.101.

The leading edge flow control has the opposite effect when compared to the trailing edge: when turned off the flow over the lip is fully attached, but when actuated, full flow separation is caused. When the flow is attached, the high speed flow over the duct lip causes a strong suction force that results in thrust and a nose-up pitching moment. When the flow is separated there is a loss of thrust and a decrease in pitching moment. While a loss of thrust sounds

disadvantageous, a cross wind in hover can cause increased vehicle thrust (see Figure 4-12, $\alpha = 90°$), resulting in an unintended upward acceleration. If the vehicle is trying to maintain a fixed altitude, this ability to cancel the added thrust from the cross wind through high bandwidth actuation is desirable.

In summary, the flow visualization results showed that both flow control concepts achieved their desired intent, and can significantly affect the flow. The next section will discuss the specific performance of each of these concepts, and how they affect the vehicle forces and moments.

6.4 Non-dimensional Approach for Ducted Fan Flow Control Data

Ducted fan vehicles present a unique problem for formulating non-dimensional coefficients for blowing momentum and vehicle forces and moments. Because the free-stream dynamic pressure used in most aerodynamic non-dimensional approaches goes to zero when the vehicle is hovering, a different approach is needed for the ducted fan. An approach that can span hover to forward flight is optimal, and therefore must be based on some common parameter to both regimes. The fan tip-speed and the flow induced through the duct are possible candidates. For body-fixed vehicle forces and moments, the form typically used for propeller thrust coefficient will be applied to the normal and axial forces as well as the pitching moment. These are represented in Equations 26 through 28, respectively.

$$C_X = \frac{F_X}{\rho D^4 n^2} \tag{26}$$

$$C_Z = \frac{F_Z}{\rho D^4 n^2} \tag{27}$$

$$C_m = \frac{M_Y}{\rho D^5 n^2} \tag{28}$$

where ρ is the air density, n is the rotational speed of the fan in revolutions per second, and D is the fan diameter. The X and Z force coefficients are comparable to the normal force and thrust coefficients of Chapter 4 (opposite sign), and the pitching moment coefficient can be converted to center of pressure movement if desired. These quantities are left in the body-fixed coordinate frame in this chapter to relate to the flight control values necessary for vehicle trim.

The blowing momentum coefficient typically used for fixed-wing flow control analysis [118] is:

$$c_{\mu} = \frac{\dot{m}_j U_j}{q_{\infty} S} \tag{29}$$

where $\dot{m}_j$ is the jet mass flow, U_j is the jet speed, q_{∞} is the free-stream dynamic pressure, and S is the wing planform area. The problem with this approach is that the free-stream dynamic pressure is zero during hover, resulting in a numerical singularity. Other researchers have used the fan tip speed as the reference velocity in the blowing momentum coefficient for the ducted fan application [18]. While the fan tip speed offers a consistent way to normalize the data, it can be several times higher than the velocity of the induced flow interacting with the flow control jets. To be more comparable to jet momentum coefficients used in other applications, the speed of the flow inside the duct was chosen as a better reference for non-dimensional jet analysis.

The flow induced through a hovering ducted fan can be calculated from momentum theory as noted in [13] (with no duct contraction or expansion) to be:

$$V_{induced} = \sqrt{\frac{T}{\rho A_{disk}}} \tag{30}$$

where T is the thrust, and A_{disk} is the area of the fan. The steady blowing momentum coefficient based upon the dynamic pressure of the induced flow then becomes:

$$c_\mu = \frac{\dot{m}_j U_j}{q_{duct} A_{duct}}, \quad q_{duct} = \frac{1}{2}\rho V_{induced}^{\ 2} \tag{31}$$

where A_{duct} is the projected area of the duct (diameter times chord) to be comparable with the planform area of a wing. Also note that substituting Eq. 30 into Eq. 31 shows that the dynamic pressure in the duct is equivalent to one half of the disk loading (total thrust divided by disk area). This can be explained through ducted fan momentum theory, which states that only one half of the thrust comes from the fan, the other half of the thrust is generated by the duct (for the case with no expansion or contraction aft of the fan).

The synthetic jet oscillatory flow requires special treatment in deriving the equivalent blowing momentum coefficient. Farnsworth et al. [97] have used a blowing momentum coefficient based on the total time-averaged momentum of the outstroke, $\bar{I}_j$, defined as:

$$\bar{I}_j = \frac{1}{\tau}\rho l_j w_j \int_0^\tau u_j^{\ 2}(t)dt \tag{32}$$

where τ is the outstroke time (half the overall period), l_j is the slot length, w_j is the slot width, and u_j is the centerline velocity of the jet, as used in the definition for U_0. Multiplying this value by the total number of jets, n_j, to get the total momentum imparted and dividing by the induced dynamic pressure and reference area yields a comparable blowing momentum coefficient:

$$c_\mu = \frac{n_j \bar{I}_j}{q_{duct} A_{duct}} \tag{33}$$

The velocity ratio, as defined by Eq. 34 and adapted from [66], is also of interest in flow control applications. It is defined relative to the induced velocity through the duct, as this is the velocity representative of the flow on which the control is acting for this application. For the tests performed, the synthetic jets operated in the range of V_R = 0.5 to 1.0, while the steady jets operated in the range of 1.5 to 5.

$$V_R = \frac{U_0}{V_{induced}} \tag{34}$$

6.5 Results and Discussion

Static (hover) tests outside the wind tunnel and wind-on tests in the tunnel were performed to assess the effects of each flow control concept on the vehicle forces and moments. The following sections detail the findings and discuss the results.

6.5.1 Static Test Results

Static tests (no wind tunnel flow) representative of hover conditions were performed for both the leading edge and trailing edge flow control configurations. While the concepts were designed to affect the vehicle horizontal flight at high angles of attack, the static capability of these flow control concepts was still of interest. The trailing edge Coandă flow control caused the duct flow to turn and thereby created normal force. The normal force coefficient data versus jet momentum coefficient are shown in Figure 6-11. Values are presented in the form of differences from the base vehicle aerodynamics since the jet blowing would be used as a control input to affect

vehicle flight. For the case of normal force, the baseline value without blowing is very close to zero.

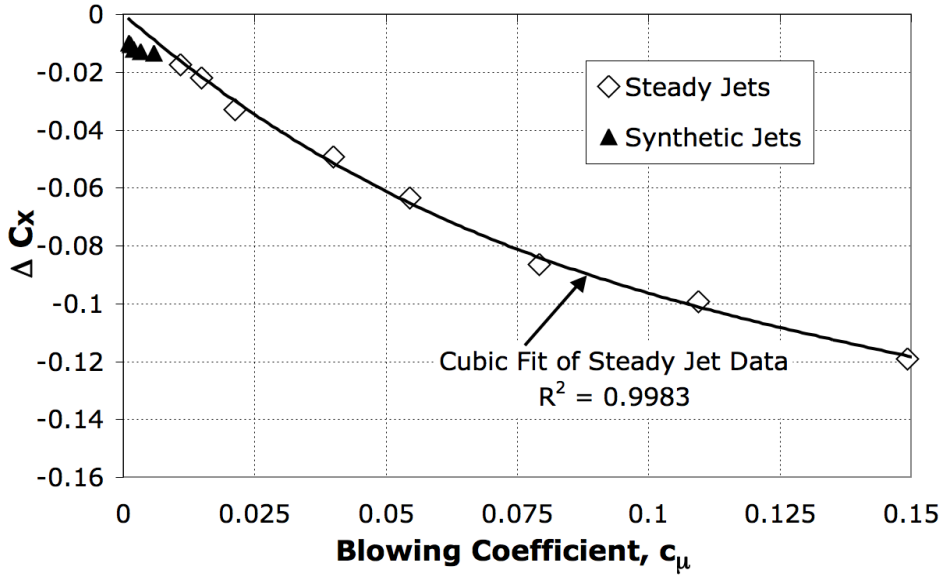

Figure 6-11. Static, change in C_X vs. blowing coefficient, trailing edge flow control.

Because the steady blowing was powered by a separate supply of high-pressure air, higher blowing coefficient levels were explored to assess the full capability of the flow control concepts. Figure 6-11 shows that the synthetic jets were not able to attain the same level of blowing coefficient, but do follow the same trend in force generation. A cubic polynomial curve fit captures the majority of the trend in the steady jet data, and the synthetic jet data exceeds this trend by roughly the magnitude of the uncertainty in this measurement (0.01). Therefore, it is likely that for a given blowing coefficient value synthetic jets are more effective, but because of the uncertainty in this data it is inconclusive.

Figure 6-12 shows the effect of trailing edge blowing on pitching moment coefficient, the primary objective of the concept. Both steady blowing and synthetic jet blowing produce the intended behavior, with the steady blowing reaching larger values than the synthetic jets due to higher blowing coefficient levels. However, comparing the trends in the data, the synthetic jet effectiveness exceeds the cubic polynomial trend line for steady blowing for a

fixed blowing coefficient. The uncertainty for this measurement is 0.004, which cannot account for this difference, thereby supporting the claim that synthetic jets of similar blowing coefficient are more effective.

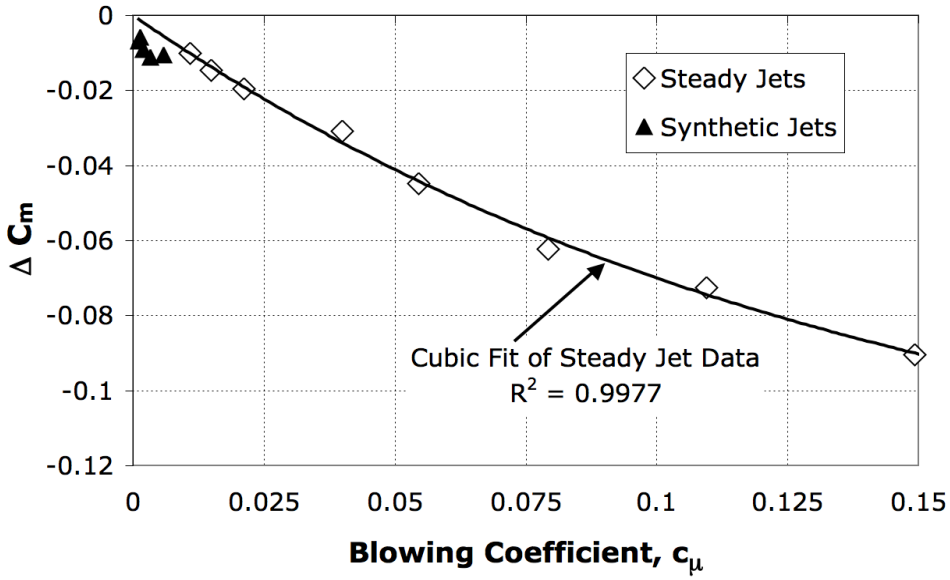

Figure 6-12. Static, change in C_m vs. blowing coefficient, trailing edge flow control.

Because the turning of the flow at the Coandă surface is expanding the stream-tube exiting the duct, it has an effect that is similar to an expansion or diffuser section in the duct. A flow expansion is effectively the same as a larger duct exit diameter, which would reduce the speed of the exit flow for a constant thrust level. This can be seen from the following momentum theory equations for hover, adapted from Pereira [13], where σ_d is the duct expansion ratio.

$$V_{exit} = V_{induced} / \sigma_d \tag{35}$$

The equation for thrust is based on the mass flow times the exit velocity, as this represents the amount of acceleration imparted to the air starting from rest:

$$T = \dot{m}V_{exit} = \rho A_{exit} V_{exit}^{2} \tag{36}$$

Solving the thrust equation for the exit velocity yields:

$$V_{exit} = \sqrt{\frac{T}{\rho A_{disk} \sigma_d}} \tag{37}$$

The ideal power required is a function of the mass flow times the exit velocity squared:

$$P = \frac{1}{2}\dot{m}V_{exit}^{2} = \frac{1}{2}\rho A_{exit} V_{exit}^{3} = \frac{T^{3/2}}{\sqrt{4\rho A_{disk}\sigma_d}} \tag{38}$$

These equations show several important features regarding the effects of flow expansion. First, the exit flow velocity relationship (Eq. 37) shows that for constant thrust, an increase in expansion ratio will decrease the exit velocity. While this happens, the mass flow is increasing, so the flow through the fixed diameter fan must be greater than the case without flow expansion. Conversely, if the flow induced through the fan is held constant (as we would expect here for a fixed RPM input for the same fan), the thrust decreases as the expansion ratio is increased. Second, the power equation shows an inverse dependence on the square root of the expansion ratio. This means that for the same thrust output, less power is required for larger expansion ratios.

These two principles predict that as the duct exit flow is expanded using the Coandă surface flow control, there is an expected decrease in thrust and power required. These findings are verified in Figure 6-13 and Figure 6-14. Figure 6-13 shows a significant variation (greater than the 0.011 uncertainty level for this channel) in thrust force due to trailing edge blowing, with all cases causing a net reduction in thrust.

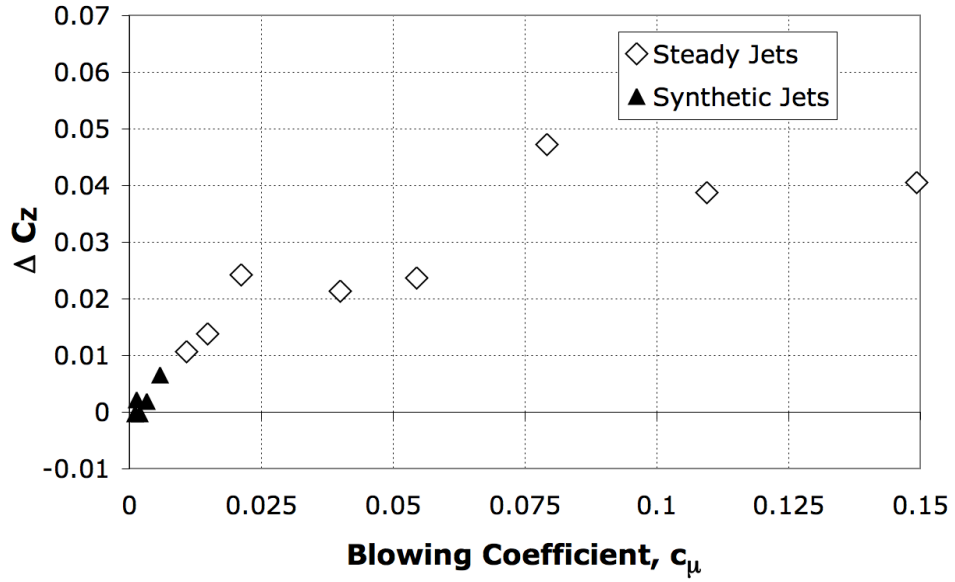

Figure 6-13. Static, change in C_Z vs. blowing coefficient, trailing edge flow control.

Similarly, Figure 6-14 shows a decrease in power required when trailing edge blowing is employed. Again the variation is greater than the uncertainty bounds of 0.018 for this data.

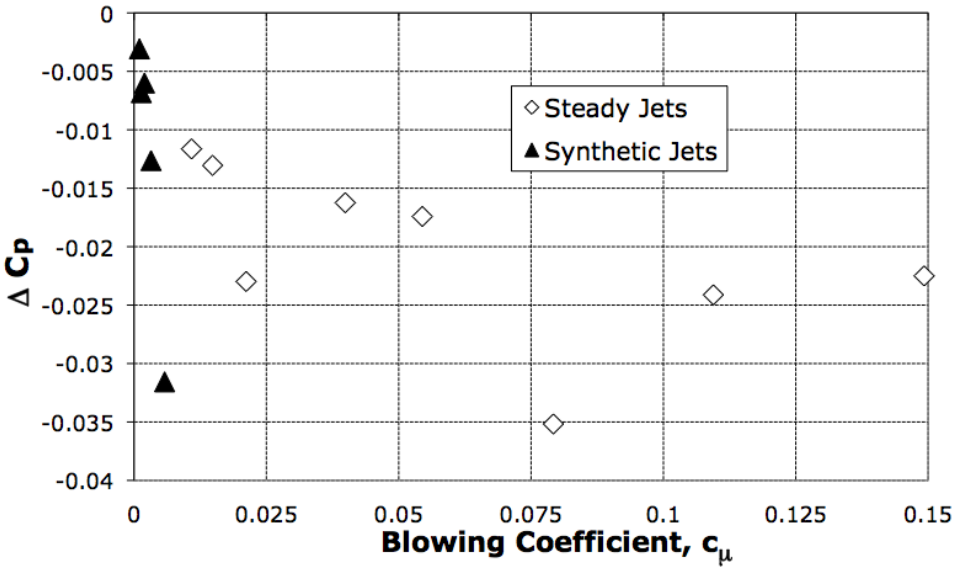

Figure 6-14. Static, change in C_P vs. blowing coefficient, trailing edge flow control.

Perhaps the most important question is that when the thrust and power are decreasing during flow control, what is the effect on system efficiency? For this assessment, Figure 6-15 shows the Figure of Merit plotted versus blowing momentum coefficient.

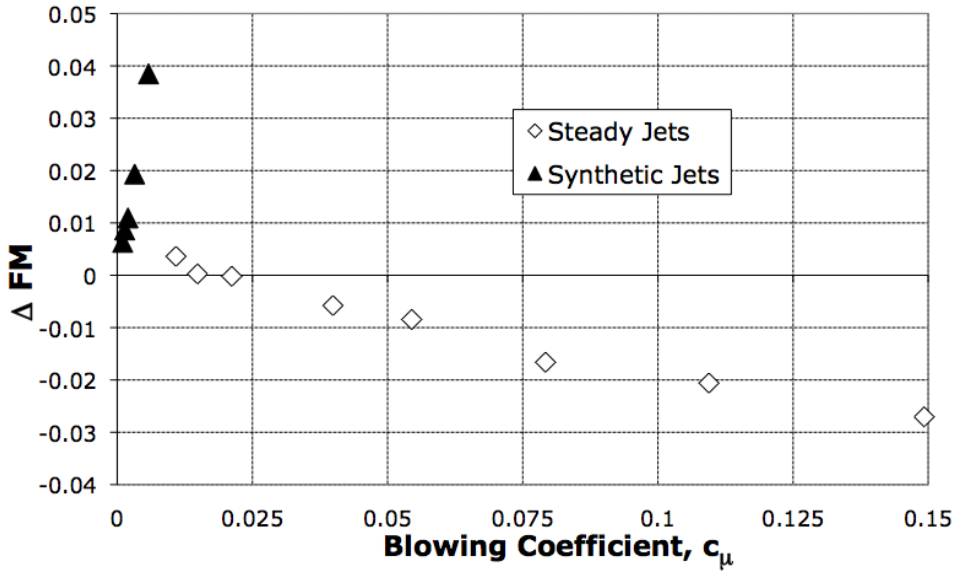

Figure 6-15. Static, change in FM vs. blowing coefficient, trailing edge flow control.

While it may appear that the synthetic jets and steady jets have two different trends in the figure, it is important to point out that the uncertainty for FM is 0.047. The uncertainty in this channel is higher than the other quantities presented because the FM uncertainty is a composite of multiple error sources (thrust and power measurements). Because of this, the trends in the static FM data cannot be considered significant. One encouraging observation is that the data, if considered as one set, are centered about zero, suggesting that this mechanism for vehicle control may have minimal effect on system efficiency.

The leading edge flow control was tested statically as well, but produced negligible effects. This is attributed to the fact that the duct lip was designed for smooth and efficient flow in hover. Effectively, the flow is too stable in hover for the synthetic or steady blowing to cause significant separation on the duct lip. This finding however does not imply that leading edge flow control will be ineffective for the target application of forward flight at high angles of attack.

6.5.2 Trailing Edge Flow Control in Forward Flight

Before discussing the changes in force and moment coefficients due to flow control for flight conditions, it is important to gain a reference point of the underlying vehicle aerodynamics. The baseline vehicle coefficient data for an angle of attack sweep at 35 ft/s is shown in Figure 6-16. The forces and moments reported in the body-fixed coordinate system described in Figure 1-3.

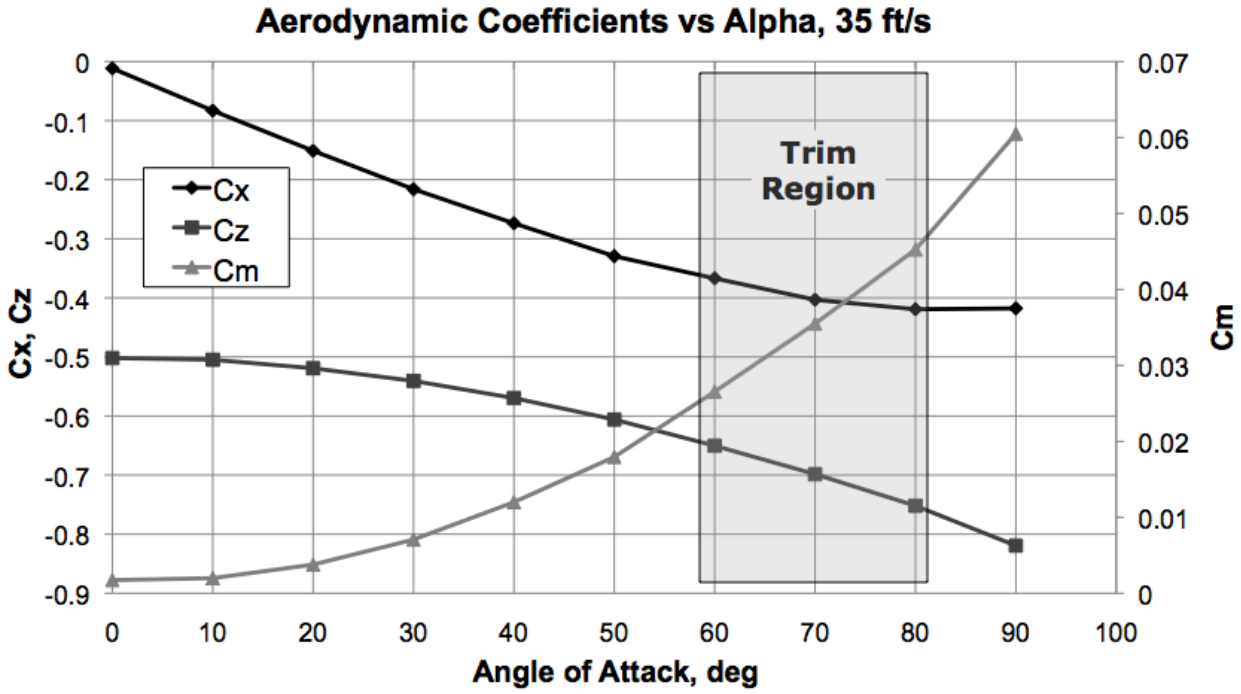

Figure 6-16. Baseline vehicle aerodynamic data with trim region.

Figure 6-16 shows the range of C_x, C_z, and C_m for the vehicle at a transition speed. The normal force and pitching moment are essentially zero at 0° angle of attack (nose directly into the wind), and increase in magnitude as angle of attack increases. The axial force (thrust) is at its lowest magnitude at 0° angle of attack (a pure axial climb orientation) and increases as the angle of attack increases. The ducted fan vehicle tilts into the wind to fly forward, and for this flight speed of 35 ft/s it would pitch forward roughly 20° (an angle of attack of 70°). Typically, control vanes in the duct exit flow would be used to counter the nose-up pitching moment to trim the vehicle (attain equilibrium). The 35 ft/s flight speed represents the transition region between hover and high-speed

flight that usually requires the highest control vane deflections. Therefore, assuming a center of mass near the duct lip, it is a goal to attain a -0.035 change in pitching moment coefficient at this flight condition to accomplish vehicle trim solely through flow control actuation. For reference, the trim condition for 17 ft/s is represented approximately by an 80° angle of attack and requires -0.034 change in pitching moment from control actuation.

The power and FM results for the same configuration and test run are shown in Figure 6-17. The power coefficient only varies a few percent over the range of angles of attack, but the FM value is roughly doubled over this same range. This is because the FM is greatly affected by the thrust variation caused by angle of attack changes. For the nominal trim condition of 70°, the power coefficient is roughly 0.425 and the FM is approximately 0.80.

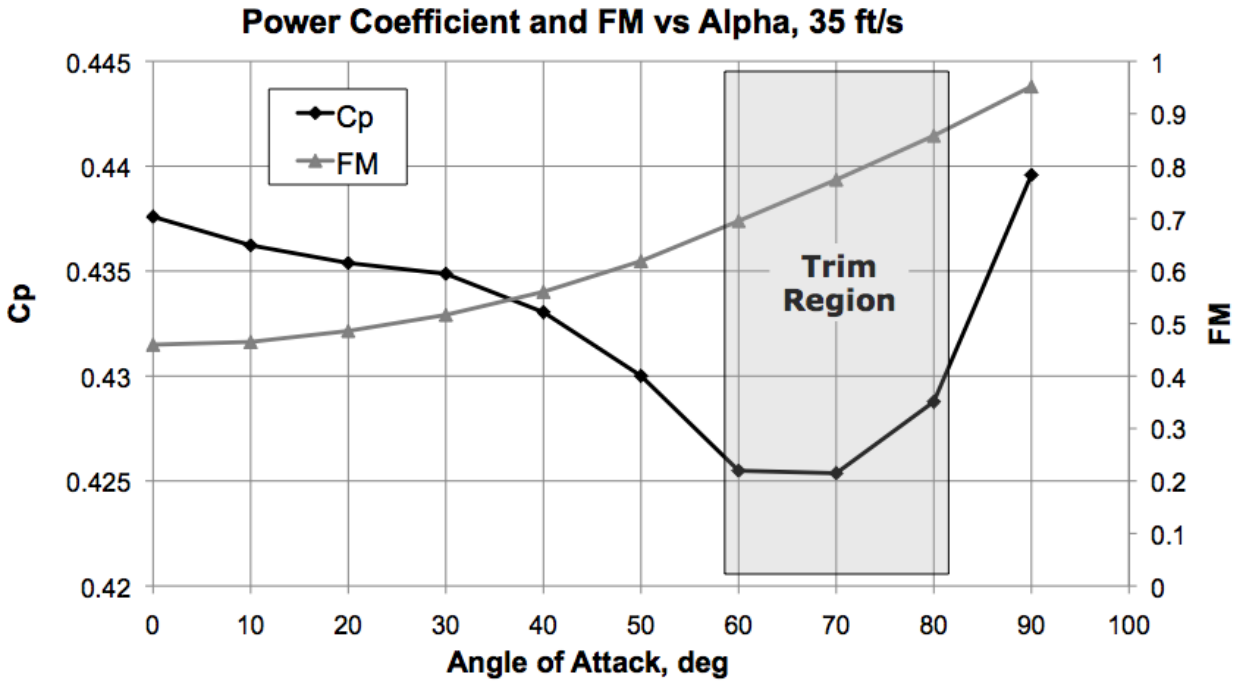

Figure 6-17. Baseline vehicle power and fm data with trim region.

The wind tunnel test results for 17 ft/s and 35 ft/s (10 and 20 knots) are shown in Figure 6-18 through Figure 6-19 for the Coandă trailing edge flow control design.

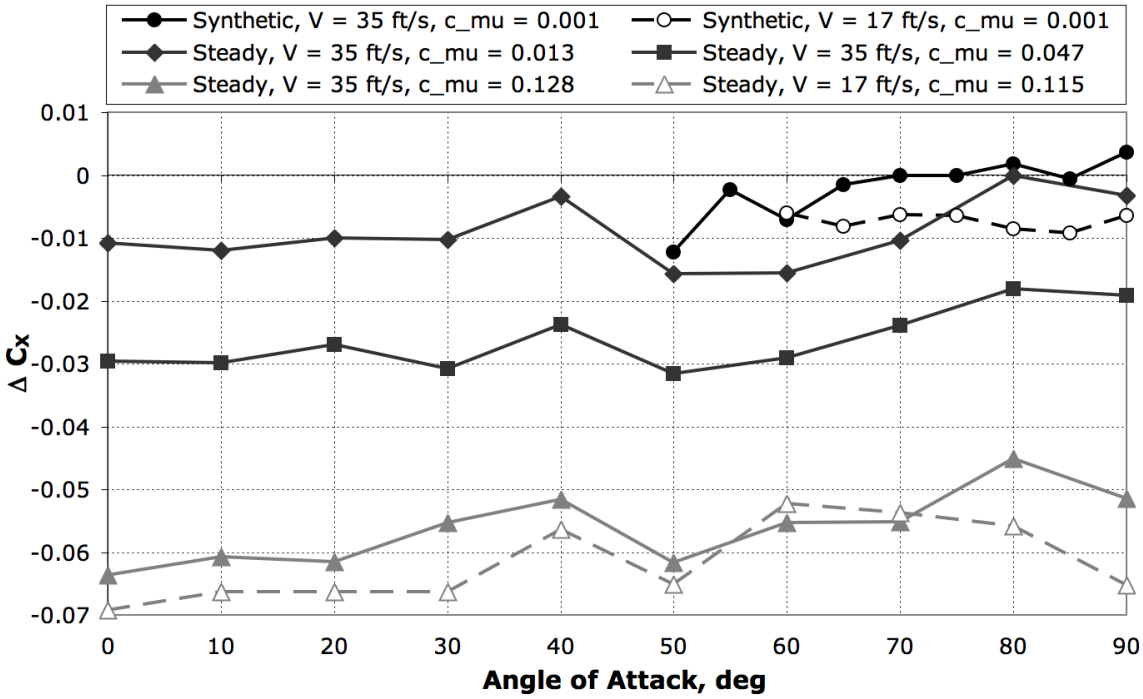

Figure 6-18. Forward flight, change in C_X vs. angle of attack, trailing edge flow control.

In Figure 6-18, the normal force results show the expected progression in magnitude of the steady blowing results, as blowing coefficient increases. The flow control also seems to be slightly more effective at slower flight conditions (17 ft/s), and this would be supported by the fact that the static results for comparable blowing coefficient were even larger magnitude (~0.1). This suggests that the effectiveness of the trailing edge flow control may diminish at high flight speeds. The same trend is observed in the synthetic jets, although the magnitude of the effect is much smaller due to the lower blowing coefficients attained.

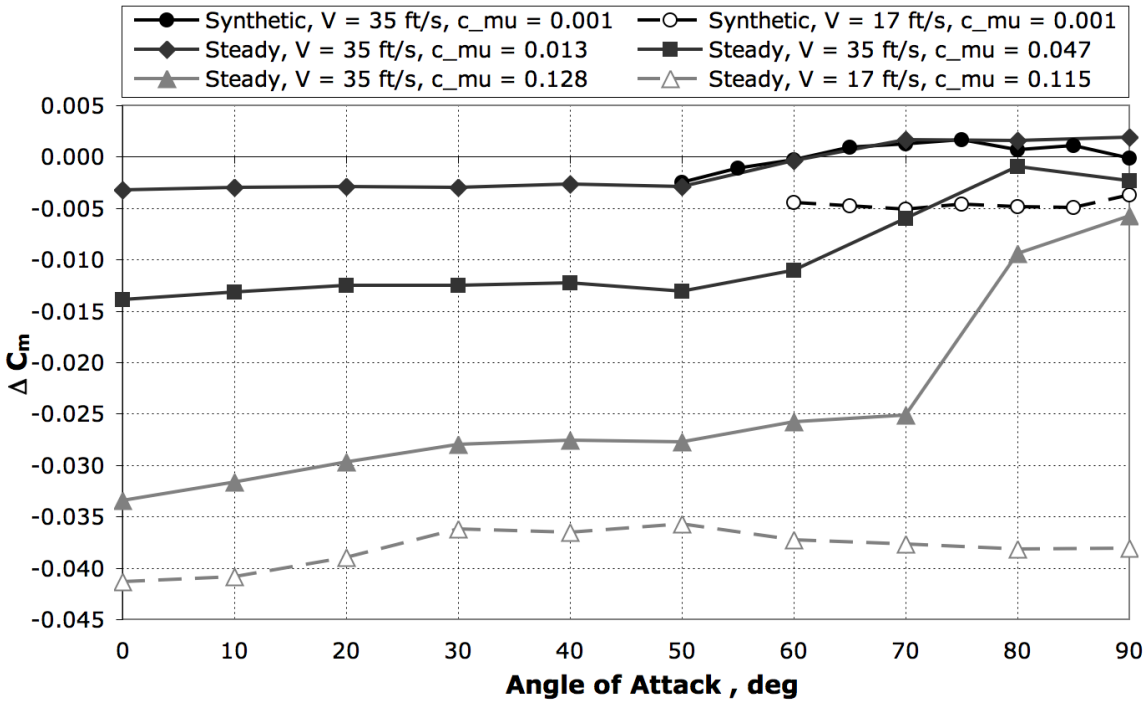

Figure 6-19. Forward flight, change in C_m vs. angle of attack, trailing edge flow control.

Figure 6-19 shows the trailing edge flow control has a significant effect on vehicle pitching moment. For reference, the base vehicle value of C_m is on the order of 0.035 for the trim angle of attack of 70° at 35 ft/s, and 0.034 for a trim angle of attack of 80° at 17 ft/s. The highest level of trailing edge steady blowing observed in the figure can provide 100% of the necessary moment for 17 ft/s flight, and can account for a large portion of it for 35 ft/s (0.025 compared with 0.035, roughly 70%). The required control moment to trim the vehicle can be reduced if the center of gravity (CG) is moved farther above the duct lip. For reference, if the center of mass were raised 0.5" in the negative z-direction of the body-fixed coordinate system (for a 12" diameter fan size), it would change the required pitching moment coefficient for trim to 0.019. In addition, the CG change would increase the moment arm from the CG to the Coandă surface, thereby increasing the control moment by a factor of 8%. This approach would allow for this control actuation scheme to provide 100% of the moment required to trim the vehicle. It should be noted that this is a very high

level of blowing and the synthetic jets are much less effective because of the substantially lower blowing coefficient levels.

The steady and synthetic jet flow control is more effective at a lower speed of forward flight, and the steady blowing results show a sudden decrease in effectiveness at high angles of attack (close to trim region). This is due to the fact that the Coandă flow control is trying to turn the ducted fan flow in the opposite direction to the free-stream. As the free-stream flow becomes faster, it is more difficult to keep the Coandă flow attached. The conclusion is that the Coandă flow control is more effective at lower angles of attack where the turned flow is not directly competing with the free-stream.

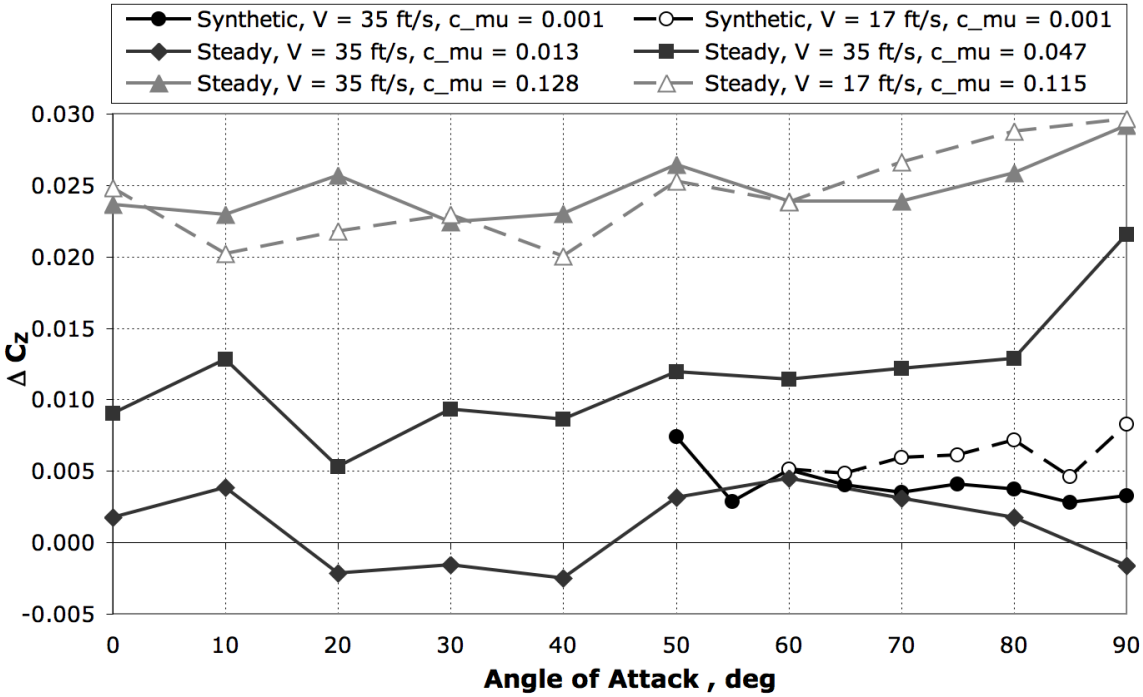

Figure 6-20. Forward flight, change in C_Z vs. angle of attack, trailing edge flow control.

In Figure 6-20, the axial force coefficient results show that the flow expansion created by the trailing edge blowing results in some thrust loss for forward flight, just as it did in hover. One aspect to note is that the normal force produced by the flow control is between two to three times the amount of thrust lost. If compared to a traditional control surface, this would be similar to the lift-to-drag ratio. However, this thrust loss effect from the Coandă flow

differs from a control surface because it does not correspond to a velocity deficit in the downstream wake due to drag. The secondary effect of control surface deflections on an aircraft system (primary effect is control force or moment) is a parasitic drag that decreases system efficiency. Control surface drag requires more power from the propulsion system to maintain a specific flight speed. Here, the effect of the flow control must be evaluated to identify how it affects the power required and efficiency of the system. The power coefficient versus angle of attack is shown in Figure 6-21.

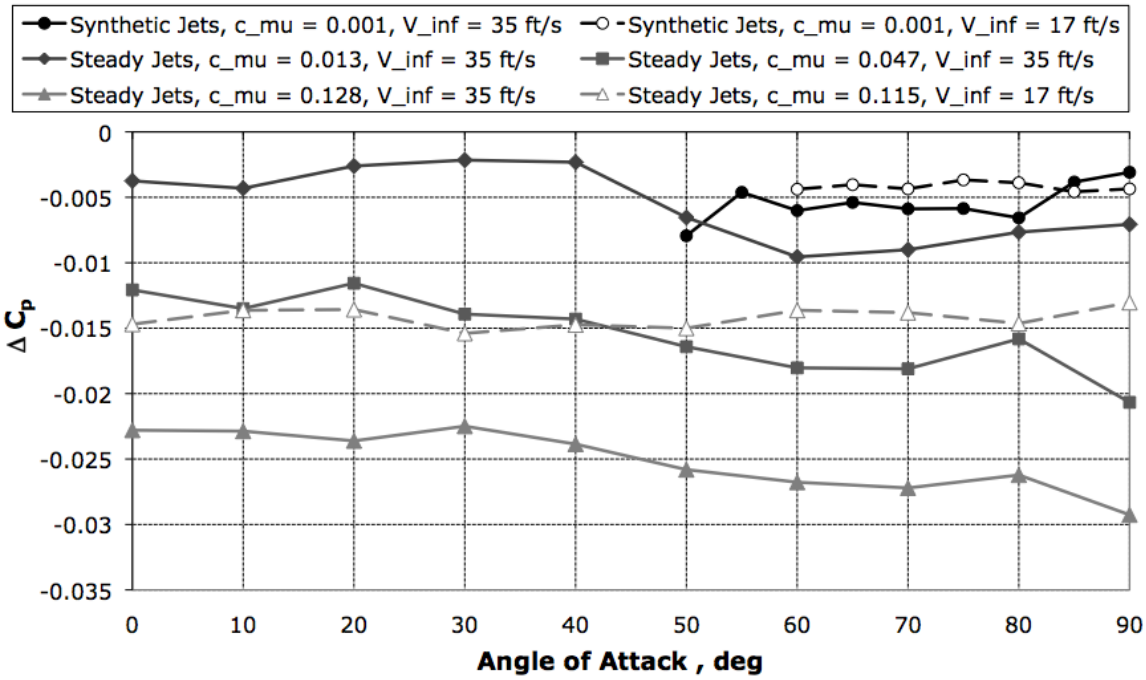

Figure 6-21. Forward flight, change in C_p vs. angle of attack, trailing edge flow control.

For every case of blowing (steady and unsteady) the power required decreased when blowing was activated. The benefit of this cannot be assessed in isolation, however. The overall efficiency of the system can be better assessed by looking at the trends in Figure of Merit, shown in Figure 6-22.

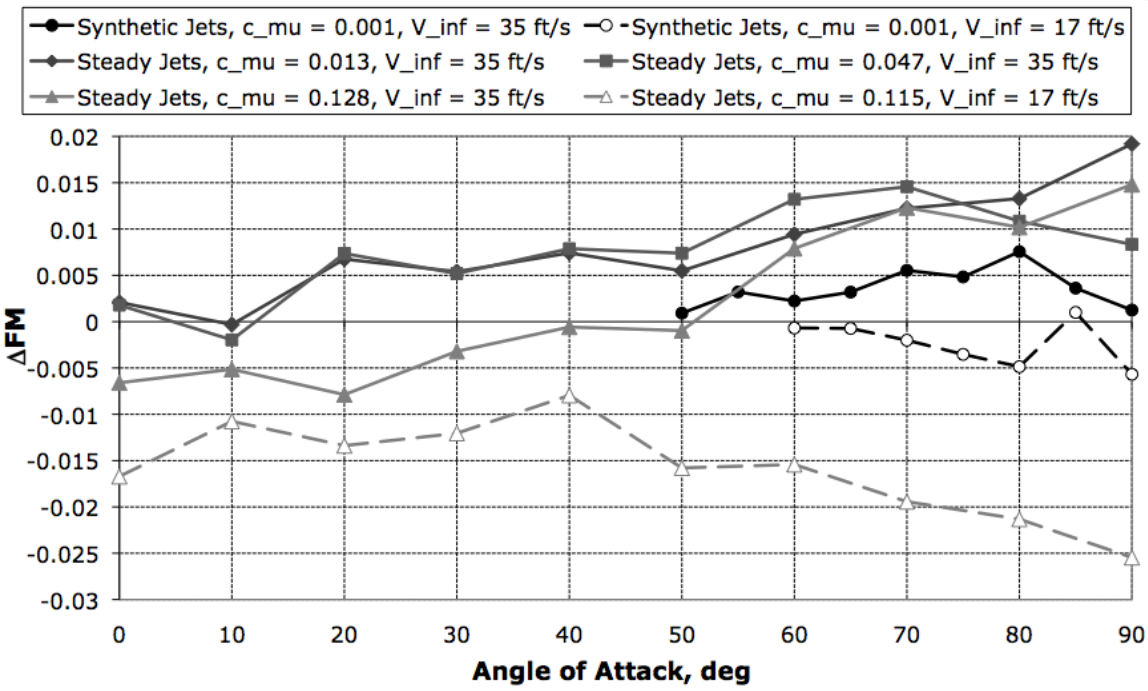

Figure 6-22. Forward flight, change in FM vs. angle of attack, trailing edge flow control.

The forward flight FM data is similar to the static data in that it is centered on zero and does not exceed the bounds on uncertainty in FM. This suggests that this trailing edge flow control scheme has little impact on vehicle efficiency, which is an excellent finding. This is in stark contrast to most control surfaces that have a parasitic effect on vehicle performance.

6.5.3 Leading Edge Flow Control in Forward Flight

While the leading edge flow control showed little effect for the hover condition, it was effective at producing separation on the duct lip for high angle of attack forward flight, as seen in the flow visualization section. The leading edge concept does not create a normal force like the trailing edge blowing, but does produce results in axial force and pitching moment as seen in Figure 6-23 and Figure 6-24.

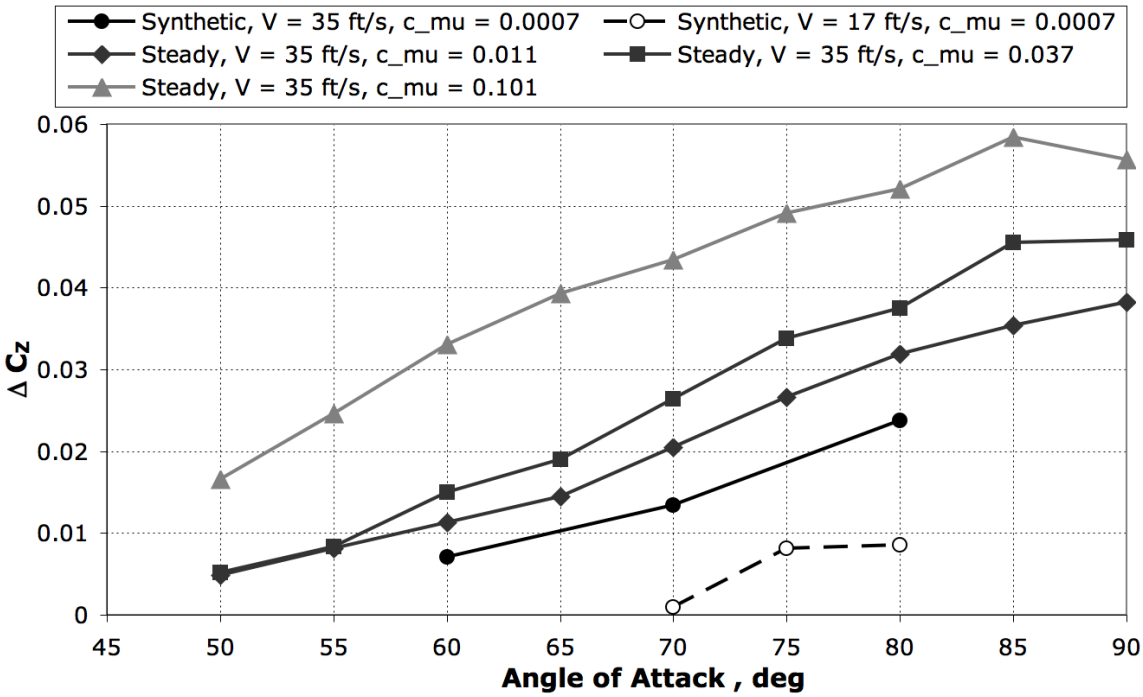

Figure 6-23. Forward flight, change in C_Z vs. angle of attack, leading edge flow control.

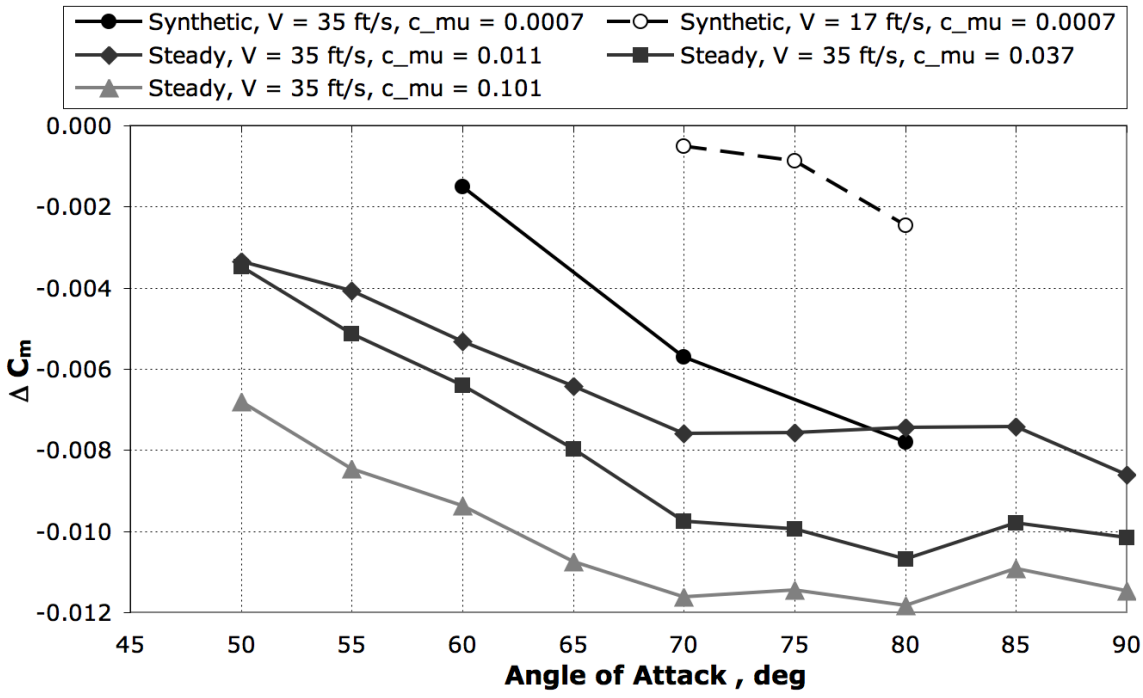

Figure 6-24. Forward flight, change in C_m vs. angle of attack, leading edge flow control.

While the trailing edge flow control concept corresponded to a control moment being created by generating a normal force, the leading edge concept shows a strong correlation between duct lip thrust and pitching moment. The

separation caused on the lip results in thrust loss (Figure 6-23) and a decrease in pitching moment (Figure 6-24). The magnitudes of the changes to pitching moment are roughly half of those seen in the steady trailing edge flow control. However, the magnitudes increase with angle of attack whereas the trailing edge concept lost effectiveness at these conditions. Higher angles of attack are where the pitching moment is largest, and represent the area of greatest need for wind gust rejection. The effects of the leading edge flow control are smaller than the value needed to completely trim the vehicle, roughly accounting for 33% of the needed -0.035 pitching moment coefficient to attain trim. Therefore, an implementation based on this concept could only augment control and not be a complete replacement for flight control surfaces.

In comparison to the trailing edge tests, the synthetic jets were much more effective in the leading edge configuration, but particularly at 35 ft/s instead of 17 ft/s. Even though the blowing coefficient for the synthetic jets is an order of magnitude lower than the steady blowing, the effects on the overall vehicle forces and moments at 35 ft/s free-stream are comparable. This suggests that duct lip separation has more of a digital nature rather than a continuous behavior. In other words, there is a threshold that must be attained to cause separation through actuation, but further increases in actuation power do not return as much benefit. This can be seen in the steady blowing as well, the greatest effect is seen going from no blowing to a blowing coefficient of 0.011. A blowing coefficient ten times greater only produces about 50% more effect on pitching moment. The lesson to be taken from this is that the nature of the flow one is trying to control is equally important or even more important than the level of blowing being employed. In this particular application of causing separation in a flow that is somewhat unstable, synthetic jets were capable of creating a comparable effect but at a blowing coefficient that was a fraction of the steady blowing coefficient value.

The effects of the leading edge blowing on the power required to turn the fan are shown in Figure 6-25.

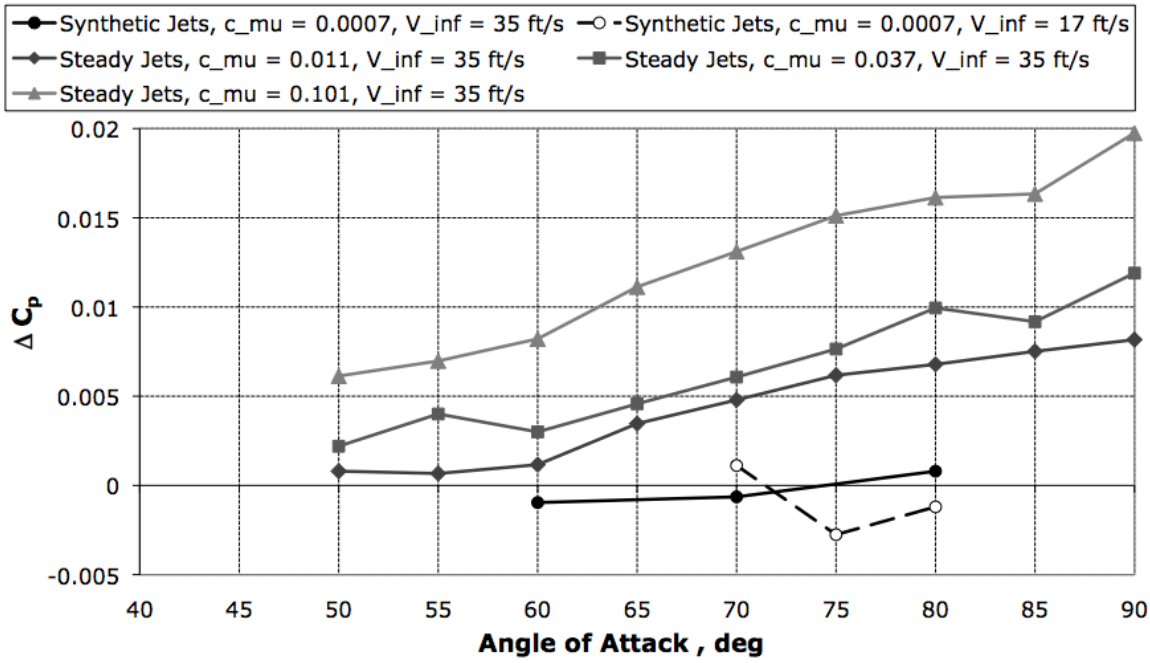

Figure 6-25. Forward flight, change in C_p vs. angle of attack, leading edge flow control.

The general trend is that there is an increase in power required as the magnitude of the blowing increases. It is theorized that this is due to the separated flow passing through the fan, and as the blowing increases this separated region is enlarged. The increase in power required grows with increasing angle of attack for the same reason: the flow is more prone to separate at higher incidence angles and results in more turbulent input to the fan.

From a system level, the impacts of the thrust loss and power increase are summarized by plotting FM versus angle of attack in Figure 6-26. Here we see significant reduction (more than two times the uncertainty value of 0.047) in FM that grows proportionally to the flow control's ability to decrease pitching moment through thrust modulation. For the trim angle of attack of 70°, the delta to FM is roughly -0.09 which represents more than a 10% reduction in Figure of Merit. This approach to mitigating the nose-up pitching moment would have detrimental implications to the vehicle performance (required throttle, fan RPM, and fuel burn).

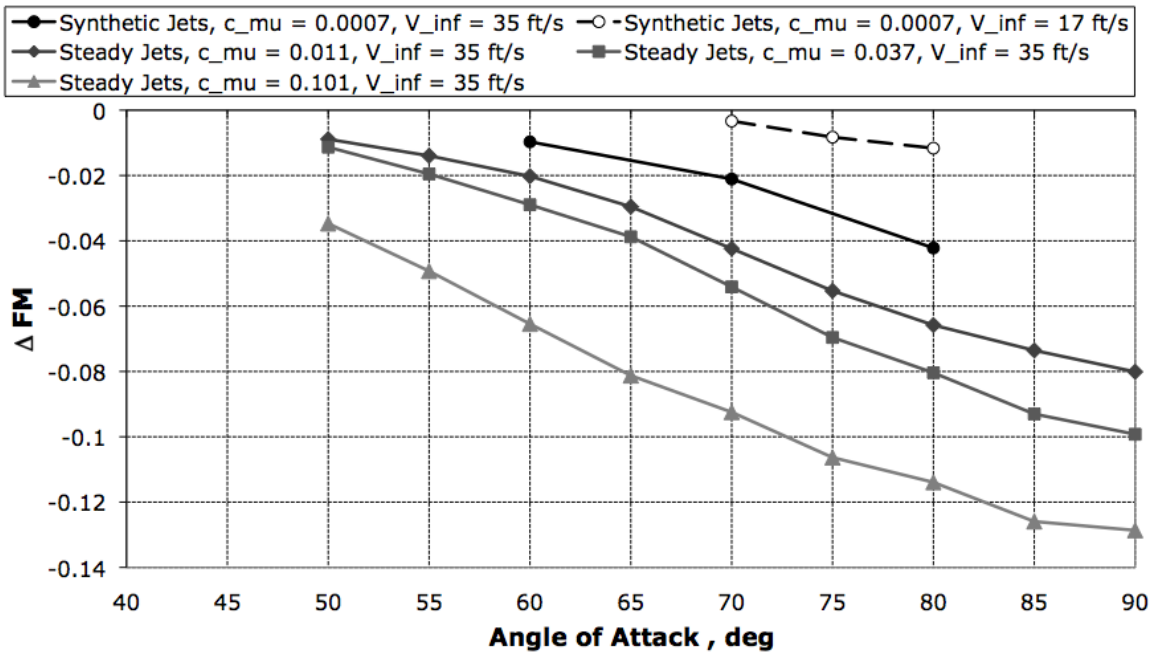

Figure 6-26. Forward flight, change in FM vs. angle of attack, leading edge flow control.

6.5.4 Comparison of the Two Flow Control Methods

The two flow control methods explored demonstrate very different approaches to accomplish the same goal of reducing vehicle pitching moment. While they both achieve the primary goal, the secondary effects are what set them apart.

The trailing edge blowing performs better for low angle of attack, and was effective (to some extent) for all conditions tested, especially hover. The effectiveness decreases for increasing flight speeds using a fixed jet output. This approach would require the flow control velocity ratio to be maintained as the flight speed increases; i.e. the jet speed would need to increase proportionally with the flight speed. One of the benefits of this approach is that overall aerodynamic efficiency does not suffer during generation of control forces and moments as it typically does in other flight control actuation schemes.

In contrast, the leading edge flow control applies to a very specific flight condition: high angle of attack flight at speeds where the flow over the lip was prone to separate. The effectiveness of this flow control grows with flight

velocity, for the range of velocities evaluated. It was easier for synthetic jets to produce a response in this configuration, even at a lower synthetic jet velocity than was attained for the trailing edge. The increasing trends in effectiveness as angles of attack increases match the need for rejecting wind gusts. Because the mechanism through which it reduces pitching moment is thrust spoiling, it has a detrimental effect on aerodynamic efficiency and would require additional propulsive power when actuated.

In light of the differences between the two flow control methods, one might expect that the selection of one over the other would be dependent on the intent of the control. For instance, if the flow control were intended to replace traditional control surfaces or be the primary control input, the Coandă trailing edge blowing would be the superior choice. A hovering vehicle that never transitions to high-speed flight would be a prime candidate for this approach. The level of blowing required to attain good vehicle control authority could be substantial, and would require significantly stronger synthetic jets than those tested. The added benefit of this approach would be that the actuation of control forces and moments would not detract from the ducted fan's propulsive efficiency for producing thrust.

The leading edge flow control would be more suitable for a vehicle with traditional control surfaces, but one that could benefit from control effectors specifically tailored to wind gust rejection. During a wind gust, there is a nose-up pitching moment and an increase in thrust that causes the vehicle to rise. The high frequency bandwidth of the synthetic jet actuators could provide the ability to maintain altitude and vehicle orientation in the face of turbulent and random wind gusts.

It is foreseeable that the two approaches could both be used simultaneously in an aircraft design; however, it is anticipated that the separated flow created at the leading edge would have a detrimental effect downstream on the trailing edge flow control.

6.6 Chapter Summary

To beneficially alter the ducted fan flow characteristics, I developed and explored two flow control concepts. The first flow control concept is to reduce pitching moment and thrust during a wind gust through the use of controlled separation of the flow over the duct lip. The second flow control concept uses a Coandă surface at the trailing edge to create control forces and moments. The target flight condition for improving performance is high angle-of-attack, low-speed flight. This condition represents the transition between hover and high-speed flight, and is also equivalent to battling wind gusts in hovering flight. These conditions typically require more control surface deflection (control allocation) to achieve equilibrium than any other point in the flight envelope. Reducing the nose-up pitching moment at this flight condition to alleviate the control allocation problem was a key objective.

Through experimentation, the new flow control concepts proved to be successful in producing aerodynamic forces and moments on a ducted fan over a large range of angles of attack. Both synthetic jets and steady jets were capable of modifying the ducted fan flow, but some cases required high values of steady blowing to create significant responses. Turning of the stream-tube exiting the ducted fan was demonstrated using a Coandă surface at the duct trailing edge, thereby creating a normal force and a decrease in pitching moment. Leading edge separation on the duct lip was induced at high angles of attack through synthetic and steady jet blowing, which also decreased pitching moment. These flow control techniques could be used as control inputs for ducted fan flight control or augmenting wind gust rejection performance. The research presented here represents the first time that synthetic jet flow control has been applied to the longitudinal aerodynamics of a ducted fan configuration.

Attaining high blowing momentum coefficients from synthetic jets is challenging since the time-averaged velocity is only a function of the outstroke, which equates to the peak velocity divided by π for pure sinusoidal flow. While

peak jet velocities of 225 ft/s (69 m/s) were attained, the synthetic jets operated at lower blowing momentum coefficients than the steady jets tested. In the trailing edge flow control cases the ducted fan application required more authority than the synthetic jets could impart, but this could be overcome with higher output synthetic jets. In contrast, triggering leading edge separation on the duct lip was one application where synthetic jets showed comparable performance to steady jets that were operating at a blowing coefficient an order of magnitude higher. These two differing outcomes demonstrate the critical nature of identifying a flow condition that can be sufficiently influenced by the momentum imparted by synthetic jets.

Chapter 7 Conclusions and Future Work

In this work, I have accomplished my prime objectives of understanding and modeling ducted fan aerodynamics and exploring how those characteristics can be altered through flow control techniques. The behavior of ducted fans was studied through research of existing work, application of novel concepts, experimentation, and analysis of the resulting data. Several contributions have been made to the scientific communities interested in these topics, as described below.

Ducted fans are unique in the realm of air vehicle design, with distinct advantages and challenges when compared with other aerodynamic configurations. Compared to other hovering vehicles, such as helicopters, quadcopters, and aerobatic fixed-wing designs, a ducted fan vehicle will hover more efficiently while lifting a fixed payload for a given vehicle diameter. Looking at it another way, for a fixed thrust value and power setting, the ducted fan will be more compact in its dimensions that these other vehicle designs. For these reasons, the ducted fan is particularly suited to applications where either minimal size or maximum payload capacity is a driving factor. Compared to traditional fixed-wing designs, the ducted fan's ability to hover in winds and fly in any direction are distinct advantages for Intelligence, Surveillance, and Reconnaissance (ISR) missions. In addition, the vertical takeoff and landing capability reduces the logistics footprint for launch and recovery when compared to a fixed-wing unmanned aerial vehicle (UAV).

The main challenge associated with the ducted fan is its nonlinear aerodynamic characteristics. The presence of the duct enhances efficiency and

thrust generation, but it also causes significant normal force and nose-up pitching moments in a crosswind, neither of which are observed with free propellers and rotors. Rotorcraft are naturally unstable, but these additional destabilizing quantities make controlling ducted fan vehicles particularly challenging. The lack of a simple and coherent model for these characteristics hinders more unified advances in overcoming these issues. In this dissertation, I provide a new and concise modeling approach that captures the nonlinear trends in a set of non-dimensional equations.

Active flow control is intended to change the overall behavior of a fluid flow through small aerodynamic inputs at key locations. This technique can improve the aerodynamics characteristics of a ducted fan, and in particular reduce the magnitude of the nose-up pitching moment in cross-winds. To accomplish this, I explore two flow control concepts: flow separation control at the duct lip, and flow turning at the duct trailing edge, using a Coandă surface. Steady and synthetic jet actuation were evaluated and compared.

Synthetic jets are novel flow control actuators that impart energy and momentum to a flow without mass injection. In the synthetic jets that were developed, a vibrating piezoelectric diaphragm in the jet cavity forced the oscillatory flow at the slot orifice. Synthetic jets draw in air from the mean flow and eject that fluid back into the mean flow with greater momentum and energy. Because synthetic jets require zero net mass flux, they do not require tubing, ductwork, or a high-pressure air supply. This is a clear advantage for packaging actuators in small UAVs. The question I answer in this work is whether synthetic jets are adequate for powering the ducted fan flow control concepts.

7.1 Ducted Fan Aerodynamics and Modeling

Wind tunnel tests of a generic, axisymmetric ducted fan design provided ample data for analysis and modeling. When testing powered models in a

closed-jet test section, wind tunnel corrections are needed to account for the presence of the walls and their effect on the test measurements. The ducted fan accelerates a portion of the tunnel mean flow, causing the remaining flow around the model to be slower than the nominal tunnel speed. Following Glauert's traditional approach for free propeller velocity corrections, I derived a new velocity correction specifically for the case of ducted fans. The flow exiting a ducted fan does not contract like a free propeller, but rather the wake maintains the same diameter as the duct exit. For the same thrust level, the ducted fan will have a slower wake velocity than a free propeller, and will entrain more of the tunnel flow. This higher mass flow through the duct results in a relatively larger velocity correction.

Analysis of the corrected wind tunnel data led to a new, concise, non-dimensional modeling scheme. This new approach captures the nonlinear characteristics of the force, moment, and power data while representing these terms in a set of simple equations. Force coefficients based on fan tip speed are plotted versus advance ratio for a range of angles of attack, leading to several observations. Each angle of attack yields a linear trend as a function of advance ratio but with differing slopes, with all lines converging through a single point. This fulcrum point shares the same thrust coefficient value as static/hover tests, but at a non-zero advance ratio value. While the vehicle is stationary in hover, these finding imply that a ducted fan self-induces a free-stream flow in the thrust direction, equivalent to a small non-zero advance ratio.

Pitch and roll moments over the complete flight envelope are successfully modeled using the concept of center of pressure (CP). The CP moves in a predictable fashion as a function of advance ratio and angle of attack. The power required to turn the fan is modeled using Figure of Merit. This term is typically a hover performance metric; however, I use this representation over the entire flight regime to produce a clear relationship relating power required

to thrust generated. The excellent correlation between the model and the data supports the validity of modeling the power in this way.

The new model is applied to a respected legacy dataset from NASA tests in the 1960s to verify the model's general validity and applicability to other datasets. The model shows excellent agreement with the NASA force and power data. This well-accepted dataset also shows the non-zero advance ratio characteristic in hover tests. The pitching moment correlation showed good agreement, but may merit further investigation.

While it is appropriate for typical ducted fan flight conditions, this modeling approach does not address the nonlinear effects of duct lip stall. Developed using an axisymmetric ducted fan configuration, this model does not account for possible asymmetries in vehicle geometry, and would require enhancements to address such characteristics. The vehicle moment modeling via center of pressure movement and the power modeling via Figure of Merit are restricted to positive thrust conditions. The model was successfully applied to experimental data spanning angles of attack from 0° to 100°, and velocities from hover to 80 knots (40 m/s).

In summary, the most influential aerodynamic terms (thrust, power, normal force, pitching moment, and rolling moment) for an axisymmetric ducted fan configuration can be modeled with a total of twelve non-dimensional terms. The equations that define the model are collected in Figure 7-1, showing concise representation of the complex aerodynamic phenomena.

$$C_T = C_{T_0} + \left(J - J_0\right) \cdot \left(C_{T_{J,\alpha=90}} + C_{T_{J\cos\alpha}} \cos\alpha\right)$$

$$FM = \frac{C_T^{1.5}}{\sqrt{\pi} C_P} = FM_0 + \left(J - J_0\right) \cdot \left(FM_{J,\alpha=90} + FM_{J\cos\alpha} \cos\alpha\right)$$

$$C_N = \left(J - J_0\right) \cdot C_{N_{J\sin\alpha}} \sin\alpha$$

$$\frac{X_{CP}}{D} = X_{CP_{J\sin\alpha}} J \cdot \sin\left(X_{CP_\alpha} \alpha\right), \quad \frac{Y_{CP}}{D} = Y_{CP_{J\sin\alpha}} J \cdot \sin\left(Y_{CP_\alpha} \alpha\right)$$

Figure 7-1: Non-dimensional model for ducted fan aerodynamics using 12 non-dimensional coefficients.

The new modeling technique attains very high correlation values for both recent and legacy ducted fan data, supporting the model's validity. This model is analogous to the linear models of airfoil performance versus angle of attack: $C_L = C_{L_{\alpha=0}} + \left(\partial C_L / \partial\alpha\right) \cdot \alpha$. While the simplified airfoil model does not describe how to design an airfoil, it does characterize the behavior for a vast majority of airfoil designs. It stands as a framework that design methods would work within to optimize and report airfoil performance. The new ducted fan model is parameterized using advance ratio, J; angle of attack, α; and the model coefficients. This model enables a representation for ducted fan aerodynamics that is comparable to the prolific form used for wings and airfoils. These new developments offer a new paradigm for understanding the fundamentals of ducted fan aerodynamics. The resulting model can concisely describe the aerodynamics of a ducted fan configuration, and can serve in future modeling of vehicles for simulation and flight control development.

7.2 Synthetic Jet Actuators

Synthetic jets have potential for use in flow control applications in UAVs with limited size, weight, and power budgets. Piezoelectric synthetic jet

actuators (SJA) for a ducted fan vehicle were developed through two rounds of experimental designs. The first round shows the performance of Macro Fiber Composite (MFC) actuators compared to a monolithic piezoceramic bimorph without a shim/substrate. Star-shaped MFC actuators were bonded to brass substrates to form unimorph diaphragms. Peak jet velocities were measured via hotwire anemometry and were compared to an off-the-shelf bimorph diaphragm. A parametric investigation of the effects of frequency, voltage, chamber depth, and driving waveform was performed.

The peak jet velocities of the MFC-based SJAs were 78% (181 ft/sec) of those generated by an off-the-shelf bimorph diaphragm (235 ft/sec). While they represent an experimental benchmark for performance, bimorph piezoelectric diaphragms are fragile and consequently are not practical for implementation in a UAV. The MFC actuators were robust and easy to handle, but were not selected for use in the final vehicle design due to their large dimensions and lower jet velocities.

The final synthetic jet actuator design, resulting from the second round of tests, was based on a low-cost 1" diameter piezoelectric unimorph disk. The actuator cavity was relatively shallow at 0.06", and the orientation of the orifice slot was parallel to the diaphragm to favor the tangential blowing applications in the ducted fan. In general, I found the mechanical resonance of the diaphragm to produce jet velocities larger than the Helmholtz frequency (acoustic resonance). Also, I found shallower cavity depths to be desirable both from a jet performance standpoint, as well as for packaging such actuators in a vehicle with limited volume. Peak jet velocities of 200 to 225 ft/sec were attained for a 0.03" x 0.80" rectangular slot, and this configuration was chosen for testing in the wind tunnel model.

The time-averaged velocity of the outstroke, the most influential parameter in flow control applications, was approximately 50 ft/s. Of particular interest to synthetic jet actuator designers is the difference between this value and the peak jet velocity (near 200 ft/s). In the literature, many researchers report only

the peak jet velocity. However, my results affirm the time-averaged outstroke velocity as the proper design metric when designing for flow control applications.

7.3 Ducted Fan Flow Control

To beneficially alter the ducted fan flow characteristics, I developed and explored two flow control concepts. The first flow control concept is to reduce pitching moment and thrust during a wind gust through the use of controlled separation of the flow over the duct lip. The second flow control concept uses a Coandă surface at the trailing edge to create control forces and moments. The target flight condition for improving performance is high angle-of-attack, low-speed flight. This condition represents the transition between hover and high-speed flight, and is also equivalent to battling wind gusts in hovering flight. These conditions typically require more control surface deflection (control allocation) to achieve equilibrium than any other point in the flight envelope. Reducing the nose-up pitching moment at this flight condition to alleviate the control allocation problem was a key objective.

Through experimentation, the new flow control concepts proved to be successful in producing aerodynamic forces and moments on a ducted fan over a large range of angles of attack. Both synthetic jets and steady jets were capable of modifying the ducted fan flow, thereby reducing the pitching moment. However, some cases required high values of steady blowing to create significant responses. Using a Coandă surface at the duct trailing edge, I demonstrated turning of the stream-tube exiting the duct. This flow turning created a normal force and a decrease in pitching moment. At the leading edge, steady and synthetic jet blowing caused separation on the duct lip at high angles of attack. This separation reduced thrust and also decreases the nose-up pitching moment.

The trailing edge blowing performs better for low angle of attack, and was effective for all conditions tested, especially hover. The effectiveness decreases as flight speed increases, using a fixed jet output strength. This approach would require the flow control velocity ratio to be maintained as the flight speed increases; i.e. the jet speed would need to increase proportionally with the flight speed. One of the benefits of this approach is that the aerodynamic efficiency does not suffer during generation of control forces and moments as it typically does in other flight control actuation schemes such as traditional control surfaces.

In contrast, the leading edge flow control applies to a very specific flight condition: high angle of attack flight at speeds where the flow over the lip is prone to separate. It was easier for synthetic jets to produce a response in this configuration, even at a lower synthetic jet velocity than was attained for the trailing edge. The growing trends in effectiveness, as angles of attack increases, match the need for rejecting wind gusts. Because the mechanism through which it reduces pitching moment is thrust spoiling, this type of flow control has a detrimental effect on aerodynamic efficiency and may require additional propulsive power when actuated. During a wind gust, there is a nose-up pitching moment and an increase in lift that causes the vehicle to rise. The high frequency bandwidth of the synthetic jet actuators could provide the ability to maintain altitude and vehicle orientation in the face of turbulent and random wind gusts.

Attaining high blowing momentum coefficients from synthetic jets is challenging since the time-averaged velocity is only a function of the outstroke, which equates to the peak velocity divided by π for pure sinusoidal flow. While peak jet velocities of 225 ft/s (69 m/s) were attained, the synthetic jets operated at lower blowing momentum coefficients than the steady jets tested. In the trailing edge flow control cases, the ducted fan application required more authority than the synthetic jets could impart. With higher output jets, however, this issue could be overcome. In contrast, triggering leading edge

separation on the duct lip was one area where synthetic jets showed comparable performance to steady jets operating at a blowing coefficient an order of magnitude higher. These two differing outcomes demonstrate the necessity of identifying a flow condition that can be sufficiently influenced by the momentum imparted by synthetic jets.

The two flow control techniques developed can be used as control inputs for ducted fan flight control or augmenting wind gust rejection performance. This research represents the first time synthetic jet flow control has been applied to the longitudinal aerodynamics of a ducted fan configuration.

7.4 Future Work

Several areas of research could flow out of these developments in ducted fan modeling and flow control. In the realm of ducted fan aerodynamics, more detailed investigations into the causes of the pitching and rolling moment behavior could benefit future designs. Applying the new modeling technique to wind tunnel datasets for other ducted fan vehicles would also determine the universality of the approach. Further extensions to the model could account for vehicle asymmetries and various control actuation schemes. Flight simulation using my new model should be compared to simulations performed with the original experimental data in lookup tables to compare the accuracy and computational performance. Flight control algorithms could be derived for ducted fan vehicles using this modeling scheme as the onboard representation of the vehicle plant.

Future work in synthetic jets could explore how to attain higher blowing momentum coefficient performance out of small actuators suitable for UAV integration. On the other hand, one could seek out applications that are more suitable for the current jet performance. Optimization of the size, weight, and power of the electronic drive circuitry would also be an area for improvement, enabling high performance SJA flow control for use in weight-sensitive aircraft.

The ducted fan flow control concepts show the ability to affect the flow into and out of a ducted fan to generate forces and moments for vehicle control. The effects of these flow control techniques could grow if the disk loading of the ducted fan vehicle design is varied. Investigation of this area may also reveal the feasibility of a ducted fan vehicle at lower disk loading that could be completely stabilized through steady or synthetic jet active flow control for hover and low-speed flight.

References

[1] DARPA, “FACT FILE: A Compendium of DARPA Programs”, Revision 1, August 2003, http://www.darpa.mil/body/pdf/final2003factfilerev1.pdf, [retrieved December 1, 2003].

[2] White, A., “Upgrades for gMAV in light of Iraq ops”, UVOnline, 22 April 2010, http://www.shephard.co.uk/news/uvonline/upgrades-for-gmav-in-light-of-iraq-ops/6185/ [retrieved May 12, 2010].

[3] Anon, "A Micro Air Vehicle (MAV) flies over a simulated combat area during an operational test flight", Navy News Service - Eye on the Fleet, http://www.navy.mil/view_single.asp?id=41139, 11/14/2006, photo credit U.S. Navy/Kenneth Takada, retrieved 3/25/2011.

[4] Anon, “Autonomous UAV Mission System (AUMS)", http://www.spawar.navy.mil/robots/air/aums/aums.html, retrieved 1/14/2011.

[5] Anon, "Hovering UAVs Provide Better Access in Difficult Situations", DARPA SBIR Success Reports Volume 1, 2007 http://www.darpa.mil/WorkArea/DownloadAsset.aspx?id=1049, retrieved 3/24/2011.

[6] McCormick, B. W., *Aerodynamics of V/STOL Flight*, Dover Publications, 1999.

[7] Fleming, J., T. Jones, W. Ng, P. Gelhausen, D. Enns, “Improving Control System Effectiveness for Ducted Fan VTOL UAVs Operating in Crosswinds”, AIAA Paper 2003-6514, 2nd AIAA UAV Conference and Workshop & Exhibit, San Diego, CA, September 2003.

[8] Graf, W., J. Fleming, W. Ng, P. Gelhausen, “Ducted Fan Aerodynamics in Forward Flight.” AHS International Specialists’ Meeting on Unmanned Rotorcraft, Chandler, AZ, January 2005.

[9] Graf, W., “Effects of Duct Lip Shaping and Various Control Devices on the Hover and Forward Flight Performance of Ducted Fan UAVs”, Masters Thesis, Virginia Tech, Blacksburg, VA, May 13, 2005.

[10] Anon, “Technical Specifications Raven RQ-11B”, www.avinc.com/downloads/AV_RAVEN-DOM_V10109.pdf, retrieved 3/25/2011.

[11] Anon, "Unmanned Aircraft Program Grows to Support Demand", U.S. Army, http://www.army.mil/-images/2010/01/13/61411/, 10/9/2009, Photo credit: U.S. Army/Michael MacLeod, retrieved 3/25/2011.

[12] Theodore, C., Tischler, M., "Precision Autonomous Landing Adaptive Control Experiment (PALACE)", DTIC Report, US Army Aeroflightdynamics Directorate (AMRDEC) Ames Research Center, CA, 2006.

[13] Pereira, J., “Hover and Wind-Tunnel Testing of Shrouded Rotors for Improved Micro Air Vehicle Design”, Ph.D. Thesis, University of Maryland, College Park, MD, 2008.

[14] Anon, "NASA - Autonomous Vehicles - Quadcopter", NASA Featured Image, http://www.nasa.gov/centers/langley/multimedia/iotw-quadcopter.html, 8/16/2010, Photo credit: NASA/Sean Smith, retrieved 3/24/2011.

[15] Anon, "Hanging on a Propeller", NASA Photo Feature, http://www.nasa.gov/centers/dryden/Features/leseberg_photo.html, 1/12/2010, Photo credit: NASA/Tom Tschida, retrieved 3/24/2011.

[16] Anon, "Tiny MAVs for Hazard Detection", U.S. Air Force Research Lab, http://www.wpafb.af.mil/shared/media/photodb/photos/100715-F-9894C-003.jpg, retrieved 3/30/2011.

[17] Kondor. S., M. Heiges, "Active Flow Control For Control of Ducted Rotor Systems", AIAA Paper 2001-117, Proceedings, 39th AIAA Aerospace Sciences Meeting & Exhibit, January 8-11, 2001, Reno, Nevada, 2001.

[18] Kondor, S., W. Lee, R. Englar, M. Moore, "Experimental Investigation of Circulation Control on a Shrouded Fan", Paper AIAA-2003-3409. Proceedings, 33rd Fluid Dynamics Conference, June 23-26, 2003, Orlando, FL.

[19] Kondor, S., "Further Experimental Investigation of Circulation Control Morphing Shrouded Fan", Paper AIAA-2005-639, Proceedings, 43rd AIAA Aerospace Sciences Meeting and Exhibit, Reno, NV, 10 - 13 January 2005.

[20] Fung, P. H., M. Amitay, "Control of a Miniducted-Fan Unmanned Aerial Vehicle Using Active Flow Control", *Journal of Aircraft*, Vol. 39, No. 4, 2002, pp. 561-571. doi:10.2514/2.2993

[21] Smith, B. L., G. W. Swift, "A Comparison Between Synthetic Jets and Continuous Jets", *Experiments in Fluids*, Vol. 34, 2003, pp 467-472, doi: 10.1007/s00348-002-0577-6

[22] Stipa, L., "Experiments with Intubed Propellers," NACA TM 655, 1932, Translated from L'Aerotecnica (Rome), pp. 923-953, Aug 1931.

[23] Kort, L., "Combined Device of a Ship's Propeller Enclosed by a Nozzle," US Patent No. 2,030,375, Feb 11, 1936, Application filed Sep 7, 1933.

[24] Sacks, A. H., J. A. Burnell, "Ducted Propellers—A Critical Review of the State of the Art", *Progress in Aerospace*, Vol. 3, 1962, pp. 85-135. doi:10.1016/0376-0421(62)90017-9

[25] Krüger, W., "On Wind Tunnel Tests And Computations Concerning The Problem Of Shrouded Propellers", NACA TM 1202, 1949, originally published in Germany 1944.

[26] Yaggy, P. F., K. W. Mort, "Wind-Tunnel Investigation Of A 4-Foot-Diameter Ducted Fan Mounted On The Tip Of A Semispan Wing", NASA Technical Note TN D-776, 1961.

[27] Yaggy, P. F., K. W. Goodson, "Aerodynamics Of A Tilting Ducted Fan Configuration", NASA Technical Note TN D-785, 1961.

[28] Grunwald, K. J., K. W. Goodson, "Aerodynamic Loads On An Isolated Shrouded-Propeller Configuration For Angles Of Attack From -10° To 110°", NASA Technical Note TN D-995, 1962.

[29] Grunwald, K. J., K. W. Goodson, "Division Of Aerodynamic Loads On A Semispan Tilting-Ducted-Propeller Model In Hovering And Transition Flight", NASA Technical Note TN D-1257, 1962.

[30] Mort, K. W., P. F. Yaggy, “Aerodynamic Characteristics Of A 4-Foot-Diameter Ducted Fan Mounted On The Tip Of A Semi-Span Wing”, NASA Technical Note TN D-1301, 1962.

[31] Mort, K. W., “Performance Characteristics At Zero Angle Of Attack For Several Fan Blade Angles of a 4-Foot-Diameter Ducted Fan”, NASA Technical Note TN D-3122, 1965.

[32] Mort, K. W., B. Gamse, “Wind-Tunnel Investigation Of A 7-Foot-Diameter Ducted Propeller”, NASA Technical Note D-4142, 1967.

[33] Black, D. M., H. S. Wainauski, C. Rohrbach, “Shrouded Propellers - A Comprehensive Performance Study”, AIAA Paper 1968-994, Proceedings of AIAA 5th Annual Meeting and Technical Display, Philadelphia, PA, October 21-24, 1968.

[34] Abrego, A., Bulaga, R., “Performance Study of a Ducted Fan System", Proceedings of AHS Aeromechanics Specialists Mtg., January, 2002.

[35] Martin, P., C. Tung, “Performance and Flowfield Measurements on a 10-inch Ducted Rotor VTOL UAV,” American Helicopter Society Paper AHS 2004-0264, 2004.

[36] Graf, W., J. Fleming, W. Ng, “Improving Ducted Fan UAV Aerodynamics in Forward Flight”, AIAA Paper 2008-430, Proceedings of 46th AIAA Aerospace Sciences Meeting and Exhibit, Reno, Nevada, 7 - 10 January 2008.

[37] Thipyopas, C., R. Barènes, J. Moschetta, “Aerodynamic Analysis of a Multi-Mission Short-Shrouded Coaxial UAV: part I – Hovering Flight”, AIAA Paper 2008-6243, Proceedings of 26th AIAA Applied Aerodynamics Conference, Honolulu, Hawaii, 18 - 21 August 2008.

[38] Akturk, A., A. Shavalikul, C. Camci, “PIV Measurements and Computational Study of a 5-Inch Ducted Fan for V/STOL UAV Applications”, AIAA Paper 2009-332, Proceedings of 47th AIAA Aerospace Sciences Meeting, Orlando, Florida, 5 - 8 January 2009.

[39] Kriebel, A. R., “Theoretical Stability Derivatives for a Ducted Propeller,” *Journal of Aircraft*, Vol. 1, No. 4, 1964, pp. 203–210.

[40] Mendenhall, M. R., Spangler, S. B., “A Computer Program for the Prediction of Ducted Fan Performance”, NASA Contractor Report CR-1495, 1970.

[41] Chang, I., Rajagopalan, R. G., “CFD Analysis for Ducted Fans with Validation”, Paper AIAA-2003-4079, 21st Applied Aerodynamics Conference, Orlando, FL, 2003.

[42] Quackenbush, T. R., Wachspress, D. A., Boschitsch, A. H., Solomon, C. L., “Aeromechanical Analysis Tools for Design and Simulation of VTOL UAV Systems”, Proceedings of American Helicopter Society 60th Annual Forum, Baltimore MD, June 7-10, 2004.

[43] Fletcher, H. S., "Experimental Investigation of Lift, Drag, and Pitching Moment of Five Annular Airfoils", NACA TN 4117, 1957.

[44] Drela, M., Youngren, H., “DFDC v0.70: Ducted Fan Design Code”, http://web.mit.edu/drela/Public/web/dfdc/, released Dec 2005, retrieved 2/22/2011.

[45] Lind, R., J. K. Nathman I. Gilchrist, "Ducted Rotor Performance Calculations and Comparisons with Experimental Data", AIAA Paper 2006-1069, Proceedings of 44th AIAA Aerospace Sciences Meeting and Exhibit, Reno, Nevada, 9 - 12 January 2006.

[46] de Devitiis, N., "Performance and Stability Analysis of a Shrouded-Fan Unmanned Aerial Vehicle", *Journal of Aircraft*, Vol. 43, No. 3, 2006, pp. 681-691. doi:10.2514/1.16210

[47] Weir, R. J., "Aerodynamic Design Considerations For A Free-Flying Ducted Propeller", AIAA Paper 88-4377-CP, AIAA Atmospheric Flight Mechanics Conference, Minneapolis, MN, Aug 15-17, 1988.

[48] Avanzini, G., S. D'Angelo G. de Matteis, "Performance and Stability of Ducted-Fan Uninhabited Aerial Vehicle Model", *Journal of Aircraft*, Vol. 40, No. 1, 2003, pp. 86-93. doi: 10.2514/2.3061

[49] Guerrero, I., K. Londenberg, P. Gelhausen A. Myklebust, "A Powered Lift Aerodynamic Analysis For The Design Of Ducted Fan UAVs", AIAA Paper 2003-6567, Proceedings of 2nd AIAA "Unmanned Unlimited" Systems, Technologies, and Operations, San Diego, California, 15 - 18 September 2003.

[50] Ko, A., O. J. Ohanian, P. Gelhausen, "Ducted Fan UAV Modeling and Simulation in Preliminary Design", AIAA Paper 2007-6375, Proceedings of AIAA Modeling and Simulation Technologies Conference and Exhibit, Hilton Head, South Carolina, 20 - 23 August 2007.

[51] Tobias, E. L., J. F. Horn, "Simulation Analysis of the Controllability of a Tandem Ducted Fan Aircraft", AIAA Paper 2008-6700, Proceedings of AIAA Atmospheric Flight Mechanics Conference and Exhibit, Honolulu, Hawaii, 18 - 21 August 2008.

[52] Pflimlin, J. M., Binetti, P., Souères, P., Hamel, T., Trouchet, D., "Modeling and attitude control analysis of a ducted-fan micro aerial vehicle", *Control Engineering Practice*, Vol. 18, 2010, pp 209-218.

[53] Avanzini, G., U. Ciniglio, and G. de Matteis, "Full-Envelope Robust Control of a Shrouded-Fan Unmanned Vehicle", *Journal of Guidance, Control, and Dynamics*, Vol. 29, No. 2, March-April 2006.

[54] Packard, A. and DJ. C. Doyal, "The Complex Structured Singular Value," *Automatica*, Vol. 29, No. 1, 1993, pp. 71-109.

[55] Hyde, R. A., *H_∞ Aerospace Control Design A VSTOL Flight Application*, Springer-Verlag, London, 1995.

[56] Franz, R., M. Milam, and J. Hauser, "Applied Receding Horizon Control of the Caltech Ducted Fan", Proceedings of the American Control Conference, Anchorage, AK, May 8-10 2002.

[57] R. Hess and M. Bakhtiari-Nejad, "Sliding Mode Control of a Nonlinear, Ducted-Fan, UAV Model", AIAA-2006-6088, AIAA Guidance, Navigation, and Control Conference and Exhibit, Keystone, Colorado, Aug. 21-24, 2006.

[58] Li, D., "Flight Control Design for Ducted Fan VTOL UAV", Paper AIAA-2006-6714, AIAA Guidance, Navigation, and Control Conference and Exhibit, 21-24 August, Keystone, CO, 2006.

[59] Spaulding, C. M., M. H. Nasur, M. B. Tischler, R. A. Hess, and J. A. Franklin, "Nonlinear Inversion Control for a Ducted Fan UAV", AIAA Paper 2005-6231, AIAA Atmospheric Flight Mechanics Conference and Exhibit, San Francisco, California, 15-18 August 2005.

[60] Eric N. Johnson; Michael A. Turbe, "Modeling, Control, and Flight Testing of a Small-Ducted Fan Aircraft", *Journal of Guidance, Control, and Dynamics*, Vol. 29, No. 4, 2006, pp. 769-779.

[61] Pflimlin, J. M., P. Souères, and T. Hamel, "Hovering Flight Stabilization in Wind Gusts for Ducted Fan UAV", 43rd IEEE Conference on Decision and Control, Atlantis, Paradise Island, Bahamas, December 14-17, 2004.

[62] Smith, B. L., A. Glezer, "The formation and evolution of synthetic jets", *Physics of Fluids*, Vol. 10, No. 9, 1998, pp. 2281-2297, doi:10.1063/1.869828.

[63] Glezer, A., M. Amitay, "Synthetic Jets", *Annual Review of Fluid Mechanics*, Vol. 34, 2002, pp. 503-529, doi:10.1146/annurev.fluid.34.090501.094913.

[64] Smith, B. L., G. W. Swift, "Synthetic Jets at Large Reynolds Number and Comparison to Continuous Jets", Paper AIAA-2001-3030, AIAA Fluid Dynamics Conference and Exhibit, 31st, Anaheim, CA, June 11-14, 2001.

[65] Holman, R., Y. Utturkar, R. Mittal, B. L. Smith, L. Cattafesta, "Formation Criterion for Synthetic Jets", *AIAA Journal*, Vol. 43, No. 10, October 2005, pp. 2110-2116.

[66] Zhong, S., M. Jabbal, H. Tang, L. Garcillan, F. Guo, N. Wood, C. Warsop, "Towards the Design of Synthetic-jet Actuators for Full-scale Flight Conditions, Part 1: The Fluid Mechanics of Synthetic-jet Actuators", *Flow, Turbulence and Combustion*, Vol. 78, 2007, pp. 283-307, doi:10.1007/s10494-006-9064-0.

[67] Rumasamy, M., J. S. Wilson, P. B. Martin, "Interaction of Synthetic Jet with Boundary Layer Using Microscopic Particle Image Velocimetry", *Journal of Aircraft*, Vol. 47, No. 2, 2010, pp. 404-422, doi:10.2514/1.45794.

[68] Gallas, Q., R. Holman, T. Nashida, B. Carroll, M. Sheplak, L. Cattafesta, "Lumped Element Modeling of Piezoelectric-Driven Synthetic Jet Actuators", *AIAA Journal*, Vol. 41, No. 2, 2003, pp. 240-247.

[69] Gallas, Q., "On The Modeling And Design Of Zero-Net Mass Flux Actuators", PhD Thesis, University of Florida, Gainesville, FL, 2005.

[70] Lockerby, D., P. Carpenter, "Modeling and Design of Microjet Actuators", *AIAA Journal*, Vol. 42, No. 2, 2004, pp.220-227.

[71] Sharma, R. N., "Fluid-Dynamics-Based Analytical Model for Synthetic Jet Actuation", *AIAA Journal*, Vol. 45, No. 8, August 2007, pp. 1841-1847, doi: 10.2514/1.25427.

[72] Gallas, Q., Wang, G., Papila, M., Sheplak, M., Cattafesta, L., "Optimisation of Synthetic Jet Actuators," AIAA Paper 2003-0635, 41st Aerospace Sciences Meeting and Exhibit, Reno, NV, 6-9 January 2003.

[73] Tang, H., S. Zhong, M. Jabbal, L. Garcillan, F. Guo, N. Wood, C. Warsop, "Towards the Design of Synthetic-jet Actuators for Full-scale Flight Conditions, Part 2: Low-dimensional Performance Prediction Models and Actuator Design Method", *Flow Turbulence and Combustion*, Vol. 78, 2007, pp. 309-329, doi:10.1007/s10494-006-9061-3.

[74] Carpenter, M. H., B. A. Singer, N. Yamaleev, V. N. Vatsa, S. A. Viken, H. L. Atkins, "The current status of unsteady cfd approaches for aerodynamic flow control", AIAA Paper 2002-3346, 2002.

[75] Viken, S., Vatsa, V., Rumsey, C., Carpenter, M., "Flow Control Analysis On The Hump Model With RANS Tools", AIAA Paper 2003-0218, 41st Aerospace Sciences Meeting and Exhibit, Reno, NV, Jan. 6-9, 2003.

[76] Roth, J., Rajagopalan, R. G., Hassan, A., "Influence Of Oscillatory Jets On Boundary Layer Characteristics Of Simple Aerodynamic Shapes", AIAA Paper 2003-3666, 21st Applied Aerodynamics Conference, Orlando, FL, 23-26 June 2003.

[77] Dandois, J., Garnier, E., Sagaut, P., "Unsteady Simulation of a Synthetic Jet in a Crossflow", *AIAA Journal*, Vol. 44, No. 2, 2006, pp. 225-238, doi:10.2514/1.13462.

[78] Park, S. H., Yu, Y. H., Byun, D. Y., "RANS Simulation of a Synthetic Jet in Quiescent Air", AIAA Paper 2007-1131, 45th AIAA Aerospace Sciences Meeting and Exhibit, Reno, NV, 8 - 11 January 2007.

[79] Rumsey, C. L., N.W. Schaeffler, I.M. Milanovic, K.B.M.Q. Zaman, "Time-accurate computations of isolated circular synthetic jets in crossflow", *Computers & Fluids*, Vol. 36, 2007, pp. 1092-1105.

[80] Rumsey, C. L., "Reynolds-Averaged Navier–Stokes Analysis of Zero Efflux Flow Control over a Hump Model", *Journal of Aircraft*, Vol. 44., No. 2, 2007, pp. 444-452, doi:10.2514/1.23514.

[81] Sharma, R. N., S. K. Siong, "Uniform, Steady Jet, and Synthetic Jet Cross-Flows Across a Circular Cylinder", AIAA Paper 2009-4170, 2009.

[82] Utturkar, Y., R. Mittal, P. Rampunggoon, L. Cattafesta, "Sensitivity of Synthetic Jets to the Design of the Jet Cavity", AIAA Paper 2002-0124, 40th AIAA Aerospace Sciences Meeting and Exhibit, Reno, NV, 14-17 January 2002.

[83] Gilarranz, J. L., L. W. Traub, O. K. Rediniotis, "A New Class of Synthetic Jet Actuators—Part I: Design, Fabrication and Bench Top Characterization", *Journal of Fluids*, Vol. 127, 2005, pp 367-376, doi:10.1115/1.1839931.

[84] Mossi, K., P. Mane, R. Bryant, "Velocity Profiles of Synthetic Jets using Piezoelectric Circular Actuators", AIAA Paper 2005-2341, Proceedings of 46th AIAA/ASME/ASCE/AHS/ASC Structures, Structural Dynamics & Materials Conference, Austin, TX, 18-21 April, 2005.

[85] Gomes, L. D., W. J. Crowther, N.J. Wood, "Towards a practical piezoceramic diaphragm based synthetic jet actuator for high subsonic applications – effect of chamber and orifice depth on actuator peak velocity", AIAA Paper 2006-2859, Proceedings of 3rd AIAA Flow Control Conference, San Francisco, CA, 5-8 June 2006.

[86] Kim, Y., K. P. Garry, "Optimization of a Rectangular Orifice Synthetic Jet Generator", AIAA Paper 2006-2862, Proceedings of 3rd AIAA Flow Control Conference, San Francisco, CA, 5-8 June 2006.

[87] Lee, S., K. J. Kim, H. C. Park, "Modeling of an IPMC Actuator-driven Zero-Net-Mass-Flux Pump for Flow Control", *Journal of Intelligent Material Systems and Structures*, Vol. 17, June, 2006, pp. 533-541. doi:10.1177/1045389X06058879

[88] Liang, Y., Y. Kuga, M. Taya, "Design of membrane actuator based on ferromagnetic shape memory alloy composite for synthetic jet applications", *Sensors and Actuators A*, Vol. 125, 2006, pp. 512–518. doi:10.1016/j.sna.2005.09.002

[89] Ohanian, O. J., P. A. Gelhausen, D. J. Inman, "Evaluation of Macro Fiber Composite (MFC) Synthetic Jet Actuators", AIAA Paper 2008-6405, 26th AIAA Applied Aerodynamics Conference, Honolulu, HI, 18 - 21 August 2008.

[90] Yang, A., "Design analysis of a piezoelectrically driven synthetic jet actuator", *Smart Materials and Structures*, Vol. 18, 2009, pp. 1-12. doi:10.1088/0964-1726/18/12/125004

[91] Amitay, M., D. Pitt, A. Glezer, "Separation Control in Duct Flows", *Journal of Aircraft*, Vol. 39, No. 4, 2002, pp. 616-620.

[92] McMichael, J., A. Lovas, P. Plostins, J. Sahu, G. Brown, A. Glezer, "Microadaptive Flow Control Applied to a Spinning Projectile", AIAA Paper 2004-2512, 2nd AIAA Flow Control Conference, 28 June – 1 July 2004, Portland, Oregon, 2004.

[93] Gilarranz, J. L., L. W. Traub, O. K. Rediniotis, "A New Class of Synthetic Jet Actuators—Part II: Application to Flow Separation Control", *Journal of Fluids*, Vol. 127, 2005, pp 377-387, doi:10.1115/1.1882393.

[94] Whitehead, J., Gursul, I., "Interaction of Synthetic Jet Propulsion with Airfoil Aerodynamics at Low Reynolds Numbers", *AIAA Journal*, Vol. 44, No. 8, 2006, pp. 1753-1766.

[95] Pavlova, A., M. Amitay, "Electronic Cooling Using Synthetic Jet Impingement", *Journal of Heat Transfer*, Vol. 128, September, 2006. doi: 10.1115/1.2241889

[96] Ciuryla, M., Y. Liu, J. Farnsworth, C. Kwan, M. Amitay, "Flight Control Using Synthetic Jets on a Cessna 182 Model", *Journal of Aircraft*, Vol. 44., No. 2, 2007, pp. 642-653, doi:10.2514/1.24961.

[97] Farnsworth, J. A. N., J. C. Vaccaro, M. Amitay, "Active Flow Control at Low Angles of Attack: Stingray Unmanned Aerial Vehicle", *AIAA Journal*, Vol. 46, No. 10, October 2008, pp. 2530-2544.

[98] Vukasinovic, B., D. Brzozowski, A. Glezer, "Fluidic Control of Separation Over a Hemispherical Turret", *AIAA Journal*, Vol. 47, No. 9, 2009, doi:10.2514/1.41920.

[99] Burley, R., D. Hwang, “Investigation of Tangential Blowing Applied to a Subsonic V/STOL Inlet”, *Journal of Aircraft*, Vol. 20, No. 11, 1982, pp. 926-934.

[100] Kondor, S., Moore, M., "The application of Circulation Control to the nacelle of a shrouded", Proceedings of the 2004 NASA/ONR Circulation Control Workshop, Part 1, NASA/CP-2005-213509/PT1, pp. 435-468; 2004.

[101] Fleming, J., T. Jones, W. Ng, P. Gelhausen, D. Enns, “Improving Control System Effectiveness For Ducted Fan VTOL UAVS Operating In Crosswinds”, AIAA Paper 2003-6514, 2nd AIAA "Unmanned Unlimited" Systems, Technologies, and Operations, San Diego, California, 15 - 18 September 2003.

[102] Fleming, J., T. Jones, J. Lusardi, P. Gelhausen, D. Enns, “Improved Control of Ducted Fan VTOL UAVs in Crosswind Turbulence”, Proceedings of 4th AHS Decennial Specialist’s Conference on Aeromechanics, San Francisco, California, January 21- 23, 2004.

[103] Quackenbush, T. R., Carpenter, B. F., Gowing, S., “Design And Testing Of A Variable Geometry Ducted Propulsor Using Shape Memory Alloy Actuation”, Paper AIAA-2005-1077, 43rd AIAA Aerospace Sciences Meeting and Exhibit, Reno, NV, 10 - 13 January 2005.

[104] Ohanian, O. J., E. Karni, W. K. Londenberg, P. A. Gelhausen, D. J. Inman, “Ducted-Fan Force and Moment Control via Steady and Synthetic Jets”, AIAA Paper 2009-3622, 27th AIAA Applied Aerodynamics Conference, San Antonio, Texas, 22 - 25 June 2009.

[105] Wilkie, W. K., Bryant, G. R., High, J. W. et al., 2000, “Low-Cost Piezocomposite Actuator for Structural Control Applications,” Proceedings, SPIE 7th Annual International Symposium on Smart Structures and Materials, Newport Beach, CA, March 5-9, 2000.

[106] AIAA Standard S-071A-1999, “Assessment of Experimental Uncertainty With Application to Wind Tunnel Testing”, 1999.

[107] Perry, A. E., Morrison, G. L., “Static and dynamic calibrations of constant-temperature hot-wire systems”, *Journal of Fluid Mechanics*, Vol. 47, pp 765-777, 1971. doi: 10.1017/S0022112071001356

[108] Barlow, J. B., W. H. Rae, A. Pope, *Low-Speed Wind Tunnel Testing*, 3rd Ed., Wiley, New York, 1999.

[109] Glauert, H., *The Elements of Aerofoil and Airscrew Theory*, 2nd Ed., Cambridge University Press, Cambridge, 1983.

[110] Hackett J. E., D. E. Lilley, D. J. Wilsden, “Estimation of Tunnel Blockage from Wall Pressure Signatures: A Review and Data Correlation” NASA CR15,224, March 1979.

[111] Mikkelsen, R., J. N. Sørensen, “Modelling of Wind Tunnel Blockage,” Proceedings of the 2002 Global Windpower Conference and Exhibition [CDROM], www.ewea.org.

[112] Fitzgerald, R. E., “Wind Tunnel Blockage Corrections for Propellers”, MS Thesis, University of Maryland, 2007.

[113] Heyson, H. H., “Linearized Theory of Wind-Tunnel Jet-Boundary Corrections and Ground Effect for V/STOL Aircraft”, NASA TR-R-124, 1962.

[114] Loeffler, A. L., J. S. Steinhoff, “Computation of Wind Tunnel Wall Effects in Ducted Rotor Experiments”, *Journal of Aircraft*, Vol. 22, No. 3, 1985, pp. 188-192. doi:10.2514/3.45106

[115] Buckingham, E., "On physically similar systems; illustrations of the use of dimensional equations", *Physical Review*, Vol. 4, No. 4, 1914, pp. 345–376. doi:10.1103/PhysRev.4.345

[116] Devore, J., *Probability and Statistics for Engineering and the Sciences*, 4th ed., Brooks/Cole Publishing, Pacific Grove, CA, 1995.

[117] “Plot Digitizer”, http://plotdigitizer.sourceforge.net/, [retrieved January 5, 2011].

[118] Englar, R. J., “Overview of Circulation Control Pneumatic Aerodynamics: Blown Force and Moment Augmentation and Modification as Applied Primarily to Fixed-Wing Aircraft”, Chapter 2, *Applications of Circulation Control Technology*, American Institute of Aeronautics and Astronautics, Reston, VA, 2006.

[119] Londenberg, W. K., Ohanian, O. J., “Application of CFD in the Design of Flow Control Concepts for a Ducted-Fan Configuration”, Proceedings of the International Powered Lift Conference, American Helicopter Society, October 5-7, 2010, Philadelphia, PA.

[120] Anderson, W. K. and Bonhaus, D. L., “An Implicit Upwind Algorithm for Computing Turbulent Flows on Unstructured Grids,” *Computers and Fluids*, Vol. 23, No. 1, 1994, pp. 1–22.

[121] O’Brien, D., “Analysis of Computational Modeling Techniques for Complete Rotorcraft Configurations”, Ph.D. Thesis, Georgia Institute of Technology, Atlanta, GA, 2006.

Appendix A: Raw Ducted Fan Aerodynamic Data

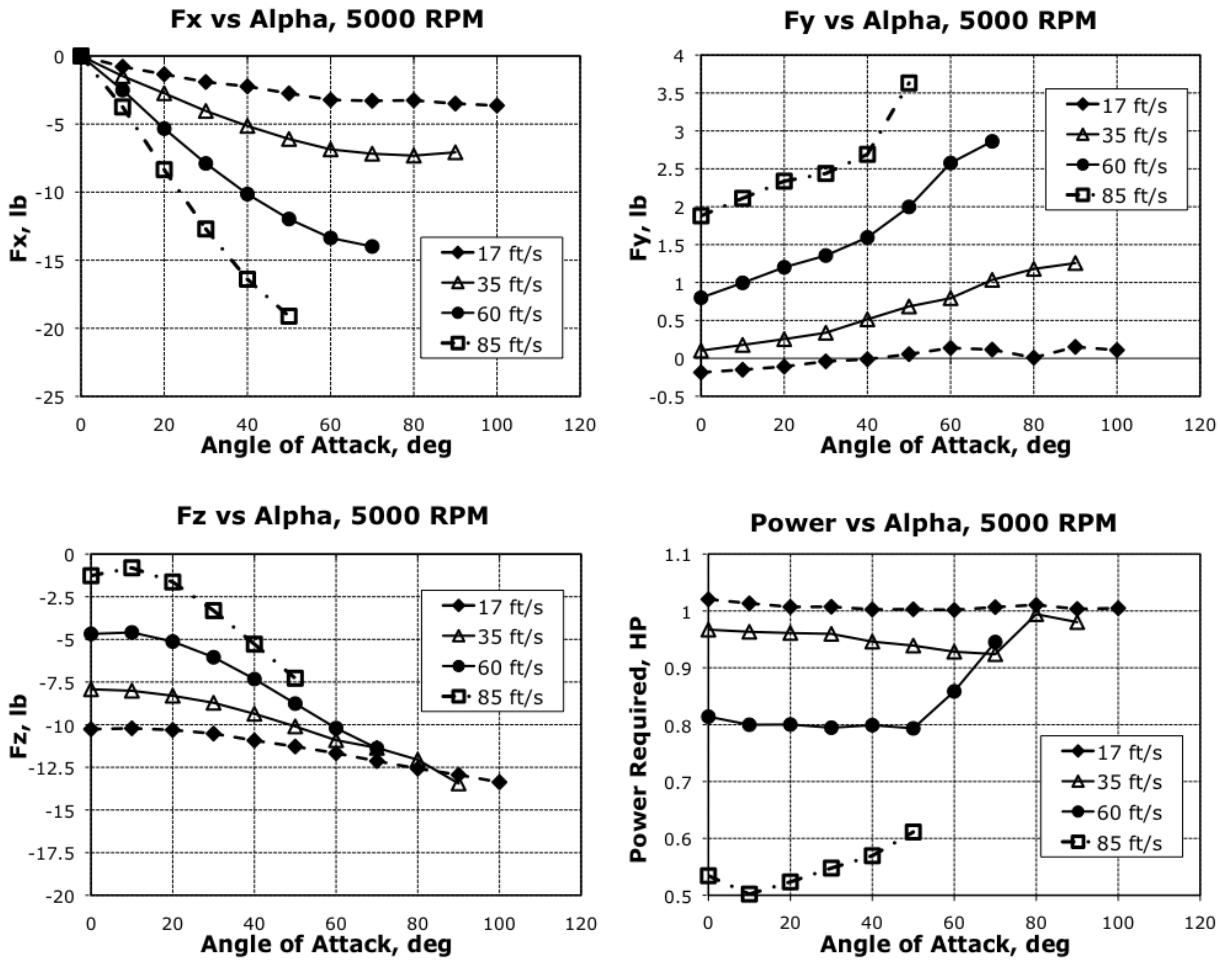

Figure A-1. Forces and Power vs. Angle of Attack, 5000 RPM.

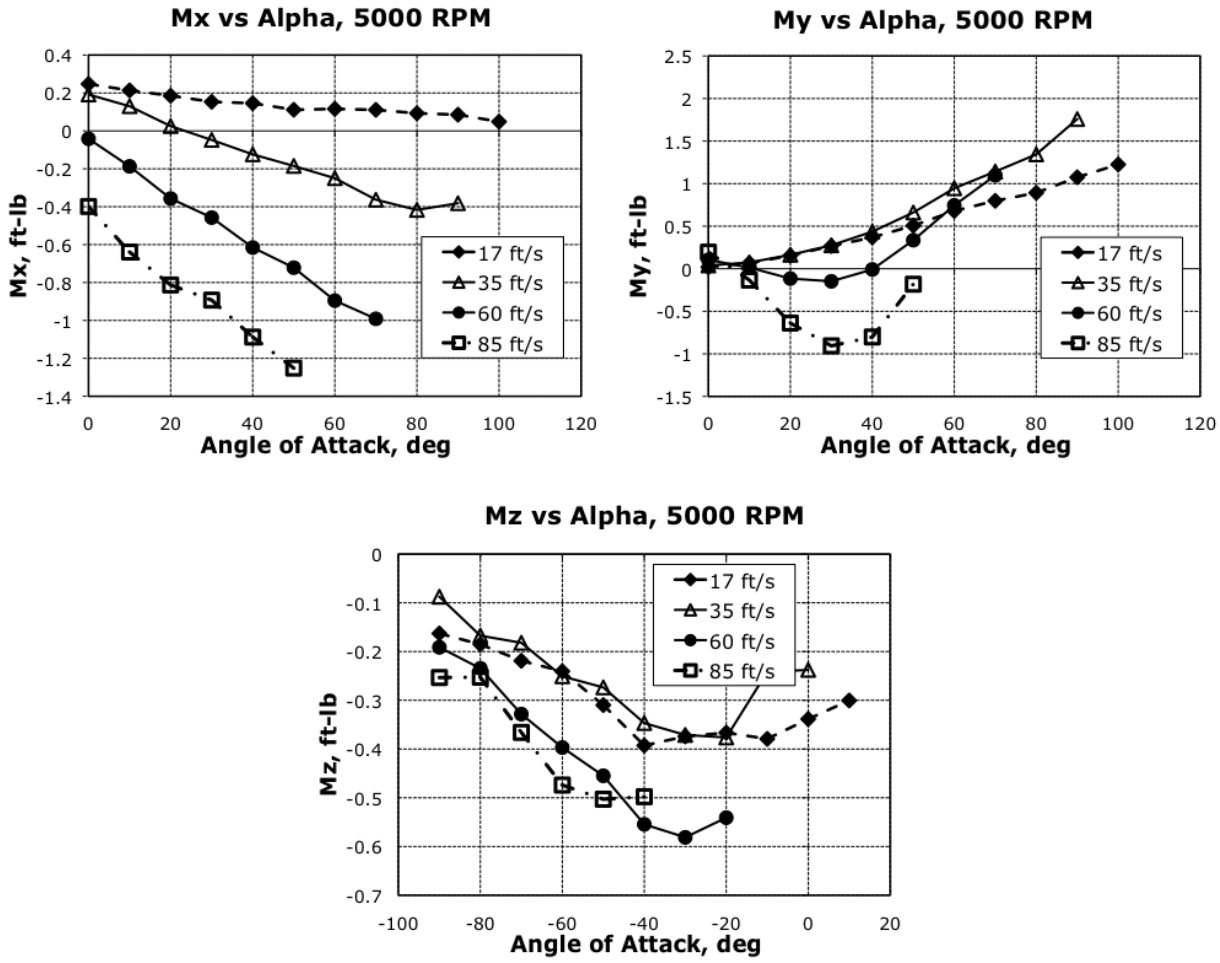

Figure A-2. Moments vs. Angle of Attack, 5000 RPM.

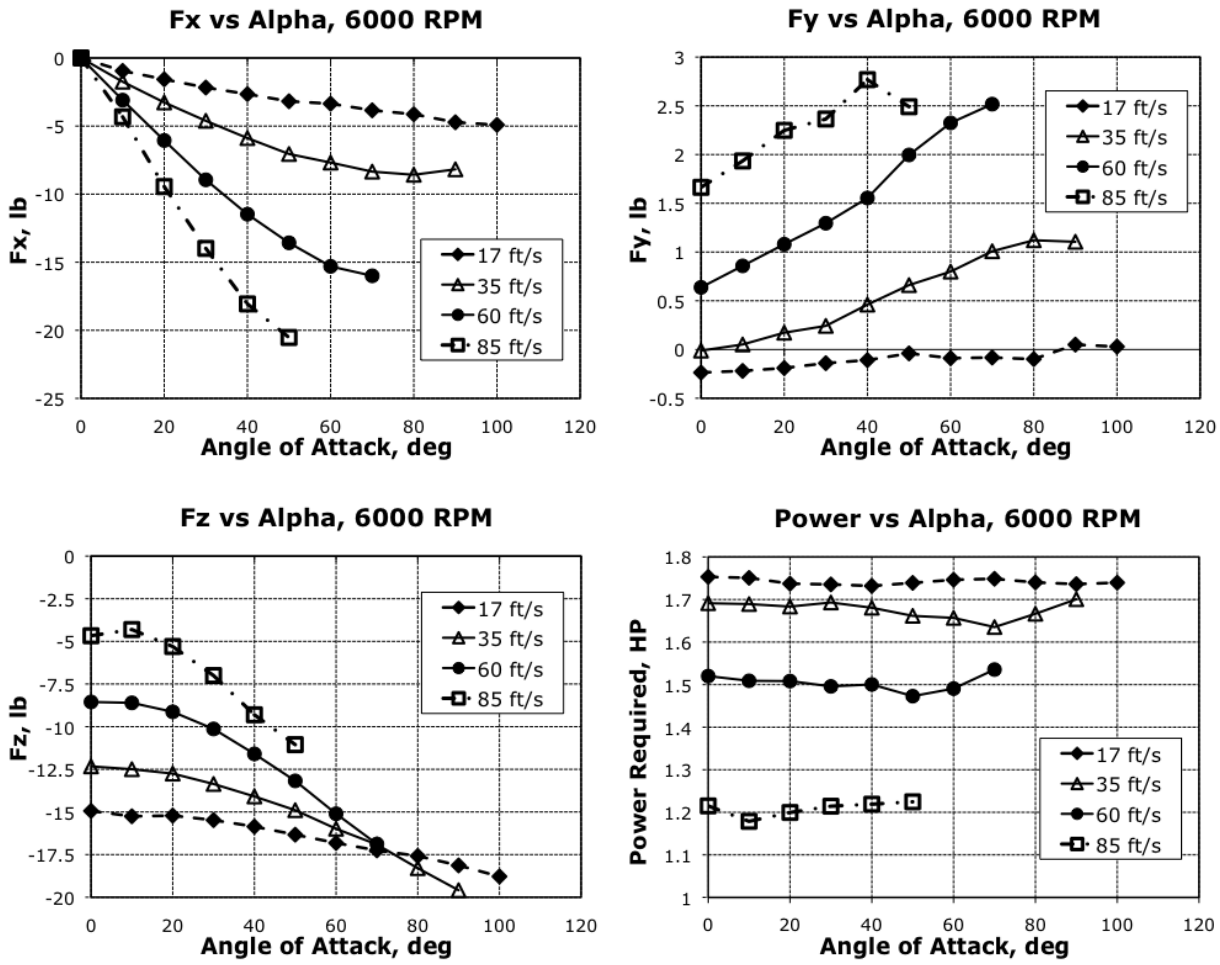

Figure A-3. Forces and Power vs. Angle of Attack, 6000 RPM.

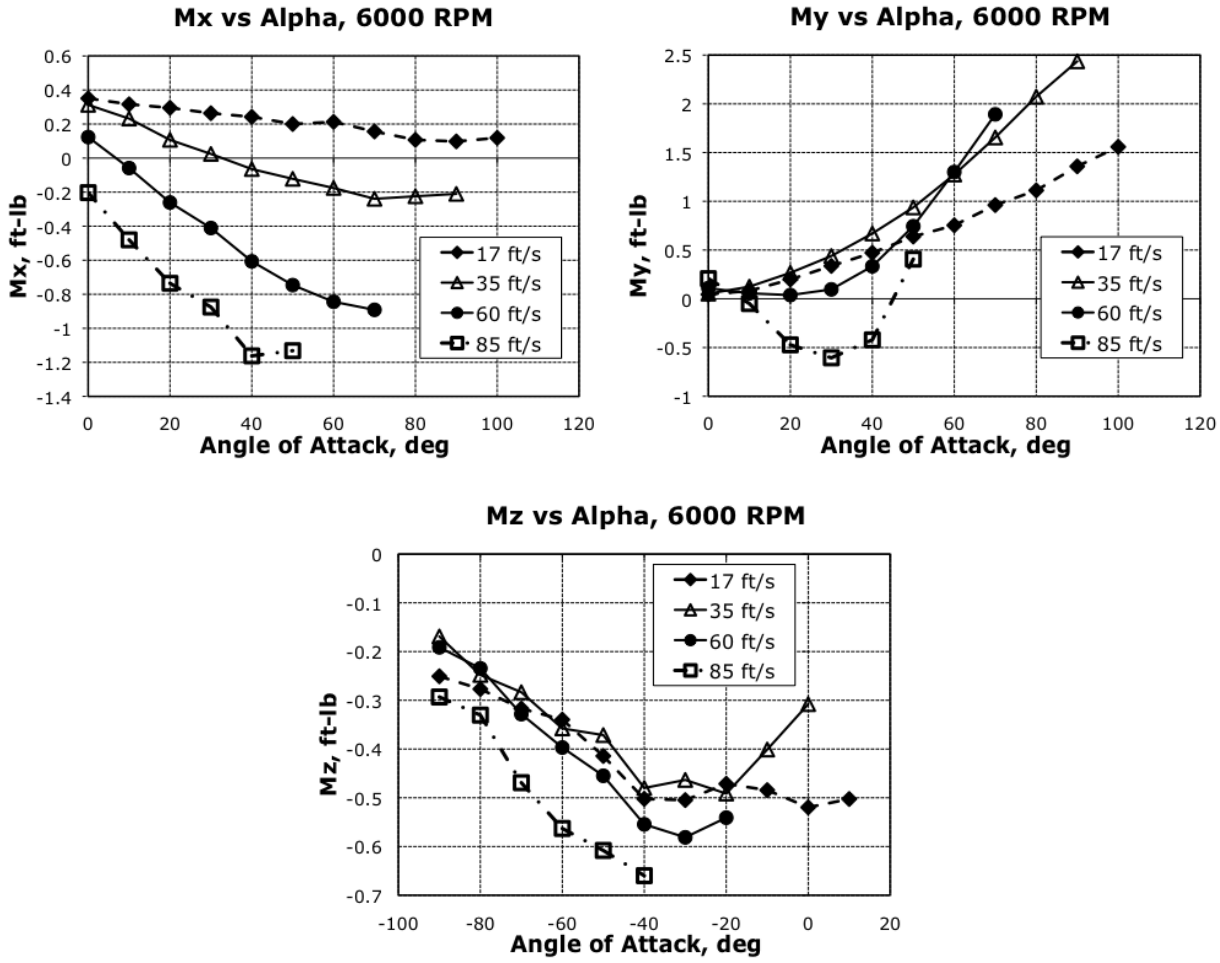

Figure A-4. Moments vs. Angle of Attack, 6000 RPM.

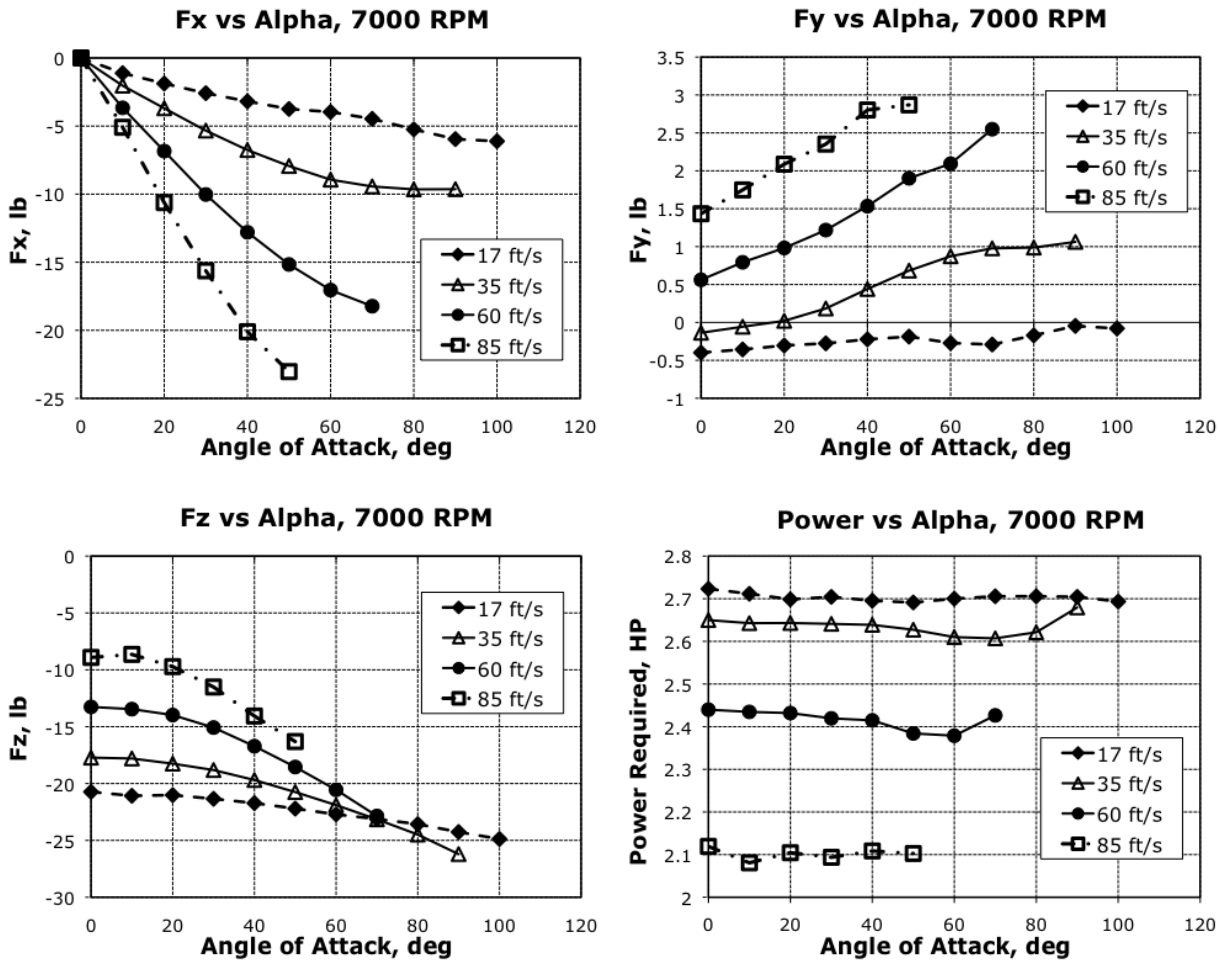

Figure A-5. Forces and Power vs. Angle of Attack, 7000 RPM.

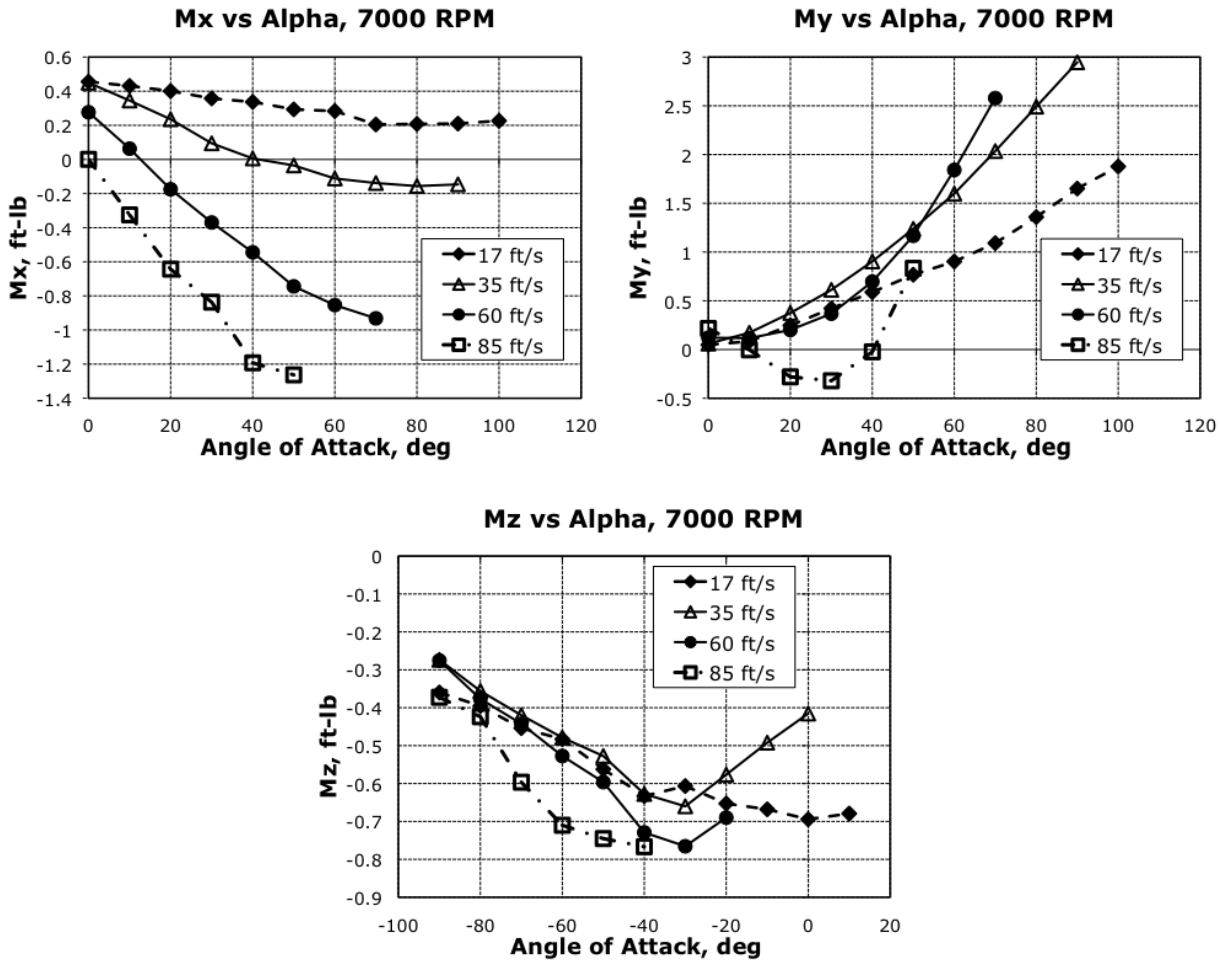

Figure A-6. Moments vs. Angle of Attack, 6000 RPM.

Appendix B: Synthetic Jet Bench Test Hardware Design

The mechanical design of the test hardware for the synthetic jet bench tests had the objective of using modular components to enable testing of a wide variety of configurations. The ability to study the sensitivity to cavity depth (volume), slot width, slot diameter, and jet orientation were all designed into the apparatus. Two rounds of bench tests were performed, with different size diaphragms, and consequently two sets of hardware were designed.

The first round compared the performance of a bimorph disk to custom-made diaphragms employing MFC start-shaped actuators in a bimorph configuration. These elements were nominally 2.5" in diameter. The CAD drawings used to manufacture this test setup are shown in Figure B-1 and B-2. The plates would stack together to attain varying cavity depths, and the diaphragm would be sandwiched between the plates. The bimorph was fragile and a neoprene rubber gasket was used between the metal plates and the bimorph electrode surfaces, which also isolated it electrically from the aluminum base block. The MFC elements were sealed in Kapton, so there were directly clamped between the metal plates.

The second round of SJA bench tests were performed with low-cost 1" diameter unimorph actuators. The modular approach was followed again, but with only a lateral jet orientation possible, as this was the mode in which the actuator would be integrated in the model for tangential blowing. The CAD drawing used to manufacture this test apparatus is shown in Figure B-3.

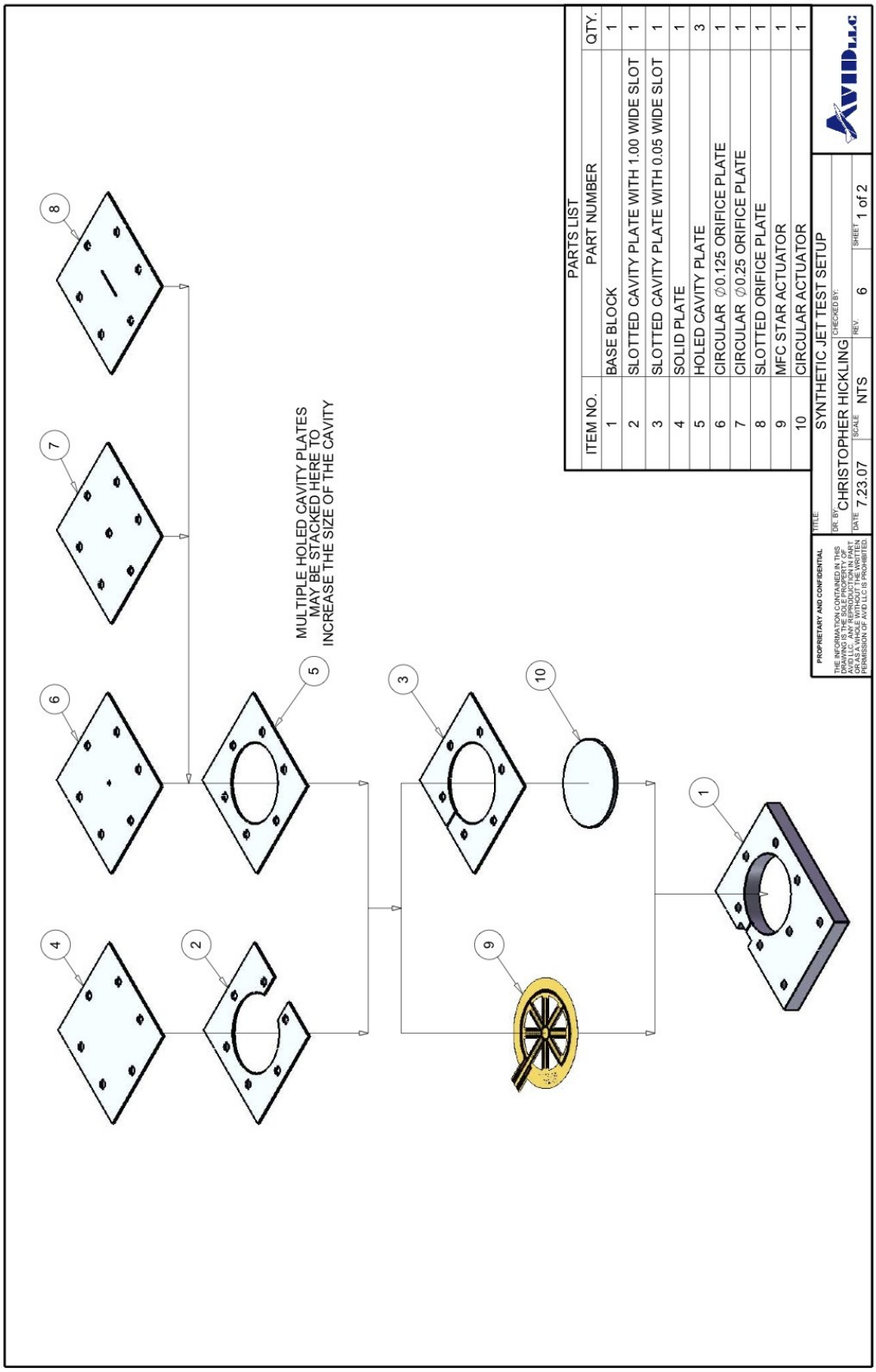

Figure B-1: Round 1 SJA Test Apparatus Assembly View

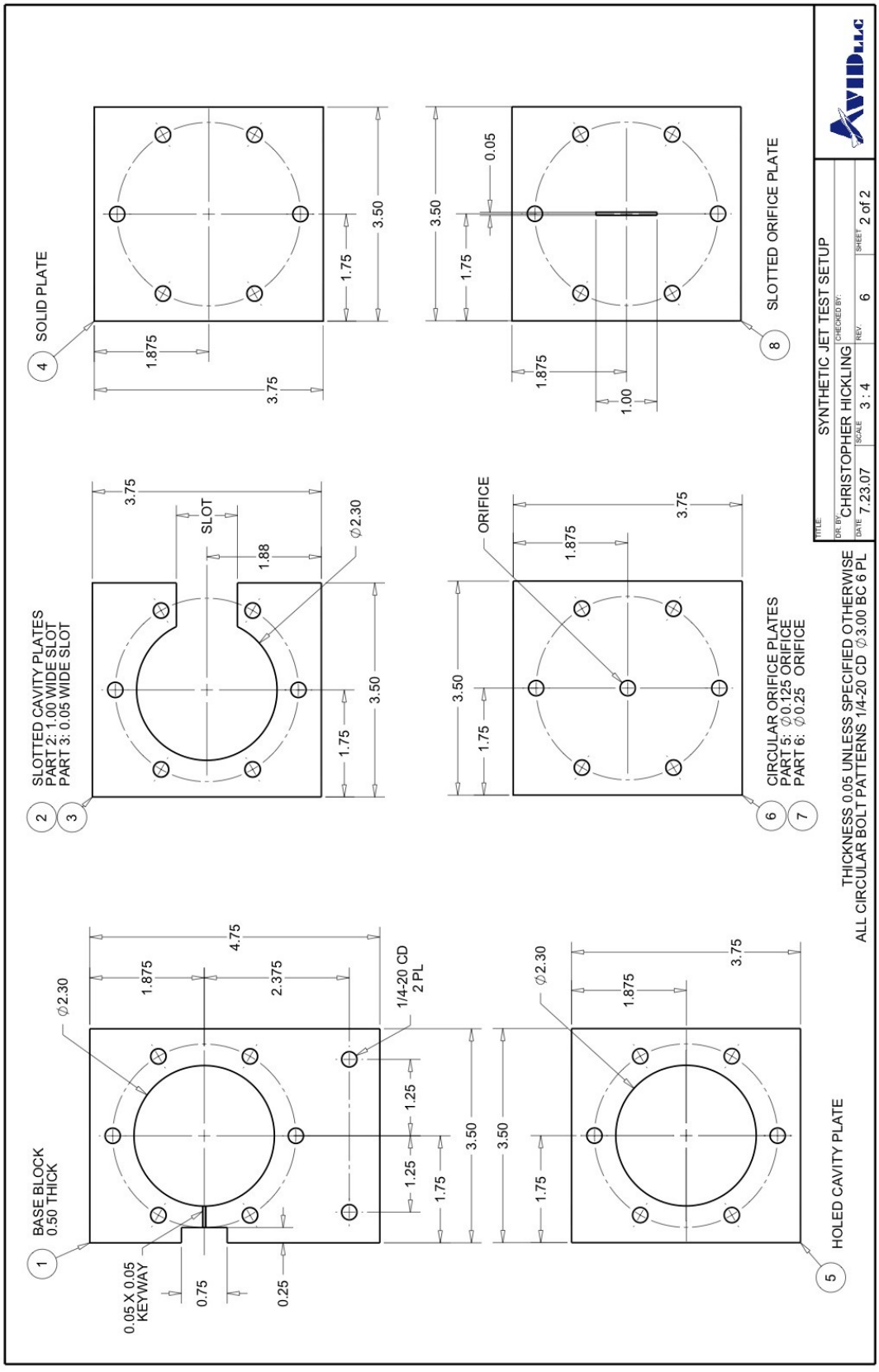

Figure B-2: Round 1 SJA Bench Test Apparatus Part Details

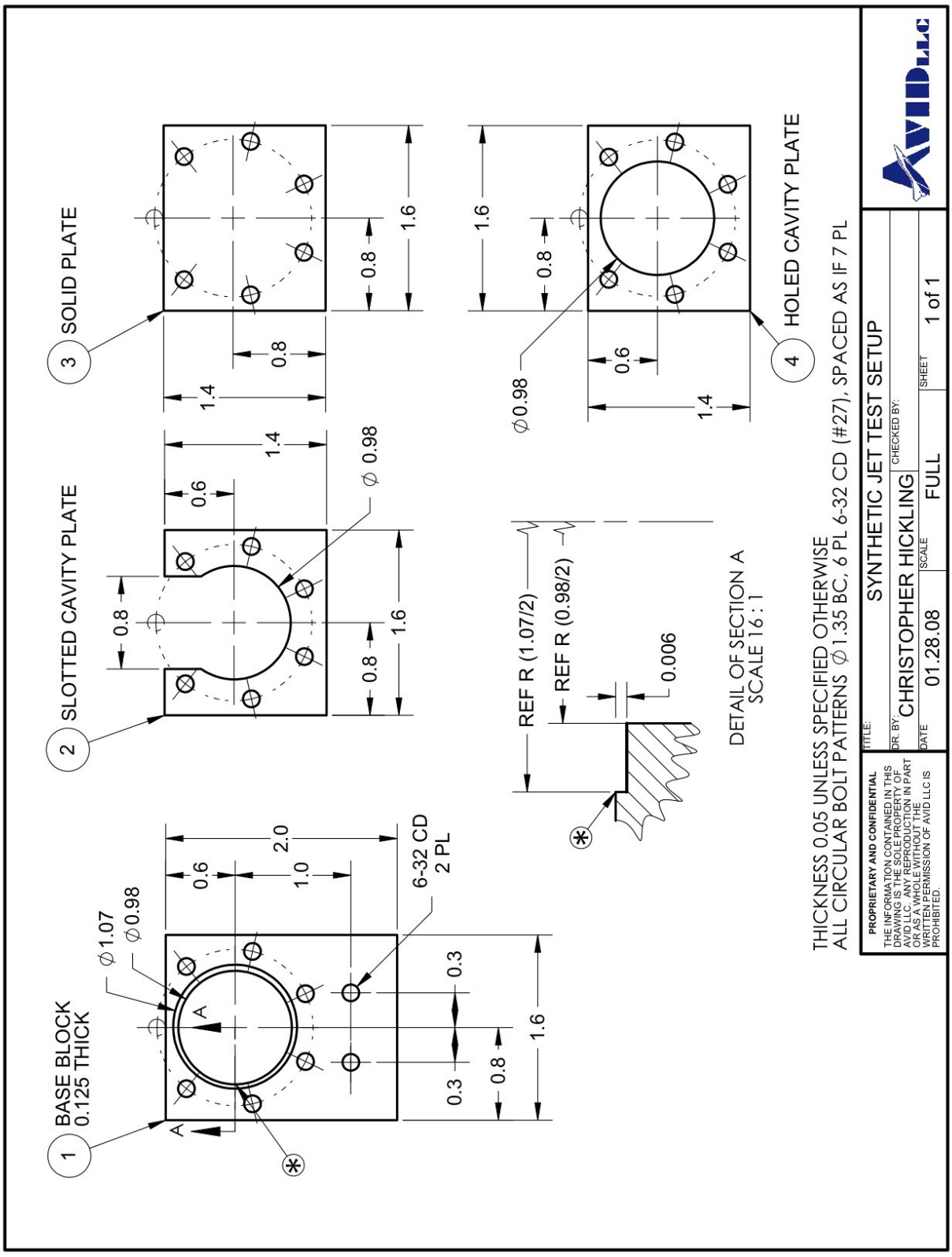

Figure B-3: Round 2 SJA Test Apparatus Part Details

Appendix C: Buckingham Pi Theorem Applied to Ducted Fan Aerodynamics

The Buckingham Pi theorem provides a method for determining non-dimensional parameters that describe a physical phenomenon. If there is an equation based on n physical variables that are based on k independent fundamental physical quantities (like mass, length, time, etc), the theorem states there is an equivalent equation based on $p = n - k$ dimensionless parameters. The original source for this method is [115], but a simpler explanation from Wikipedia[1] was followed to carry out the method.

To find the dimensionless parameters, a dimensional matrix that relates the original variables to the fundamental units is created. For the case of the ducted fan, the set of variables that affect the thrust force are: thrust T ($m\text{-}l/t^2$), density ρ (m/l^3), free-stream velocity V (l/t), fan rotation speed n (rad/t), fan diameter D (l), and angle of attack α (rad). The dimensional matrix has a column for each of these variables, and rows for each type of fundamental unit. Note that angles measured in radians are considered dimensionless. The dimensional matrix for this case is:

$$A = \begin{array}{c} \begin{matrix} T & \rho & V & n & D & \alpha \end{matrix} \\ \begin{bmatrix} 1 & 1 & 0 & 0 & 0 & 0 \\ 1 & -3 & 1 & 0 & 1 & 0 \\ -2 & 0 & -1 & -1 & 0 & 0 \end{bmatrix} \end{array} \begin{matrix} m \\ l \\ t \end{matrix}$$

Using the open-source math software, Maxima, to solve for the nullspace of this matrix. This results in the vectors that span the nullspace (the basis) that are used to construct the dimensionless parameters:

[1] http://en.wikipedia.org/wiki/Buckingham_%CF%80_theorem

$$nullspace(A) = \begin{bmatrix} -1 \\ 1 \\ 0 \\ 2 \\ 4 \\ 0 \end{bmatrix}, \begin{bmatrix} 0 \\ 0 \\ -1 \\ 1 \\ 1 \\ 0 \end{bmatrix}, \begin{bmatrix} 0 \\ 0 \\ 0 \\ 0 \\ 0 \\ -1 \end{bmatrix}$$

Each dimensionless parameter is of the form, where the exponents are directly taken from the nullspace basis vectors:

$$\Pi_i = T^{a1} \rho^{a2} V^{a3} n^{a4} D^{a5} \alpha^{a6}$$

Linear combinations of the basis vectors are allowed to arrive at more meaningful physical quantities. In this case, each vector needs to be negated (sign change) such that the final non-dimensional terms are:

$$\Pi_1 = \frac{T}{\rho n^2 D^4} = C_T, \quad \Pi_2 = \frac{V}{nD} = J, \quad \Pi_3 = \alpha$$

This result matches the non-dimensional terms that are the independent variables in the new model equation: thrust coefficient C_T, J, and α. A similar process can be used for moments and power. The center of pressure was simply non-dimensionalized by divided by the diameter. The figure of merit was already a non-dimensional term and did not need further modification.